Experimental and theoretical study of hot electrons in the context of the shock ignition approach to inertial confinement fusion

Alessandro Tentori

université de BORDEAUX

Thesis

SUBMITTED IN PARTIAL FULFILLMENT OF THE REQUIREMENTS
FOR THE DEGREE OF

Doctor of Philosophy in Plasma Physics

UNIVERSITÉ DE BORDEAUX, ÉCOLE DOCTORALE DES SCIENCES ET DE L'INGÉNIEUR
SECTION : ASTROPHYSIQUE, PLASMAS, NUCLÉAIRE

Experimental and theoretical study of hot electrons in the context of the shock ignition approach to inertial confinement fusion

by
Alessandro Tentori
supervised by
Dimitri Batani
Arnaud Colaitis

Defended on the 23th of February 2022 in Talence (France)
Board of examiners:

Atzeni, S.	Full Professor, Università di Roma La Sapienza	**Reviewer**
Rosmej, O.	Associate Professor, Goethe University Frankfurt	**Reviewer**
Tikhonchuk, V.	Professor Emeritus, Université de Bordeaux, CELIA	**President**
Theobald, W.	Senior Scientist, University of Rochester, LLE	**Examiner**
Wei, M.	Senior Scientist, University of Rochester, LLE	**Examiner**
Cristoforetti, G.	Researcher, Istituto nazionale di ottica, CNR	**Invited**
Raffestin, D.	Research Engineer, CEA-DAM, CELIA (France)	**Invited**
Batani, D.	Full professor, Université de Bordeaux, CELIA	**Director**
Colaitis, A.	Research Engineer, Université de Bordeaux, CNRS, CELIA	**CoDirector**

Acknowledgments

Looking back, if 10 years ago someone had told me "you will go in France for a PhD", I would have said "you're crazy, I would never go". After these three years, I am convinced that having moved in France for a PhD was one of the best choice in my life. Not only from the scientific point of view, but also on a human level. This is thanks to all the wonderful people that I have met during this path.

First of all I would like to thank Dimitri Batani, my supervisor, that took me in his group and gave this great opportunity. I will remember his working method, his kindness and his patience. Many times I asked him scientific questions and he always welcomed me in his office with a smile, suggesting and giving me books and papers to read (papers that are usually very difficult to find!). His large scientific knowledge is something that helped me a lot during these three years. I would also like to thank Dimitri for having taught me the importance of working in an international environment, exchanging ideas and knowledge with other groups from all over the world. I think that this is very important for a student, and not everybody has this opportunity.

The second person that I would like to thank is Arnaud Colaitis, the co-director of the thesis work. The first time I saw Arnaud here in CELIA he was presenting his work to the group and I though "wow, this guy does incredible things and I really would like to work with him!". Useless to say that I was very happy when Dimitri proposed me to have him as co-director. I really would like to thank Arnaud for having followed closely the work and for having been always ready to answer to my questions. I really enjoyed working with him and I learnt a lot. I appreciated his kindness and I am still impressed by his scientific knowledge and the work that he is carrying out here in CELIA. I was really lucky to have him as co-director and I tried to learn from him the maximum I could, both from the scientific and human point of view.

I also would like to thank all the collaborators with whom I had the pleasure to work with, in particular Wolfgang Theobald from Rochester and Gabriele Cristoforetti and Petra Koester from Pisa. I am sure that all the fruitful discussions that we had improved the scientific quality of the work.

A special thanks goes to Didier Raffestin and Philippe Nicolai. They were always ready to answer to my questions, welcoming me in their office with a big smile. We had a lot of discussions and I am sure that this helped me a lot during my PhD. Furthermore, their kindness helps in promoting a very good working environment here at CELIA, and this is very important especially for students which take the first steps in the working world.

Then I would like to thank the jury members. I was honoured to have the opportunity to present my work in front of such experts. A big thank to Olga Rosmej, Stefano Atzeni and Mingsheng Wei for having carefully read my manuscript and for having appreciated the job (also Wolfgang Theobald and Gabriele Cristoforetti were in the jury panel, already cited as collaborators). I would like to thank them also for the interesting discussion taken during my PhD defense. A special thanks goes to Vladimir Tikhonchuk, that has done a careful analysis and correction of my PhD thesis, from which arose a discussion of three hours in his office. I hope to have other discussions and the possibility of working with him in the future.

Let me also take the opportunity here to thank a person in particular: Matteo Passoni, a professor at Politecnico di Milano. Matteo was the supervisor of my master thesis work, and he followed me during my study path at Politecnico di Milano. The work of Matteo is very important, since he takes care that each student of nuclear engineering follows an adequate studying path, which provides a solid background in engineering and in physics. It is useless to say that my previous studies at Politecnico di Milano helped me a lot to face all the difficulties meet during the PhD.

A thesis work is for sure a challenging and busy period, but it was made less difficult by the presence of colleagues and friends. A special thanks go to my close colleagues tovarish Lena and fantaros Donaldi. I think that without them these three years would not have been so funny. In particular, thanks to Lena for having me taught the Russian basis and for having made me notice, in a kind and polite way, that I should dress better in a working enviroment. Thanks to Donaldi for all the funny moments and for having accepted the fact that I am allergic and I can't enjoy meals like he does (he ate spaghetti for 2 weeks in Japan because of my allergy). A special thanks also to my co-bureau Alexandre and Corisande for all the funny moments we spent together and for having listened to my many whatsapp vocals. Let me also say that the greatest achievement in these three years was the fact that Alexandre used the Italian expression "boh" to say "I don't know".

Special thanks also to the others CELIA students: in particular to Eduardo (scusa Edo, non credo che qualcuno abbia capito che ti chiami Edoardo) for all the interesting discussions and funny moments and political debates; to Diego and Duncan, I am so sorry that we started playing football and I have to leave :(; Paul, Thibault, Victorien and Julien for all the funny moments that we spent together. When I arrived I though that French people have cold personality, but in reality it is exactly the opposite. I really enjoyed these three years!

I would like also to give a special thanks to my former colleagues: Alessandro Ruocco, Gabriele Birindelli and Pedro Gonzalez. They helped me to enter in such a big and unknown world like elder brothers. Their example and their guide was very important for me when I arrived here.

A special thanks also to other colleagues that I had the opportunity to meet: Luke, Christos, Francesco, Phill, Antoine, tovarish Nikita, Micha, Gabriel and Romain.

I would like to thank also the the administrative and informatic staff of the CELIA laboratory composed by Sophie, Celine, Sonia (ciao bella), Richard and Gaetan. Your patience, your kindness and your professionalism are essential for the laboratory.

I would like to thank all the friends that I met here in Bordeaux, with which I spent great time and evenings: Nadia, Giovanni, Sally, Silvia, Cristina, Giuliano, Giuliana, Johannes, Julien (futuro premio nobel), Stephane, Marine, Sergio and David.

A great thanks to all my family, to my parents, my grandparents and zio and zia, who supported me and accepted this separation, even if for them it was hard. I am sure that soon we will be all together again enjoying the meal prepared by nonna. A special thought to Roberto and Anna, that are growing and living the years of Liceo without me. A spe-

cial thanks and a great thought to my sister Eleonora, that is completing her studies and taking care of all the family without me. Especially in this difficult period of pandemic, I know that my help at home would have made the difference. I also would like to thank all the family members and friends that supported me with enthusiasm from Italy, and they never forgot to text me: Daniela and Roberto, Carlo and Carla, Doris, Tommaso, zia Livia and zio Raf.

Finally, I would like to thank Gloria. Without her support and her love, probably I would only have accomplished half of the work. Thank you for your support, for having accepted my working weekends, for having waited for me at home late in the evening, and for having been by my side all the time. I will be soon with you in Strasbourg and a bright future is waiting for us.

Communications related to this thesis

Several parts of this work have been communicated to the scientific community. We give here a list of the publications in peer-reviewed journals.

- L. Antonelli et al. *Laser-driven strong shocks with infrared lasers at intensity of* 10^{16} W/cm^2. In: Physics of Plasmas 26.11, p. 112708. doi: 10.1063/1.5119697. eprint: https://doi.org/10.1063/1.5119697. url: https://doi.org/10.1063/1.5119697.

- S.D. Baton et al. *Preliminary results from the LMJ-PETAL experiment on hot electrons characterization in the context of shock ignition*. In: High Energy Density Physics 36, p. 100796. issn: 1574-1818. doi: https://doi.org/10.1016/j.hedp.2020.100796. url: https://www.sciencedirect.com/science/article/pii/S1574181820300550.

- P. Koester et al. *Bremsstrahlung cannon design for shock ignition relevant regime*. In: Review of Scientific Instruments 92.1, p. 013501. doi: 10.1063/5.0022030. eprint: https://doi.org/10.1063/5.0022030. url: https://doi.org/10.1063/5.0022030.

- A. Tentori et al. *Experimental characterization of hot-electron emission and shock dynamics in the context of the shock ignition approach to inertial confinement fusion*. In: Physics of Plasmas 28.10, p. 103302. doi: 10.1063/5.0059651. url: https://doi.org/10.1063/5.0059651.

- A. Tentori et al. "*3D Monte-Carlo model to study the transport of hot electrons in the context of Inertial Confinement Fusion: Part I*" In preparation.

- A. Tentori et al. "*3D Monte-Carlo model to study the transport of hot electrons in the context of Inertial Confinement Fusion: Part II*" In preparation.

Contents

Chapter 0

Introduction

Controlled nuclear fusion is a promising form of power generation that can overcome the problematic related to the exploitation of conventional oil and coal-based sources. In 2020, the global energy consumption was based on oil (31%), coal (27%), natural gas (25%), nuclear fission (4%) and renewable sources (13%) [1]. The exploitation of fossil fuels is based on chemical reactions that produce a copious amount of CO_2:

$$\begin{aligned} &\mathrm{C} + \mathrm{O_2} \rightarrow \mathrm{CO_2} + Q \ \ (Q = 3.6 \text{ eV}) \,, \\ &\mathrm{CH_4} + 2\mathrm{O_2} \rightarrow \mathrm{CO_2} + 2\mathrm{H_2O} + Q \ (Q = 9.22 \text{ eV}). \end{aligned} \tag{1}$$

In the equations, Q represents the amount of energy released by the reaction. Since these are based on the association or dissociation of molecules (i.e. chemical reactions), the Q values are of the order of $\sim$eV. This low value of released energy imposes the need of burning a considerable amount of fuel to satisfy energy demand. This poses important concerns regarding the global warming and the air pollution, since the CO_2 produced remains in the atmosphere trapping the heat. Moreover, the world population growth makes the fossil fuels an insufficient resource for satisfying the energy demand on long time scales.

The renewable energy, notably solar, wind, tidal power and pumped hydro emit less greenhouse gases compared to fossil fuel, but they present other issues difficult to overcome. In particular, the aleatory nature of the source makes the produced power discontinuous and the grid load must be supplied using baseline reactors based on fossil or nuclear fuel.

Nuclear fission represents a very efficient form of energy production, since the energy released by nuclear reactions is $\sim 10^6$-10^7 times greater than the energy released by the chemical ones. From a practical perspective, the fission of 1 gram of Uranium 235 produces the same amount of energy as the combustion of 3 tons of coal [2]. As an example, the uranium-235 fission reaction reads:

$$^{235}\mathrm{U} + \mathrm{n} \rightarrow \mathrm{F_1} + \mathrm{F_2} + \nu\mathrm{n} + Q \ (Q = 211 \text{ MeV}), \tag{2}$$

where F_i are the fission fragments and ν is the number of neutrons released during the reaction. Despite that nuclear fission power plants do not produce significant air pollutants, a large disadvantage comes from the spent fuel treatment. In particular, the spent fuel is composed of highly radioactive nuclei that present a radiation hazard for extended periods of time. Long-lived fission products must be isolated from biological systems for time scales of the order of 10^5-10^6 years. Several schemes have been proposed to achieve this isolation, but no system has yet been adopted that can guarantee isolation over this

long time period.

Nuclear fusion could be one of the solutions to the energy problem, because it offers ecological and safety advantages compared to the exploitation of fossil or fissile fuels. Fusion fuel can be extracted from seawater and no long-lived radioactive waste is produced (particular care should be however given to the choice of the chamber material to avoid activation). There is one considerable disadvantage, however: to be combined, two light nuclei should overcome the Coulomb barrier. This can be done by giving the nuclei a high initial kinetic energy, i.e. accelerating the nuclei to high velocities. To reach a high number of reactions, it is thus necessary to raise the bulk temperature of the material. In this way, the Coulombic repulsion can be overcome and the short-range attractive nuclear force comes into play.

Although it is quite easy to obtain nuclear reactions in laboratory, nowadays it is still not possible to generate more energy from the fusion mechanism than what is invested in the experiment [3]. This happens because, at such high temperatures, matter tends to disassemble as a consequence of the high pressure. As such, it is necessary to confine the reactants in some way. In the sun, the confinement is driven by the gravitational force. On earth, the two main schemes being investigated to confine a plasma and to keep it at temperatures sufficiently high for the reactions to occur are the *Magnetic Confinement Fusion* and the *Inertial Confinement Fusion*. In magnetic confinement, the plasma is confined by a carefully designed magnetic field configuration and heated by external sources, such as resistive heating or cyclotron heating. In inertial confinement, a solid fuel shell is compressed from many directions with intense laser (or particle) beams. The fuel is heated and ignited from the mechanical work done on the gas inside the target during the compression, or using other methods. Nuclear fusion research as conceived for civilian purposes started in 1950s and it continues nowadays [4].

0.1 Nuclear Fusion

In every atomic nucleus, the mass of the system is smaller than the sum of the masses of its constituents, if measured separately. Namely, the energy mass of a nucleus is less than the sum of the masses of protons and neutrons that constitute it. For a given nucleus, the binding energy, which is the energy needed to separate all the nucleons, is easily calculated according to the *mass defect law*:

$$B(Z,N) = \left[Zm_p + Nm_n - m(Z,N)\right] c^2, \tag{3}$$

where m_p and m_n are the proton and the neutron mass respectively, $m(Z,N)$ the mass of the nucleus and c is the speed of light. The binding energy per nucleon $B(Z,N)/A$ as a function of the mass number is shown in Fig. 1. This quantity increases quickly with A for light nuclei and decreases slowly from 8.5 MeV down to 7.5 MeV, after $A \simeq 60$. This illustrate that the fusion of two light nuclei produces a nucleus with greater binding energies, releasing thus the energy in excess. Similarly, breaking heavier nuclei into light nuclei also releases energy. In this latter case, the energy gain is nearly 1 MeV per nucleon, and thus about 200 MeV are gained in each event (See eq. (2)).

Considering nuclear fusion, the choice of the fuel influences the confinement requirements. As mentioned above, in order to produce energy, it is necessary to confine the plasma at

high temperature for a time window long enough for a sufficient number of fusion reactions to occur. Naturally, one would like to keep the temperature reached by the fuel as low as possible. The hydrogen isotopes, deuterium and tritium, have smaller Coulomb barrier to overcome compared to other elements. As such, even if their energy output is less, they are the best candidates for current fusion applications. Furthermore, deuterium can be produced from sea water, while tritium can be generated by bombarding lithium with neutrons directly in the reactor. For what concerns the radiation hazard, tritium is a beta emitter with half-life of 12.32 years, however much less compared to the $\sim 10^4 - 10^5$ years that characterize the elements in the spent nuclear fuel coming from a fission reactor. The fusion reactions of interest are:

$$\begin{aligned} &\mathrm{D} + \mathrm{T} \rightarrow \alpha\,(3.52\ \mathrm{MeV}) + \mathrm{n}\,(14.06\ \mathrm{MeV})\,(Q = 17.58\ \mathrm{MeV})\,, \\ &\mathrm{D} + \mathrm{D} \rightarrow \mathrm{T}\,(1.01\ \mathrm{MeV}) + \mathrm{p}\,(3.03\ \mathrm{MeV})\,(Q = 4.04\ \mathrm{MeV})\,, \\ &\mathrm{D} + \mathrm{D} \rightarrow \mathrm{He}^3\,(0.82\ \mathrm{MeV}) + \mathrm{n}\,(2.45\ \mathrm{MeV})\,(Q = 3.3\ \mathrm{MeV})\,, \\ &\mathrm{He}^3 + \mathrm{D} \rightarrow \mathrm{p}\,(14.67\ \mathrm{MeV}) + \alpha\,(3.67\ \mathrm{MeV})\,(Q = 18.3\ \mathrm{MeV})\,. \end{aligned} \tag{4}$$

When two nuclei fuse, a compound nucleus is formed that splits immediately into the two reaction products. Since the reacting particles have energies in the range of 1-10 keV, the reaction products carry a total kinetic energy that is equal to Q and it is possible to write:

$$\frac{1}{2} m_b v_b^2 + \frac{1}{2} m_Y v_Y^2 \simeq Q, \tag{5}$$

where m and v are the final masses and velocities of the two products b and Y. The momentum conservation reads:

$$m_b v_b \simeq m_Y v_Y \tag{6}$$

and the two particles are emitted in opposite direction. From these two conservation equations, it is clear how the lighter product takes the larger amount of energy:

$$\begin{aligned} \frac{1}{2} m_b v_b^2 &= \frac{Q}{1 + m_b/m_Y}, \\ \frac{1}{2} m_Y v_Y^2 &= \frac{Q}{1 + m_Y/m_b}. \end{aligned} \tag{7}$$

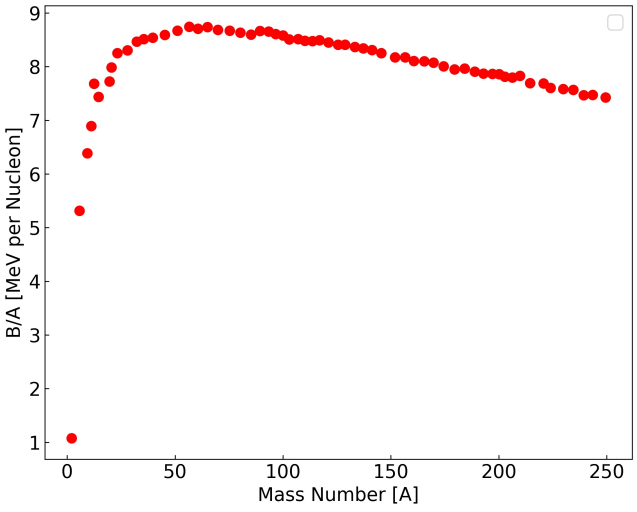

Figure 1: Binding energy per nucleon as function of atomic mass A, from [5].

In a hypothetical fusion reactor, it will be necessary to convert this kinetic energy into thermal energy to produce electrical power.

An important figure of merit that characterizes nuclear reactions is the cross section $\sigma(v)$. This quantity expresses the probability of having a reaction when two particles collide. Fig 2 (a) shows the behaviour of the cross sections as a function of the center of mass energy, considering the DT and the DD reactions. In general, the cross sections increase with the center of mass energy up to a maximum, but then they start decreasing because of the reduction of the interaction time between the two particles. In particular, the DT cross section shows a maximum of 5 barn for center of mass energies around $60 - 70$ keV. This maximum is due to the ^{5}He compound nucleus formation. The DD cross section presents values about 100 times lower compared to the DT ones.

A fusion reactor will have a net energy gain if the energy released exceeds the energy losses and the initial energy investment to heat the fuel. Following the Lawson's paper [6], we report the criteria which should be satisfied to obtain an energy gain greater than one. In particular, as done in [6] and in the books [5] [7], the energy balance is computed neglecting the thermal conduction and the bremsstrahlung losses and considering only the energy invested to heat up the fuel and the output energy. The power output of a nuclear reactor is related to the *Reaction Rate*, defined as the probability of having a reaction per unit time and unit volume. If a gas of particles 1, characterized by a distribution in velocity $g_1(\mathbf{v}_1)$, collides with a gas of particles 2, characterized by a distribution in velocity $g_2(\mathbf{v}_2)$, the reaction rate reads:

$$R_{12} = n_1 n_2 \int \mathrm{d}\mathbf{v}_1 \int \mathrm{d}\mathbf{v}_2 g_2\left(\mathbf{v}_2\right) g_1\left(\mathbf{v}_1\right) \left|\mathbf{v}_1 - \mathbf{v}_2\right| \sigma\left(\left|\mathbf{v}_1 - \mathbf{v}_2\right|\right) = n_1 n_2 \langle \sigma v \rangle_{12} \left[\frac{1}{\mathrm{cm^3 s}}\right]. \quad (8)$$

Here n_1 and n_2 are the densities of the species 1 and 2, respectively. Considering n_1=n_2=$N/2$ and introducing the mass density $\rho = \sum_j n_j m_j = N\bar{m}$, where $\bar{m}$ is the average nuclear mass, this quantity is proportional to the square of the density mixture, i.e.:

$$R_{12} = \frac{\rho^2}{4\bar{m}^2} \langle \sigma v \rangle_{12}. \quad (9)$$

This equation indicates the role of the fuel density in achieving efficient release of fusion energy. Multiplying the reaction rates by Q and considering as an example an ion density of 10^{15} cm^{-3}, the volumetric power output is:

$$P_{out} = \frac{N^2}{4} \langle \sigma v \rangle Q \ \left[\frac{\mathrm{W}}{\mathrm{cm^3}}\right]. \quad (10)$$

Fig. 2 (b) reports the power output for the reactions D-T and D-D, considering the particle velocity described by the Maxwell Boltzmann distribution function:

$$g\left(\mathbf{v}\right) = N \left(\frac{m}{2\pi T}\right)^{3/2} e^{-mv^2/2T}. \quad (11)$$

In this equation, m is the mass of the particles and T the temperature.

Considering now the bremsstrahlung losses for a plasma in which particles are described in velocity by a Maxwell-Boltzmann distribution function (eq. (11)), the volumetric power

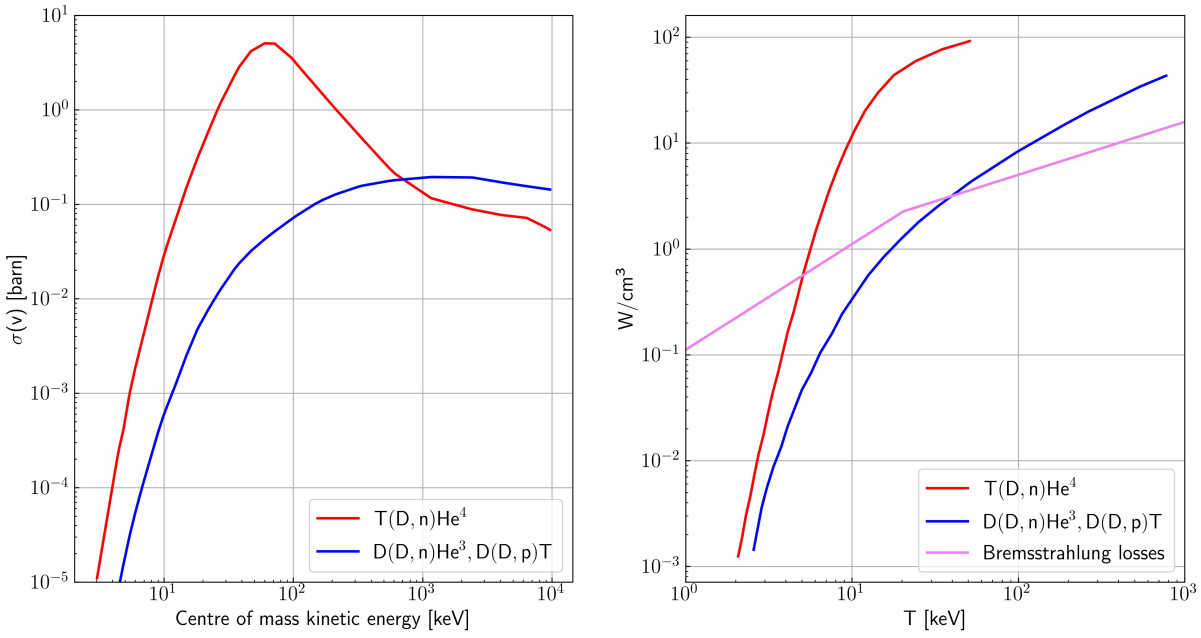

(a) (b)

Figure 2: (a) Cross sections as function of center of mass energy for the reactions $\mathrm{T(D,n)He^4}$, $\mathrm{D(D,n)He^3}$, $\mathrm{D(D,p)T}$. Data is taken from [8]. (b) Comparison of bremsstrahlung losses with power output of D-D and D-T reactions, for interacting particles characterized by a Maxwellian distribution function in velocity with temperature T (see eq. (11)). Quantities are calculated considering an ion density of $\sim 10^{15}\mathrm{cm}^{-3}$. Data is taken from Ref.[5].

radiated reads [5], [6]:

$$P_{br} = 0.5 \times 10^{-30} Z^2 N n_e T^{1/2} \left[\frac{\mathrm{W}}{\mathrm{cm}^3}\right]. \tag{12}$$

Here T is the plasma temperature in keV and N and n_e are the ion and the electron densities in $1/\mathrm{cm}^3$. The bremsstrahlung losses as a function of T are reported by the violet line in Fig. 2 (b). From the figure, it is possible to see that there is a temperature at which the fusion output exceeds the bremsstrahlung losses, which is of the order of 4 keV for D-T and 50 keV for D-D reactions. This suggests that, in the temperature region that is likely to be achievable in a thermonuclear fusion reactor (1- 10 keV, T $\sim 10^7$-10^8 Kelvin), the D-T reaction is the favored one. To calculate the energy balance for a thermonuclear fusion reactor, as done in the Lawson paper [6] [5], the bremsstrahlung term is neglected and the energy needed to heat the plasma is compared to the energy output. We are thus considering plasma temperatures for which the volumetric power output is greater compared to the bremsstrahlung losses (see Fig. 2 (b)). The energy needed to heat up a plasma composed by ions and electrons ($n_i = n_e = N$) is:

$$E_k = 3NT, \tag{13}$$

where T is the temperature reached. As such, to have a positive gain, it is necessary that:

$$\begin{aligned} P_{out}\tau > 3NT, \\ \tau N > 3NT \Rightarrow N\tau > \frac{12T}{\langle v\sigma \rangle Q}, \end{aligned} \tag{14}$$

where τ is the confinement time. This relation is called Lawson criterion and it allows to estimate the minimum product of ion density and confinement time to obtain an energy gain greater than one. In the case of DT fuel at 5-10 keV, the Lawson criterion becomes $\tau N \simeq 10^{14} - 10^{15}$ s cm^{-3}. As previously mentioned, the two main approaches that have been pursued in the last decades to obtain fusion energy are the magnetic and the inertial confinement fusion. Magnetic confinement tries to fulfil the Lawson criterion confining low density plasmas (10^{14} cm^{-3}) for long time ($\tau \sim 1 - 10$ s). In inertial fusion, confinement times are extremely short $< 10^{-10}$ s, but the densities reached by the fuel are typically greater than 10^{25} cm^{-3}. Let us remark that these criteria are derived under optimistic assumptions and they are necessary, though not sufficient for the successful operation of a thermonuclear reactor. More detailed calculations in which the bremsstrahlung and the conduction losses are accounted are shown in Ref. [8].

0.2 Inertial Confinement Fusion

In inertial confinement fusion, a small amount of fuel material is compressed to very high densities and temperatures by exploiting the radiation produced by high-power laser beams. The scheme was first proposed by Nuckolls [9] and Basov [10] in 1972. Starting from energy considerations, a fusion reactor can be operational only if the energy extracted from the process exceeds the input energy. When the mechanism was proposed, it was believed that 60 kJ of laser energy would have been sufficient to generate an equal thermonuclear energy. Unfortunately, several inefficiencies have had to be taken into account during the years. First of all, not all the laser energy heats up the fuel and the implosion by rocket effect has low efficiency. Several unwanted mechanisms such as hot electron production or light backscattering reduce the quantity of light absorbed, causing a reduction of the implosion performance. Furthermore, the efficiencies by which the fusion target chamber and subsequent turbines convert fusion output to electricity should be accounted. Finally, the conversion of electric energy into laser energy is also heavily inefficient.

Simple calculations of the requirements to be fulfilled by an hypothetical fusion reactor are shown by Rosen (1999) [11]. Let P_{in} be the amount of electric power supplied to run the driver (the laser) and η_D the efficiency through which this latter converts the input energy into the energy delivered on the target. If G is the target gain, the output fusion power reads $P_{out} = G\eta_D P_{in}$. If η_{th} is the conversion efficiency of output fusion energy to electricity (i.e. turbine and target chamber efficiency) and f the recycle fraction to run the driver, the following relation is obtained:

$$P_{in} = P_{out} f = P_{in} f \eta_D G \eta_{th} \Rightarrow f \eta_D G \eta_{th} = 1. \tag{15}$$

Considering reasonably $\eta_{th} \sim 0.4$ and $f \sim 0.25$, the criterion on the gain and on the driver efficiency is $G\eta_D > 10$. If $\eta_D \sim 0.1$, the criterion requires a gain of ~ 100. To obtain such

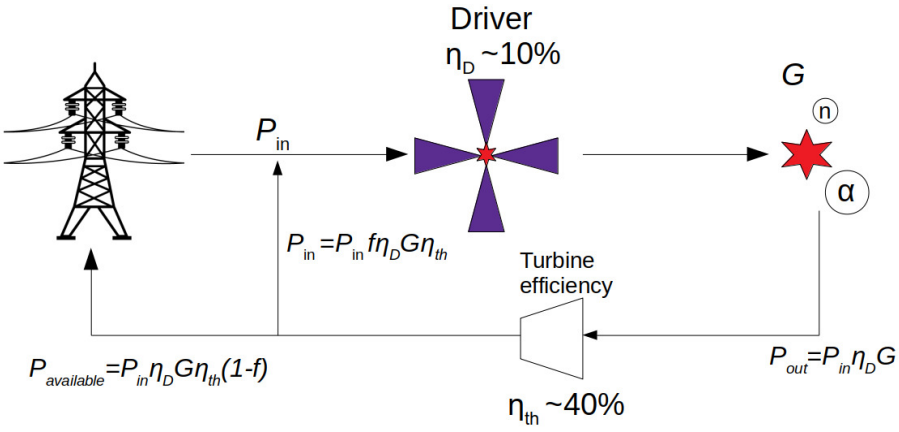

Figure 3: Schematic of power flow on an electric plant.

high values of gain, it is necessary to burn a considerable fraction of fuel. The burnt fuel fraction reads [12] [11]:

$$f_b = \frac{\rho R}{\rho R + 8\sqrt{\bar{m}_{DT} c_s / \langle \sigma v \rangle}}, \tag{16}$$

where c_s is the speed of sound, ρR the areal density of the fuel, $\bar{m_D}$ is the mass of a "DT" nucleus (∼2.5 AMU) and $\langle \sigma v \rangle$ the average reactivity, as defined in eq. (8). The function $H_b = 8\sqrt{\bar{m}_{DT} c_s \langle \sigma v \rangle}$ depends on the fuel temperature, and it has values around 6-9 g/cm^2 in a temperature range that goes from 10 up to 100 keV [11] [8]. Taking $H_b = 6$, the formula (16) becomes:

$$f_b = \frac{\rho R}{\rho R + 6}. \tag{17}$$

The fuel burn up required to obtain sufficiently high gains is around 1/3 [11]. Considering this requirement, a condition on the fuel areal density from formula (17) is obtained: $\rho R = 3$ g/cm^2. In each implosion, the energy released should be of the order of GJ, in order to not damage the reactor vessel. If we assume a burn-up of 30% and considering that the energy per gram produced by the DT fusion is $3.4{\times}10^{11}$ J/g, one should limit the fuel mass to a few mg. Some considerations on the compression level can be drawn recasting the capsule mass formula as a function of ρR: for a spherical target $M = \frac{4\pi}{3}\rho R^3 = \frac{4\pi}{3}(\rho R)^3/\rho^2$. Fixing the product $\rho R = 3$ g/cm^2, burning 5 mg of fuel would require $\rho \sim$190 g/cm^3. As such, considering that the initial cryogenic fuel density is 0.250 g/cm^3, a compression factor of $\sim$ 1000 should be achieved. If 5.5 $\times 10^8$ J are produced by burning 5 mg of fuel (considering the 30% of fuel burn-up), 5 shots per second would provide an energy of ∼3 GW of fusion power. Taking into account all the losses and the fraction of energy required to run the driver, 1 GW of power delivered to the electric grid would be realistic.

The historical and standard approach to ICF is the *hot-spot ignition*. In this scheme, only a small mass of the target is brought to the required conditions of density and temperature to initiate the reactions. Subsequently, the α particles produced will heat up the dense cold shell around the hot-spot, igniting the remaining fuel part. During the years, several target and laser configurations have been proposed to achieve the goal [13] [8] [14] [15]. Usually, ICF capsules are spheres of 1.5 - 3 mm radius, composed by an external high Z ablator of tens of μm which contains a DT-ice cryogenic shell of hundreds of μm and density of ∼0.25 g/cm^3. The central part of the sphere is filled with DT vapour at

$\sim$0.0005 g/cm^3. As the laser interacts with the ablator, this latter ionizes and vaporizes in a process called *ablation*. The pressure resulting from the ablation at the shell surface reaches values around 100 Mbar. Because of momentum conservation, the inner part of the capsule moves inward and the center is compressed to high densities and temperatures. The mechanism is explained in detail in the following.

Compression must be achieved following the isentropic curve as closely as possible. According to the second law of thermodynamics, the variation of the internal energy e of an amount of matter, due to an heat transfer $\mathrm{d}q = T\mathrm{d}S$ and a work done $-p\mathrm{d}V$ reads:

$$\mathrm{d}e = T\mathrm{d}S - p\mathrm{d}V. \tag{18}$$

Here ds is the specific entropy, p the pressure and V the specific volume of the amount of matter. In an isentropic compression, the term $T\mathrm{d}S$ is zero, thus minimizing the invested energy. Compressions as closest as possible to the isentropic are provided in ICF using a sequence of shocks of increasing strength. As shown in Sec. 1.3.2, shock waves produce large amounts of entropy and it is not possible to compress indefinitely the matter using a single shock wave. As such, these shocks should be carefully timed in order to coalesce in the inner part of the shell [8] [7]. This is needed to avoid shell preheat or the formation of rarefaction waves. If the inner part of the shell is preheated by the premature arrival of shocks or by other mechanisms, the compression will be more difficult. Pressure increase from a few Mbar up to 100 Mbar can be achieved either using a continuous low intensity foot pulse [continuous-pulse (CP) design] [14] [16], or by launching a sequence of shocks of increasing strength using laser *pickets* [multiple-shock(MS) designs] [15] [17]. These pre-compression beams will launch a compression wave propagating through the ice-DT shell. When this wave breaks out into the shell inner surface, the latter expands forward, launching a shock in the gas and a rarefaction wave in the shell. When the rarefaction wave arrives at the shell outer surface, the latter starts accelerating and the so-called *acceleration phase* begins. Before the breaking out of compression wave into the vapour, the pulse power is risen rapidly, originating a second shock that merges with the previous in the inner surface of the ice layer. This will keep the shell close to the shock front travelling inside the gas. When the laser is turned off, the shell is travelling at approximately constant velocity. The inward motion of the shell originates a shock wave that propagates in the vapour region. This shock is reflected at the centre of the capsule and it bounces back encountering the incoming inner shell surface, which in turn is impulsively decelerated. The shock experiences a series of reflections and the shell decelerates at each reflection, in the so-called *impulsive deceleration phase* [18]. After some reflections, the shock becomes weak and the gas and the shell develop a fairly uniform pressure creating the so called *hot spot*. At this stage, the inner shell is not completely stopped and it decelerates up to stagnation acting like a rigid piston that heats up the hot spot thanks to the $p\mathrm{d}V$ work [18] [19]. Here the kinetic energy of the imploding capsule is converted into internal energy and the hotspot pressure and temperature keep increasing. The hot spot mass also increases because of the ablation of the shell inner surface. When the deceleration phase ends, the shell stagnates and the pressure is almost constant throughout the hot spot and the shell [20] [21] [22]. If the areal density of the region surrounding the hot-spot is sufficiently high, the α particles generated by fusion reactions will deposit energy triggering an outward burning wave. This phase is called *ignition and burning phase*. During this time, a very high pressure is created and the remaining fuel will blow apart, ending the ICF cycle. Fig. 4 reports an example of target configuration and pulse shape as proposed in [15].

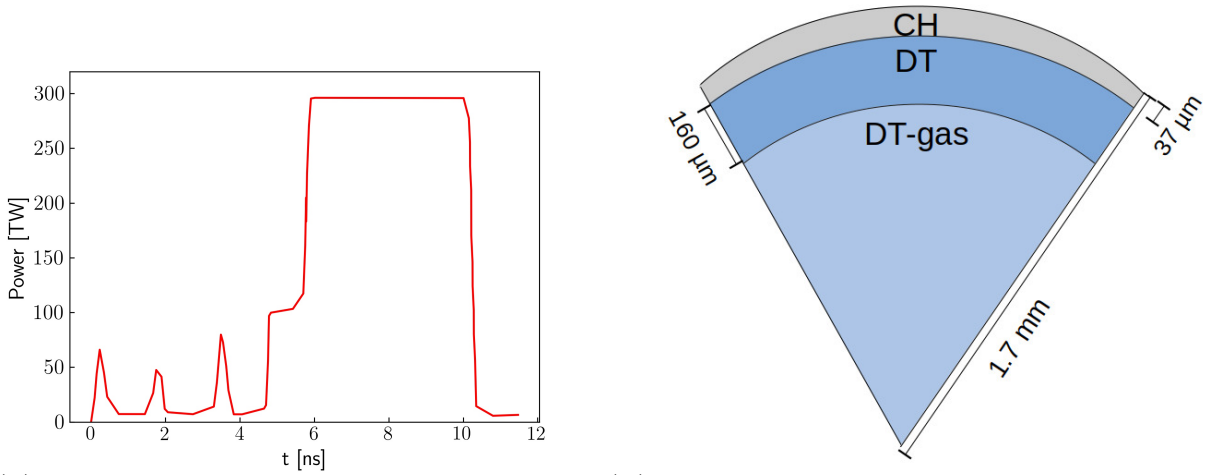

(a) (b)

Figure 4: Capsule configuration and pulse shape proposed in Ref [15]. The design predicts a gain of 48 with 1.5 MJ of laser energy.

One of the potential issues that can compromise the implosion is the shell preheat due to the presence of *hot electrons*. In particular, the high intensity reached by the main driver ($\sim 8 \times 10^{14}$ W/cm^2) overcomes the threshold for the generation of different mechanisms that generate electrons with suprathermal velocities, the so-called hot electrons (see Chap. 1). These electrons can move from the ablation front up to the center of the target, preheating the fuel and making it less compressible. As an example, a preheat deposited energy equal to the Fermi energy of the fuel would mean the need of a double pressure to obtain a given density [12]. An important figure of merit that characterizes the implosion performance is the shell *adiabat* α. The adiabat is defined as the ratio between the shell pressure and the Fermi pressure of the electron gas. Preheat effects due to a not correct shock timing or due to hot electron energy deposition will increase the shell pressure, causing an increase of the adiabat. This implies lower shell compressibility and thus greater laser energy to maintain the performance. Calculations show that the energy required for the shell to ignite scales as $\sim \alpha^{1.88}$ [16] [22].

0.3 Shock ignition approach to inertial confinement fusion

The Shock Ignition approach (SI) is an alternative ICF scheme based on the separation of the compression and ignition phase. The scheme was first proposed by Shcherbakov in 1983 [23] and subsequently reconsidered by Betti [24] as a possible application in NIF-scale facilities. Here the cryogenic shell is initially imploded at low velocity using a laser pulse of $\sim 10^{14}$ W/cm^2 and successively ignited with strong spherically convergent shock. This strong shock is generated by a high intensity laser spike at the end of the laser compression pulse. The ignitor launching time should be carefully chosen in order to maximize the shock pressure after its interaction with previously launched shocks. High values of pressure are obtained thanks to the collision of the ignitor shock with the return shock, generated by the pre-pulse, at the shell inner interface. As a result of the collision, two new shocks are generated: one moving inward and another moving outward. The

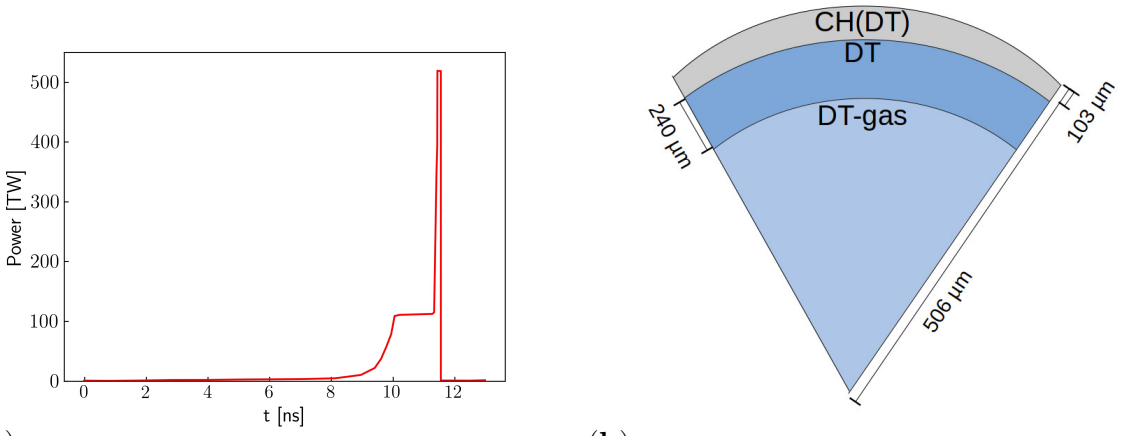

(a) (b)

Figure 5: Capsule configuration and pulse shape proposed by Betti [24].

inward shock accelerates the inner shell surface, rising the pressure of the hot spot. As such, differently to the conventional ICF scheme, the stagnating core is composed by a non isobaric assembly with a peaked pressure in the hot spot.

In the original design proposed by Betti, the compression pulse consisted of an isentropic compression pulse with a peak power of 110-130 TW. The ignitor spike has intensities around 10^{15}-10^{16} W/cm^2, for a total power of 550 TW delivered in 100-300 ps. Both the compression and the ignition pulse can be delivered by the same laser system. Fig. 5 shows a typical target and laser pulse configuration employed in SI.

There are several potential advantages of such approach compared to the conventional ICF scheme. First of all, the lower implosion velocity and the possibility of using thicker targets make the hydrodynamic instabilities less dangerous. Furthermore, lower ignition threshold and higher gains are predicted by the non isobaric assembly of the fuel with peaked values of pressure in the central hot spot [8][25][26]. Such higher gain comes from the fact that smaller energy is required to compress the cold fuel, which does not need to be in pressure equilibrium with the hot spot. Since 2007, several experimental and theoretical investigations were performed to study the feasibility of the scheme [27] [28] [29] [30] [31].

As already mentioned in Sec. 0.2 for the conventional ICF scheme, possible issues in SI can come from the hot electrons generated by the laser-plasma interaction considering the high intensities of the ignitor pulse (i.e. 10^{15} - 10^{16} W/cm^2). According to their energy, these electrons can propagate beyond the shock front and penetrate in the dense shell, preheating it [32]. Moreover, hot electrons can increase the hotspot mass by ablating the inner shell interface, changing the condition of the hot spot [33]. These two effects are deleterious for the SI scheme and they can increase the energy threshold for ignition. On the other side, if they are not too energetic, hot electrons can assist in the formation of the shock, increasing the shock pressure with beneficial effects for the implosion [34]. Therefore, a critical step for assessing the feasibility of shock ignition is the characterization in terms of energy and intensity of the hot electron population and to understand its effects on the hydrodynamic evolution of the target.

0.4 Goal of the thesis work

As explained in Sec. 0.3 and 0.2, the role of hot electrons generated by the high intensity laser driver in the implosion schemes is controversial and nowadays debated. These electrons can propagate up to the inner part of the cryogenic shell, preheating and ablating it. In the conventional ICF scheme (Sec. 0.2), the presence of hot electrons is generally considered deleterious and it should be limited as much as possible [35][36]. In the case of shock ignition, the ignitor spike is launched after the compression phase, when the target areal density has already reached high values. In particular, if the outer part of the shell presents sufficiently high values of ρR, it stops hot electrons that can in turn contribute to the shock pressure. On the contrary, if the shell is not dense enough and electrons are too energetic, they propagate up to the inner part of the cryogenic fuel preheating it. As such, a critical step for answering the feasibility of the two schemes is the characterization in terms of energy and intensity of the hot electron beam, understanding its effect on the capsule implosion.

As shown in Chapt. 2, in the last decades an important effort has been made by the scientific community to characterize and understand the role of hot electrons in ICF and in particular in SI regimes. Experimental campaigns in spherical and planar geometry were devoted to their characterization and to study their effect on the target hydrodynamic. For this purpose, several diagnostics are being built and the understanding on their performance is constantly increasing. Moreover, hydrodynamic codes are being developed to interpret these experiments and to model the entire implosion scheme. The increase of the computational power at disposal allows to build more and more complex and detailed codes. Having in mind of simulating the entire implosion process, these numerical tools should treat the laser-plasma interaction, the hydrodynamic evolution of targets and the transport of fusion products. In particular, considering the possible issues related to the presence of hot electrons, an adequate modelization of the hot electron transport in fusion targets will allow to assess the problem with more confidence and more robust implosion schemes can be proposed.

On this basis, the thesis work develops in two parts. The first part is dedicated to the experimental characterization of hot electrons emitted by the laser plasma interactions in condition relevant for SI. We will present results coming from experimental campaigns conducted in different facilities, thus exploring different laser-plasma conditions. A methodology for the interpretation of these experiments is presented, coupling different numerical tools. Special emphasis is given to the post-processing techniques of different x-ray spectrometers. A brief discussion on the influence of hot electrons on the shock dynamics is also presented.

The second part of the thesis work is devoted to the development of a hot electron transport model, with the aim of future implementation in 3D hydrodynamic codes. In particular, we chose a 3D Monte-Carlo method to describe the electron propagation in ionized or partially ionized targets. This model will be useful to study the effect of hot electrons in SI schemes, but also to interpret future planar or spherical target experiments. An initial evaluation on the preheat effect driven by hot electrons on a typical SI implosion scheme is performed using this model.

0.5 Manuscript Outline

The manuscript is organized as follows:

- **Chapter I: Laser Plasma interaction in the context of Inertial Confinement Fusion**

  The first chapter provides the theoretical description of different quantities and phenomena relevant for the thesis work. In the first part, the chapter introduces some basic plasma quantities and three different mathematical descriptions of plasmas. These concepts are particularly useful in modelling the laser plasma interaction and the hot electron propagation in ICF targets. Then we give a brief outline of different mechanisms that characterize the laser plasma interaction for regimes relevant to ICF and in particular to SI. Special emphasis is devoted to the processes that are involved in hot electron generation. A simplified mathematical description of these mechanisms is given, reporting also some relevant results of recent numerical investigations. Finally, a short digression on the hydrodynamic evolution and shock dynamics considering ICF targets is presented.

- **Chapter II: State of the art of hot electrons in Shock Ignition: effects and characterization**

  The chapter presents and critically discusses a list of theoretical and experimental investigations on the role of hot electrons in ICF. In the first part, we report the results of experiments in which the effect of hot electrons on shock formation was investigated, considering different laser conditions. Then some experimental and theoretical investigations performed in the last decade on the role of hot electrons in the context of the SI scheme are presented. This allows to better understand the background and the objectives of the thesis work. Thereafter, a brief description of the principal diagnostics involved in laser-plasma experiments is reported, focusing the attention on the x-ray spectrometers. In the last part of the chapter, we summarize the results of several experiments aimed at characterizing the hot electrons in conditions relevant to ICF. These experiments are grouped according to the laser facility in which they were conducted. Different laser facilities provide different laser characteristics and thus different interaction regimes. We report in particular experiments conducted at PALS (Prague Asterix Laser System, Czech technical university in Prague), OMEGA (Laboratory for Laser Energetics, University of Rochester) and NIF (National Ignition Facility, Livermore).

- **Chapter III: Experimental characterization of hot electrons in SI relevant regime**

  This chapter presents the results of recent experimental campaigns aimed at characterizing hot electrons in SI regime, considering different laser-plasma conditions according to the capabilities of the facility.

  We report the results of an experimental campaign conducted on OMEGA-EP in 2018, in which hot electrons and the shock dynamics were characterized using different diagnostics. In particular, we present a detailed description of the diagnostic

techniques and we propose a post-processing methodology to analyse the x-rays spectrometers. These spectrometers were used to characterize hot electrons in terms of energy and intensity, and their response was simulated using Monte-Carlo methods. The hot electron characteristics inferred using the spectrometers were then used as input to model the hot electron source in hydrodynamic simulations, in order to study the hydrodynamic evolution of the target.

The same methodology is applied to analyse spectrometer data coming from other experimental campaigns conducted at PALS and at LMJ (Laser Megajoule, CEA, Bordeaux). It is important to remark that only the capabilities of LMJ allow to explore plasma conditions (in terms of coronal scale length and temperature) peculiar of SI.

- **Chapter IV: A 3D Monte-Carlo method to study the transport of hot electrons in the context of Inertial Confinement Fusion**

  We present, in this chapter, a Monte-Carlo method to simulate the hot electron transport in ionized or partially ionized target. This model will be implemented in 3D hydrodynamic codes, and it will be useful to study the effects of hot electrons on the implosion schemes and to interpret future experimental campaigns.

  In the first part of the chapter, the relevant physical mechanisms and quantities are discussed critically. In particular, a discussion on the physics of the background material (a laser irradiated target) is presented in the first section, showing the models used to calculate the ionization degree. Thereafter, a discussion on the electron scattering phenomena that occur in ionized matter is shown. In particular, we propose an analytical differential cross section that describes the collision between a hot electron and a partially ionized atom in plasma. Subsequently, the stopping power formulas which describe the electron energy losses are reported. In the two last sections of the chapter, we report on the algorithm followed to build the code and its benchmark against other MC methods.

- **Chapter V: Plasma MC method: Two cases of study**

  This chapter reports on two numerical studies conducted using the MC code presented in Chap. IV and developed during this thesis work at CELIA. The analysis of laser-plasma experiments aimed at characterizing hot electrons, presented in Chap. II and III, is based on "cold" MC codes, i.e. codes in which several features of a laser irradiated target are neglected. In particular, these cold MC methods do not account for the hydrodynamic evolution of the target and the ionized state of the atoms composing it. As such, it is important to understand which is the margin of error introduced in analysing such experiments using cold codes. For this purpose, we reconsidered the analysis of the OMEGA-EP experiment presented in Chap. III using our plasma MC method developed in Chap IV. In particular, the propagation of hot electrons in cold or in laser irradiated target is compared and a detailed study is conducted to understand which are the processes which influence the electron transport in the two cases.

  In the second part of the chapter, we present a numerical investigation on the effect

of hot electrons on a typical implosion scheme, evaluating the DT shell preheat as a function of the hot electron characteristics.

Conclusions of this work are presented in Chap VI.

Chapter 1

Laser Plasma interaction in the context of Inertial Confinement Fusion

In this chapter, we will give a theoretical description of various phenomena relevant for ICF which are useful to understand the subjects covered in the thesis work. In Sec. 1.1 we present some relevant features of plasma physics in order to be able to understand the coronal laser-plasma interaction, the hot electron propagation and the shock dynamics. First, the Debye-Huckel and the collision theory are presented, stressing the validity limits for the two models. Then a brief description of three plasma models is successively reported: the kinetic, the multi-fluid and the single-fluid models. In particular, the kinetic model is at the foundation of the hot electron transport code presented in Chap. 4, while the multi-fluid model is useful to give a first analytical description of different mechanisms that occur in the corona during the laser-plasma interaction. In Sec. 1.2, these mechanisms are described, focusing the attention on the processes related to hot electron generation. Finally, a description of the hydrodynamic evolution of a laser irradiated target is given in Sec. 1.3. In particular, a brief discussion on the ablation pressure and the shock waves propagation in planar geometry is presented, considering the single-fluid plasma model. The single fluid hydrodynamic model is at the foundation of the CHIC hydrodynamic code [37], widely used in this thesis work.

1.1 Plasma Physics

In this section, we present some features of plasma physics, considering quantities that are relevant to describe the laser-plasma interaction and the hot electron propagation in the ICF regime. We also present three mathematical models that can be used to describe a plasma: kinetic, multi-fluid and single fluid models. The hot electron propagation model presented in Chap. 4 is based on the resolution of the kinetic equation, while the fluid models are used in the description of the hydrodynamic evolution of a laser irradiated target.

1.1.1 Debye-Huckel theory

A plasma is a ionized gas consisting of charged particles that show collective behaviour. The gas is quasi-neutral, meaning that the Coulomb forces between the particles tend

to neutralize the local charge imbalance. The quasi-neutrality is expressed through the formula:

$$n_e = \sum_\alpha n_\alpha Z_\alpha, \tag{1.1}$$

where n_e is the electron density, n_α and Z_α are the ion density and the ionization state for the specie α, respectively. In plasma, the behaviour of the electrostatic potential ϕ generated by a point charge q differs from the potential generated by the same charge in vacuum (i.e. $\phi = q/r$). This is due to the charge density that accumulates around the point charge. In particular, let us consider a two species plasma composed by electrons and ions of charge Z, distributed according to Maxwell-Boltzmann statistics with a common temperature T. The charge density in the vicinity of the probe particle $q = +Ze$ located at $\mathbf{x}$=0 is:

$$\rho_c = Ze\delta(0) - n_e e \exp\left(\frac{e\phi}{T}\right) + n_i eZ \exp\left(-\frac{eZ\phi}{T}\right), \tag{1.2}$$

where e is the electron charge and δ indicates the Dirac delta distribution. Considering this, the Poisson equation reads:

$$\nabla^2\phi = -4\pi\rho_c = -4\pi\left[Ze\delta(0) - n_e e \exp\left(\frac{e\phi}{T}\right) + n_i eZ \exp\left(-\frac{eZ\phi}{T}\right)\right]. \tag{1.3}$$

In the case of *weakly coupled plasma*, the soultion of this equation can be obtained analytically. In such plasmas, ions and electrons move almost freely in space and the motion of one of these particles weakly affects the motion of the others. This happens for high temperature, low density plasmas. In this case, the condition $|q\phi| \ll T$ holds and, after the series expansion of the exponentials, eq. (1.2) becomes:

$$\rho_c = Ze\delta(0) - \frac{e^2\phi}{T}\left(n_e + n_i Z^2\right). \tag{1.4}$$

Recasting now eq. (1.3) in spherical coordinates, (i.e. assuming that the charges are distributed according to spherical symmetry) and introducing the *Debye length* [38]:

$$\lambda_D^{-2} = 4\pi\frac{e^2}{T}\left(n_e + n_i Z^2\right), \tag{1.5}$$

eq. (1.3) writes:

$$\frac{1}{r}\frac{\mathrm{d}}{\mathrm{d}r}\left(r^2\frac{\mathrm{d}\phi}{\mathrm{d}r}\right) = -4\pi Ze\delta(0) + \frac{\phi}{\lambda_D^2}. \tag{1.6}$$

The solution of this equation, considering $\phi \to 0$ for $r \to \infty$ and $\phi = q/r$ for $r \to 0$, has the form of Yukawa potential [39]:

$$\phi(r) = \frac{q}{r}\exp\left(-\frac{r}{\lambda_D}\right). \tag{1.7}$$

Eq. (1.7) displays that the potential of any given charge in a plasma falls exponentially, decaying faster than if the charge would have been in vacuum. That is due to the formation of a polarization charge in the sphere of radius λ_D around the probe particle q. This polarization charge screens the electric field generated by the point charge q, that has influence only in the region included in the Debye sphere (i.e. the sphere with radius λ_D centred on q). For a multi-species plasma, the Debye length reads:

$$\lambda_D = \frac{1}{\sqrt{4\pi e^2\left(\frac{n_e}{T_e} + \sum_\alpha \frac{n_\alpha Z_\alpha^2}{T_\alpha}\right)}}, \tag{1.8}$$

where α labels the quantity related to the specie α. For a coronal plasma created by a laser interaction in ICF regime, λ_D has values around $\sim 10^{-6}$ - 10^{-7} cm [40].

Eq. (1.2) is valid only if there are numerous particles within the Debye sphere, i.e.:

$$N_D = (n_e + n_i)\,(4\pi/3)\,\lambda_D^3 \gg 1, \tag{1.9}$$

where N_D is called *plasma parameter*. In particular, a plasma is known as *ideal plasma* when the number of particles in the Debye sphere is much lager than 1. If the ion density increases, the Debye length may become smaller than the average distance between ions R_i:

$$R_i = \left(\frac{4\pi}{3} n_i\right)^{-1/3}, \tag{1.10}$$

and the Debye-Huckel theory is no longer valid. This is due to the fact that, at such high densities, the Debye sphere contains on the average less than one ion and the statistical treatment of equation (1.2) cannot be justified. Considering also the condition $|q\phi| \ll T$, it follows that the basic assumption of the Debye theory is valid in low density high temperature plasmas, where the average interionic distance is large and the Coulomb interaction of a given ion with other plasma particles is relatively small [41] [42].

1.1.2 Collision theory

In plasma, the particle motion is influenced by collisions. A basic description of the collision theory is given in this section, considering a rarefied plasma in which the Coulomb elastic scattering is dominant and external fields are absent. When the plasma is not dense, small angle-scatterings are predominant over large angle deflections, as showed in the following.

A probe particle (electron) that moves with velocity v in an homogeneous plasma, will experience Coulomb collisions only with particles inside the Debye sphere λ_D. As such, the

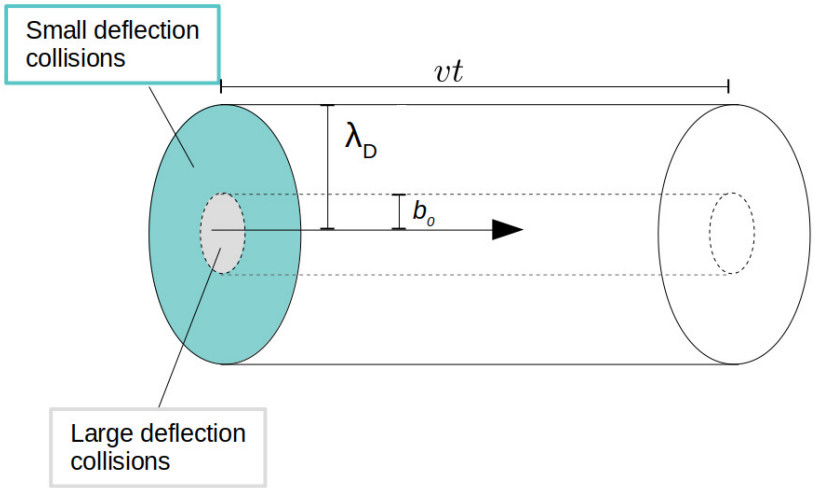

Figure 1.1: Interaction volume of a charged particle that moves in a plasma with velocity v. The particle interacts with other plasma particles contained in the cylinder of radius λ_D. For an impact parameter between λ_D and b_0 the particle experiences small angle deflections, while for impact parameters less than b_0 large angle deflections occur.

number of collisions which the electron undergoes in a time t will be related to the number of particles in the cylinder of height vt and radius λ_D (see Fig. 1.1). The frequency of collision is thus given by the relation:

$$\nu = \frac{N\pi\lambda_D^2 vt}{t} = N\pi\lambda_D^2 v, \tag{1.11}$$

where N is the plasma density. According to classical physics, the scattering angle in the center of mass between two colliding charged particles q_1 and q_2 follows the Rutherford relation:

$$\tan\left(\frac{\theta}{2}\right) = \frac{q_1 q_2}{\mu v^2}\frac{1}{b}, \tag{1.12}$$

where b is the *impact parameter*, μ is the reduced mass of the two particles and θ the scattering angle. Introducing the *Landau parameter*:

$$b_0 = 2\frac{q_1 q_2}{\mu v^2}, \tag{1.13}$$

the Rutherford relation (1.12) can be written as:

$$\tan\left(\frac{\theta}{2}\right) = \frac{b_0}{2b}. \tag{1.14}$$

From this equation, it is easy to see that the Landau parameter gives an order of magnitude for the impact parameter at which collisions cause a large-angle deflection. As an example, if $b{=}b_0$, the scattering angle is 53°. As such, the collision frequency for large-angle scattering phenomena can be written as:

$$\nu_L = N\pi b_0^2 v, \tag{1.15}$$

and the small-angle collision frequency reads:

$$\nu_S = N\pi\left(\lambda_D^2 - b_0^2\right)v. \tag{1.16}$$

If $\lambda_D \gg b_0$, soft collisions are predominant over hard collisions. The figure of merit to evaluate the validity of this condition is the so-called *Coulomb logarithm*:

$$\ln(\Lambda) = \ln\left(\frac{\lambda_D}{b_0}\right). \tag{1.17}$$

Considering an electron that moves with thermal velocity $v_{th}{=}\sqrt{2T/m_e}$ colliding with fixed ions ($\mu \sim m_e$, $v \sim v_{th}$), the Landau parameter (1.13) reads:

$$b_0 = \frac{2e^2}{m_e v_{th}^2} = \frac{e^2}{T} = \frac{1}{4\pi N\lambda_D^2}, \tag{1.18}$$

and the Coulomb logarithm is:

$$\ln(\Lambda) = \ln\left(4\pi N\lambda_D^3\right). \tag{1.19}$$

For typical ICF coronal plasma parameters (i.e. $N \simeq 10^{20}\,[\mathrm{cm}^{-3}]\,, \lambda_D \simeq 7\times10^{-7}\,[\mathrm{cm}]$), we obtain $\Lambda \simeq 400$ and $\ln(\Lambda) \simeq 6$. This indicates that small scattering angle collisions are more frequent than large angle collisions, i.e. $\nu_S \gg \nu_L$. For $\ln(\Lambda) \sim 4$ hard collisions

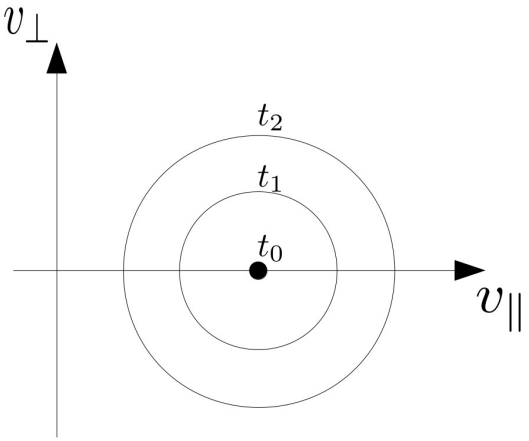

Figure 1.2: Schematical representation of the evolution of the velocity distribution function for a system of particles with initial velocity $\mathbf{v}_0$ that collide with immobile ions. The three curves refers to three different times $t_0 < t_1 < t_2$.

can not be neglected.

To evaluate the overall effect of small-angle scatterings on the velocity distribution of the incident particle, it is necessary to look at the standard deviation of the perpendicular velocity $< \Delta v_\perp^2 >$. Because of symmetry, the mean perpendicular velocity remains zero $< v_\perp > = 0$, but $< \Delta v_\perp^2 >$ grows in time (see Fig. 1.2). It is possible to define the frequency ν_c as the growth rate of $< \Delta v_\perp^2 >$ due to soft collisions [43]:

$$\nu_c = \frac{1}{v^2}\frac{\mathrm{d}}{\mathrm{d}t} < \Delta v_\perp^2 > . \tag{1.20}$$

For electrons that scatter on immobile ions, the centre of mass frame corresponds to the laboratory frame, and each collision produces a variation in the perpendicular velocity given by:

$$\Delta v_\perp^2 = v^2 \sin^2(\theta) \simeq v^2\theta^2 \simeq v^2\frac{b_0^2}{b^2} \tag{1.21}$$

(considering the Rutherford relation for small scattering angles (1.12)). Since the scattering events are independent from each other, the standard deviation due to N_b collisions with parameter b writes:

$$< \Delta v_\perp^2 >_b = N_b \Delta v_\perp^2 = N_b v^2 \frac{b_0^2}{b^2}. \tag{1.22}$$

Considering the ion density N, the number of collisions that the probe particle experiences in the time t with impact parameter between b and $b + \mathrm{d}b$ reads (see Fig. 1.1):

$$< \Delta v_\perp^2 >_b = 2\pi N v^3 t b_0^2 \frac{\mathrm{d}b}{b}. \tag{1.23}$$

Integrating this quantity between the maximum impact parameter λ_D (because particles placed at distances greater than λ_D do not have any influence on the incident particle) and the minimum impact parameter b_0 (according to the small-angle scattering approximation), we obtain:

$$< \Delta v_\perp^2 > = \int_{b_0}^{\lambda_D} < \Delta v_\perp^2 >_b = \int_{b_0}^{\lambda_D} 2\pi N v^3 t b_0^2 \frac{\mathrm{d}b}{b} = 2\pi N v^3 t b_0^2 \ln\left(\frac{\lambda_D}{b_0}\right) \tag{1.24}$$

and thus from eq. (1.20):

$$\nu_c = \frac{8\pi N q_1^2 q_2^2}{m_e^2 v^3} \ln(\Lambda). \tag{1.25}$$

This is the small-angle collision frequency that modifies the perpendicular velocity distribution of the incident beam. Comparing this quantity with the hard scattering collision frequency (1.15), one has:

$$\frac{\nu_c}{\nu_L} = 2\ln\Lambda. \tag{1.26}$$

Since $\Lambda > 1$, we can conclude that a large deflection of the beam is produced mainly by the cumulative effect of many small collisions rather than by a single hard collision.

Considering now scattering between electrons and fixed ions (i.e. $q_1 = -e, q_2 = \mathrm{Z}e, \mu \sim m_e, v \sim v_e, n = n_i = n_e/Z$) and considering that electrons move with thermal velocity $v_e = \sqrt{2T_e/m_e}$, equation (1.25) gives:

$$\nu_{ei}^{fixed} = \frac{8\pi e^4}{2^{3/2} m_e^{1/2}} \frac{Z n_e}{T_e^{3/2}} \ln(\Lambda). \tag{1.27}$$

A general formula that describes the collision frequency between two species in plasma ji was derived by Spitzer (1963) [44] and reported also in Ref. [45], and it reads:

$$\nu_{ij} = \frac{8(2\pi)^{1/2} n_j Z_i^2 Z_j^2 e^4 \ln\Lambda}{3 m_i m_j} \left(\frac{T_i}{m_i} + \frac{T_j}{m_j}\right)^{-3/2}. \tag{1.28}$$

Atzeni [8] reports the formulas for collision frequencies between electrons and ions and between ions, respectively, as:

$$\nu_{ei} = \frac{4(2\pi)^{1/2} n_i Z_i^2 e^4 \ln\Lambda_e}{3 m_e^{1/2} (T_e)^{3/2}}; \quad \nu_{ii} = \frac{4(\pi)^{1/2} n_i Z_i^4 e^4 \ln\Lambda_i}{3 m_i^{1/2} (T_i)^{3/2}}. \tag{1.29}$$

The differences in the coefficients between the formulas (1.27) and (1.29) are due to the fact that the first considers static ions, while the second integrates over all the possible particles velocities. In case of plasma composed by multiple species, the average collision rate is determined by substituting in the formulas the effective charge $Z_{eff} = \langle Z^2 \rangle / \langle Z \rangle$. Here $\langle\rangle$ denotes the average over all the ion species [46].

1.1.3 Kinetic and Fluid description of plasma

Several mathematical descriptions of a plasma can be found in literature, which differ according to their complexity and level of detail. We present here the kinetic and the fluid descriptions, which are particularly useful to model the phenomena of our interest.

Kinetic Description

The kinetic approach is a statistical method that allows to describe the microscopic evolution of plasma in space and time. This is achieved considering the evolution of the *distribution function* $f_\alpha(\mathbf{r}, \mathbf{v}, t)$, which describes the α-particle density in a small 6-dimensional volume $\mathrm{d}\mathbf{r}\mathrm{d}\mathbf{v}$ centred at the point ($\mathbf{r}$,$\mathbf{v}$). In the case of collisional plasmas, f_α satisfies the *Boltzmann* equation [47]:

$$\frac{\partial f_\alpha}{\partial t} + \mathbf{v} \cdot \frac{\partial f_\alpha}{\partial \mathbf{x}} + \frac{q_\alpha}{m_\alpha} \left(\mathbf{E} + \frac{\mathbf{v} \times \mathbf{B}}{c}\right) \cdot \frac{\partial f_\alpha}{\partial \mathbf{v}} = C_\alpha, \tag{1.30}$$

where the term C_α describes the collision of the specie α with all other species. In particular, C_α is a term of source or sink that models the particles that enter or exit from the volume $\mathrm{d}\mathbf{r}\mathrm{d}\mathbf{v}$ because of collisions. If the plasma is composed by multiple species, C_α is the sum of all the collisional terms of the specie α with the other species:

$$C_\alpha = \sum_\beta C_{\alpha\beta}. \tag{1.31}$$

The kinetic equation (1.30), coupled with Maxwell's equations, is a complete description of the plasma, and allows to describe phenomena for which the knowledge at the microscopic scale is required (for example the Landau Damping). If C_α=0 the plasma is collisionless and eq. (1.30) is named *Vlasov equation*. On the contrary, it is possible to model the term C_α according to the Fokker-Planck theory [48] [43]. In this case, eq. (1.30) is named *Fokker-Planck equation*. The transport of ions and electrons in matter obeys the kinetic Fokker-Planck equation. In the literature, it is possible to find electron transport models and codes based on the solution of this equation [49]. A detailed derivation of the plasma kinetic theory and its application can be found in Refs.[50] [51] [52].

Multi-Fluid Description

If one is interested in phenomena which vary on hydrodynamic length scales L much greater than the particle free paths, and if the collision frequency is much less than the oscillation frequency, the plasma can be treated as a continuous medium. In this case, the molecular and the microscopic structure can be neglected. The plasma is thus described by macroscopic hydrodynamic quantities (like velocities, density, pressure...).

The fluid equations are derived considering higher momenta of the Boltzmann equation (1.30). Considering the first two momenta, the *mass* and the *momentum* equations for the specie α are [52] [43]:

$$\begin{cases} \frac{\partial n_\alpha}{\partial t} + \nabla \cdot (n_\alpha \mathbf{u}_\alpha) = n_\alpha \langle C_\alpha \rangle , \\ m_\alpha n_\alpha \left(\frac{\partial}{\partial t} + \mathbf{u}_\alpha \cdot \nabla \right) \mathbf{u}_\alpha + \nabla : \underline{\mathbf{P}_\alpha} - q_\alpha n_\alpha \left(\mathbf{E} + \frac{\mathbf{u}_\alpha}{c} \times \mathbf{B} \right) = m_\alpha n_\alpha \langle C_\alpha \mathbf{v} \rangle_\alpha . \end{cases} \tag{1.32}$$

Here n_α is the density for the specie α, $\mathbf{u}_\alpha$ is the fluid velocity and $\underline{\mathbf{P}_\alpha}$ is the pressure tensor. The collisionals term $\langle C_\alpha \rangle_\alpha$ and $\langle C_\alpha \mathbf{v} \rangle_\alpha$ are obtained integrating the term C_α in the velocity space and they read:

$$\langle C_\alpha \rangle_\alpha = \frac{1}{n_\alpha} \int C_\alpha \mathrm{d}\mathbf{v}_\alpha = \frac{1}{n_\alpha} \sum_\beta \int C_{\alpha\beta} \mathrm{d}\mathbf{v}_\alpha, \tag{1.33}$$

$$\langle C_\alpha \mathbf{v} \rangle_\alpha = \frac{1}{n_\alpha} \int C_\alpha \mathbf{v} \mathrm{d}\mathbf{v}_\alpha = \frac{1}{n_\alpha} \sum_\beta \int C_{\alpha\beta} \mathbf{v} \mathrm{d}\mathbf{v}_\alpha. \tag{1.34}$$

Let us notice that, if only Coulomb collisions are considered (i.e. chemical or nuclear reactions are not present), $\langle C_\alpha \rangle_\alpha$=0. This states that the number of particles of the α specie in the plasma does not vary because of Coulomb collisions. The term $\langle C_\alpha \mathbf{v} \rangle_\alpha$ describes the momentum transfer from the specie α to all other plasma species. Since the total momentum is conserved, in a two species plasma ij the terms C_{ij} should satisfy the following condition:

$$\int m_i \mathbf{v}_i C_{ij} \mathrm{d}\mathbf{v}_i + \int m_j \mathbf{v}_j C_{ij} \mathrm{d}\mathbf{v}_j = 0. \tag{1.35}$$

The momentum transfer from the population i to the population j equals the momentum transfer from the population j to the population i.

As shown in the next section, these equations are useful to derive a first mathematical treatment of the various processes that characterize the laser-plasma interaction that occurs in corona in ICF regime (see Sec. 1.2).

Single Fluid Description

In some cases, a simpler description of the plasma seen as a single fluid can be useful, loosing the information on the single population. This is accomplished by introducing the quantities:

$$\begin{cases} \rho = \sum_\alpha m_\alpha n_\alpha & \text{mass density} \\ \mathbf{u} = \frac{1}{\rho}\sum_\alpha m_\alpha n_\alpha \mathbf{u}_\alpha & \text{center of mass velocity} \\ \mathbf{j} = \sum_\alpha q_\alpha n_\alpha \mathbf{u}_\alpha & \text{current density} \end{cases} \tag{1.36}$$

and then by adding the equations (1.32) for all the species. In the absence of electric and magnetic fields and neglecting the anisotropic part of the pressure tensor, the *Single fluid equations* are [41] [53]:

$$\begin{cases} \frac{\partial \rho}{\partial t} + \nabla \cdot (\rho \mathbf{u}) = 0 \\ \rho\left(\frac{\partial \mathbf{u}}{\partial t} + \mathbf{u}\cdot\nabla\mathbf{u}\right) = -\nabla p \\ \frac{\partial}{\partial t}\left(\rho\varepsilon + \frac{1}{2}\rho u^2\right) + \nabla\cdot\left[\rho\mathbf{u}\left(\frac{1}{2}u^2 + \varepsilon\right) + P\mathbf{u}\right] = \rho Q \end{cases} . \tag{1.37}$$

Here ε is the specific internal energy and Q is the power generated per unit mass by an external source. These three relations are the continuity equations for mass, momentum and energy, respectively. These equations are usually coupled with an equation of state to close the system. The equation of state describes the thermodynamic properties of the fluid and it allows to express the internal energy as a function of pressure and density, i.e. $\varepsilon = \varepsilon(\rho, P)$. For an ideal gas, the equation of state reads:

$$\varepsilon = \frac{P}{(\gamma - 1)\,\rho}, \tag{1.38}$$

where γ is the polytropic index ($\gamma = 5/3$ for a monoatomic gas). The single-fluid equation is particularly useful in describing the shock propagation in laser irradiated target, and the model is at the basis of hydrodynamic codes like the Celia Hydrodynamic Code (CHIC) [54]. In particular, CHIC uses a single-fluid model with two temperatures, one for ions and another for electrons. This is needed to consider the energy transfer between the alpha particles generated by the nuclear reactions and the plasma ions.

1.2 Electromagnetic wave propagation in plasma and laser-plasma interaction

In this section, we give a description of the most relevant features that characterize the propagation of an electromagnetic wave in plasma. This is done by coupling the plasma multi-fluid equations with the Maxwell's equations (Sec. 1.2.1). Plasma is described at first considering a cold collisionless model 1.2.2. Then we show how an increase of complexity considering thermal and collisional effects allows to describe important mechanisms

such as the inverse bremsstrahlung absorption 1.2.3 and the propagation of electron and ion plasma waves 1.2.4.

In the last part of this section, we will give a brief description of the processes that take place in the coronal plasma in regimes relevant for ICF. We focus our attention in particular on the Resonant Absorption (RAB), on the Stimulated Raman Scattering (SRS) and on the Two-Plasmon decay (TPD). These processes are responsible for the generation of hot electrons that can compromise implosions.

1.2.1 Dispersion Relation

The description of the propagation of electromagnetic waves in plasmas relies on the coupling between the Maxwell's equations and the equations that describe the plasma. The macroscopic Maxwell's equations for the fields $\mathbf{E}$ and $\mathbf{B}$ in CGS system read:

$$\begin{cases} \nabla \cdot \mathbf{E}(\mathbf{r},t) = 4\pi\rho(\mathbf{r},t) & \textit{Gauss' law;} \\ \nabla \cdot \mathbf{B}(\mathbf{r},t) = 0 & \textit{Gauss' law for magnetism;} \\ \nabla \times \mathbf{E}(\mathbf{r},t) = -\frac{1}{c}\,\frac{\partial \mathbf{B}(\mathbf{r},t)}{\partial t} & \textit{Maxwell-Faraday law;} \\ \nabla \times \mathbf{B}(\mathbf{r},t) = \frac{4\pi}{c}\mathbf{j}(\mathbf{r},t) + \frac{1}{c}\frac{\partial \mathbf{E}(\mathbf{r},t)}{\partial t} & \textit{Maxwell-Ampere law} \end{cases}, \tag{1.39}$$

where ρ and $\mathbf{j}$ are the charge and the current densities respectively, i.e.:

$$\begin{cases} \rho = \sum_\alpha n_\alpha q_\alpha \\ \mathbf{j} = \sum_\alpha n_\alpha q_\alpha \mathbf{u}_\alpha. \end{cases} \tag{1.40}$$

Considering a plane monochromatic wave with a frequency ω that propagates in an uniform medium, $\mathbf{E}(\mathbf{r},t)$=$\mathbf{E}_0\ \mathrm{e}^{i(\mathbf{k}\cdot\mathbf{r}-\omega t)}$ and Fourier transforming the equations (1.41) yields:

$$\begin{cases} i\mathbf{k} \cdot \mathbf{E}(\mathbf{k},\omega) = 4\pi\rho(\mathbf{k},\omega) \\ i\mathbf{k} \cdot \mathbf{B}(\mathbf{k},\omega) = 0 \\ i\mathbf{k} \times \mathbf{E}(\mathbf{k},\omega) = \frac{i\omega}{c}\mathbf{B}(\mathbf{k},\omega) \\ i\mathbf{k} \times \mathbf{B}(\mathbf{k},\omega) = \frac{4\pi}{c}\mathbf{j}(\mathbf{k},\omega) - \frac{i\omega}{c}\mathbf{E}(\mathbf{k},\omega) \end{cases}. \tag{1.41}$$

Multiplying the Farady law by $\mathbf{k}\times$ and substituting in the Ampre-Maxwell law, we obtain:

$$\mathbf{k} \times (\mathbf{k} \times \mathbf{E}) = -\frac{1}{c^2}\left(4\pi i\omega\mathbf{j} + \omega^2\mathbf{E}\right). \tag{1.42}$$

Considering the linear problem, (i.e. small perturbations), the relation between the current density $\mathbf{j}$ and the electric field $\mathbf{E}$ reads:

$$\mathbf{j}\,(\omega,\mathbf{k}) = \underline{\boldsymbol{\sigma}}\,(\omega,\mathbf{k}) : \mathbf{E}\,(\omega,\mathbf{k}), \tag{1.43}$$

where $\underline{\boldsymbol{\sigma}}\,(\omega,\mathbf{k})$ is the electric conductivity tensor. Introducing the identity tensor $\underline{\mathbf{I}}$, and considering that $\mathbf{E} = \underline{\mathbf{I}} : \mathbf{E}$, equation (1.42) becomes:

$$\mathbf{k} \times (\mathbf{k} \times \mathbf{E}) = -\frac{\omega^2}{c^2}\left(\underline{\mathbf{I}} + \frac{4\pi i}{\omega}\underline{\boldsymbol{\sigma}}\right) : \mathbf{E}. \tag{1.44}$$

Introducing now the dielectric tensor:

$$\underline{\boldsymbol{\epsilon}}\,(\omega,\mathbf{k}) = \underline{\mathbf{I}} + \frac{4\pi i}{\omega}\underline{\boldsymbol{\sigma}}\,(\omega,\mathbf{k}), \tag{1.45}$$

and writing the cross product $\mathbf{k} \times (\mathbf{k} \times \mathbf{E})$ in tensorial form, i.e.:

$$\mathbf{k} \times (\mathbf{k} \times \mathbf{E}) = \mathbf{k} (\mathbf{k} \cdot \mathbf{E}) - k^2 \mathbf{E} = \underline{\mathbf{kk}} : \mathbf{E} - k^2 \mathbf{E} = k^2 \left(\frac{\mathbf{kk}}{k^2} - \underline{\mathbf{I}} \right) : \mathbf{E}, \tag{1.46}$$

it is possible to write the wave equation (1.42) in the form:

$$\left[\frac{c^2 k^2}{\omega^2} \left(\frac{\mathbf{kk}}{k^2} - \underline{\mathbf{I}} \right) + \underline{\boldsymbol{\epsilon}} \right] : \mathbf{E} = 0. \tag{1.47}$$

This equation represents a system of three scalar equations in the components of $\mathbf{E}$. As an example, considering the wave vector $\mathbf{k}$ oriented along the $\mathbf{z}$ axis (i.e. $\mathbf{k}=k\hat{\mathbf{z}}$), the wave equation (1.47) reads:

$$\begin{bmatrix} \epsilon - \frac{k^2 c^2}{\omega^2} & 0 & 0 \\ 0 & \epsilon - \frac{k^2 c^2}{\omega^2} & 0 \\ 0 & 0 & \epsilon \end{bmatrix} \begin{bmatrix} E_x \\ E_y \\ E_z \end{bmatrix} = \begin{bmatrix} 0 \\ 0 \\ 0 \end{bmatrix}. \tag{1.48}$$

The existence of solutions is given by the condition:

$$\det \left[\frac{c^2 k^2}{\omega^2} \left(\frac{\mathbf{kk}}{k^2} - \underline{\mathbf{I}} \right) + \underline{\boldsymbol{\epsilon}} \right] = 0. \tag{1.49}$$

This relation is called **dispersion relation**, and it models the electromagnetic wave propagation in plasma. The plasma here is described by the dielectric tensor ϵ and, according to the complexity of the model, several mechanisms can be investigated.

1.2.2 Waves in cold plasma

The simplest approach consists in describing the plasma with fluid equations, neglecting the collisions and the thermal effects. This approximation is called *"cold plasma approximation"*, and it neglects the effects of the particle thermal motion on the wave propagation. In particular, this approximation can be used when the thermal velocity is small compared to the wave phase velocity $v_{th} \ll v_{ph}$. According to this approximation, the continuity and the momentum equations for the specie α read:

$$\begin{cases} \frac{\partial n_\alpha}{\partial t} + \nabla \cdot (n_\alpha \mathbf{u}_\alpha) = 0, \\ \\ n_\alpha m_\alpha \frac{\partial \mathbf{u}_\alpha}{\partial t} + n_\alpha m_\alpha (\mathbf{u}_\alpha \cdot \nabla) \mathbf{u}_\alpha = n_\alpha q_\alpha \left(\mathbf{E} + \frac{\mathbf{u}_\alpha}{c} \times \mathbf{B} \right). \end{cases} \tag{1.50}$$

Considering an equilibrium state defined by $\mathrm{n}_{0\alpha} \neq 0$, $\mathbf{u}_{0\alpha}$=0, $\mathbf{E}_0$=0 and $\mathbf{B}_0$=0, we consider small perturbations of the unperturbed quantities:

$$\begin{cases} n_\alpha = n_{0\alpha} + n_{1\alpha} \\ \\ \mathbf{u}_\alpha = \mathbf{u}_{0\alpha} + \mathbf{u}_{1\alpha} = \mathbf{u}_{1\alpha} \\ \\ \mathbf{E} = \mathbf{E}_0 + \mathbf{E}_1 = \mathbf{E}_1 \\ \\ \mathbf{B} = \mathbf{B}_0 + \mathbf{B}_1 = \mathbf{B}_1 \end{cases}. \tag{1.51}$$

Substituting these quantities in the momentum equation (1.50) and considering only first order terms we obtain:

$$m_\alpha \frac{\partial \mathbf{u}_{1\alpha}}{\partial t} = q_\alpha \mathbf{E}_1. \tag{1.52}$$

Fourier transforming eq. (1.52), a relation for the perturbed velocity of the specie α is found:

$$\mathbf{u}_{1\alpha} = \frac{i}{\omega}\frac{q_\alpha}{m_\alpha}\mathbf{E}_1. \tag{1.53}$$

Inserting this relation in the definition of the current density (1.43) the conductivity tensor $\underline{\boldsymbol{\sigma}}(\omega, \mathbf{k})$ writes:

$$\underline{\boldsymbol{\sigma}}(\omega, \mathbf{k}) = \frac{i}{\omega}\sum_\alpha \frac{n_{0\alpha} q_\alpha^2}{m_\alpha} = \sigma(\omega). \tag{1.54}$$

The conductivity tensor reduces to a scalar because of the simplifying assumptions of the model: the absence of a magnetic field and the fact that we neglected the pressure tensor removed the sources of anisotropy and thus the spatial dependences. Considering the plasma frequency $\omega_P^2 = \sum_\alpha \frac{4\pi n_{0\alpha} q_\alpha^2}{m_\alpha}$, the form of the dielectric tensor (1.45) that describes a cold collisionless plasma writes:

$$\underline{\boldsymbol{\epsilon}}(\omega, \mathbf{k}) = 1 + \frac{4\pi i}{\omega}\sigma(\omega, \mathbf{k}) = 1 - \frac{\omega_p^2}{\omega^2} = \epsilon(\omega). \tag{1.55}$$

By imposing the condition (1.49), the following dispersion relation is obtained:

$$\epsilon\left(\epsilon - \frac{k^2 c^2}{\omega^2}\right)^2 = 0. \tag{1.56}$$

This equation has two solutions, that correspond to two different oscillation modes.

First solution: $\epsilon = 0$

The first solution is obtained by imposing ϵ=0 and the three equations (1.48) are satisfied only for $E_x = 0$, $E_y = 0$, $E_z \neq 0$. This solution corresponds to longitudinal waves characterized by ω^2=ω_P^2. These waves are called *Langmuir oscillations* and they have a phase and group velocities defined by the relations:

$$v_f = \frac{\omega_{ep}}{k}, \quad v_g = \frac{\mathrm{d}\omega}{\mathrm{d}k} = 0. \tag{1.57}$$

Since the group velocity is zero, these waves do not propagate in plasma. On the contrary, the phase velocity ranges from zero to ∞ according to the value of k. Since the validity of the cold model relies on the condition $v_{th} \ll v_{ph}$, it is necessary to consider also the thermal effects to better describe the behaviour of these modes for high values of k.

Second solution $\epsilon = \frac{k^2 c^2}{\omega^2}$

The other solution of the equation (1.56) is obtained for $\epsilon = \frac{k^2 c^2}{\omega^2}$, satisfied by $E_x \neq 0$, $E_y \neq 0$, $E_z = 0$. This indicates the presence of transverse waves, in which the electric field is perpendicular to the wave vector $\mathbf{k}$. The dispersion relation is given by the equations:

$$\omega^2 = \omega_P^2 + k^2 c^2, \tag{1.58}$$

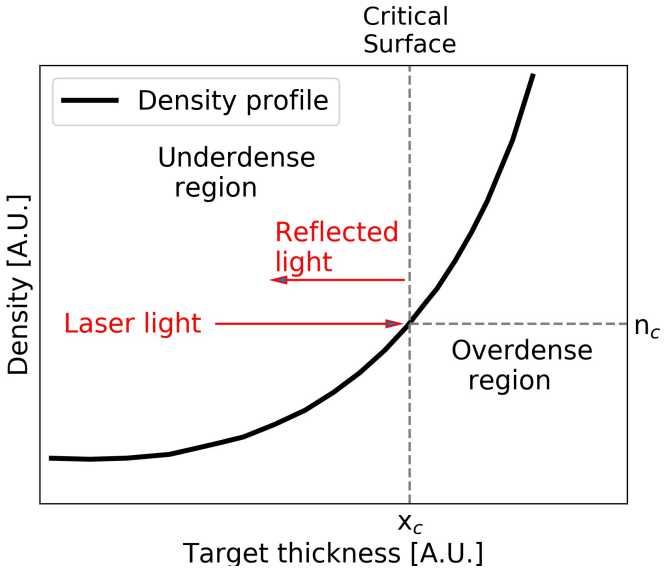

Figure 1.3: Typical density profile obtained by irradiating a target with a laser pulse in ICF regime. The laser light propagates in the underdense region, while it can not propagate in the overdense plasma.

$$k = \frac{\sqrt{\omega^2 - \omega_p^2}}{c}. \tag{1.59}$$

From these, the phase and the group velocities read:

$$v_f = \frac{\omega}{k} = \sqrt{\frac{\omega_{pe}^2}{k^2} + c^2} > c; \quad v_g = \frac{\mathrm{d}\omega}{\mathrm{d}k} = \frac{c}{\sqrt{\frac{\omega_{pe}^2}{k^2 c^2} + 1}} < c. \tag{1.60}$$

Since $v_f > c$, it is correct to neglect thermal effects to describe these modes. Furthermore, since $v_g \neq 0$, these waves propagate in plasma.

For $\mathbf{k} \to \infty$ ($\omega \to \infty$) the dispersion relation (1.58) leads to the one of a plane wave propagating in vacuum, i.e. $\omega \simeq kc$. The plasma particles do not have sufficient time to respond to the perturbation. For smaller frequencies, $\omega \leq \omega_p$, plasma particles reorganize themselves to neutralize the wave electric field and k becomes imaginary. In this condition the wave becomes evanescent. The density at which this occurs is called *critical density*, and in terms of the laser wavelength is written:

$$n_c = \frac{1.1 \times 10^{21}}{\lambda^2\,[\mu m^2]} \quad \left[\mathrm{cm}^{-3}\right]. \tag{1.61}$$

For a typical ICF laser configuration (λ=351 nm), the critical density has values $n_c \sim 9\times10^{21}$ $[\mathrm{cm}^{-3}]$, much lower than solid density (around $\sim 10^{23}$ $[\mathrm{cm}^{-3}]$ for CH). This indicates that the laser radiation does not propagate up to the solid part of target. A typical density profile of plasma ablated surface is shown in Fig. 1.3.

1.2.3 Inverse Bremsstrahlung - Collisional Absorption

The cold plasma model presented in Sec. 1.2.2 does not account for the energy transfer between waves and plasma. This is related to the fact that particle collisions are neglected. When electrons oscillate in the laser electric field, part of the oscillation energy

is converted into thermal energy via electron-ion collisions. This process is known as *"Inverse Bremsstrahlung absorption"*. To describe this mechanism it is necessary to model the collisional term in the momentum equation (1.32):

$$n_\alpha m_\alpha \frac{\partial \mathbf{u}_\alpha}{\partial t} + n_\alpha m_\alpha \left(\mathbf{u}_\alpha \cdot \nabla\right) \mathbf{u}_\alpha = n_\alpha q_\alpha \left(\mathbf{E} + \frac{\mathbf{u}_\alpha}{c} \times \mathbf{B}\right) + R_\alpha. \tag{1.62}$$

Here we neglected the thermal effects, since we are interested in the propagation of transverse waves for which $v_f \gg v_{th}$ and the cold approximation holds (see Sec. 1.2.2). The term R_α describes the rate of change of momentum for the specie α induced by collisions with other species:

$$R_\alpha = n_\alpha m_\alpha \left\langle C_\alpha \mathbf{v} \right\rangle_\alpha = n_\alpha m_\alpha \int \sum_\beta C_{\alpha\beta} \mathbf{v} \mathrm{d}\mathbf{v}. \tag{1.63}$$

For a plasma composed of electrons interacting with stationary ions, R_α can be expressed in terms of the electron-ion relaxation time τ_{ei}. This quantity sets the timescales on which the two species exchange momentum between them. It is the inverse of the electron-ion collision frequency, i.e. $\tau_{ei} \simeq \nu_{ei}^{-1}$ (see eq. (1.29)) [52]. Considering this, the collisional term in the momentum equation reads:

$$R_e = -\frac{m_e n_e \nu_{ei} \mathbf{u}_e}{\tau_{ei}} = -m_e n_e \nu_{ei} \mathbf{u}_e. \tag{1.64}$$

Considering as in the cold plasma approximation (see Sec. 1.2.2) small perturbations of the equilibrium state, the linearized momentum equation becomes:

$$\frac{\mathrm{d}\mathbf{u}_e}{\mathrm{d}t} = -\frac{e\mathbf{E}}{m_e} - \frac{\mathbf{u}_e}{\tau_{ei}}. \tag{1.65}$$

Following the mathematical passages showed in Sec. 1.2.2, it is possible to derive the electron fluid velocity $\mathbf{u}_e$, the conductivity tensor and the dielectric tensor in the Fourier space. In particular, the dielectric tensor has the form:

$$\epsilon\left(\omega\right) = 1 - \frac{\omega_{pe}^2}{\omega\left(\omega + i\nu_{ei}\right)}. \tag{1.66}$$

The presence of the imaginary part, not present in the cold plasma approximation (1.55), models the exchange of energy between the transverse wave and the plasma. The electromagnetic wave releases energy in plasma and it is thus damped. Mathematically, the damping is described by the imaginary part of the wave vector k. For the transverse waves, the solution of (1.49) gives:

$$k^2 = \frac{\omega^2}{c^2} - \frac{\omega_{pe}^2 \omega}{c^2\left(\omega + i\nu_{ei}\right)} \tag{1.67}$$

and considering $\nu_{ei} \ll \omega$ the imaginary part of k writes:

$$\kappa_{ib} = 2\mathrm{Im}k = \left(\frac{\nu_{ei}}{c}\right)\left(\frac{\omega_{pe}^2}{\omega^2}\right)\left(1 - \frac{\omega_{pe}^2}{\omega^2}\right)^{-1/2}. \tag{1.68}$$

As such, the wave will propagate in plasma exponentially decaying in intensity according to the law:

$$\mathbf{E} = \mathrm{E}_0 \mathrm{e}^{(i\mathrm{Re}(k)r - \omega t)} \mathrm{e}^{-\kappa_{ib} r}. \tag{1.69}$$

Substituting the definition of critical density eq. (1.68) becomes:

$$\kappa_{ib} = 2\mathrm{Im}k = \left(\frac{\nu_{ei}\left(n_c\right)}{c}\right)\left(\frac{n_e^2}{n_c^2}\right)\left(1-\frac{n_e}{n_c}\right)^{-1/2}. \tag{1.70}$$

This equation shows that the process of inverse bremsstrahlung absorption is maximum around the critical density (note that the equation diverges for $n_e \sim n_c$).

The variation of the laser intensity that passes through a slab of plasma in the z direction follows the law:

$$\frac{\mathrm{d}I}{\mathrm{d}z} = -\kappa_{ib} I \tag{1.71}$$

and the total fraction of absorption reads:

$$\alpha_{abs} = \frac{I_{in} - I_{out}}{I_{in}} = 1 - \exp\left(-\int_0^L \kappa_{ib}(z)\mathrm{d}z\right). \tag{1.72}$$

Difficulties in the solution of these equations come from the fact that the plasma is usually inhomogeneous and not stationary. In particular, κ_{ib} depends on electron density and temperature. For moderate laser intensities and long pulse duration (i.e. $I{\leq}10^{14}$ W/cm^2 $t \sim 1$ ns) we can consider the plasma temperature constant, and solution for eq. (1.72) can be found considering particular plasma profiles. As an example, Ginzburg [55] considered a normal incidence laser beam on a linear density profile plasma:

$$n_e = n_c\left(1-\frac{z}{L}\right), \tag{1.73}$$

obtaining:

$$\alpha_{abs} = 1 - \exp\left(-\frac{32}{15}\frac{\nu_{ei}\left(n_c\right)L}{c}\right). \tag{1.74}$$

Kruer [52] derived α_{abs} for oblique incidence in a linear density profile:

$$\alpha_{abs} = 1 - \exp\left(-\frac{32}{15}\frac{\nu_{ei}\left(n_c\right)L}{c}\cos^5(\theta)\right) \tag{1.75}$$

and in an exponential profile, i.e. $\mathrm{n}_e{=}\mathrm{n}_{cr}\exp(\text{-}z/L)$:

$$\alpha_{abs} = 1 - \exp\left(-\frac{8}{3}\frac{\nu_{ei}\left(n_c\right)L}{c}\cos^3(\theta)\right). \tag{1.76}$$

Discussing briefly the validity domain of the model, the main assumption $\nu_{ei} \ll \omega$ does not hold at the first stages of the laser interaction, when the laser intensity is low and the plasma is cold. Furthermore, as shown in Sec. 1.2.5, at earlier interaction stages other laser absorption mechanisms can prevail over the collisional absorption. However, rapidly the corona heats up and the model enter in its validity domain. We also notice that, since the model describes a phenomenon that occurs in the coronal plasma, the soft collision theory is sufficient to give an adequate modelling of the collision frequency ν_{ei} (see Sec. 1.1.2). Let us also mention that the reported model is a simple academic model. Usually, in hydrodynamic codes, more complex treatment of the phenomenon are used and the absorption coefficient is calculated in term of laser power and not on the intensity [56].

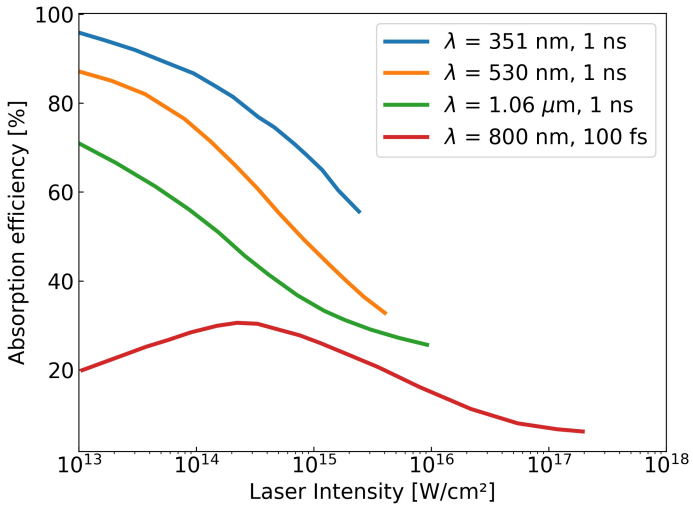

Figure 1.4: Experimental absorption percentages for a solid with a low atomic number (Aluminium) versus the incident laser intensity. Experimental results obtained with laser wavelengths varying from 0.351 μm up to 1.06 μm are presented. The pulse duration was 1 ns, except for data at λ=0.8 μm. The data is a summary of results obtained at the Lawrence Livermore National Laboratory, the Los Alamos National Laboratory, the Laboratory for Laser Energetics, the Naval Research Laboratory, KMS fusion, the Institute for Laser Engineering at Osaka University and the Ecole Polytechnique [60] [13].

The collisional absorption depends strongly on the laser wavelength, as also reported experimentally in [57][58][59]. As an example, in [57] terphane foils were irradiated with different laser wavelengths, energies and pulse durations. In particular, the laser wavelengths were 1.06 μm, 0.53 μm and 0.26 μm. The main results obtained were the following: absorption decreases when the laser intensity increases, and it increases when the pulse duration increases and the wavelength decreases. For λ=1.06 μm, authors suggest that at, low intensity ($\leq 10^{13}$ W/cm^2), the main absorption mechanism is inverse bremsstrahlung absorption, but its contribution decreases down to $\sim$30% for laser intensity of 2×10^{15} W/cm^2. For λ=0.26 μm at 4×10^{14}W/cm^2 the efficiency is around $\sim$90%. This can be explained because lower wavelength lasers can penetrate where the plasma is denser and more collisional. The decrease of the absorption efficiency with intensity is explained considering that collisional absorption is efficient when enough collisions take place. Higher laser intensity produces higher coronal plasma temperature T_e, and thus lower collisional frequencies ν_{ei}, that scale with the temperature as $T_e^{-3/2}$ (see eq. (1.27)). Fig 1.4 shows the behaviour of collisional absorption efficiency with laser energy, considering different irradiation conditions.

1.2.4 Thermal effects in plasma: electron and ion plasma waves

The presence of thermal effects influences waves for which $v_f \leq v_{th}$. As shown in Sec. 1.2.2, this condition is relevant for longitudinal waves. The thermal effects are expressed through the pressure term in the momentum equation of the system (1.32). Coupling the

system (1.32) with the polytropic equation for each specie:

$$\frac{\mathrm{d}}{\mathrm{d}t}\left(p_\alpha n_{0\alpha}^{-\gamma}\right) = 0, \tag{1.77}$$

and considering as in Sec. 1.2.2 small perturbations of the equilibrium quantities, the dielectric tensor that describes a warm plasma (1.45) has the form:

$$\epsilon(\omega) = 1 - \sum_\alpha \frac{\omega_{p\alpha}^2}{\omega^2 - k^2 v_{0\alpha}^2} = 1 - \frac{\omega_{pe}^2}{\omega^2 - k^2 v_{0e}^2} - \frac{\omega_{pi}^2}{\omega^2 - k^2 v_{0i}^2}. \tag{1.78}$$

Here we considered a plasma composed of two species (electrons and ions) and $v_{\alpha 0}$ is the acoustic velocity of the specie, i.e. $v_{0\alpha}^2 = \frac{\gamma_\alpha p_{0\alpha}}{m_\alpha n_{0\alpha}}$. Considering the condition (1.49), to obtain the longitudinal component of the electric field different from zero, it is necessary to impose $\epsilon = 0$. From this, two solutions are found:

$$\omega_{ek}^2 \simeq \omega_{pe}^2 + k^2 v_{0e}^2; \quad \omega_{ik}^2 \simeq k^2 v_{0i}^2 \left[\frac{k^2 + \omega_{pe}^2/v_{0e}^2 + \omega_{pi}^2/v_{0i}^2}{k^2 + \omega_{pe}^2/v_{0e}^2}\right]. \tag{1.79}$$

The first solution corresponds to the dispersion relation for *electron plasma waves* (EPW or *Langmuir waves*). These waves represent an electron charge density fluctuation that propagates in plasma, since $v_g \neq 0$. Let us notice that for $k \to 0$ the behaviour predicted by the cold plasma approximation is reproduced (Langmuir oscillations at $\omega = \omega_{ep}$).

The second solution corresponds to three cases, according to the values of k:

- $k < \frac{1}{\lambda_{De}}$: *Ion acoustic waves* (IAW) with dispersion relation $\omega^2 = k^2 c_s^2$, where $c_s^2 = T_e/m_i$ is the ion-acoustic velocity.
- $\frac{1}{\lambda_{De}} < k < \frac{1}{\lambda_{Di}}$: *Ion plasma oscillations* with dispersion relation $\omega^2 = \omega_{pi}^2$
- $k > \frac{1}{\lambda_{Di}}$ (not considering the Landau Damping): *Ion plasma waves* with dispersion relation $\omega^2 = \omega_{pi}^2 + k^2 v_{i0}^2$.

A detailed mathematical derivation of these equations can be found for example in Refs. [43] and [52]. As shown in Sec. 1.2.6, electron and ion plasma waves play an important role in several laser-plasma processes that occur in the underdense region. In particular, the decaying of an electromagnetic wave in plasma waves is an important process widely studied in ICF, because of the detrimental side effects that may occur from this coupling.

1.2.5 Oblique Incidence: Resonant Absorption

Resonance absorption (RAB) of laser light occurs when the electromagnetic wave is obliquely incident on a steeply rising plasma density and the electric field of the wave has a component along the density gradient, i.e. $\mathbf{E} \cdot \nabla \mathrm{n}_e \neq 0$ (Fig. 1.5) [8]. In this case, the wave is termed p-polarized and the oscillation generates fluctuations in charge density. An obliquely incident light wave that propagates in an inhomogeneous plasma reflects at density lower than n_c, i.e at $\mathrm{n}_e = n_c \cos^2\theta$, where θ is the angle of incidence between laser and target normal [52]. From this layer, an evanescent wave can tunnel through to the critical layer. There, the longitudinal component of the electric field can resonantly excite electron plasma oscillations (Langmuir oscillations, see Sec. 1.2.2). A schematic picture

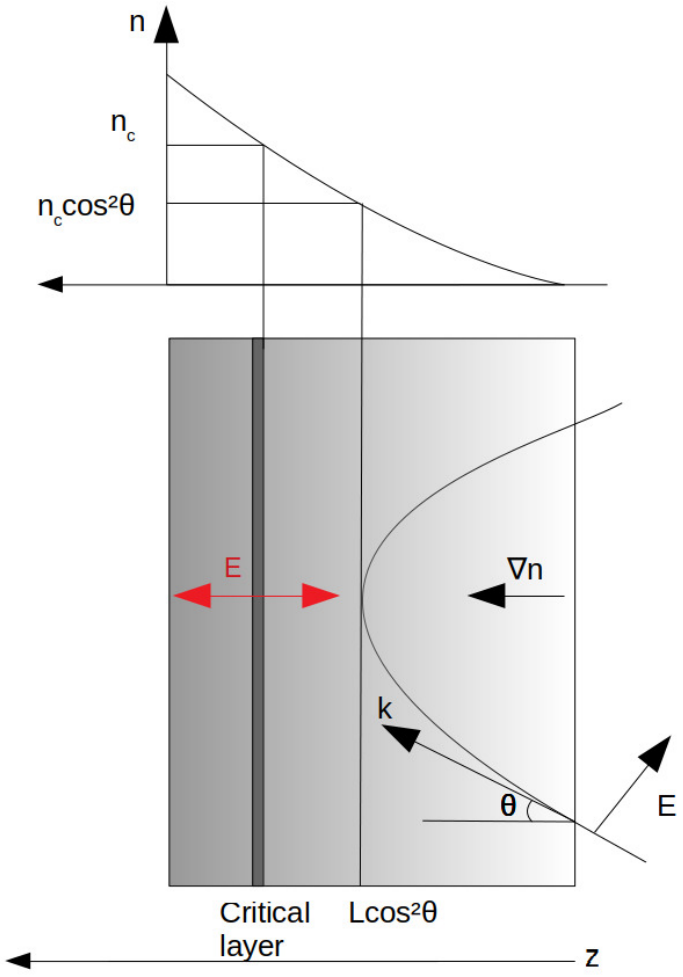

Figure 1.5: A sketch illustrating an electromagnetic p-polarized wave incident onto an inhomogeneous plasma slab, with a linear density profile (i.e n_e=$n_{cr}z/L$). The wave reflects at densities lower than the critical one. Thanks to the tunnel effect, there is a possibility that a nonvanishing longitudinal component of the electric field reaches the critical layer, exciting electron plasma waves.

of the process is shown in Fig. 1.5. The existence of the singularity in the electric field at the critical surface can be easily seen considering the Poisson equation in the dielectric plasma medium [61] [52]:

$$\nabla \cdot (\epsilon(z)\mathbf{E}) = \epsilon(z)\nabla \cdot \mathbf{E} + \nabla\epsilon(z) \cdot \mathbf{E} = 0, \tag{1.80}$$

where $\epsilon(z) = 1 - \omega_{pe}^2(z)/\omega^2$. Considering the dependence of ϵ on z, eq. (1.80) becomes:

$$\nabla \cdot \mathbf{E} = -\frac{1}{\epsilon}\frac{\partial\epsilon(z)}{\partial z}E_z, \tag{1.81}$$

and a Gauss type equation is obtained. In this equation, the source term is represented by the longitudinal term of the field and the resonant response happens for $\epsilon = 0$, i.e. $\omega_{pe} = \omega$. Note that, in reality, ϵ does not entirely vanish at the critical density because of electron-ion collisions.

A detailed calculation of the behaviour of E_z around the critical layer was presented for the first time by Denisov [62] [63], and it is also reported in more recent books and

articles [52] [60] [64] [65]. The value of the field E_d around the critical density is defined by:

$$E_d = \frac{E_{FS}}{\sqrt{2\pi\omega L/c}}\phi(\tau), \tag{1.82}$$

where E_{FS} is the value of the free-space electric field, $\tau=(\frac{\omega L}{c})^{1/3}\sin\theta$ and $\phi \simeq 2.3\tau\exp(-2\tau^3/3)$. This field vanishes as $\tau \to 0$ (i.e. when $\theta=0$), since in this condition the longitudinal component of the electric field is zero. The field also vanishes for $\tau \to \infty$, i.e. when the wave has to tunnel through a large distance to reach the critical layer. The optimum angle of incident for which the field has its maximum is $\tau \simeq 0.8$, i.e. $\sin\theta = 0.42\lambda/L$. As such, for longer plasma scale-lengths ($L >> \lambda$) the resonant absorption occurs mostly for light almost at normal incidence. For large laser intensities ($I > 10^{16}$ W/cm^2), the pondermotive force steepens the plasma density such that the condition $L \simeq \lambda$ is possible. In this situation, the peak of RAB happens at $\theta \sim 24°$ [66] [60].

The laser intensity absorbed by RAB in the case of linear density profile is given by the formula [52] [7]:

$$I_{abs} \simeq \omega\frac{LE_d^2}{8}, \tag{1.83}$$

and the fraction of laser light absorbed is:

$$\alpha_{abs} = \frac{\pi\omega L}{c}\frac{E_d^2}{E_{FS}^2} = \frac{\phi(\tau)}{2}. \tag{1.84}$$

These quantities do not depend on the electron-ion collision frequency, like in the case of inverse bremsstrahlung absorption. As such, RAB can dominate over the bremsstrahlung absorption for high plasma temperatures and short plasma-scale lengths.

Ref [67] presents a theoretical and experimental study on the role of RAB for conditions relevant to direct-drive implosions on the OMEGA Laser System. In particular, the process was studied considering planar CH targets irradiated with an UV (λ=351 nm) laser beam with intensities around 10^{14}-10^{15} W/cm^2. The angle of incidence of the laser beam was 23° and the pulse duration was around 1 ns. Numerical simulations demonstrated an important contribution of RAB during both the short laser rise-time of 100 ps and in the first 200300 ps of the laser pulse.

Although RAB can be very efficient where inverse bremsstrahlung absorption is inefficient, its main feature is that only a small part of electrons carries most of the absorbed energy. As such, as side effect, a copious amount of hot electrons are generated. As shown in the next chapter, these electrons can have detrimental effects on the shock ignition scheme, since they can preheat the fuel before the shock arrival, compromising the compression. As such, several experimental and numerical investigations were performed to understand the main features of hot electrons emitted by RAB, exploring different laser-plasma regimes [68][69][70][71][72][73]. Planar CH targets or spherical glass targets were studied considering laser pulses of hundreds of ps (from 100 ps up to 500 ps), and the hot electron Maxwellian temperature T_h was evaluated for a wide range of intensities and wavelengths. In general, T_h scales with $I\lambda^2$ following the scaling laws [7] [74]:

$$T_h\,[\mathrm{keV}] = 10\left(\frac{I\lambda^2}{10^{15}\mathrm{Wcm^{-2}}\mu\mathrm{m^2}}\right)^{0.30\pm0.05} \quad \text{if } I\lambda^2 > 10^{15}\ \mathrm{Wcm^{-2}}\mu\mathrm{m^2}, \tag{1.85}$$

$$T_h\,[\mathrm{keV}] = 10\left(\frac{I\lambda^2}{10^{15}\mathrm{Wcm^{-2}}\mu\mathrm{m}^2}\right)^{2/3} \text{ if } I\lambda^2 < 10^{15}\ \mathrm{Wcm^{-2}}\mu\mathrm{m}^2. \tag{1.86}$$

Another interesting experimental investigation on the RAB is presented in Ref. [75]. In particular, the article reports a decrease of the conversion efficiencies of laser energy into hot electron energy with an increase of laser pulse duration. This is valid for moderate irradiation regimes i.e. $I\lambda^2 < 10^{15}\ \mathrm{Wcm^{-2}}\mu\mathrm{m}^2$. In particular, the conversion efficiency goes from ∼7% in the case of short pulses (100 ps) down to 2% for longer pulses (>400 ps). Authors suggest that this reduction is linked to an increased fraction of laser light absorbed by inverse bremsstrahlung in larger plasma and shallower density gradients.

1.2.6 Parametric Instabilities

In the SI regime several processes arise in the underdense region of the plasma, coupling non-linearly electromagnetic and plasma waves. These processes represent the so-called *parametric instabilities* [76] [8]. In contrast to resonance absorption, they may occur in uniform plasma, but only if the laser intensity overcomes a threshold value. For ICF applications, these instabilities are generally deleterious, since they can prevent part of the laser light from arriving at the critical density where more efficient absorption mechanisms occur (i.e. collisional absorption, Sec. 1.2.3). Furthermore, these instabilities can create highly energetic electrons that can propagate beyond the shock front degrading the hotspot conditions and the implosion. The dominant parametric instabilities occurring in ICF regime are:

- Stimulated Raman scattering (SRS): a laser pump with frequency $\omega_0 > 2\omega_{pe}$ couples with a scattered transverse wave and an electron plasma wave;
- Two Plasmon decay (or $2\omega_{pe}$ instability) (TPD): a laser pump with frequency $\omega_0 = 2\omega_{pe}$ decays into two electron plasma waves.
- Stimulated Brillouin scattering (SBS): a laser pump with frequency $\omega_0 > \omega_{pe}$ couples with a scattered transverse wave and an ion acoustic wave;
- Langmuir Decay instability (LDI): an electron plasma wave decays into an ion acoustic wave and another electron plasma wave.

Tab. 1.1 lists all these processes specifying the density at which they take place.

Instability type	Daughter waves	Coupling density
Stimulated Raman scattering	e.m. + electron wave	$\leq n_{c/4}$
Two Plasmon decay	electron wave + electron wave	$\sim n_{c/4}$
Stimulated Brillouin scattering	e.m. + ion wave	$< n_c$
Langmuir Decay instability	electron wave + ion wave	

Table 1.1: List of parametric instabilities that take place in the underdense region of plasma. E.m. stands for electromagnetic wave. The densities at which the instability takes place is reported in the third column.

In the following, a brief overview of the four processes will be given, focusing attention particularly on SRS and TPD. In ICF regime, SRS and TPD are thought to be the main processes responsible for the generation of hot electrons that can propagate beyond the shock front, preheating the fuel and compromising the implosion.

Stimulated Raman Scattering

The Stimulated Raman Scattering (SRS) is a process that involves the coupling of a large amplitude light wave into a scattered light wave plus an electron plasma wave [52]. The matching conditions for the frequency and the wave number are:

$$\begin{cases} \omega_0 = \omega_s + \omega_{ek} \\ \mathbf{k}_0 = \mathbf{k}_s + \mathbf{k}_{ek} \end{cases}, \tag{1.87}$$

where ω_0 ($\mathbf{k}_0$) is the frequency (wave number) of the incident light, ω_s ($\mathbf{k}_s$) the frequency (wave number) of the scattered light and ω_{ek} ($\mathbf{k}_{ek}$) the frequency (wave number) of the electron plasma wave. Fig. 1.6 shows schematically the process. Since the minimum frequency of a light wave propagating in plasma is ω_p, the instability requires that $\omega_0 \geq 2\omega_p$, i.e. $n \leq n_c/4$. Similarly, a k-vector matching condition must be respected. However, even if these conditions are fulfilled, it is necessary that the intensity of the incoming laser wave exceeds a certain threshold in order for the process to occur.

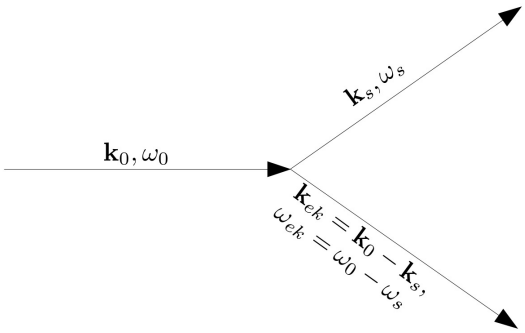

Figure 1.6: Schematic diagram of the SRS process: a photon with frequency ω_0 and wave number $\mathbf{k}_0$ decays into an electron plasma wave and into an electromagnetic wave. The electron plasma wave has frequencies and wave number ω_{ek} and $\mathbf{k}_{ek}$, respectively, while the scattered electromagnetic wave has frequencies and wave number ω_s and $\mathbf{k}_s$, respectively.

The basic physics of SRS is explained in the following. Let E_0 be the amplitude of a transverse electric field with wave number $\mathbf{k}_0$ propagating through a plasma. Let δn be the electron density fluctuation associated to an electron plasma wave. Since electrons oscillate in the field with velocity $v_0 = eE_0/m\omega_0$, a transverse current $\delta\mathbf{J}$=-$e\mathbf{v}_0\delta n$ is generated. With proper matching of the frequencies, this transverse current generates a scattered light wave with amplitude $\delta\mathbf{E}$. This scattered light beats with the incident light wave to produce a variation in the wave pressure $\nabla(\mathbf{E}_0 \cdot \delta\mathbf{E})/4\pi$. This pressure generates further densities perturbations which can reinforce the initial fluctuation. This feedback loop leads to the Raman instability. Mathematically, the process is described in [52] [77] [78] [79]. The electric and magnetic fields are expressed in terms of the vector potential in the Coulomb gauge:

$$\begin{cases} \mathbf{B} = \nabla \times \mathbf{A}, \\ \mathbf{E} = -\nabla\phi - \frac{1}{c}\frac{\partial \mathbf{A}}{\partial t}, \end{cases} \tag{1.88}$$

obtaining the wave equation:

$$\left(\frac{1}{c^2}\frac{\partial^2}{\partial t^2} - \nabla^2\right)\mathbf{A} = \frac{4\pi}{c}\mathbf{J} - \frac{1}{c}\frac{\partial \nabla\phi}{\partial t}. \tag{1.89}$$

Plasma is described by the fluid model (1.32), considering the massive ions as fixed neutralizing background:

$$\frac{\partial \mathbf{u}_e}{\partial t} + \mathbf{u}_e \cdot \nabla \mathbf{u}_e = -\frac{e}{m}\left(\mathbf{E} + \frac{\mathbf{u}_e \times \mathbf{B}}{c}\right) - \frac{\nabla p_e}{n_e m}. \tag{1.90}$$

Considering a small perturbation in the field and in the electron density:

$$\mathbf{A} = \mathbf{A}_0 + \tilde{\mathbf{A}},\ n = n_0 + \tilde{n}_e, \tag{1.91}$$

and linearising the equations, the following system is found:

$$\begin{cases} \left(\frac{\partial^2}{\partial t^2} - c^2\nabla^2 + \omega_p^2\right)\tilde{\mathbf{A}} = -\frac{4\pi e^2}{m}\tilde{n_e}\mathbf{A}_0 \\ \left(\frac{\partial^2}{\partial t^2} + \omega_{pe}^2 - 3v_{0e}^2\nabla^2\right)\tilde{n_e} = \frac{n_0 e^2}{m^2 c^2}\nabla^2\left(\mathbf{A}_0 \cdot \tilde{\mathbf{A}}\right) \end{cases}. \tag{1.92}$$

Here $\tilde{\mathbf{A}}$ is the vector potential of the scattered EM wave, $\mathbf{A}_0$ the field of the pump wave and $\tilde{n}_e$ the electron density fluctuation. The first equation describes an electromagnetic wave driven by the current generated by the electron density perturbations oscillating in the field of the pump. The second equation represents an electron plasma wave driven by the coupling of the pump field $\mathbf{A}_0$ with the scattered field $\tilde{\mathbf{A}}$: $\nabla^2\left(\mathbf{A}_0 \cdot \tilde{\mathbf{A}}\right)$.

As previously mentioned, the laser intensity should overcome a threshold value in order for the process to be triggered. From eq (1.92), Ref. [77] derives a formula for the SRS intensity threshold considering oblique laser light incidence:

$$\frac{u_0^2}{c^2}\left[\frac{\omega_0}{c}\left(\frac{\mathrm{d}\,\ln(n)}{\mathrm{d}z}\right)^{-1}\right]^{4/3} > f_s\left(\omega_{pt}, \theta\right), \tag{1.93}$$

where

$$f_s\left(\omega_{pt}, \theta\right) = \frac{\left(\omega_p^2/\omega_0^2\right)^{1/3}}{\left(2 - 2\omega_p/\omega_0 - \omega_p^2/\omega_0^2\right) \pm 2\left(1 - \omega_p/\omega_0\right)^{1/2}\sin\theta}. \tag{1.94}$$

Here ω_0 is the laser frequency, u_0 is the quiver velocity of electrons in pump field and θ the laser angle of incidence. u_0 can be related to the laser intensity considering the following formulas: $u_0 = \frac{eE_0}{m_e\omega_0}$, $I = \frac{c\sqrt{\epsilon}|E_0|^2}{8\pi}$. Ref. [35] presents a simplified version of the formula (1.93) considering normal incidence and evaluating the quantities at $\mathrm{n}_c/4$:

$$\frac{u_0^2}{c^2} = \frac{2^{4/3}}{3}\left(\frac{c}{\omega_0 L_n}\right)^{4/3}, \tag{1.95}$$

$$I_{SRS} = \frac{2^{1/3}}{\sqrt{3}}\left(\frac{c}{\omega_0 L_n}\right)^{4/3}\frac{m_e^2\omega_0^2 c^3}{8\pi e^2}. \tag{1.96}$$

In shock ignition regime (i.e. λ=351 nm, plasma scale-lengths greater than 100 μm and coronal temperatures of few keV) the threshold intensity is below 10^{15} W/cm^2. As such, during the laser spike, this process acquires importance and it may reflect a significant portion of laser light.

An important feature of SRS is the conversion of laser energy into hot electrons having

temperatures much higher than bulk electron temperature [80] [81]. Recent Particle-in-cell simulations reported hot electron temperatures of $\sim$ 30 keV for interaction regimes typical of SI (i.e. UV laser intensities of 10^{15} - 10^{16} W/cm^2 interacting with plasma characterized by density-scale lengths around 300-500 μm and bulk electronic temperatures of few keV)[82][83][84]. Ref. [85] reports a simple relation to derive the EPW phase velocity and thus the velocity that the electron can acquire:

$$v_\phi = c\left[\frac{1}{x^2}\frac{n}{n_c} + 3\frac{v_e^2}{c^2}\right], \tag{1.97}$$

where x=$k_{ek}c/\omega_0$ and v_e the electron thermal velocity in the corona. From this $T_h = \frac{1}{2}m_e v_\phi^2$.

As RAB generated electrons, these electrons can propagate beyond the shock and preheat the fuel, making the compression more difficult. As such, as shown in the next chapter, a great effort has been made by the scientific community in the last decade to better understand their features and to understand the behaviour of SRS.

Two Plasmon decay

An electromagnetic wave incident on an inhomogeneous plasma with increasing density may decay into two electron plasma waves, in a process called "Two Plasmon decay" (TPD) [52]. The frequency and the wave number should satisfy the following matching conditions:

$$\begin{cases} \omega_0 = \omega_{ek1} + \omega_{ek2} \\ \mathbf{k}_0 = \mathbf{k}_1 + \mathbf{k}_2 \end{cases} \tag{1.98}$$

where ω_0 ($\mathbf{k}_0$) is the laser light frequency (wave number) and $\omega_{ek1}(\mathbf{k}_1)$ and $\omega_{ek2}(\mathbf{k}_2)$ are the frequencies (wave numbers) of the electron plasma waves.

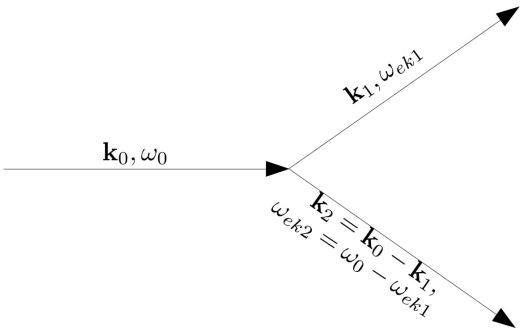

Figure 1.7: Schematic diagram of the TPD process: a photon with frequency ω_0 and wave number $\mathbf{k}_0$ decays into two electron plasma waves with frequencies ω_{ek1} and $\omega_{ek2} = \omega_0 - \omega_{ek1}$ and wave numbers $\mathbf{k}_1$ and $\mathbf{k}_2 = \mathbf{k}_0 - \mathbf{k}_1$.

The process takes place near $n_{c/4}$, where $\omega_0 = 2\omega_{pe}$. The two plasma waves have frequencies approximately ω_{pe}, such that the instability is also called the"$2\omega_{pe}$" instability.

Refs. [86] and [52] present a mathematical treatment of the phenomenon. Electrons are described by the warm fluid equations while ions are considered fixed. The continuity

and the momentum equations for electrons (1.32) read:

$$\begin{cases} \frac{\partial n_e}{\partial t} + \nabla \cdot (n_e \mathbf{u}_e) = 0, \\ \frac{\partial \mathbf{u}_e}{\partial t} + (\mathbf{u}_e \cdot \nabla \mathbf{u}_e) = -\frac{\nabla p}{nm} - \frac{e}{m} \left(\mathrm{E} + \mathbf{u}_e \times \mathbf{B}/c \right). \end{cases} \tag{1.99}$$

Considering small perturbations from the equilibrium, i.e. $n_e = n_0 + \tilde{n_e}$, $\mathbf{u}_e = \mathbf{v}_{os} + \tilde{\mathbf{u}_L}$, where n_0 is the un-perturbed ion density and $\mathbf{v}_{os}$ is the velocity of electron oscillation in the field (i.e. $\mathbf{v}_{os} = \frac{e\mathbf{A}_0}{mc}$), the equations are linearised and Fourier transformed to obtain a system that describes the density perturbations for the two plasma waves:

$$\begin{aligned} &\left(-\omega^2 + \omega_{pe}^2 + 3v_e^2 k^2\right) \tilde{n_e}\left(k, \omega\right) + \\ &+ \frac{\mathbf{v}_{os}}{2} \cdot \left[\omega \mathbf{k} \tilde{n_e}\left(k - k_0, \omega - \omega_0\right) + n_0 k^2 \tilde{\mathbf{u}_L}\left(k - k_0, \omega - \omega_0\right)\right] = 0, \end{aligned} \tag{1.100}$$

$$\begin{aligned} &\left[-\left(\omega - \omega_0\right)^2 + \omega_{pe}^2 + 3v_e^2 \left(k - k_0\right)^2\right] \tilde{n_e}\left(k - k_0, \omega - \omega_0\right) + \\ &+ \frac{\mathbf{v}_{os}}{2} \cdot \left[\left(\omega - \omega_0\right) \mathbf{k} \tilde{n_e}\left(k, \omega\right) + n_0 \left(\mathbf{k} - \mathbf{k}_0\right)^2 \tilde{\mathbf{u}_L}\left(k, \omega\right)\right] = 0. \end{aligned} \tag{1.101}$$

In particular, these equations describe the coupling of electron plasma waves with wave number k and $k - k_0$ by the laser light. Notice that $\omega_{pe}^2 + 3v_e^2 k^2 = \omega_{ek}^2$ and $\omega_{pe}^2 + 3v_e(k - k_0)^2 = \omega_{ek-k_0}^2$ (see Sec. 1.2.4).

A peculiar feature of TPD is the generation of the $\frac{3}{2}\omega_0$ signal due to the secondary scattering of the incident wave. The backward propagating plasma wave generated in the decay at quarter-critical density may in turn scatter the incident laser wave, producing a scattered electromagnetic wave with $\omega = \frac{3}{2}\omega_0$. This radiation can leave the plasma and it may be detected using proper diagnostics (see Chap. 2), testifying the presence of the process.

The intensity threshold for TPD reads [87]:

$$I_{TPD} = \frac{8.2 T_{keV}}{L_{\mu m} \lambda_{\mu \mathrm{m}}}, \tag{1.102}$$

where I_{TPD} is the laser intensity in units of PW/cm^2, $\lambda_{\mu m}$ the laser wavelength in μm, T_{keV} and $L_{\mu m}$ the coronal plasma temperature and the scale-length expressed in keV and μm, respectively. In SI regime, similarly to SRS, the intensity threshold is around 10^{14} W/cm^2. It is important to notice that the intensity threshold for TPD shows a dependency on the plasma temperature, differently from SRS case. Higher plasma temperature will increase the value of intensity threshold.

An important feature of TPD is the generation of energetic electrons produced by the two $2\omega_{pe}$ plasmons [88] [89]. Ref. [88] presents the first experimental study of hot electrons generated by TPD using CO_2 lasers at intensities of $\sim 10^{14}$W/cm^2. The hot electron emission was maximum about the 45° with respect to the laser $\mathbf{k}$ vector in both the forward and backward directions. Electron Maxwellian temperatures around 60 keV were measured. TPD generated electrons with Maxwellian temperatures around 60 -100 keV are also predicted by recent PIC simulations performed considering SI relevant laser-plasma conditions [90] [91]. These highly energetic electrons can represent an issue for the SI scheme, since they can propagate beyond the shock front and preheat the DT shell.

Stimulated Brillouin Scattering

The Stimulated Brillouin scattering instability represents the coupling of an incident electromagnetic wave into a scattered light plus an ion-acoustic wave (see Sec. 1.2.4) [92]. The matching conditions for the frequency and the wave number are:

$$\begin{cases} \omega_0 = \omega_s + \omega_{ik}, \\ \mathbf{k}_0 = \mathbf{k}_s + \mathbf{k}_{ik}, \end{cases} \tag{1.103}$$

where $\omega_0(\mathbf{k}_0)$ is the frequency (wave number) of the incident light, $\omega_s(\mathbf{k}_s)$ the frequency (wave number) of the scattered light and $\omega_{ik}(\mathbf{k}_{ik})$ the frequency (wave number) of the ion acoustic wave. Fig. 1.8 shows schematically the process. Since the ion acoustic frequency

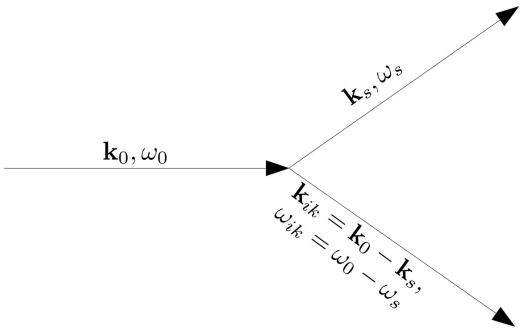

Figure 1.8: Schematic diagram of the SBS process: a photon with frequency ω_0 and wave number $\mathbf{k}_0$ decays into an ion plasma wave and into an electromagnetic wave. The ion plasma wave has frequencies and wave number ω_{ik} and $\mathbf{k}_{ik}$, respectively, while the scattered electromagnetic wave has frequencies and wave number ω_s and $\mathbf{k}_s$, respectively.

is much less than the laser frequency, nearly all the energy of the incident photon can be transferred to the scattered light wave. The mathematical treatment of the phenomenon presented in [52] is similar to SRS (see Sec. 1.2.6), except for the fact that ions are no longer considered as fixed. Coupling the fluid equations (1.32) with the Maxwell's equations for the field (1.89), an equation for the low frequency density fluctuation $\tilde{n}_i$ is derived:

$$\frac{\partial^2 \tilde{n}_i}{\partial t^2} - c_s^2 \nabla^2 \tilde{n}_i = \frac{n_0 e^2}{m_e M_i c^2} \nabla^2 \left(\mathbf{A}_0 \cdot \tilde{\mathbf{A}} \right). \tag{1.104}$$

Here M_i represents the ion mass. This equation describes the excitation of an ion acoustic wave by the interaction between the incident and the scattered light waves.

Like SRS and TPD, SBS occurs only if the laser intensity overcomes a given threshold [76]:

$$I_{SBS} = \frac{5 \times 10^{15}}{L_{\mu\mathrm{m}} \lambda_{\mu\mathrm{m}}} T_{keV} \text{ W/cm}^2. \tag{1.105}$$

In this equation, $L_{\mu\mathrm{m}}$ and T_{keV} are the plasma density scale length and coronal temperature expressed in μm and keV, respectively. $\lambda_{\mu\mathrm{m}}$ is the laser wavelength expressed in μm. Considering typical SI parameters, the threshold is around 10^{14} W/cm^2.

Because of the large amount of backscattered light, the instability can significantly degrade the absorption laser, with detrimental effects for ICF schemes.

Langmuir decay instability

The Langmuir Decay Instability [93] is a process by which a primary electron plasma wave decays into a secondary electron plasma wave and an ion acoustic wave. This process may repeat itself, i.e. the secondary electron plasma wave decays in another electron plasma wave and an ion acoustic wave. In this case, the process is called *LDI cascade* [94].

1.2.7 Landau Damping and Electron heating

We have reported, in the previous sections, different mechanisms whereby intense laser light couples either with EPW (RAB and TPD) or into both EPW and electromagnetic scattered waves (SRS). In Sec. 1.2.4, the dispersion relation for EPWs was obtained starting from the fluid description of plasma. If one takes into account the corpuscular nature of plasma, an important damping mechanism arises, the so called *"Landau Damping"*. In this process, the wave interacts with particles of velocity close to its phase velocity. Most particles are not resonant, i.e. their velocity along the wave propagation is different from the wave phase velocity (i.e. $u \neq \omega/k$). These particles simply oscillate in the field, not experiencing gain or loss in energy. On the contrary, those electrons with $u \sim \omega/k$ stay roughly in phase with the wave and more efficiently exchange energy with it. These electrons are called **resonant** and they can be efficiently accelerated or decelerated. Qualitatively, it is possible to demonstrate that, for particles moving slightly slower than the wave, acceleration is a stronger effect than deceleration. As such, on the average, slower particles gain energy from the wave that is damped. The opposite is true for particles that travel slightly faster than the wave. As an example, Fig. 1.9 illustrate the mechanism considering a general electron velocity distribution function $f_e(u)$. The slower particles outnumber the faster ones and the wave loses more energy than it gains, being therefore damped. The analytical treatment of this phenomenon was firstly proposed by Landau [95], but it can be also found in more recent books [51][43][50]. It is based on the coupling

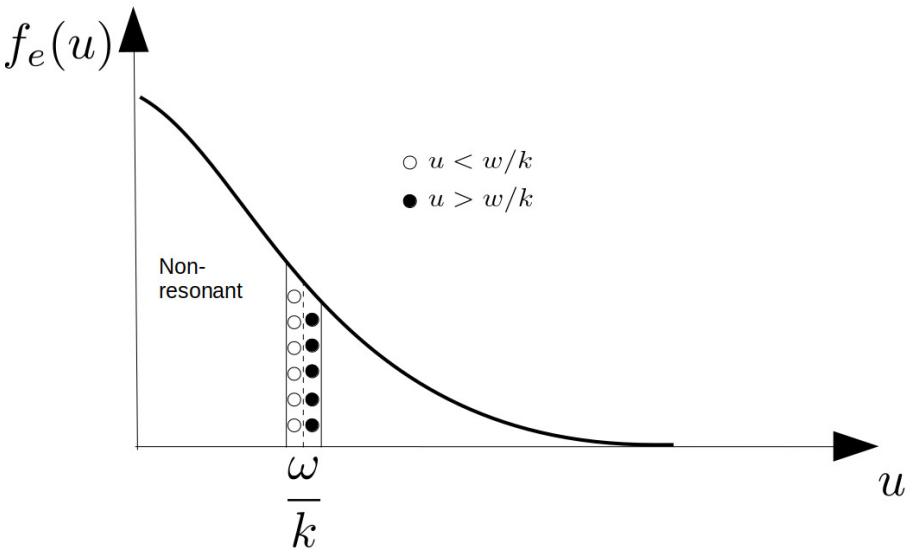

Figure 1.9: Illustration of the Landau Damping mechanism considering a general electron velocity distribution function $f_e(u)$: filled circles represent electrons with velocity $u > \omega/k$ that give energy to the wave. White circles represent electrons with $u < \omega/k$ that gain energy from the wave.

between the Vlasov (1.30) equation and the Gauss equation for the longitudinal electric field (1.39). As such, the phenomenon is collisionless.

In a large amplitude electron plasma wave, the oscillation velocity of an electron in the field can be large enough to bring an initial non-resonant particle in the resonance region. When numerous particles interact with the wave, a strong nonlinear damping results and the electrons are efficiently accelerated by the wave that is thus damped. The mechanism of hot electron generation in ICF regime is not completely understood and still debated in the scientific community. The book of Mulser [96] offers a mathematical description of the process. Recent theoretical models of hot electron generation from TPD implemented in numerical codes can be found in Ref [90] [97].

1.3 Hydrodynamic Evolution of the target

When laser light with intensities around 10^{13}-10^{15} W/cm^2 interacts with a solid target, a plasma state is suddenly created and the material starts to evaporate. The whole region in which the laser-plasma interaction takes place is called the corona. Here, the laser penetrates up to the critical density and deposits energy which is then transmitted into the target by thermal conduction. After some instants, distinct regions develop: the coronal part, the conduction region, the shocked region and the unperturbed solid. Fig. 1.10 shows a schematic picture of the different zones, reporting the plasma conditions.

The corona is separated from the conduction region by the critical surface. In the conduc-

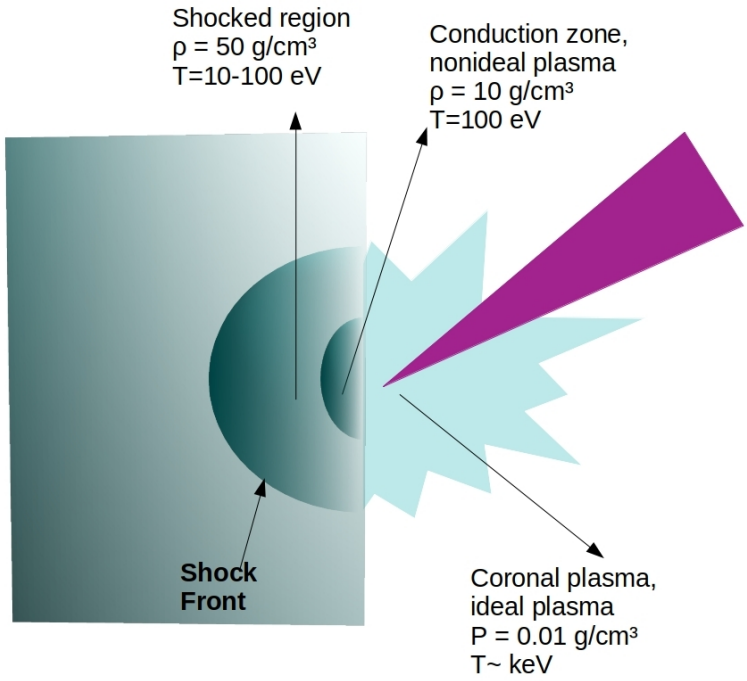

Figure 1.10: Laser beam interacting with a solid target. Shock-compressed solid matter is formed, with a dense ablation zone and a low density corona. The laser interaction occurs in the low-density ideal plasma, while heat conduction, hydrodynamic phenomena and hot electron transport occur in the solid target, which is in a strongly coupled plasma state.

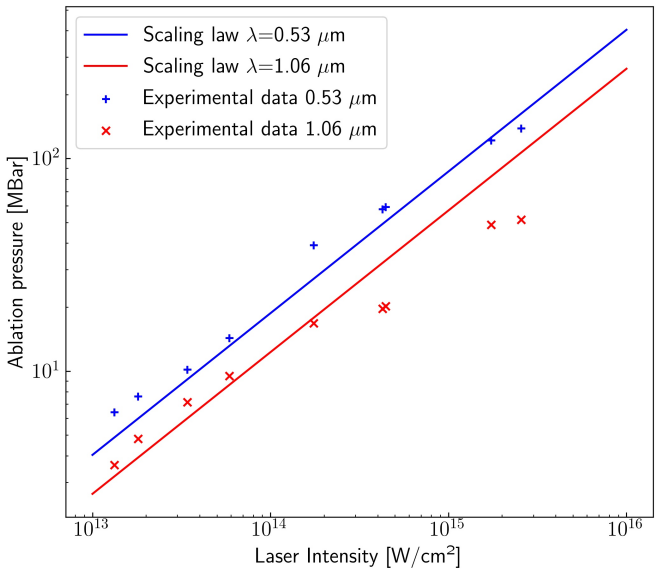

Figure 1.11: Ablation pressure produced by laser-driven ablation as a function of the absorbed laser intensity. Results from experiments with laser wavelength of 0.53 μm and 1.06 μm are reported by blue and red crosses, respectively. Ablation pressure predicted by the analytic expression (1.106) are indicated by the red and the blue curves, for $\lambda =$ 0.53 μm and 1.06 μm, respectively.

tion zone, thermal energy is transported to the colder dense part mostly through electronic conduction (Spitzer-Harm model [8] [52]). In this domain, the density is between 0.01 g/cm^3 and the solid density, while the temperature goes from ∼keV of the corona down to ∼100 eV. At the critical density the plasma blows off in the direction of the laser with the sound speed velocity. The pressure generated by this rocket effect leads to the creation of a shock wave that propagates in the solid target. The shocked region reaches densities greater several times the solid density and temperature of tens of eV. The shock propagates in the unperturbed target. The temperature and the density reached in this zone are greater compared to the cold undriven solid. This happens because of the presence of several processes like radiative heating or hot electron energy deposition. In particular, hot electrons that propagate beyond the shock front can preheat the unperturbed region, raising its temperature at values around some eV.

1.3.1 Ablation Pressure

The laser-driven ablation mechanism that occurs at the ablation surface is described by the *stationary ablation model* [8]. The model makes the hypothesis that the ablated material is transparent to the external radiation and the absorption is localized near the critical density. The plasma flow velocity is subsonic in the conduction zone and supersonic in the corona. The inward acceleration of the fuel is driven by the ion blowing off. In ICF, this acceleration toward the centre of the capsule drives the implosion.

In planar geometry, in the case of plastic targets, the ablation pressure is related to

the absorbed laser intensity and to the wavelength according to the scaling law [98] [99]:

$$p_a = 57 \left(I_{abs} \ / \lambda_L \right)^{2/3} . \tag{1.106}$$

Fig. 1.11 shows how the experimental measurements for the ablation pressure follow the scaling law (1.106), considering an absorbed laser intensity that ranges from 10^{13} up to 10^{15} W/cm^2. The ablation pressure generates a shock wave that propagates in target.

1.3.2 Shock Waves

A shock wave is a discontinuity in density, velocity and temperatures that propagates with velocities greater than the sound speed of the lower density plasma lying ahead [53]. A first analytical description of shock waves can be given considering an ideal gas compressed by a piston that moves with velocity u. The undisturbed gas ($t = 0$) is characterized by density ρ_0, pressure p_0, internal energy ε_0 and velocity $\mathrm{u}_0 = 0$. The continuity equations (1.37) can be used to derive the state of the gas (ρ_1, p_1, u_1, ε_1) and the propagation velocity of the discontinuity in the undisturbed fluid D. In the laboratory frame, the mass flow going in the shock front through a surface area S is $\dot{m}_0 = \rho_0 \left(u_0 - D \right) S$, while the downstream fluid of mass that gets out of the shock front is $\dot{m}_1 = \rho_1 \left(u_1 - D \right) S$. The mass conservation law at the discontinuity surface reads:

$$\rho_0 \left(u_0 - D \right) = \rho_1 \left(u_1 - D \right) . \tag{1.107}$$

Analogous considerations for momentum and energy conservation at the discontinuity surface yield:

$$p_0 + \rho_0 \left(u_0 - D \right)^2 = p_1 + \rho_1 \left(u_1 - D \right)^2 , \tag{1.108}$$

$$\frac{p_0}{\rho_0} + \frac{\left(u_0 - D \right)^2}{2} + \varepsilon_0 = \frac{p_1}{\rho_1} + \frac{\left(u_1 - D \right)^2}{2} + \varepsilon_1 . \tag{1.109}$$

These relations are called *jump conditions* and they represent the flow of variables through the discontinuity surface. Since the discontinuity is infinitesimally thin, no accumulation of mass, momentum or energy can take place within it. In the shock reference frame these equations read:

$$\begin{cases} \rho_1 v_1 = \rho_0 v_0 , \\ p_1 + \rho_1 v_1^2 = p_0 + \rho_0 v_0^2 , \\ \varepsilon_1 + \frac{p_1}{\rho_1} + \frac{v_1^2}{2} = \varepsilon_0 + \frac{p_0}{\rho_0} + \frac{v_0^2}{2} , \end{cases} \tag{1.110}$$

where $v_0 = -D$ and $v_1 = -\left(D - u \right) = -\left(D - u_1 \right)$. Coupling these three equations with the equation of state (for example the polytropic equation (1.38)), we obtain a system

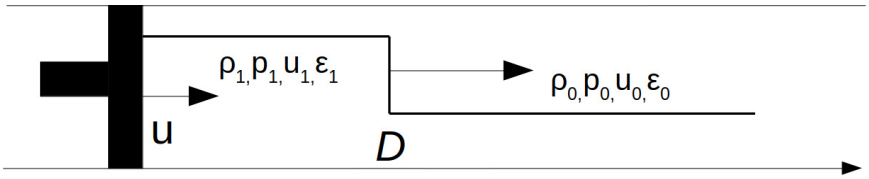

Figure 1.12: Schematic representation of shock wave propagation. The wave is produced by a piston that moves into the gas with constant velocity u. The gas state is described by the hydrodynamic quantities ρ, p, u, ε, subscripted by "0" for the upstream quantities and by "1" for the downstream quantities. D is the shock velocity.

of four equations for the four downstream unknown quantities ρ_1, p_1, u_1, ε_1 and the unknown shock velocity D. As such, an experimental measure of one of the five unknowns allows to determine the others. As an example, in experiments, shock velocity is usually determined by measuring the time emission from the rear surface of a planar target.

From eq. (1.110) the following relations are found:

$$\frac{\rho_1}{\rho_0} = \frac{(\gamma+1)\,p_1 + (\gamma-1)\,p_0}{(\gamma-1)\,p_1 + (\gamma+1)\,p_0}, \tag{1.111}$$

$$D = u_0 \pm \sqrt{\frac{(\gamma+1)\,p_1 + (\gamma-1)\,p_0}{2\rho_0}}, \tag{1.112}$$

$$u_1 = u_0 \pm \sqrt{\frac{2\,(p_1-p_0)^2}{\rho_0\left[(\gamma+1)\,p_1 + (\gamma-1)\,p_0\right]}}, \tag{1.113}$$

$$\frac{\varepsilon_1}{\varepsilon_0} = \frac{p_1}{p_0}\frac{(\gamma-1)\,p_1 + (\gamma+1)\,p_0}{(\gamma+1)\,p_1 + (\gamma-1)\,p_0}. \tag{1.114}$$

From these relations, it is evident that the shock wave cannot rise the downstream density indefinitely. In particular, for $p_1 \gg p_0$, eq. (1.111) becomes:

$$\frac{\rho_1}{\rho_0} = \frac{\gamma+1}{\gamma-1}, \tag{1.115}$$

and for a monoatomic perfect gas with constant specific heat ($\gamma = 5/3$) the maximum ratio between the final and initial density is 4. Even at high temperatures and pressures, when the specific heats are no longer constant because of molecular dissociation and ionization, the density ratio remains finite and does not increase without limit. As such, as reported in Sec. 0.3 and 0.2, to compress the fuel at the required densities for ignition to occur, it is not possible to use a single strong shock wave. It is necessary to shape the laser beam in order to produce multiple shocks that merge in the inner part of the shell.

An important quantity related to the shock dynamics is the entropy. For a perfect gas with constant specific heat the entropy is given by the formula:

$$S = c_v \ln\left(pV^\gamma\right), \tag{1.116}$$

where V is the specific volume of the gas. As such, the difference between the entropy on each side of the shock front becomes:

$$S_1 - S_0 = c_v \ln\left(\frac{p_1 V_1^\gamma}{p_0 V_0^\gamma}\right) = c_v \ln\left\{\frac{p_1}{p_0}\left[\frac{(\gamma-1)\,(p_1/p_0) + (\gamma+1)}{(\gamma+1)\,(p_1/p_0) + (\gamma-1)}\right]^\gamma\right\}. \tag{1.117}$$

For $p_1 \to p_0$ the expression leads to $S_1 \simeq S_0$, while as the shock strength (p_1/p_0) increases also $S_1 - S_0$ increases monotonically, approaching infinity as $p_1/p_0 \to \infty$. The increase of entropy indicates that a shock wave is a dissipative irreversible phenomenon. As shown in Chapt. 0, in SI the fuel is firstly pre-compressed keeping the deposited entropy as low as possible, and then ignited with a strong shock that deposits a large amount of entropy in the hot-spot.

1.4 Conclusion

We have presented, in this chapter, some basic concepts of plasma physics, that allow to understand the hot electron generation and propagation in the context of ICF. In Sec, 1.1 some basic features of plasma physics are reported, considering in particular the Debye Huckel theory, the collision theory and the mathematical description of three plasma models. These concepts are particularly useful in the description of the laser plasma interaction and the hot electron propagation in ionized targets. In Sec. 1.2, a list of various mechanisms that characterize the laser-plasma interaction and the hot electron generation for intensities relevant to SI is shown. In particular, for RAB, SRS and TPD a brief state of the art considering some experimental and theoretical works related to the hot electron production was presented. It is important to point out that what is reported here is not exhaustive, since the topic of laser-plasma interaction is a very rich topic. We did not describe several important phenomena, such filamentation or the description of ponderomotive force [52] [50].

In Sec. 1.3, a simple description of the hydrodynamic evolution of a target irradiated by laser intensities relevant for ICF is reported. In particular, the ablation pressure and the shock wave dynamics were briefly discussed, giving a simple modelization that allows to better understand the planar experimental investigations presented in this work.

In the next chapter, we will give an overview of the most important theoretical or experimental investigations on the characterization and on the effects of hot electrons in ICF context.

Chapter 2

State of the art of hot electrons in Shock Ignition: effects and characterization

In the Shock Ignition and in the traditional approaches to inertial confinement fusion, laser intensities of the order of $\sim 10^{15}$ - 10^{16} W/cm^2 are required to ignite the hotspot (see Sec. 0.2 and 0.3). These values of laser intensity exceed the thresholds for the generation of different laser-plasma instabilities (LPI), which take part in the underdense region of the plasma, preventing part of the laser energy from arriving at the critical surface. In particular, part of the laser energy is scattered or converted into highly energetic electrons by stimulated Raman scattering (SRS) and two-plasmon decay (TPD) instabilities [52] (see Sec. 1.2.6). A critical issue for answering the feasibility of the ICF schemes is to understand the role of this hot electron population on the implosion performance. The major concern related to the presence of hot electrons is related to the fact that they can penetrate through the solid dense shell, preheating the cryogenic DT fuel or ablating its inner surface before the shock arrival. As pointed out in Sec. 1.2.3, collisional absorption decreases with the laser wavelength, while the nonlinearity of the laser-plasma interaction is characterized by the coupling parameter $I_L\lambda_L^2$. As such, long wavelength and high intensity laser beams are mainly absorbed due to resonant effects, accompanied by the generation of hot electrons. Issues related to the penetration of hot electrons generated by long wavelength lasers (CO_2, λ=10 μm) were reported in the first ICF experiments [100] [101] [102] [103]. The hot electron Maxwellian temperature reported in the articles was around 50 - 80 keV. In particular, a first experimental investigation on CO_2 laser driven implosion is showed in Ref. [104]. Here, the authors claimed a poor spherical shell compression because of the presence of hot electrons. Lower electron temperatures ($\sim$20 keV) were found in Nd:glass laser experiments [105]. This suggested the possibility of using shorter wavelength laser pulses ($\lambda = 0.5$ - 0.25 μm) to compress the targets [106] [9].

While in conventional ICF the presence of hot electrons is detrimental, in SI they are produced by the final high intensity spike, when the target areal density ρr is quite large. If the target areal density is sufficiently high, electrons will be stopped in part in the compressed ablator and in the outer regions of the imploding shell, increasing the shock pressure with beneficial effects for the SI scheme. On the contrary, if the capsule areal density is not sufficiently high, the electron beam can preheat the pre-compressed DT dense shell degrading the performance of implosion.

In the following sections, we report different theoretical or experimental studies in which the two effects are investigated. We report also the most relevant laser-plasma experiments performed in the last decades, aiming at characterizing hot electrons in conditions relevant to SI.

2.1 Ablation pressure driven by hot electrons

Hot electrons could contribute to the ablation pressure, if the target areal density is larger compared to their range. Ref. [34] presents a model to describe the formation of ablation pressure driven by a monoenergetic electron beam that propagates in a planar DT plasma (steplike profile with density ρ=10 g/cm^3). Hot electrons propagate in the target behind the ablation front created by thermal electrons and they deposit energy in the plasma according to their range. If their stopping length is much shorter than the target thickness, the target heating causes mass ablation and the shock is driven by rocket effect. The energy deposited is redistributed between internal and kinetic energy of the expanding plasma, in a transient time called *loading time*. The plasma is thus heated and it starts expanding. If the intensity of the electron beam is of the order of $\sim 10^{15}$W/cm^2, the heating proceeds rapidly and the thermal conduction does not have sufficient time to take place. The pressure applied by the heated layer on the colder plasma launches a strong shock. In Ref. [107], the following scaling law is proposed to describe the maximum ablation pressure reached after the loading time:

$$p_h = 175 I_b^{2/3} \rho^{1/3} \text{MBar}, \tag{2.1}$$

where I_b is the intensity of the electron beam in PW/cm^2 and ρ is the density in g/cm^3. After reaching its maximum value, the pressure will decrease as the square root of time:

$$p(t) = p_h (t_h/t)^{1/2}. \tag{2.2}$$

Considering a monochromatic electron beam with kinetic energy of 50 keV and intensity of 1 PW/cm^2, that propagates in compressed DT plasma with density 12 g/cm^3, it is possible to estimate that the pressure may achieve values of 400 MBar in a loading time

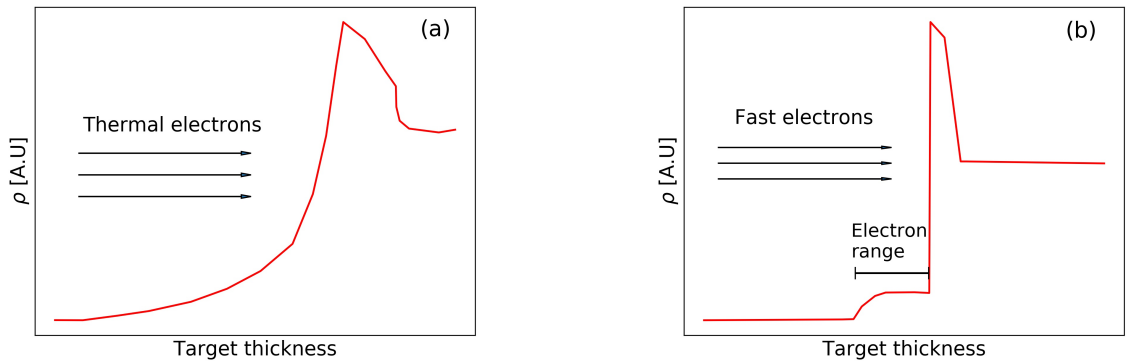

Figure 2.1: Density profile of ablation front of solid material in the case of (a) laser ablation in stationary regime; (b) hot electron beam in non stationary regime after the loading time.

of 20 ps. This simplified model suggests that it is possible to achieve high shock pressures driven by hot electrons in high density solid materials. However, this study is limited by the simplifying condition of monoenergetic electron beam in a steep density profile. In SI it is necessary to consider that electrons are generated during the spike in a time window longer compared to the loading time presented in [34] and [107]. Furthermore, electrons generated by laser-plasma interaction present a broad spectrum in energy and in momentum direction.

The effects of hot electrons on the ablation pressure and on the shock formation were studied experimentally in [108], [109] and [110]. In these experiments, Al or Cu solid targets were irradiated using the first ($\lambda_1 = 1314$ nm) or the third ($\lambda_3 = 438$ nm) harmonic of the PALS laser system [111]. The pulse duration was of the order of hundreds of picoseconds, and the intensity on target was varied from $\sim 10^{13}$ up to $\sim 10^{16}$ W/cm^2 by reducing the laser beam radius R_L (from 600 μm down to 35 μm). This allowed to access different domains of laser absorption: in the region $4 \times 10^{12} < I\lambda^2 < 10^{14}$ W/cm^2 the inverse bremsstrahlung dominates, while for $10^{15} < I\lambda^2 < 1.5 \times 10^{16}$ W/cm^2 the radiation is absorbed primarily by resonance absorption and other non-linear processes, accompanied by the generation of electrons. The two mechanisms lead to different plasma plume characteristics and, as a consequence, different shock waves and craters are produced. As shown by Fig. 2.2, for the third harmonic the crater volume showed a parabolic behaviour with the laser radius, reaching a maximum around 300 μm. In the λ_1 case, the dependence of the crater volume with the radius was reproduced, although its maximum was less pronounced. For low values of laser radius (i.e. higher intensity) the dependence was reversed. To explain this behaviour, the authors proposed two different analytical models to describe the thermodynamic properties that influence the plasma plume and the consequent shock formation. In the case of Inverse Bremsstrahlung, the absorption and the mass ablation occur in the plasma region near the critical density, while in the case of resonance absorption the vaporized mass is defined by the thickness of the target heated by hot electrons. For this purpose, the authors consider a monochromatic electron spectra characterized by a given range l_0. Where the inverse bremsstrahlung absorption

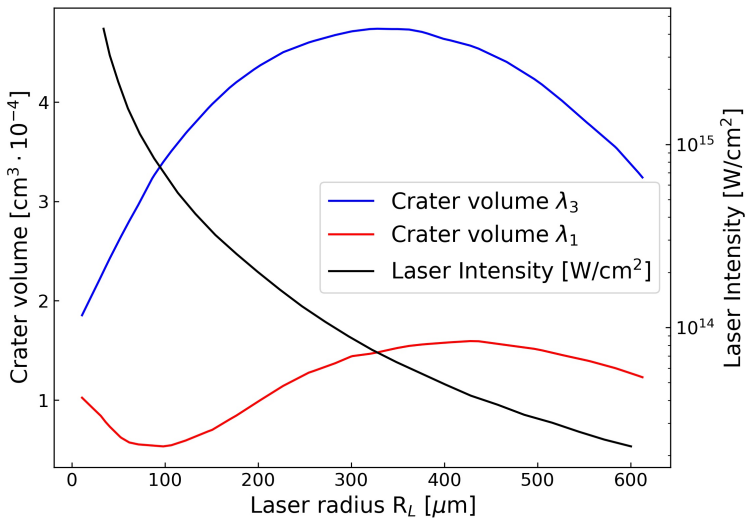

Figure 2.2: Behaviour of the crater volume as a function of the laser spot radius R_L, for the two irradiation wavelengths λ_1=1314 nm (red curve) and λ_3=438 nm (blue curve). The laser intensity is indicated by the black curve [108].

dominates (i.e. for $R_L > 300$ μm), the efficiency of energy transfer to the shock wave under irradiation by the third harmonic is approximately three times higher than the efficiency obtained with the first harmonic. This fact is due to the presence of higher critical plasma densities (see eq. (1.61)), and it is reflected in greater crater volumes [112]. Decreasing the beam radius, the plasma plume experiences a transition from planar expansion to spherical one. This causes a reduction of the density near the ablation surface, and thus a decrease of the efficiency of the inverse bremsstrahlung absorption. However, this effect is in competition with the increase of the ablation density due to the heating of fast electrons. In particular, for the first harmonic, at $R_L \sim 35$ μm the beneficial effects due to the presence of hot electrons prevails over the density lowering.

2.2 The role of the hot electrons in the Shock Ignition scheme

In SI approach to ICF a spherical target is imploded to achieve high compression of the fuel by means of a high intensity laser spike ($I \sim 10^{15} - 10^{16}$ W/cm^2) that launches a strong converging shock (see Sec. 0.3). The hot electrons generated by the high intensity spike can propagate into the imploded target, preheating the inner part of the DT-shell before the shock arrival. This preheat makes the compression more difficult and it can compromise the implosion.

We present, in this section, different experimental or theoretical investigations of the shell preheat caused by hot electrons.

2.2.1 Experimental studies on the effects of hot-electrons on the implosion scheme

Ref. [113] presents an experimental study of low-adiabat cryogenic D_2 implosion in which the peak intensity was varied in a range from $\sim 3\times10^{14}$ to $\sim 1\times10^{15}$ W/cm^2. Higher laser intensities enhance the hot electron production, and the aim of the experiment was to study their effects on the implosion. The experiment was performed using the 351-nm, 60-beams OMEGA Laser System [114], varying the on-target energy from $\sim$13 kJ up to $\sim$24 kJ. The targets were 860 μm diameter shells consisting of 4 μm thick deuterated plastic layer ablator (CD) and $\sim$95 μm inner D_2 ice layer. Hot electrons were assumed to have a Maxwellian distribution in energy, and their temperature and flux were characterized exploiting the x-ray radiation emitted by their propagation in the target (see Sec. 2.3). The two quantities were found to increase monotonically within the range of the considered laser intensities, as shown in Fig. 2.3. In particular, the hot electron temperature rose from 50 keV up to 150 keV, implying longer penetration depths into the target. Implosion performances were evaluated considering as figure of merit the areal density reached by the shell, inferred from the spectra of secondary protons. The highest compression was achieved at the lowest laser intensities, while gradual areal-density degradation was observed at higher intensities (see Fig. 2.3). This effect is due to the hot electron preheating. The preheating energy necessary to significantly degrade the compression was estimated to be $\sim$40 J, i.e. the $\sim$0.2% of the drive energy (for this particular configuration). Authors estimated this value considering the ideal plasma model. One should also note that these are low convergence targets, which inherently reach lower ρr

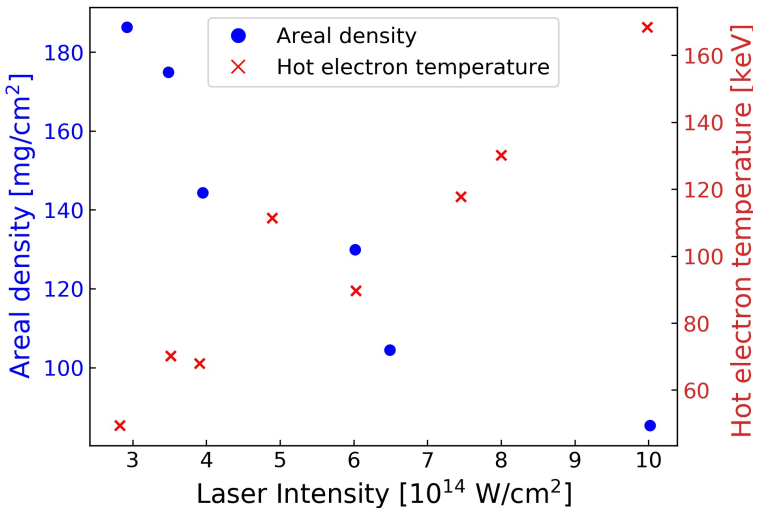

Figure 2.3: Evolution of the areal density (blue dots) and the hot electron temperature (red crosses) with the laser intensity measured in the experiment [113].

and hence are more susceptible to HE preheat.

Ref. [32] presents an experimental investigation on the effects of hot electrons generated at different times during the fuel assembly. Deuterated plastic shells (34.8 μm CH(D), 435 μm radius) filled with ~10 atm of D_2 were imploded with the OMEGA 40 UV beams, for an on-target energy of ~15 kJ. After the compression phase, 20 spike pulses delivered a total energy of ~5 kJ in ~600 ps on the sphere. Different shots were performed launching the spike pulse at different times, from 2.4 ns up to 3.2 ns after the start of the compression pulses. The areal density and the neutron yield were considered as the figures of merit to evaluate the performance of the implosion. Detrimental effects were observed when the spike was launched early (t = 2.4 ns). At that time, the areal density was not sufficiently high to stop electrons, resulting in fuel preheating. For latest spike launch time, the areal density was higher and only the outer part of the shell was preheated. The inner part stayed at low adiabat, which is essential to reach high compression. This principle is consistent with numerical findings presented in [33] (see Sec. 2.2.2).

A recent experimental study on the degradation of the ρr due to hot electron preheat is presented in Ref. [115]. Here authors assert the importance of characterizing the total energy that electrons deposit in the DT fuel and, more specifically, in the inner part of the shell. To evaluate the energy deposition in the DT shell, two different types of targets were irradiated with the same laser conditions: a DT layered target with an outer plastic ablator shell (Fig. 2.4 (a)) and an ablator-only target with the same mass of the layered target (Fig. 2.4 (b)). The x-ray signal measured in the two implosions differs only because of the hot electrons slow down in DT rather than in plastic. This difference is therefore proportional to the preheat energy deposited in the DT layer (payload). The deposition profile along the DT layer is then evaluated replacing the DT-ice shell with a Cu-doped plastic shell of different radius (Fig. 2.4 (c)).

Authors found a ρr degradation of ~20% due to the presence of hot electrons with temperature T_h=60 keV, carrying a total energy E_{tot}^{hot}=44 J (retrieved using the bremsstrahlung

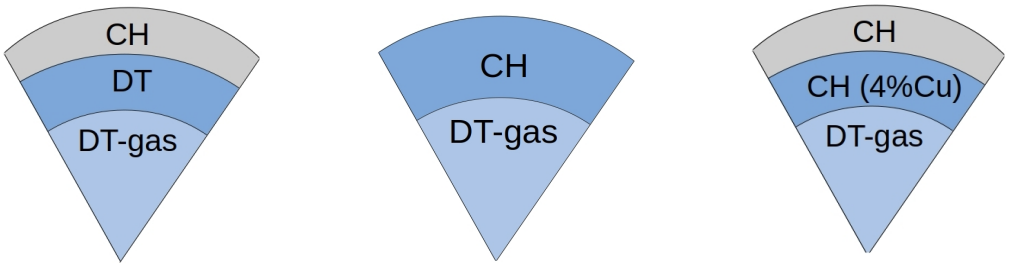

(a) DT-layered (b) ablator-only (c) Cu-doped payload

Figure 2.4: Configuration of the irradiated targets used in [115].

radiation, see Sec. 2.3.2)

2.2.2 Numerical studies on the effects of hot-electrons on the implosion scheme

A first numerical study on the competition between the increase of shock pressure and shell preheat driven by hot electrons is presented in Ref. [116], in the framework of the HiPER project. Here authors evaluate the effects of an exponential electron energy spectrum with temperature of 30 keV and intensity 1 PW/cm^2 on the implosion of a DT target. The target is a DT fusion capsule initially precompressed to high density by a 10 ns pulse (λ=351 nm, 250 kJ), as proposed in [117]. The laser plasma interaction and the hydrodynamic evolution of the target were computed using CHIC hydrodynamic code [37], while the electron transport and energy deposition were simulated using the Vlasov-Fokker-Planck code M1 [118]. Authors show that the areal density reached by the target after the compression phase was not sufficient to inhibit the hot electron preheat, compromising the implosion.

Ref. [33] presents a detailed numerical investigation on the effects of hot electrons on the implosion scheme using the CHIC radiative hydrodynamic code [37]. A target composed by a high Z ablator of 15 nm (Al, 2.7 g/cc), 31 μm of CH (1.05 g/cc), 220 μm DT-ice shell (0.253 g/cc) and 737 μm of DT-gas hotspot (10^{-4} g/cc) was imploded with a typical SI laser beam configuration. A pre-compression beam compressed the capsule at lower velocity, followed by the ignitor pulse. This latter was launched at different times in a window that goes from 13 ns up to 13.6 ns (see Fig. 2.5). Electrons were generated during the spike pulse, encountering different areal densities according to the starting time. Different cases were considered, varying the power of the ignitor spike from 200 TW (*nominal case*), up to 500 TW (*high power case*). The laser wavelength set in the simulations was 351 nm and the beam was normally incident to the target normal. The propagation of laser light in plasma was modelled using Paraxial Complex Geometrical Optics [119]. This decomposes the laser beam in individual Gaussian beamlets for which diffraction is accounted for, and the linear inverse Bremsstrahlung absorption at the critical density is calculated. In addition, the model accounts for the conversion of laser energy into hot electrons generated at the critical density by RAB, at the quarter critical density by TPD and below $n_c/4$ by SRS. Electron beams were described by exponential distribution functions in energy ($f(E)\ \alpha\ \exp(-E/T_h)$), in which intensities and temperatures were computed according to scaling laws that account for the laser-plasma conditions [120]. Hot electrons propagated along straight lines and deposited energy considering the

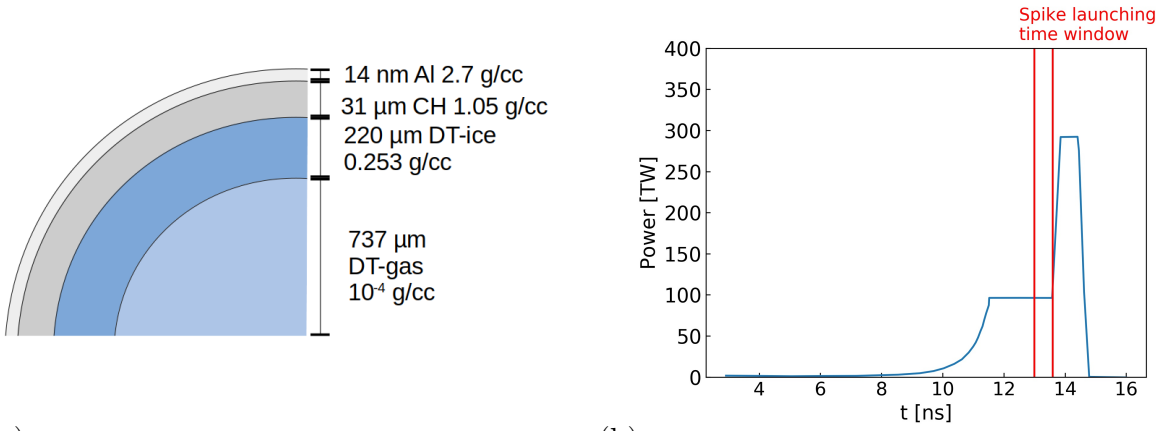

(a) (b)

Figure 2.5: Configuration of the simulated (a) target and (b) laser pulse considered in the numerical investigation reported in Ref. [33]. The laser pulse consists in a low intensity pre-compression beam followed by a high intensity spike. Different simulations are performed launching the spike in a time window that goes from 13 ns up to 13.6 ns, as indicated by the red lines in the figure.

plasma stopping power formulas [121] [122] [123]. The angular scattering on background plasma particles widened the electron beams according to the Lewis' theory [124] [125] [126] (see appendix E). SRS, TPD and RA produced electrons at temperatures of ∼43 keV, ∼98 keV and ∼1.4 keV, with conversion efficiency with respect to laser energy of ∼ 1.2%, 0.94% and 0.12%, respectively. Simulations without the presence of hot electrons were also presented (woHE). In the case woHE, the ignition window occurred for a ignitor launching time that goes from 13.2 ns up to 13.5 ns, with spike peak power that ranges from ∼80 TW up to ∼200 TW. On the other side, the simulations with hot electrons did not predict ignition in these time and power windows. After the pre-compression phase, the areal density of the ablator was sufficient to stop electrons with energies up to 50-70 keV. Higher energy electrons propagated in the compressed DT shell, which at the beginning of the spike plateau was able to stop particles up to 170 keV. The DT bulk was thus preheated and the adiabat raised up to ∼2.3 at the shock convergence. In addition of preheating the fuel, hot electrons ablate the inner shell surface increasing the hotspot mass and enhancing the radiative losses. Because of these detrimental effects, ignition was predicted to be achieved with a 500 TW spike launched at t_s=[13.4,13.6]ns. The ignition window was thus reduced and shifted to higher times compared to the case woHE. In particular, the window was closed for that times for which the preheat was significant. This domain corresponds to the temporal window in which the shell areal density was still too low, and electrons were not stopped in the first layers. On the other side, launching the ignitor shock at time later than 13.6 ns, led to a late shock entry in the hotspot with the respect to shell stagnation.

Refs. [127][128][129] present a recent theoretical study on the effects of hot electrons on a typical SI implosion scheme (Fig. 2.6). The target (29 μm CH ablator - 171 μm ice DT - 840 μm gas DT) was imploded using the third harmonic of the Nd-laser radiation with a total delivered energy of 605 kJ. The pulse duration was 13.9 ns and the high intensity spike was launched at 13.6 ns. Hydrodynamic simulations in which the hot electrons energy deposition is accounted were performed to study the implosion. Electrons were

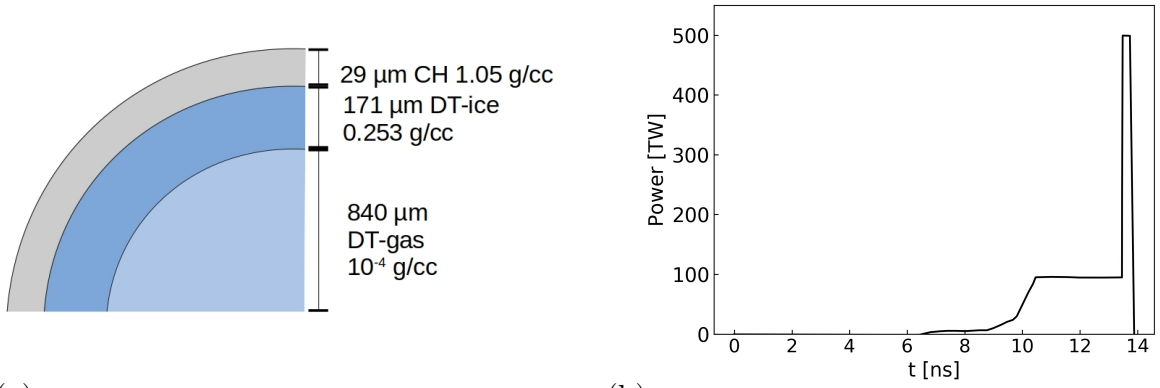

(a) (b)

Figure 2.6: Configuration of the simulated (a) target and (b) laser pulse considered in the numerical investigation reported in [127].

produced isotropically around the quarter-critical plasma density, assuming a Maxwellian spectrum in energy. The simulated set of temperature and conversion efficiencies were respectively 20 keV $\leq T_h \leq$ 100 keV and $0.1 \leq \eta \leq 0.4$. Considering a spike energy of 137 kJ, the total energy contained in the electron beam was 27 kJ $\leq E_h \leq$ 55 kJ. Energy deposition in the target was computed according to the electron-plasma stopping power formulas, which account for the Coulomb collisions with free and bound electrons. The positive effect of the pressure increase was dominant for temperatures up to 50 - 60 keV. However, the energy transferred to DT-fuel increased monotonically with an increase of T_h. As such, the shell preheating leaded to the ignition failure for hot electron temperatures exceeding 90 - 100 keV.

2.2.3 Electron shock ignition

Ref. [130] presents an implosion scheme based on hot electron driven shock. In the case where the electron stopping range is much shorter compared to target thickness, the electron heating causes mass ablation and the shock is driven by rocket effects (see Sec. 2.1). On the other hand, if their range is a finite fraction of the in-flight shell, elevated fluxes of hot electrons can generate a strong shock by direct heating [131]. In this case, the shock launching pressure can be estimated considering the simple ideal plasma model: $P \sim (2/3)E_h/V_h$, where V_h is the heated shell volume and E_h is the electron deposited energy. The target and the laser pulse configuration proposed are similar to the ones used in the SI scheme. A spherical shell (CH, DT-ice, DT-gas) is compressed by low intensity beams ($\sim$10 ns) followed by the ignitor spike ($\sim$200 ps, 100 kJ, 3.4×10^{15}W/cm^2). 1D PIC simulations were performed considering plasma features typical of NIF imploded targets to calculate the hot electron spectrum that is generated in that regime. In particular, simulations predicted the generation of electrons with a Maxwellian distribution with temperature of 50 keV and conversion efficiencies up to $\sim$25% of laser energy. The hot electron driven shock was simulated using a 2D hydrodynamic code in which the electron propagation and energy deposition are modelled. In particular, electrons lose energy because of binary collisions with plasma free electrons and by exciting plasma waves [123]. The Lewis' theory is used to calculate the spatial moments of the electron distribution function [125] [126]. With a hot electron energy of 25 kJ, a peak pressure of 2 GBar

is achieved if the beam is launched at 10.3 ns. The study predicts the target ignition when the hot electron energy exceeds 10 kJ and a gain around ∼130 is achieved with a hot electron energy of 40 kJ. Authors emphasize the importance of a correct implosion design, reaching high values of areal densities to prevent fuel preheating.

2.3 Diagnostics commonly used to characterize hot-electrons in laser-plasma experiment

The investigations presented in Sec. 2.2 emphasize the importance of an accurate experimental characterization of the hot electrons emitted in laser-plasma conditions relevant for shock ignition. To address this point, several experiments in planar or spherical configuration were conducted in the last two decades, exploring different conditions and regimes. Usually, information about hot electrons was inferred exploiting the x-rays emitted by their propagation in targets. In particular, it is possible to consider the bremsstrahlung radiation or the characteristic de-excitation lines of elements that compose the targets. The backscattered laser light can also give information about the processes that generate the electrons. An overview of different diagnostics usually implied in such laser plasma experiments is presented in this section, discussing briefly their working principles.

2.3.1 Imaging Plates

One of the major concerns in experiments in which high intensities lasers are involved is the generation of strong electromagnetic pulses (EMP) that could damage the electronics. As such, it is necessary to rely on passive detection systems, which are not affected by these phenomena. Imaging plates (IP) are a two-dimensional passive detectors for ionizing radiation, characterized by a high sensitivity and reusability [132][133]. There are three types of imaging plates commonly used in laser-plasma experiments, that differ according to composition and properties. Typically, the sensible part of the plate is composed by a phosphor layer ($BaFBr_{0.85}$,$I_{0.15}$ doped with europium) deposited on a support layer (usually made of Mylar). A magnetic layer ($ZnMn_2Fe_5NO_{40}H_{15}C_{10}$) is used in the case where magnetic attachments are required. In some cases, a protective layer of Mylar is applied. The three typologies and their composition are listed in Tab. 2.1: The MS-type are the most sensitive and the most commonly used in laser-plasma experiments, the SR-type present the greatest resolution and the TR-type are the most appropriate for tritium detection. The mechanism of radiation detection is explained in the following. The radiation energy is absorbed by the phosphor and Eu^{2+} is ionized at Eu^{3+}, after the

Typology	MS	SR	TR
Protective layer	9 μm	6 μm	0 μm
Phosphor layer	115 μm	120 μm	50 μm
Support layer	190 μm	188 μm	250 μm
Magnetic layer	160 μm	160 μm	160 μm
C_{PSL} [10^{-4} PSL/keV]	7.50 ±1.13	2.80 ±0.42	3.20±0.48

Table 2.1: Composition and thicknesses of the various layers composing the imaging plates, for the three typologies considered. The value of the C_{PSL} parameter that relates the PSL signal to the energy deposition is reported for the three cases.

emission of a photoelectron. These electrons are trapped in the lattices defects, composing a metastable FBr^- compound. The recombination of these hole-electron centers can be spontaneous, causing the decreasing of the signal stored by the IP in time (*fading*) [134] [135], or photo-stimulated. In this latter case, the information is recovered by radiating the IPs with a red laser in a dedicated scanner and then collecting the 3.2 eV photon that results from the $Eu^{3+} \rightarrow Eu^{2+}$ transition [136]. This emission is called Photo Stimulated Luminescence (PSL), and its intensity is proportional to the radiation dose deposited in the IP. An accurate calibration over a wide range of photon energies (1-200 keV, with data extrapolated up to 1 MeV) is presented in Refs. [137] [138] [139] and [140]. In particular, authors suggest a linear relation between the PSL signal and the deposited energy,

$$\mathrm{PSL} = C_{\mathrm{PSL}} \cdot E_{dep}, \tag{2.3}$$

inferring the parameter C_{PSL} for the three IP types (see Tab. 2.1). Imaging plates can be also used to detect charged particles in laser-plasma experiments [141].

2.3.2 Bremsstrahlung spectrometer

The propagation of fast electrons in matter results in a continuous bremsstrahlung emission. The photon distribution function that results from this emission can give information about intensity and energy of the electron beam that generated it.

A first concept of time-integrated Bremsstrahlung spectrometer composed by a stack of imaging plates alternated by filters of different materials was proposed in Ref. [142]. X-rays propagate into the stack according to their energy: the higher is the photon energy, the more it propagates inside the stack, depositing energy in deeper IPs (see Fig. 2.7). The stack is usually encapsulated in high-Z container, with the aim of reducing the background signal from the fluorescence of vacuum chamber walls. Plasma debris or fast electrons are prevented from entering the stack using a magnetic field or additional plastic filters placed at the entrance. According to the filter material, thicknesses and dispositions, the spectrometer can detect photons with a range that goes from ∼10 keV up to 1 MeV.

As an example, a schematic view of the CELIA bremsstrahlung spectrometer is shown in Fig. 2.8. In particular, the 3D image of the instrument is shown in Fig. 2.8 (a) and the configuration of filters and IP in Fig 2.8 (b). The thickness of each filter is reported in

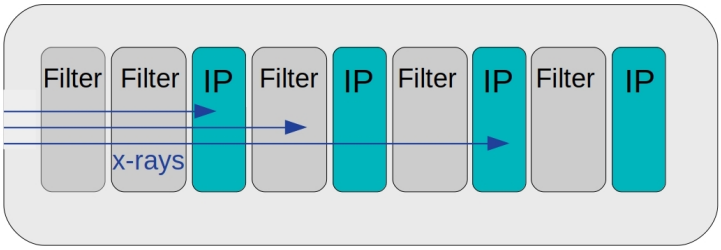

Figure 2.7: Schematic representation of the bremsstrahlung spectrometer. Filters of different materials and IPs are interleaved. The bremsstrahlung radiation enters in the stack from the left and photons propagate according to their energy. The stack is usually encapsulated in high-Z containers to reduce background signal.

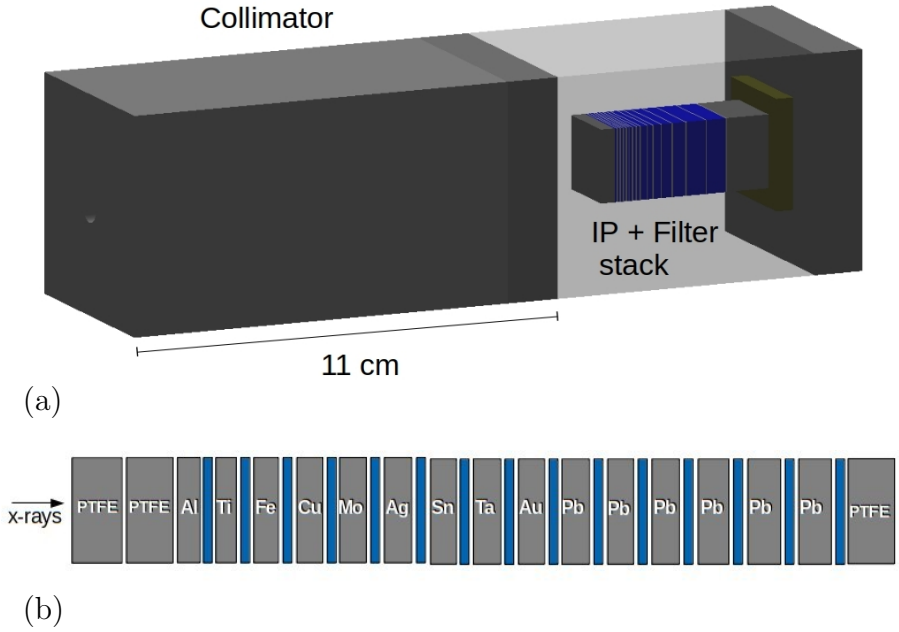

Figure 2.8: (a) Schematic 3D view of the CELIA bremsstrahlung spectrometer. The stack of filters and IPs is contained in a box of lead. An 11 cm lead collimator is placed at the entrance of the stack to protect it from the plasma background. (b) Schematic disposition of filters and IPs that composes the CELIA bremsstrahlung spectrometer. X-rays penetrate the stack from the left.

Tab. 2.2. The stack is encapsulated in a lead container and a further lead collimator of 11 cm is placed at its entrance. This configuration allows to detect and deconvolute x-ray with energies ranging from ∼15 keV up to 1 MeV.

Another recent configuration of time-integrated bremsstrahlung spectrometer was proposed in [143]. Here authors propose a stack composed by 25 IPs and filters optimized to ensure sufficient sampling of the high energy region of the photon distribution function. This is useful in the SI regime, where hot electrons produced through parametric instabilities can be well approximated with multi-temperature Maxwellian distributions [144]. In particular, the characterization of the high energetic component of hot electron distribution (i.e. $T_h \geq 60$ keV) is a crucial step for SI, since it is linked to the shell preheat (see Sec. 2.2).

The post-processing of these diagnostics relies on Monte-Carlo simulations in which the response of each IP to monochromatic photon spectra is calculated. In particular, it is necessary to calculate the deposited energy per photon $D_i(k)$, in the *k-th* IP for the *i-th* monoenergetic beam. For an arbitrary photon distribution function $f_{\mathrm{ph}}(E)$, it is possible

Material	PTFE	Al	Ti	Fe	Cu	Mo	Ag	Sn	Ta	Au	Pb	Pb	Pb	Pb	Pb	Pb
Thickness [mm]	10	0.1	0.1	0.1	0.1	0.1	0.15	0.5	0.5	1.56	1	2	3	4	6.4	6.4

Table 2.2: Thicknesses and material of the filters employed in the CELIA instrument. X-rays are incident on the PTFE layer.

to calculate the energy deposition E_t in the k-th IP using to the formula:

$$E_t(k) = \sum_{i=1} \int_{E_i}^{E_{i+1}} f_{ph}(E) \frac{D_i(k) + D_{i+1}(k)}{2} dE. \quad (2.4)$$

The inference of the bremsstrahlung spectrum is done considering a specific form of photon distribution function dependent on free parameters, that are then calculated using minimization techniques with experimental data. Information on the electron beam are finally inferred using Monte-Carlo codes in which the electron propagation in target and the bremsstrahlung generation on the detector are simulated. Since the post-processing techniques of this diagnostic are still under debate in the scientific community, a detailed methodology of analysis is proposed in Chap. 3.

We also mention that the detection of the bremsstrahlung spectrum during the OMEGA or NIF experiments is routinely accomplished using the time-resolved hard x-rays spectrometer [145] [146] [147]. This detector is composed by four channels in which a fast scintillator (BaF crystal) is coupled with a photomultiplier tube. Filters of different thicknesses and materials (usually aluminium or copper) are used to deconvolute the bremsstrahlung spectrum.

2.3.3 K-alpha spectrometer

The propagation of fast electrons in matter results in the excitation of inner atomic shells with a possible emission of characteristic x-ray lines. Therefore, the targets usually used in experiments are composed of a CH ablator followed by layers of materials for which this emission is enhanced and well known. As an example, titanium tracers, with characteristic K_α x-ray line at 4.5 keV, or copper tracers, with characteristic K_α line at 8.1 keV, are commonly used. The intensity of the K_α radiation produced depends on the number of hot electrons that reached the tracer and on their residual energy. This radiation, particularly peaked around the characteristic line of the material, can be dispersed using a spherical bent crystal on detectors (usually imaging plates or CCD spectrometers). The geometry of the diagnostic is thus based on the well-known Bragg law formula:

$$n\lambda = 2d\sin(\theta), \quad (2.5)$$

where n is the diffraction order, λ is the x-ray wavelength, d is the crystal lattice spacing and θ the diffraction angle. Several configurations of the spectrometer are proposed in

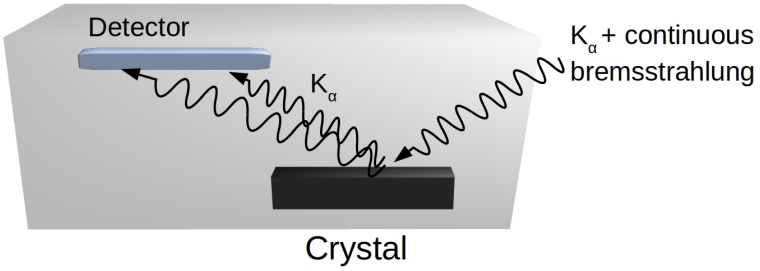

Figure 2.9: Schematic representation of the k-alpha spectrometer. Radiation is dispersed by a crystal according to the Bragg law. K_α photons are thus reflected on the sensible part of the instrument which collects them. A shield of high-Z material is usually used to protect the system from background radiation.

the literature, based on quartz crystals [148], Highly Oriented Pyrolytic Graphite [149] or silicon crystals [150] [151]. The detector is usually placed in a high-Z enclosure to shield it from background radiation. Knowing the reflectivity of the crystal and the solid angle subtended by the diagnostic, it is possible to retrieve the number of photon per steradian produced in that direction by hot electrons. If the spectrometer presents high resolution in energy, it can be also used to estimate the temperature reached by the tracer after electron heating. In the case of material in standard conditions, the characteristic lines of emission are characterized by an exact value in energy (for instance 8047 eV in the case of copper). The passage of hot electrons heats up the material and ionizes atoms, causing a shifting of the emission lines and subsequent broadening of the peaks. This broadening is related to the temperature reached by the tracer [152][150] [151]. The schematic working principle of the diagnostic is shown in Fig. 2.9.

2.3.4 Backscattered light spectrometer

The measurement of backscattered laser light gives important information on laser-plasma coupling and in particular on the development of laser-plasma instabilities [153]. Part of the laser energy is prevented from coupling efficiently to the target because of the presence of SBS, SRS or TPD (see Sec. 1.2.6). Furthermore, SRS and TPD are the mechanisms responsible for the generation of the suprathermal electron population that can preheat fuel and degrade implosion performance in ICF.

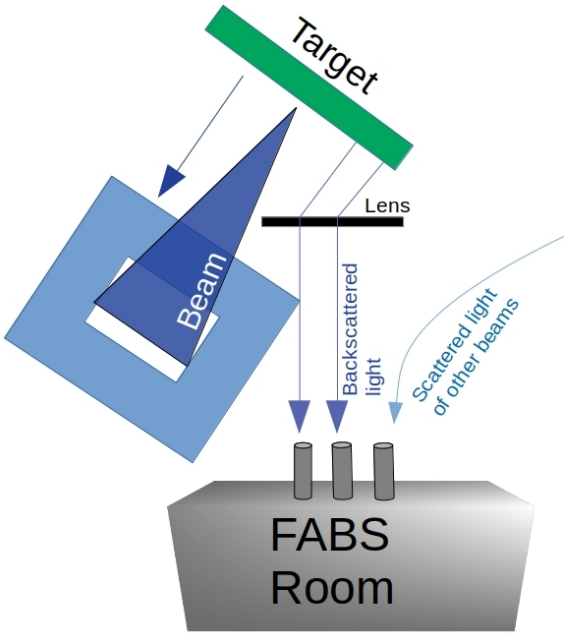

(a)

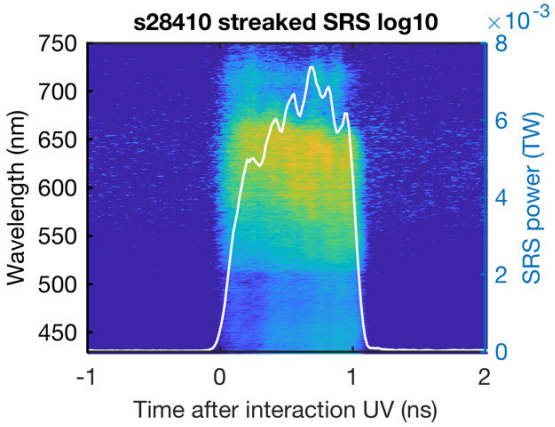

(b)

Figure 2.10: (a) Schematic representation of the FABS system used at the NIF and at OMEGA-60. (b) Backscattered light spectra obtained by shooting a plastic CH target with an UV laser at intensity of 10^{16} W/cm^2. The pulse duration was 1 ns. The curve indicates the backascatterd light power detected in time. The absolute values of power indicated on the y axis are not significant, because the diagnostic covers a small solid angle. The spectrum was taken in an experiment conducted at the OMEGA-EP facility using the SABS.

A full aperture backscattered system (FABS) [154] [155] is used at the National Ignition Facility [156] [157] and at the 60-beam Omega laser system in Rochester [114] [158] to detect the backscattered light. In particular, the instrument resolves SBS over a wavelength range of 348 to 354 nm and SRS or TPD over 400-700 nm. The power time history of the signal is also measured. The basic working principle of the diagnostic is reported in the following. Before reaching the sensitive part, light is directed in a diffuser to reduce the intensity. This is needed because the high intensity of the backscattered light damages the electronics. Fibres equipped with filters then drive the signals (SBS or SRS) to detectors. Diodes are used to measure the power-time history of both SRS and TPD, while a combination of spectrometers and CCD resolves the spectrum. It is important to remark that the instrument detects not only the retro-diffsued light of one beam, but it can also catch the forward scattered light coming from other beams. A schematic picture of the FABS is shown in Fig. 2.10(a), while a typical time-resolved backascatterd spectrum is shown in Fig. 2.10(b). The spectrum is obtained for a 1 ns UV ($\lambda = 351$ nm) pulse at $\sim 10^{16}$ W/cm^2 on CH target. Two distinct features are seen in this spectra: a convective SRS signal between ∼530 and 680 nm and the $\omega/2$ (700 nm) radiation associated to the TPD instability. The white curve represents the light scattered power detected in time. The spectrum was obtained using the sub-aperture backscatterd spectrometer (SABS) in an experiment conducted at OMEGA-EP. The working principle of the SABS is the same as the one of the FABS, but it covers a smaller solid angle. Because of this, the absolute values in power reported in the figure are not significant.

2.4 Experimental campaigns

Experiments investigating the generation of hot electrons in SI relevant conditions have been performed in the last decade, exploring several laser plasma regimes depending on the capabilities of the various installations. In these experiments, beside the characterization of the hot electron source, also shock dynamics studies were usually conducted. Experiments can be conducted in planar or spherical geometry. Planar target geometry allows for a simpler experimental setup, in which less laser beams are required. Furthermore, large number of diagnostics is compatible with the planar geometry, being particularly useful for accurate comparison with numerical simulations. Spherical experiments allow to reproduce the convergence effect and are more adequate to study SI. However, a greater number of irradiation beams and thus experimental complexity is required. A summary of different experiments aimed at characterizing hot electrons is listed below, reporting the laser-plasma conditions achieved and the obtained results. It is important to remark that, in SI regime, the coronal plasma scale length and the electronic temperature are $L_n \sim 600$ μm and $T_e \sim 5$ keV, respectively. Such configuration can only be achieved at the NIF [157] [156] or the LMJ facilities [159] [160].

2.4.1 Planar experiments at PALS

In the last decade, a series of experiments aimed at characterizing hot electrons were conducted at the PALS (Prague Asterix Laser System) [161] [162] [163] [164] [165] [166]. The laser PALS can deliver energies of the order of 0.5 kJ in a pulse duration of about 300 ps, with an irradiation wavelength of 1314 nm (1ω) or 438 nm (3ω) [111]. An auxiliary beam can provide an extended plasma corona before the arriving of the main pulse.

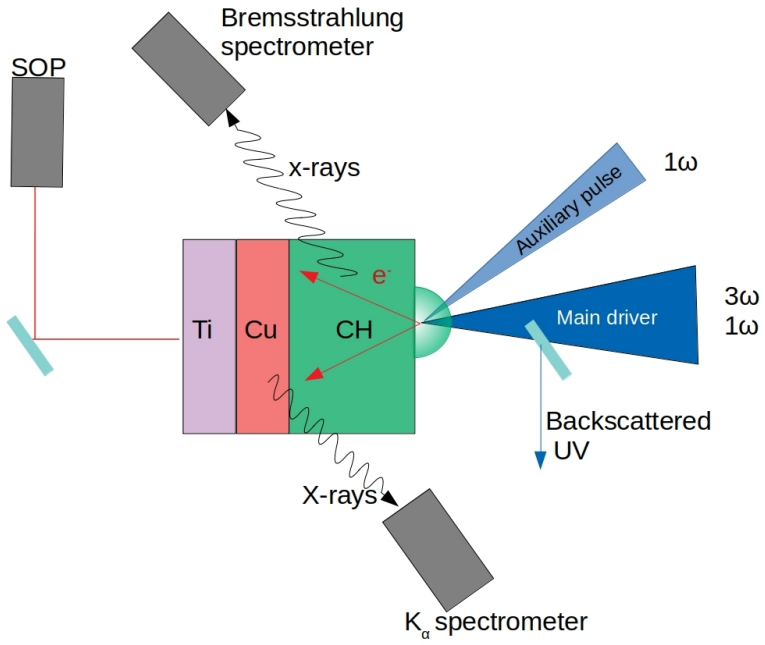

Figure 2.11: Main scheme of SI experiments performed at PALS. A multilayer planar target is irradiated by a pre-compression beam followed by the main driver that launches a strong shock and generates copious amount of hot electrons. Several diagnostics are used to characterize the electron beam and the laser backscattered light.

The density-scale length and the plasma coronal temperature reached in these conditions are lower than those envisaged in a full SI experiment, but the laser intensity delivered on targets can reach values of 10^{15} - 10^{16} W/cm^2. The scheme was similar for all the experiments reported: a laser beam with intensities around 10^{15} - 10^{16} W/cm^2 was incident on planar targets. These were composed by plastic ablators ($\sim$tens μm thick), on which the laser was focused, followed by mid-Z tracers (usually copper or titanium). An auxiliary pulse (I$\sim 7\times10^{13}$-10^{14} W/cm^2) was used to create a pre-plasma with coronal quarter-critical density scale length around $\sim$100 - 150 μm. The main pulse, usually of duration around 250-300 ps, was delayed up to 1.2 ns to study different pre-plasma conditions. Distributed phase plates (DDP) were used in the experiments, except for shots for which higher intensities were required (i.e. $\geq 10^{16}$W/cm^2). The laser spot was usually $\sim$100 μm.

The bremsstrahlung or the characteristic K$_\alpha$ radiation emitted by the propagation of electrons through the layers is used to characterize the hot electron source. This is done considering that electrons are energetically described by 2D Maxwellian functions of the type $f_e(E) = \frac{N_e}{T_h} e^{-\frac{E}{T_h}}$, inferring the value of the temperature T$_h$ and the laser to hot electrons energy conversion efficiency η. Backscatter spectrometers were used to measure the backscattered light coming from different phenomena (SBS, SRS, TPD).

In addition to hot electron characterization, in most of the cases the shock dynamics was usually studied. This was achieved using dedicated systems like VISAR (Velocity Interferometer System for Any Reflector) and SOP (Streaked Optical Pyrometry) diagnostics [167] [166] [168] [169]. A schematic summarizing of the standard diagnostic configuration in these experiments is given in Fig. 2.11.

PALS Planar Experiments							
Ref.	Year	Target	λ [nm]	E_{tot} [J]	$I/10^{15}$ [W/cm^2]	T_h [keV]	η [%]
[161]	2010	CHCuAl	438 (3ω)	20-250	1 10	30-50	≤ 0.1
[162]	2013	(C_8H_7Cl)CuAl	438 (3ω)	200	9	20-50 $\pm$10	0.1 $\pm$0.02
[163]	2016	Cu	1315 (1ω)	440	20	29^{+8}_{-4}	0.11-0.23
[163]	2016	Cu	438 (3ω)	170	9	37^{+34}_{-11}	0.4-0.8
[164]	2017	(C_8H_7Cl)TiCu	438 (3ω)	300	6	25 $\pm$8	0.1$\pm$0.05
[165]	2018	CHTiCu	438 (3ω)	200	3	20 $\pm$6	$0.28^{+0.28}_{-0.064}$
[165]	2018	CHTiCu	1315 (1ω)	650	10	30 $\pm$9	$5.32^{+6.90}_{-0.26}$
[166]*	2019	CHTi	1315 (1ω)	700	10	40 $\pm$5 85 $\pm$5	3.5 $\pm$ 0.5 1.8 $\pm$0.5

Table 2.3: Summary of SI relevant experiments performed at PALS. The target configuration and the key laser parameters used in each experiment are reported. In particular, we indicate the laser wavelength λ, the total laser energy delivered on target E_{tot} and the vacuum laser intensity I. The hot electrons temperatures T_h and the laser to hot electron energy conversion efficiencies η measured are reported in the last two columns. The experiments in which the laser wavelength used was 1315 nm (1ω) are highlighted in grey. $*$ Authors assert that only the 50% of laser energy was contained in the focal spot, i.e. 350 J delivered on targets. Furthermore, no auxiliary beam was used to create pre-plasma conditions [166].

Here we focus on the results pertaining to the characterization of the hot electrons. Tab. 2.3 summarizes the key experimental parameters used in experiments performed in the last decades, showing also the obtained results. In particular, the hot electron temperature T_h (assuming a Maxwellian distribution) and the laser to hot electrons energy conversion efficiencies η are reported for each experiment. Overall, we can observe low values of T_h, around $\sim$30 keV, and conversion efficiencies always lower than 1%, except for the shots at 1ω presented in [165] and [166]. On the other hand, in [163] higher values of conversion efficiencies are found for the 3ω case compared to the 1ω case. Authors suggest to introduce other mechanisms of HE generations, but further theoretical and numerical investigations are required to better understand this behaviour.

The hot electron temperatures and conversion efficiencies were measured considering the bremsstrahlung or the K_α measurements. However, the configuration of the diagnostics did not allow to detect the presence of a double temperature hot electron population. Only in [166] authors considered a two-temperatures distribution function to interpret the experimental data.

2.4.2 Planar and spherical experiments at OMEGA

In the last decades, SI experiments aimed at studying hot electrons were performed at the Omega laser system at the University of Rochesters Laboratory of Laser Energetics [158] [114]. The OMEGA60 laser consists in 60 ultraviolet (λ=351 nm UV) beams of light symmetrically distributed about a target chamber in a truncated icosahedron pattern. Each beam can deliver 500 J on target, for a total energy of 30 kJ. Omega EP (extended

OMEGA Planar Experiments									
Ref.	Year	Target	Beams	τ [ns]	E_{tot} [kJ]	$I/10^{15}$ [W/cm^2]	L_n [μm] T_e [keV]	T_h [keV]	η [%]
[170]	2000	CHTiV	$10^{o.}$	1	4.85	1.5	? ?	$\geq$50	?
[171][172] [173]	2012	CHMoCH	$4^{o.}$	2-2.5	9	0.1-0.7	400 2.6	20-90	1
[174]	2014	$CHMoSiO_2$	$1^{p.p.}$ $2^{m.d.\ o.}$	1.6 $\sim$0.8	5-7.2	0.6 1.4	350 2-2.9	70	1.8
[175]	2016	CHMoCH CHAgCH	$4^{o.}$	2-2.5	9	0.1-0.7	270-400 1.5-2.4	20-60	1-3
[176]	2020	CHCuAl	1-$2^{p.p.}$ $1^{m.d.}$	2-4 1	1.8-6.4 1.4	0.2 10	330 1.8	27$\pm$9	0.8$\pm$0.7
[176]	2020	CHCuAl	1-$2^{p.p.}$ $1^{m.d.}$(IR)	2-4 0.1	1.8-6.4 2.5	0.2 5	380 1.1	87$\pm$10	2.4$\pm$0.4

Table 2.4: Summary of SI relevant planar targets experiments performed at OMEGA. Target configuration and key laser parameters used in each experiment are reported. The number of beam focused on target is followed by the superscript "p.p." for the pre-plasma creation beams or by "m.d." if the beams were used as main drivers. The superscript "o." indicates that beams overlapped on target. The pulse duration τ, the total energy delivered by the beams E_{tot} and their intensities I are reported both for the pre-compression beams and the main drivers, if available. The coronal quarter-critical plasma density scale-length L_n and electronic temperature T_e are shown for experiments in which they were measured or calculated. The hot electron temperatures T_h and the laser to hot electron energy conversion efficiencies η measured are reported in the last two columns. The experiment in which the laser wavelength used was 1054 nm (1ω) is highlighted in grey. In all the other cases, the laser wavelength was 351 nm (UV).

performance) is a high-energy petawatt addition. The system consists of four beamlines with long-pulse capability ranging from 0.1 to 10 ns, delivering typical intensities on target of 10^{15} - 10^{16} W/cm^2 with wavelength of 351 nm. The energies provided by the beams are limited by the UV optical coating damage threshold and it is possible to reach 2.5 kJ per beam for 1 ns pulses, or 6.5 kJ per beam in the case of 10 ns pulses.

In the experiments reported, laser beams were focused on multilayer targets generating a strong shock and a copious amount of hot electrons. The setup varies from PALS configuration in the number of beams and energy per beam. Hot electrons are characterized in terms of temperature T_h and conversion efficiency η using various x-rays spectrometers. Tab. 2.4 summarizes the key experimental parameters and the results obtained in the experiments performed in the last decades. The irradiation wavelength was of 351 nm, unless otherwise specified.

Experiments in spherical geometry aimed toward the SI framework were also conducted at OMEGA60. In order to overcome the intensity limitation of the standard 60-beams implosions, the 40 + 20 beams laser configuration can be adopted. 40 beams are used to implode the capsule at low intensity, followed by 20 beams tightly focused to reach intensities up to $\sim 8\times10^{15}$W/cm^2. This allows to study the implosion performance considering different figure of merits, such as the neutron yield and the areal density (see Sec. 2.2). Additional studies on LPI and in particular on hot electron generation were

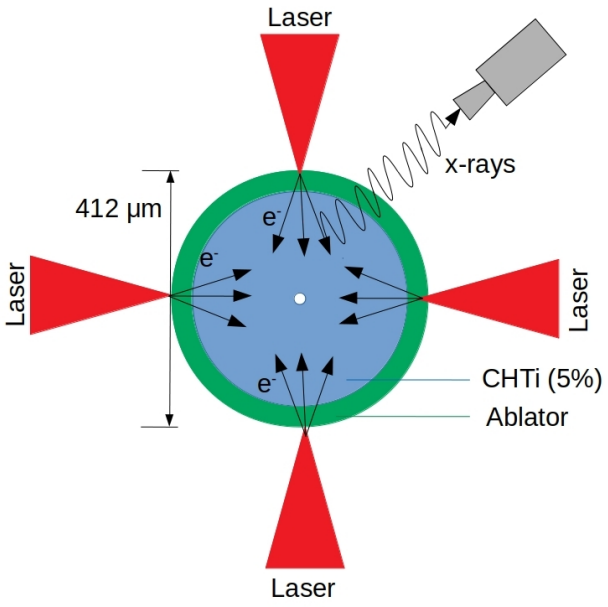

Figure 2.12: Main scheme of spherical SI experiments performed at OMEGA. A spherical target is symmetrically irradiated by 60 beams. Targets are usually composed by concentric shells of plastic ablators followed by mid-Z tracers or D_2, according to the aim of the experiment. The characterization of hot electrons exploits the x-ray radiation emitted by their propagation. The example reported in figure corresponds to the target used in [177].

performed in last years. Similarly to planar target experiments, hot electrons are characterized exploiting the x-ray radiation emitted by their passage in targets. The imploded capsules are usually composed by concentric shells of different materials, sometimes filled by deuterium and tritium to study neutron yield. Tab 2.5 presents the results of relevant spherical configuration experiments, conducted at OMEGA in the last decade. Overall, higher electron energies (T_h >50 keV) were observed in cases of overlapping beams, as also underlined in [183] [174]. Low hot electron temperatures (T_h ∼30 keV) were observed in cases in which beams were tightly focused, or in the case in which only one beam was used as main driver. This is consistent with the experiments performed at PALS (Sec. 2.4.1), in which only one beam was used to generate hot electrons. The application of beam smoothing techniques reduces the conversion efficiencies. This is consistent with the behaviour of the SRS emission detected by the FABS. The SRS-backscattered signal is lower (up to ∼5 times) in shots where the SSD is applied [179] [177] [184], while SBS and TPD seems to not be influenced [179].

The conversion efficiency shows a dependence on the ablator material [177]. This is in part related to the fact that mid-Z material shortens the density scale length and increases the coronal electronic temperature, suppressing the TPD but also the SRS [185] [36] (however note that different materials produce different damping of the plasma waves, i.e. different hot electron generation). As such, mid-Z materials were recently proposed as possible ablators for SI targets, with the aim of reducing hot-electron preheat [186].

Another important parameter that affects the shell preheat is the hot electron beam divergence. Ref. [187] reports an experimental investigation, conducted at the OMEGA

OMEGA Spherical Experiments									
Ref.	Year	Target	Beams	τ [ns]	E_{tot} [kJ]	$I/10^{15}$ [W/cm^2]	L_n [μm] T_e [keV]	T_h [keV]	η [%]
[178]	2012	$(CD)D_2$	$40^{p.p.}$ 20	2.7 0.6	14 5	? 0.5-8	170 1.8	30-40	?
[179] [180] [181]	2015	$CHCH(Ti_{0.05})$	$60^{p.p.}$ $60^{o.}$	1 1	? 22-26	$\leq$0.1 6	120 3.5	60-80	7.6, 3.3^{SSD}
[177]	2017	$CHCH(Ti_{0.05})$ $BeCH(Ti_{0.05})$ $CCH(Ti_{0.05})$ $SiO_2CH(Ti_{0.05})$	$60^{p.p.}$ $60^{o.}$	1 1	? 22-26	? 5	125 3.6	60-80	8, 3^{SSD} 2, 1^{SSD} 3, 2^{SSD} 4, 2^{SSD}
[32]	2018	$(CD)D_2$	$40^{p.p.}$ 20	2.7 0.6	15.3 5.7	? 1.5	? ?	38$\pm$3.4	1.6$\pm$0.3

Table 2.5: Summary of SI relevant spherical target experiments performed at OMEGA. The target configuration and the key laser parameters used in each experiment are reported. The acronym (CD) indicates deuterated plastic. The number of beam focused on target is followed by the superscript "p.p." for the pre-plasma creation beams. The superscript "o." indicates that beams overlapped on the target. The pulse duration τ, the total energy delivered by the beams E_{tot} and their intensities are reported either for the pre-compression beams and the main drivers, if available. The coronal quarter-critical density scale-length L_n and electronic temperature T_e are shown for experiments in which they were measured or calculated. The hot electron temperatures T_h and the laser to hot electron energy conversion efficiencies η measured are reported in the last two columns. The superscript "SSD" indicates that the values of conversion efficiency was measured when spectral dispersion smoothing on beams was applied [182].

facility, aiming at studying this feature. Mo-coated shells of increasing diameter were suspended within an outer CH ablator shell. These were irradiated by the 60 OMEGA beams smoothed by distributed phase plates, with laser energy around 22 kJ. The production of hot electrons occurred in the ablator, and the Mo layers served as tracers. The electron beam divergence was evaluated by the relative change in the K_α signal for the various Mo-shell diameters. The increase of the signal with the Mo-shell diameter indicates a wide angular divergence of the electron beam.

2.4.3 Experiments at NIF

Laser-plasma interaction experiments started recently at the National Ignition Facility [156] [157], allowing access for the first time to regimes of plasma density scale lengths and coronal electron temperatures relevant to direct-drive ICF (i.e. L_n ~500-700 μm and T_e ~3-5 keV). The results of a first planar configuration experiment are reported in Ref. [188] and [189]. Planar disks composed by CH or SI were irradiated with 32 (inners) or 32+64 (inners + outers) NIF beams, with intensities ranging from $\sim 6\times10^{14}$W/cm^2 up to 1.5×10^{15}W/cm^2. The pulse duration was 8 ns and the irradiation wavelength 351 nm. All the beams were equipped by SSD. According to hydrodynamic simulations, the quarter critical density scale length and coronal temperature rose up to 500-700 μm and 3-5 keV in the first 2 ns of irradiation, reaching then quasi-stationary conditions.

For the plastic target, the measured hot electron temperature was around 50 keV with conversion efficiency ranging from 1$\pm$0.4% to 5.1$\pm$0.9% as the laser intensity increased

from $\sim 6 \times 10^{14}$ W/cm^2 up to 1.5×10^{15} W/cm^2. Shots on Si targets showed the same values of T_h (i.e. $\sim$50 keV) but lower conversion efficiencies, ranging from 1 up to $\sim$3%. This agrees with the results presented in the previous section on mid-Z ablators. Considering the optical emission, authors suggest that SRS is the dominant mechanism, and its intensity is consistent with the fraction of hot electrons measured.

2.5 Conclusion

This chapter shows an ensemble of recent theoretical and experimental works aimed at studying the problematic of hot electrons in the context of the ICF. In particular, in the first part of the chapter, we presented some studies on the hot electron effect on the ablation pressure and on the shell preheat. These investigations, however, were conducted on the basis of 1D or 2D hydrodynamic codes, or by exploiting simplified analytical models to study the hot electron propagation. It is clear that, having a disposal a 3D hydrodynamic code in which a module of hot electron propagation is included will allow to better interpret the experiments and to realize more robust theoretical investigations. As such, as reported in Sec. 0.4, one of the goal of the thesis work is to build a 3D hot electron transport model, with the aim of future implementation in hydrodynamic codes. Clearly, this model should consider the scattering phenomena and the energy losses which an electron undergoes propagating in a plasma and in particular in ionized or partially ionized laser irradiated target.

For what concerns the hot electron characterization, further efforts are required to understand the behaviour of the diagnostics and the reliability of the numerical methods used to interpret the experimental data. As an example, the articles listed in Sec. 2.4 present their results in terms of hot electron temperatures and conversion efficiencies, but a detailed discussion on the post-processing techniques of the diagnostics is usually omitted. As such, one of the goal of the thesis work is to perform a detailed study on the behaviour of the x-rays spectrometers, notably the bremsstrahlung and the K_α spectrometers, proposing a methodology of data post-processing. One approximation introduced in this analysis is the fact that these post-processing techniques are based on "cold" Monte-Carlo methods, i.e. models in which the hydrodynamic evolution of the targets and their plasma state are not accounted. In Chap. 5, we present a numerical study using our 3D hot electron transport code to understand the margin of error introduced in analysing the laser plasma experiments using cold codes. However, we remark that the prospect of using a hydrodynamic code coupled with a module of hot electron propagation in which the bremsstrahlung and the K_α generation is simulated will offer the possibility of a more robust experimental analysis.

Moreover, further experimental investigations are required to confirm the obtained results and in particular the values of T_h and η. Notably, it is important to understand the link between these quantities and the development of the laser-plasma processes responsible for the hot electron generation, in order to explain the differences between the experiments. For example, in the 1ω experiments conducted at PALS, hot electron temperatures around 30 keV were found (using the single temperature distribution function), while in the OMEGA experiment the value of T_h was 87 keV. In addition, if one considers the experiments in which only one beam at 3ω was tightly focused on targets, the temperatures ranged from 20 up to 50 keV, but with conversion efficiencies less than the 1%

in the PALS experiments and around a few percent in the OMEGA experiments. Finally, when multiple beams overlapped on targets, the uncertainty on the values of T_h was even bigger, with temperatures going from 20 up to 90 keV (considering OMEGA planar and spherical targets experiments). As such, in order to reduce the uncertainties on the parameters, to confirm the experimental results found and to explain the differences obtained considering different regimes, further experimental and theoretical investigations are required . This should be done especially in real SI conditions, were only few data have been collected up to the present day. On this basis, we present in the next chapter the results of three experiments aimed at characterizing the hot electrons, conducted at the OMEGA-EP, PALS and LMJ laser facilities. In particular, as done in the experiments presented in this chapter, the characterization of the hot electrons will rely on bremsstrahlung measurements. We will thus apply the same analysis methodology and diagnostic technique to obtain information on the hot electron characteristics in three different laser-plasma conditions. Let us mention that only in the experiment conducted at the LMJ facility, real SI conditions are achieved.

Chapter 3

Experimental characterization of hot electrons in SI relevant regimes

We report on the results of different experimental campaigns conducted in the last years, where we characterized hot electrons in SI regime. These experiments were held in different facilities, exploring different laser-plasma conditions according to their capabilities. We present in particular the results coming from three experiments in planar target configuration, conducted at the OMEGA-EP [158], PALS [111] and LMJ [159] laser facilities. The scheme and the aim of these experiments were similar: characterize hot electrons and the shock dynamics. Several diagnostics were involved to reach the goal and to measure accurately the physical quantities of interest. Here we focus our attention in particular on the post-processing techniques of different x-ray spectrometers: the K_α and the bremsstrahlung spectrometers. As shown in Chapt. 2, these spectrometers detect the radiation emitted by the hot electron propagation in the target and they are used to characterize the hot electron flux in terms of energy and intensity. Despite these diagnostics have been widely used in laser plasma experiments in the last decade, the comprehension of their behaviour is not completely understood and still debated by the scientific community. As such, in the next section, we propose a post-processing methodology to analyse the data coming from these diagnostics.

The chapter is structured as follows. In Sec. (3.1) we present the analysis of the data coming from an OMEGA-EP experimental campaign. We first report on the detailed description of the experimental set-up and the post-processing techniques of different diagnostics, describing the analytical and the numerical methods applied. We next present the results of the experiment, in particular the characterization of the hot electrons in terms of energy and intensity and their influence on the shock dynamics. In Sec. 3.2 and 3.3, the preliminary results of two experimental campaigns, at PALS and at LMJ, respectively, are presented. Similarly to the OMEGA-EP experiment, these experiments aimed at characterizing hot electrons and at studying their influence on the shock dynamics. Since these two experiments are currently being analysed (at the moment of writing), we report only the results coming from the post processing of the bremsstrahlung spectrometers.

The results are then compared with other experiments in which the irradiation conditions were similar.

3.1 Experimental characterization of hot electron emission and shock dynamics at laser intensity relevant for SI

We report on the results of an experimental campaign conducted at the OMEGA-EP laser facility, aimed at characterizing the hot electrons and the shock dynamics using several x-rays spectrometers and by performing a shock radiography [190].

The experimental setup is described in the first section 3.1.1, while in section 3.1.2 we report a detailed description of the post processing techniques of the x-ray spectrometers data. The spectrometer analysis gives a first information on the hot electron temperature T_h (i.e. their mean kinetic energy) and on the conversion efficiency of laser energy into hot electron energy (η). However, a large uncertainty on these two parameters was found (i.e. T_h[keV] $\in$ [20,50] and $\eta \in$ [2%,13%]). As such, these values were used as input in hydrodynamic simulations with the aim of reproducing the experimental radiographs and trying to constrain the problem. In particular, in Sec. 3.1.3, we describe in detail the setting of the hydrodynamic simulations and the comparison with the experimental shock radiographs. Finally, in section 3.1.4, the influence of the hot electrons on the shock dynamics is discussed, considering different hydrodynamic quantities.

3.1.1 Experimental setup

The experiment was performed in the target chamber of the 4-beam OMEGA-EP laser facility[158] at the Laboratory for Laser Energetics of the Rochester University. One or two high intensity UV interaction beams (B1, B4) ($\lambda = 351$ nm, 1.0 ns square pulse, beam energy of $\sim$1.25 kJ, $f/6.5$) irradiated a multi-layer targets to produce a strong shock wave and copious amount of hot electrons. The UV interaction beams were tightly focused on the target surface without phase plates to a focal spot size of $\sim$130 μm, providing a nominal vacuum laser intensity of $\sim 1 \times 10^{16}$ W/cm^2 for one beam and $\sim 2 \times 10^{16}$ W/cm^2 for two beams. Planar targets consisted of two layers (175 or 250 μm CH/ 20 or 10 μm Cu) fabricated to 500 μm diameter disks. These were mounted on a 50 μm thick CH slab aiming at inhibiting hot electron recirculation. The UV interaction lasers impinged on front of the 175 (or 250) μm thick CH layer at an angle of incidence of 23° with respect to the target normal. The Cu middle layer served as a tracer for hot electrons emitting Cu K_α x-rays of 8.05 keV. Multiple x-ray diagnostics characterized the emission generated by the hot electron population in order to obtain information on their energy spectrum.

The total yield of Cu K_α was measured by an absolutely calibrated Zinc von Hamos x-ray spectrometer (ZnVH)[149]. This spectrometer uses a curved HOPG crystal in von Hamos geometry to diagnose the x-ray spectrum in the range of $7-10$ keV. A high-spectral resolution x-ray spectrometer (HRS) used a spherically bent Si [220] crystal coupled to a charge-coupled device to measure the time-integrated x-ray emission in the 7.97- to 8.11 keV range [150]. The hot electron produced bremsstrahlung radiation was diagnosed by two time-integrating hard x-ray spectrometers (BMXSs) [142] at 25° and 65° off the target rear normal, respectively. The instruments are composed of a stack of fifteen imaging plates (IP) of MS type [132], alternated by filters of different metals. The x-rays propagate into the stack creating a signal in the IPs according to their energy: higher energy photons propagate deeper in the stack. A schematic view of the filters disposition is shown in Fig.

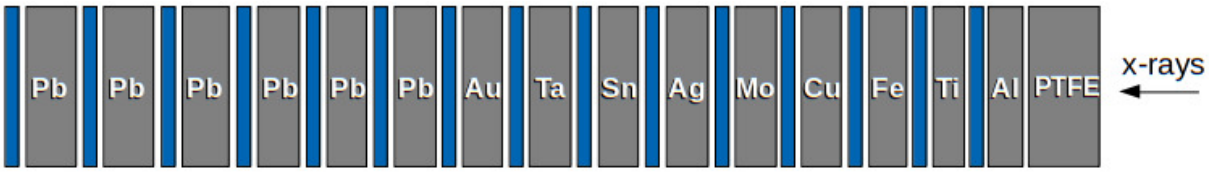

Figure 3.1: Schematic disposition of the filters (in grey) and imaging plates (in blue) of the BMXS instrument. X-rays are penetrating the stack from the right.

3.1, while their thicknesses is reported in Tab 3.1. The whole stack is encapsulated in a cylindrical lead container in order to reduce the background signal and a further 10 mm filter of Polytetrafluoroethylene $(C_2F_4)_n$ (PTFE, teflon) is placed in front of the stack shielding it from plasma debris. In addition, this filter blocks low-energy photons coming from the coronal plasma and the copper K_α signal, while allowing higher energy photons produced by the propagation of hot electrons in the target. A streaked Sub-Aperture Backscattering Spectrometer (SABS) diagnosed the temporally resolved spectrum of the SRS backscattered light (430 nm to 750 nm). However, the total SRS reflected power could not be directly measured due to the small collecting area.

An UV beam (B3) with a 3 ns square pulse irradiated a V foil target to produce backlighter with a high flux of x-ray radiation at 5.2 keV, vanadium He_α line, used as source to perform time resolved radiographs (see Fig. 3.2). A total energy of ∼2.7 kJ impinged on the V foil. The average intensity ranged from 3×10^{14} W/cm^2 to 5×10^{14} W/cm^2. A 50 μm thick CH heat shield placed between the backlighter and the target absorbed the soft x-ray radiation from the V foil in order to prevent any premature x-ray preheat of the multi-layer target. A four strip x-ray framing camera (XRFC) [191] equipped with an 4×4 array of 20-μm-diam. pinholes captured sixteen 2-D images of the shock front with 6× magnification at various times. The time and the spatial resolutions of the camera were ∼100 ps and ∼15 μm respectively. Finally, 1-D time-resolved radiography was obtained by replacing the XRFC with a slit imager and an x-ray streaked camera. The PJX streak camera [192] was operated in inverse mode with an 6 mm x 90 μm input slit and 10 μm x 1000 μm imaging slit providing a total magnification of 20x. The spatial resolution was about 10 μm and 40 ps of temporal resolution. Tab. 3.2 presents a list of the performed shots considered here, indicating the availability of experimental data from the diagnostics.

3.1.2 Post processing of the x-ray spectrometer data

We report, in this section, a detailed description of the post-processing techniques of the data coming from the BMXS (the bremsstrahlung spectrometers) and the ZNVH and HRS (the k-alpha spectrometers). The bremsstrahlung spectrum detected by the

Material	PTFE	Al	Ti	Fe	Cu	Mo	Ag	Sn	Ta	Au	Pb	Pb
Thickness [mm]	10	0.1	0.1	0.1	0.1	0.1	0.15	0.5	0.5	1.56	1	2
Material	Pb	Pb	Pb	Pb								
Thickness [mm]	3	4	6.4	6.4								

Table 3.1: Thicknesses of the filters employed in the BMSX instrument. X-rays are incident on the PTFE layer.

Shot Number	Interaction beam on target	BMXS	ZNVH	Radiography	HRS
#28406	B4	Available	Available	2-D Not Available	Available
#28407	B1	Available	Available	2-D Available	Available
#28410	B1+B4	Available	Not Available	2-D Available but not exploitable	Available
#28412	B1	Available	Available	1-D Available	Available
#28415	B1+B4	Available	Available	1-D Available but not exploitable	Available

Table 3.2: Summary of performed shots. Shot number and the correspondent interaction laser beam focused on target are shown. The availability of experimental data coming from x-ray spectrometers and from radiography is indicated. In the radiographies #28410 and #28415 the poor contrast of the images makes the radiographies not exploitable.

BMXS is first retrieved by simulating the diagnostic response using Geant4 MC code and then by applying the chi-square method with the experimental data. After that, the bremsstrahlung spectrum and the k-alpha signals detected by the spectrometers are reproduced by performing simulations of electron transport in target. In this way, it is possible to retrieve the intensity and the mean kinetic energy of the hot electrons emitted in the shot.

Time-integrating hard x-ray spectrometer BMXS

The BMXSs are made by a stack of 15 image plate detectors with metal filters interleaved in-between (see Sec. 3.1.1). After recording the signal, the imaging plates are read in a dedicated scanner which induces Photo Stimulated Luminescence (PSL). Fig. 3.3 shows the signal recorded in shot #28407. In general, all the shots had signal up to the seventh or eighth IP. The background noise is around 1% of the signal of the seventh IP and it does not influence the measurement. The PSL value is related to the absorbed dose by a calibration curve [137].

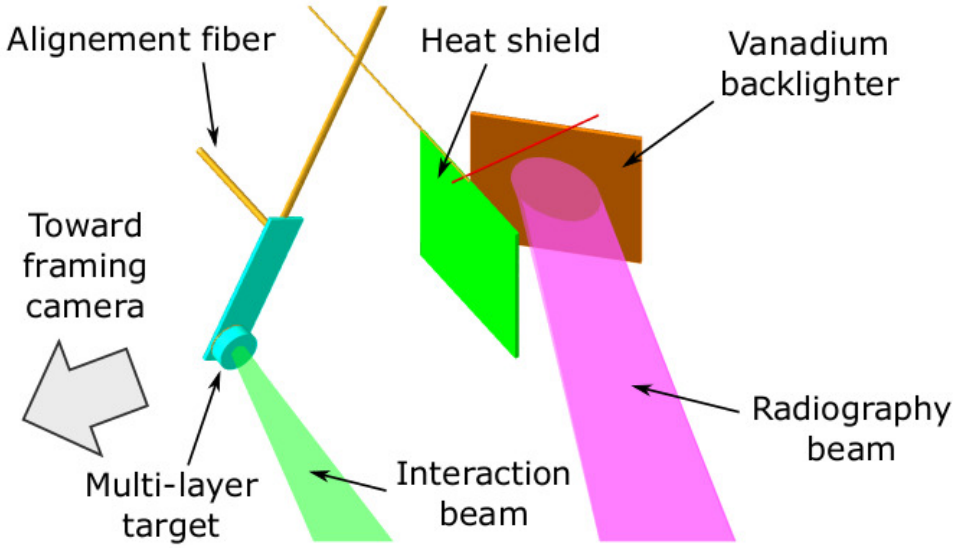

Figure 3.2: Experimental setup for x-ray radiography. A UV beam irradiated a V foil and one or two high intensity UV beams interacted with the multi-layer target. An x-ray framing camera equipped with a pinhole array captured images of the shock front at various times.

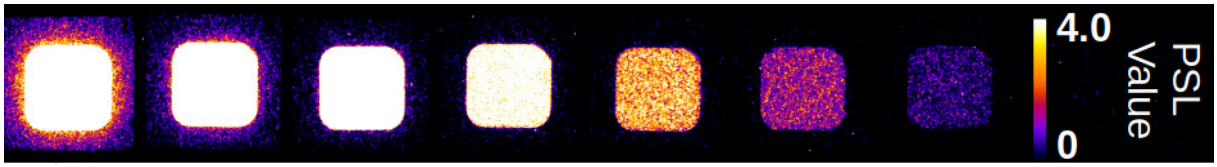

Figure 3.3: Example signals obtained in the IP stack for shot #28407.

To extract the x-ray spectrum which led to a given energy deposition, one must first characterize the response of each IP inside the BMXS to a monochromatic x-ray beam. This is calculated by performing MC simulations in which the 3D detector geometry is reproduced. The simulations were performed with the Geant4 MC code [193] using the Penelope physics library [194]. Here we used 46 logarithmically spaced photon spectral bins from 5 keV to 1 MeV in order to calculate the deposited energy per photon $D_i(k)$, in the *k-th* IP for the *i-th* energy bin. Results are shown in Fig. 3.4. For a generic photon distribution function $f_{\mathrm{ph}}(E)$ it is possible to calculate the energy deposition E_{t} in the k-th IP using to the formula:

$$E_{\mathrm{t}}(k) = \sum_{i=1}^{45} \int_{E_i}^{E_{i+1}} f_{\mathrm{ph}}(E) \frac{D_i(k) + D_{i+1}(k)}{2} \mathrm{d}E. \tag{3.1}$$

Considering the decaying behaviour of the signal through the IPs, we chose an exponential photon distribution function of the type $f_{\mathrm{ph}}(\mathrm{A_{ph}}, \mathrm{T_{ph}}, E) = \frac{\mathrm{A_{ph}}}{E} e^{-E/\mathrm{T_{ph}}}$ with free parameters $\mathrm{A_{ph}}$ and $\mathrm{T_{ph}}$. The choice of this type of $f_{\mathrm{ph}}(E)$ is related to the fact that, as remarked later, this is the shape of photon distribution function produced on the detector by a 2-D electron Maxwellian distribution function that propagates inside the target. The values of the free parameters $\mathrm{A_{ph}}$ and $\mathrm{T_{ph}}$ are found fitting the experimental data by performing

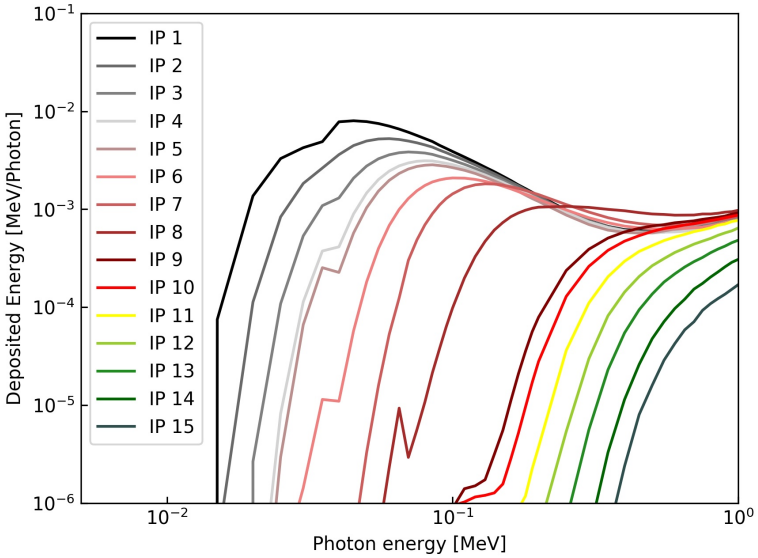

Figure 3.4: Response curves for each IP in the BMXS spectrometer calculated using MC simulations.

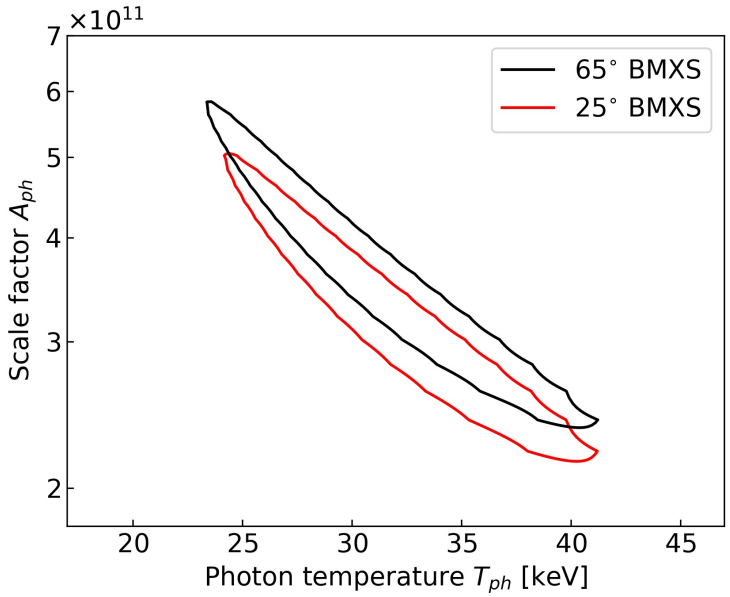

Figure 3.5: Contours of parameters A_{ph} and T_{ph} leading to a reduced χ^2 of 1 in the post processing of data from the two BMXS, for shot #28407. Results for the spectrometers placed at 25° and 65° are given in red and black respectively.

a reduced χ^2 test (see appendix A). The latter reads:

$$\chi^2 = \frac{1}{\nu}\sum_{k=1}^{N_{ip}} \frac{(E_t(k) - E_{exp}(k))^2}{\sigma^2_{exp}(k)} \rightarrow 1, \tag{3.2}$$

where $E_t(k)$ is the calculated deposited energy, $E_{exp}(k)$ the experimental one, σ^2_{exp} the variance of the experimental value and ν is the number of degrees of freedom. σ^2_{exp} should be the signal variance in each k-th IP measured considering a large number of identical shots. However, since in our case the number of shots is limited and the conditions are different from shot to shot, σ^2_{exp} is computed considering the variance of the mean value of the signal in the image, extracted using imageJ. Let us also specify that ν is defined as the number of fitting points (i.e. the number of IP in which there is the signal) minus 2, i.e. the number of free parameters used to fit the data. Fig. 3.5 shows the ensemble of possible values for parameters A_{ph} and T_{ph} that lead to $\chi^2 \rightarrow 1$ for the two spectrometers, for shot #28407. In general a good agreement between the two spectrometers was observed for all shots. Since there are several combinations of possible values for the parameters A_{ph} and T_{ph} that can reproduce the measurements, in the continuation of our analysis we consider three representative points for each BMXS (see Fig. 3.6): the two extreme points (f_{ph1} and f_{ph3}) and the central point (f_{ph2}). The proposed method presents a large uncertainty in the determination of the parameters A_{ph} and T_{ph}. Nevertheless, the three obtained curves lead to an energy deposition in the IPs that is consistent with the experimental error of the measure (see Fig. 3.6 **b**). The error is evaluated considering the standard deviation calculated from the signal in the IPs. The degeneracy of the solutions requires to constrain the problem using other experimental results.

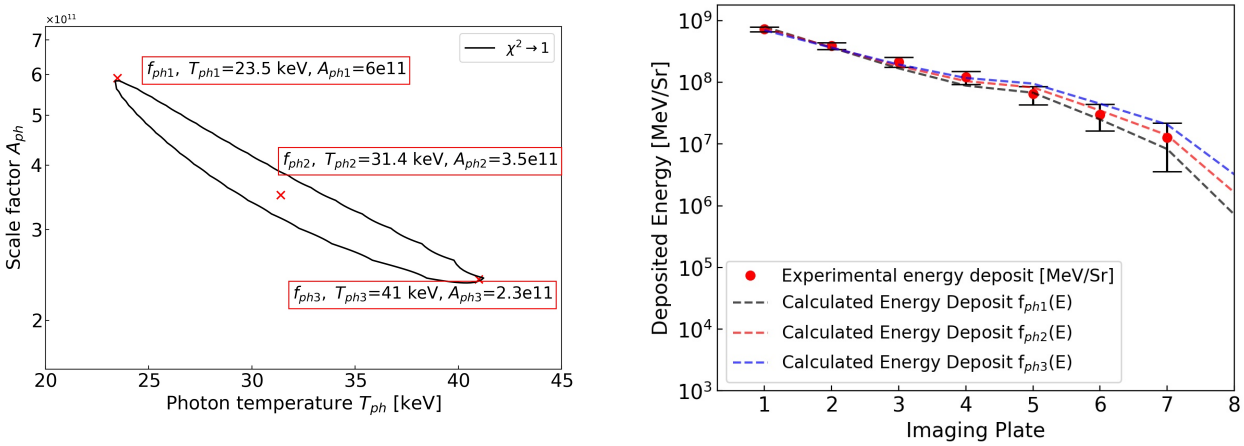

(a) (b)

Figure 3.6: (**a**) Contours of parameters A_{ph} and T_{ph} leading to a reduced χ^2 of 1 in the post processing of the BMXS placed at 65° for the shot #28407. The three representative points with the corresponding values of A_{ph} and T_{ph} are indicated. (**b**) Experimental deposited energy in the IPs (red dots) and theoretical energy deposition expected considering the three f_{ph} (dashed lines).

K_α spectrometers

The two K_α spectrometers, the ZNVH and the HRS, are based on the same working principle: a crystal disperses the x-ray photons on the sensitive part of the detector. In the ZNVH a passive detection system is used, the imaging plate, while the HRS uses a CCD. Knowing the calibration of the spectrometers, it is possible to reconstruct the x-ray

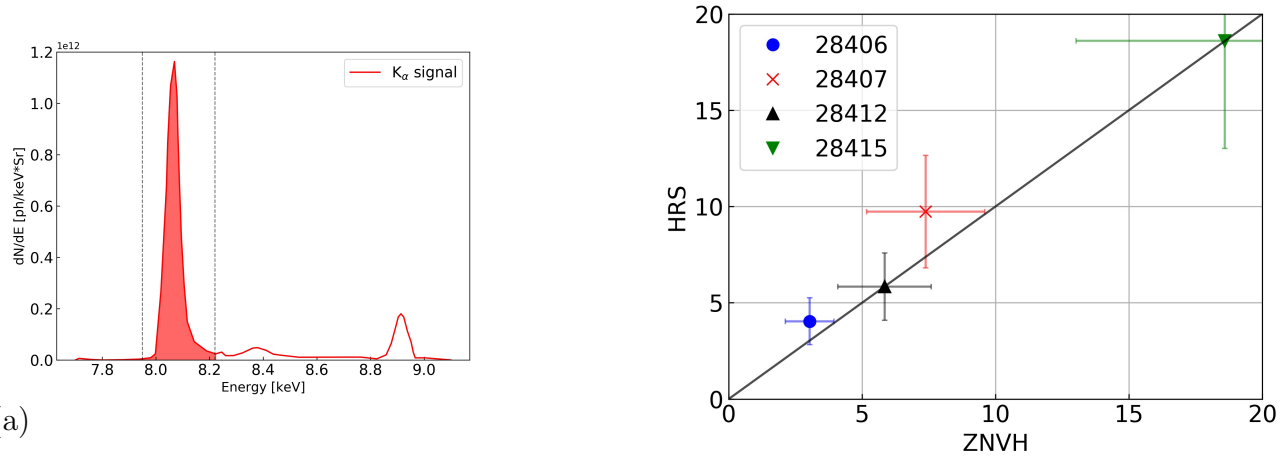

(a) (b)

Figure 3.7: (a) X-ray spectrum detected by the ZNVH spectrometer for the shot #28407, after the background correction. (b) Ratio between the signal detected by the HRS and ZNVH, normalized by 10^{10} ph/sr. The two spectrometers yield data consistent with each other.

spectrum detected. Fig. 3.7 shows the signal detected by the ZNVH for the shot #28407, after a correction for the background. In the figure, it is possible to appreciate how the Cu K_α peak is well resolved by the diagnostic. The integral of the peak gives the total number of K_α photons per steradian that reached the instrument. As shown by Fig. 3.7 (b), the two spectrometers gave a consistent response in terms of order of magnitude. As such, in the continuation of our analysis, we will consider only the data from the ZNVH.

Post-processing of the BMXS and ZNVH

Information on the hot electron population is inferred by simulating the propagation of the hot electron beam in the target and finding the parameters that reproduce both the bremsstrahlung emission and the K_α signal detected by the diagnostics. These simulations are performed with Geant4 [193], which allows for a detailed description of the electron collision in matter and x-ray emission. Unfortunately, the code does not account for the hydrodynamic evolution of the target and the collective effects, but these are playing a minor role in determining the x-ray emission due to electron propagation. For sufficiently large laser spot, the 1D assumption that the product ρr is the same for cold and for ablated target holds, where r is the target length and ρ is the mass density for the two cases. Hence, at first order, electrons should lose a similar amount of energy crossing a cold target or the real irradiated one.

While the geometry and composition of targets are fully described in the simulation, reproducing the exact position and geometry of the detectors would require significant computational resources in order to achieve acceptable statistics. Indeed, the spectrometers were mounted on the chamber wall at 1.8 meters from TCC. For these reasons, the detectors in the MC simulation are represented by spherical coronas at the correct angle and distance. This approach improves statistics, but assumes cylindrical symmetry (see Fig. 3.8).

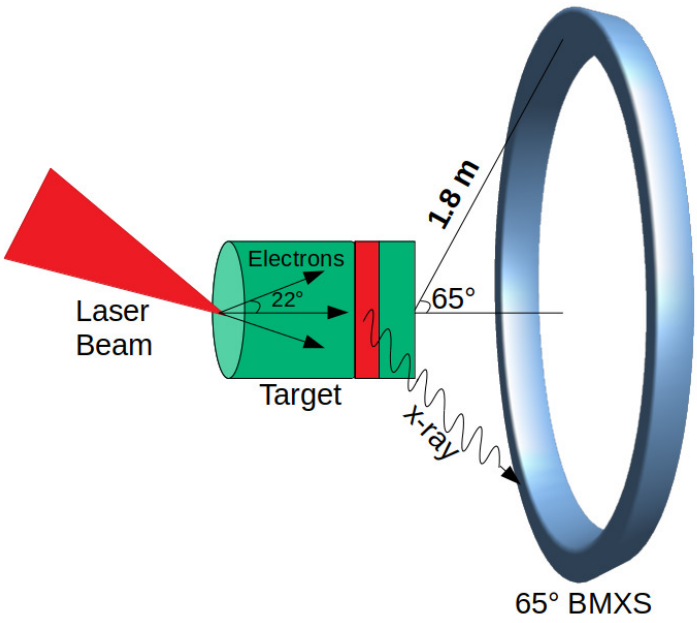

Figure 3.8: Schematic illustration of target and detector configuration set in Geant4 simulation.

Electron spectra $f_e(E)$							
		$f_{e1} \rightarrow f_{ph1}$		$f_{e2} \rightarrow f_{ph2}$		$f_{e3} \rightarrow f_{ph3}$	
Initial divergence	Beam incidence	N_{e1} [10^{16}]	T_{h1} [keV]	N_{e2} [10^{16}]	T_{h2} [keV]	N_{e3} [10^{16}]	T_{h3} [keV]
22°	0°	4.0	22	1.3	31	0.5	43
45°	0°	4.2	22	1.3	32	0.6	42
22°	23°	4.2	22	1.3	32	0.5	43
45°	23°	4.0	22	1.3	32	0.5	43

Table 3.3: Coefficients N_e and T_h of the electron distribution functions $f_e(E)$ that generate the three $f_{ph}(E)$ detected by the 65° BMXS, for shot #28407, for all the possible combinations of initial beam divergences and incidences.

An electron beam with a size of 100 μm is injected from the front side of the target where the laser impinges. Various cases are considered for the beam initialization : $\pm$ 45° or $\pm$ 22° of initial divergence and of 0° or 23° of inclination with the respect to target normal. Bremsstrahlung and K_α generation were simulated using the Penelope [194] and Livermore [195] physics libraries. Simulations were conducted by launching 22 monochromatic beams with logarithmic-spaced energies from 5 keV up to 300 keV. The 2D Maxwellian $f_e(N_e, T_h, E) = \frac{N_e}{T_h} e^{-E/T_h}$ that reproduces both the bremsstrahlung spectrum $f_{ph}(E)$ on the BMXS and the K_α signal on the ZNVH is then reconstructed. In the function, N_e represents the total number of electrons and T_h the average electron kinetic energy or the temperature.

Concerning the bremsstrahlung spectrometers, as shown in Sec. 3.1.2, three possible photon distribution functions are considered. Tab. 3.3 shows the electron distribution functions $f_e(N_e, T_h, E)$ that generate the three photon distributions $f_{ph}(E)$ on the 65° BMXS, for shot #28407. Since no significant differences were observed between the two

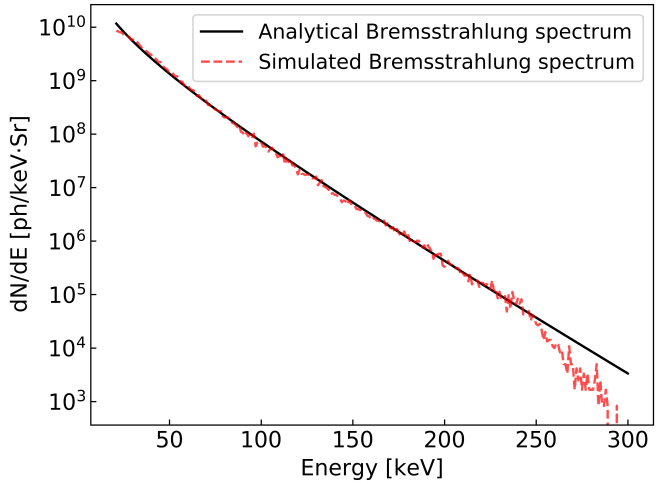

Figure 3.9: Comparison of the bremsstrahlung spectra $f_{ph1}(E)$ in black and simulated one resulting from $f_{e1}(E)$ reported in Tab. 3.3 in red. The bremsstrahlung spectra comes from the post-processing of the 65° BMXS for the shot #28407. The laser to hot-electrons energy conversion efficiency is ~11% for the curve $f_{e1}(E)$.

physics libraries in the simulation of the bremsstrahlung radiation, only the results from Penelope are shown. As can be observed, there are no remarkable differences between different initial divergences and inclinations of the input electron beam. The low mean kinetic energy of electrons leads to severe large-angle scattering that causes the particles to lose their directionality. This strengthens the initial assumption of cylindrical symmetry. As an example, Fig. 3.9 compares $f_{\mathrm{ph1}}(E)$ and the simulated bremsstrahlung spectra produced on the 65° BMXS using the f_{e1}(E). For these particular target configurations and energy ranges, the photon distribution produced by an exponential distribution function of electrons has the form of $f_{\mathrm{ph}}(E) = \frac{\mathrm{A_{ph}}}{E} e^{-E/\mathrm{T_{ph}}}$. This justifies the initial choice of fitting the BMXS signal with these kind of functions (see Sec. 3.1.2). Across all shots, it is possible to observe an average electron temperature $\mathrm{T_h}$ that spans from 20 keV up to 45 keV, with absolute number of electrons $\mathrm{N_e}$ ranging from $5{\cdot}10^{15}$ up to $5{\cdot}10^{16}$.

Concerning the K_α simulations, similarly to the generation of the bremsstrahlung spectrum, the initial configurations of the electron beam is not seen to influence the K_α emission. Therefore, only results from the simulations with ±22° initial divergence and at normal incidence beam are reported. Fig. 3.10 shows possible values $\mathrm{N_e}$ and $\mathrm{T_h}$ that reproduce the K_α signal on the ZNVH, combined with the values obtained previously by the BMXS, for the shots #28406 and #28407. A disagreement of about 25% is found between the libraries Livermore and Penelope in reproducing the K_α. Since they predict that the same amount of electrons reaches the copper with an identical energy distribution, the discrepancy must be attributed to differences in the computation of the cross section for the K-shell ionization $\sigma_k(E)$. These differences are however comparable to the relative standard deviation of the experimental measures of $\sigma_k(E)$ [196].

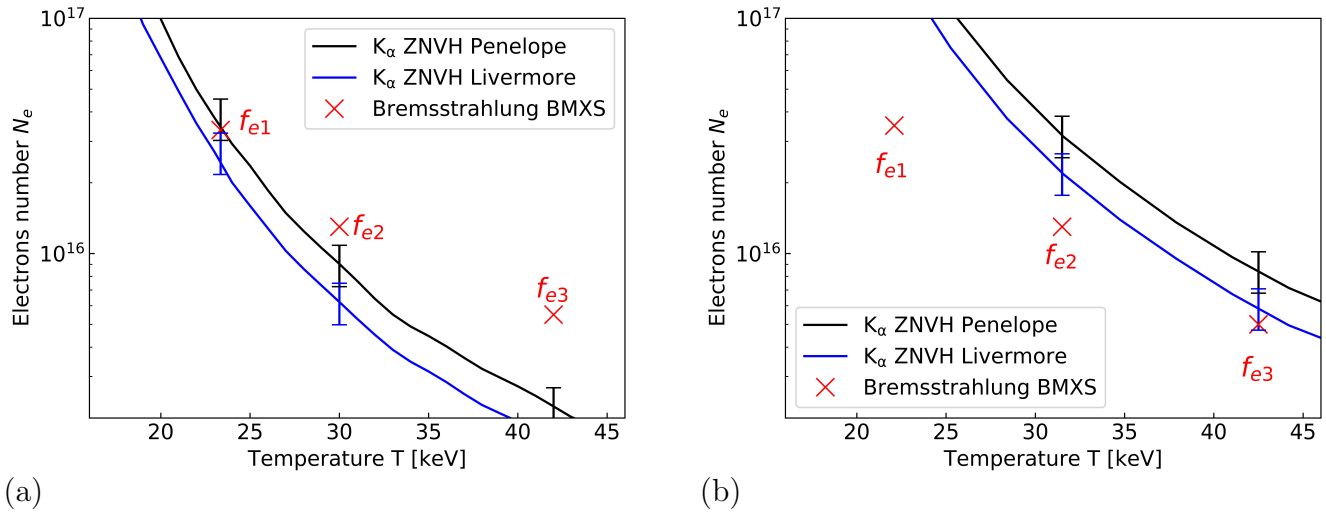

Figure 3.10: Map of possible values of $\mathrm{N_e}$ and $\mathrm{T_h}$ that can reproduce the experimental data (K_α and bremsstrahlung spectrum) for shots #28406 (a) and #28407 (b). The black and the blue lines result from K_α simulations with libraries Penelope and Livermore, respectively. The red crosses indicate the average values coming from the two BMXS, using the three representative points scheme. The experimental error on the K_α signal, evaluated to be around 20%, is shown by error bars.

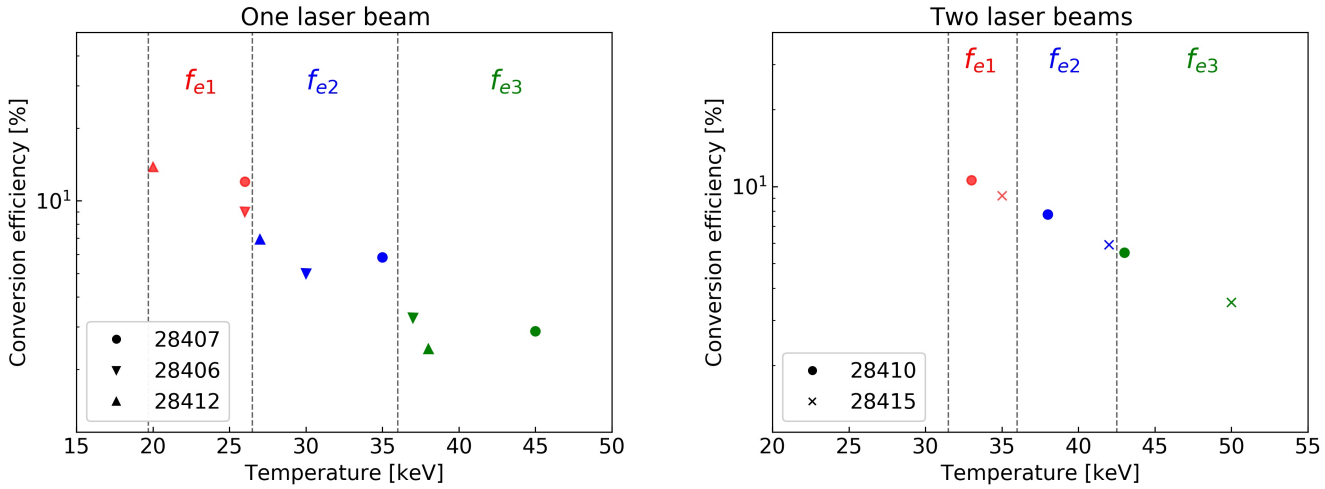

(a) (b)

Figure 3.11: Laser to hot electron conversion efficiency as a function of temperature. Fig. (a) reports the shots in which one beam was focused on target (1250 J): #28406, #28407, #28412. Fig. (b) reports shots #28410 and #28415 with two laser beams (2500 J). The three main areas, corresponding to the three $f_e(E)$ detected by the BMXS and ZNVH, are reported in red, blue and green for each shot, respectively.

The disagreement between the results considering different shots does not allow to reduce the ranges of values for N_e and T_h. It is thus necessary to keep the three representative points considered in the analysis so far.

Figure 3.11 illustrates the conversion efficiency of laser energy into hot electron energy for the five shots, considering for each the three possible f_e. Points in between are chosen in case of significant discrepancies between the response of the BMXS and ZNVH (Fig. 3.10). In shots using a single interaction beam, three main regions can be identified: from 20 keV to 26 keV with efficiencies around 10%, from 27 keV to 35 keV with efficiencies around 6% and from 36 keV up to 45 keV with efficiencies around 2-3%. The shots performed with two laser beams show similar conversion efficiencies and slightly higher temperatures. In order to discriminate between the three regions, we use all these values as input of hydrodynamic simulations and we evaluate which reproduces the experimental evolution seen in the radiographs.

3.1.3 Hydrodynamic evolution of the target and effect of the hot electrons

Time-resolved radiographs

The shock propagation in the target was monitored by x-ray radiographs taken at different times. Fig. 3.12 shows the array of sixteen radiographs captured by the XRFC for the shot #28407. Among these, Fig. 3.13 shows the radiography at 250 ps and at 1.150 ns. At 250 ps, when the target is still cold, it is possible to see the CH ablator of 175 μm thickness, the copper plate of 20 μm, the plastic holder of 50 μm and a $\sim$ 15 μm of glue between the holder and the copper. This indicates a correct alignment of the XRFC and a low value of parallax for the images of the third column of the array. In

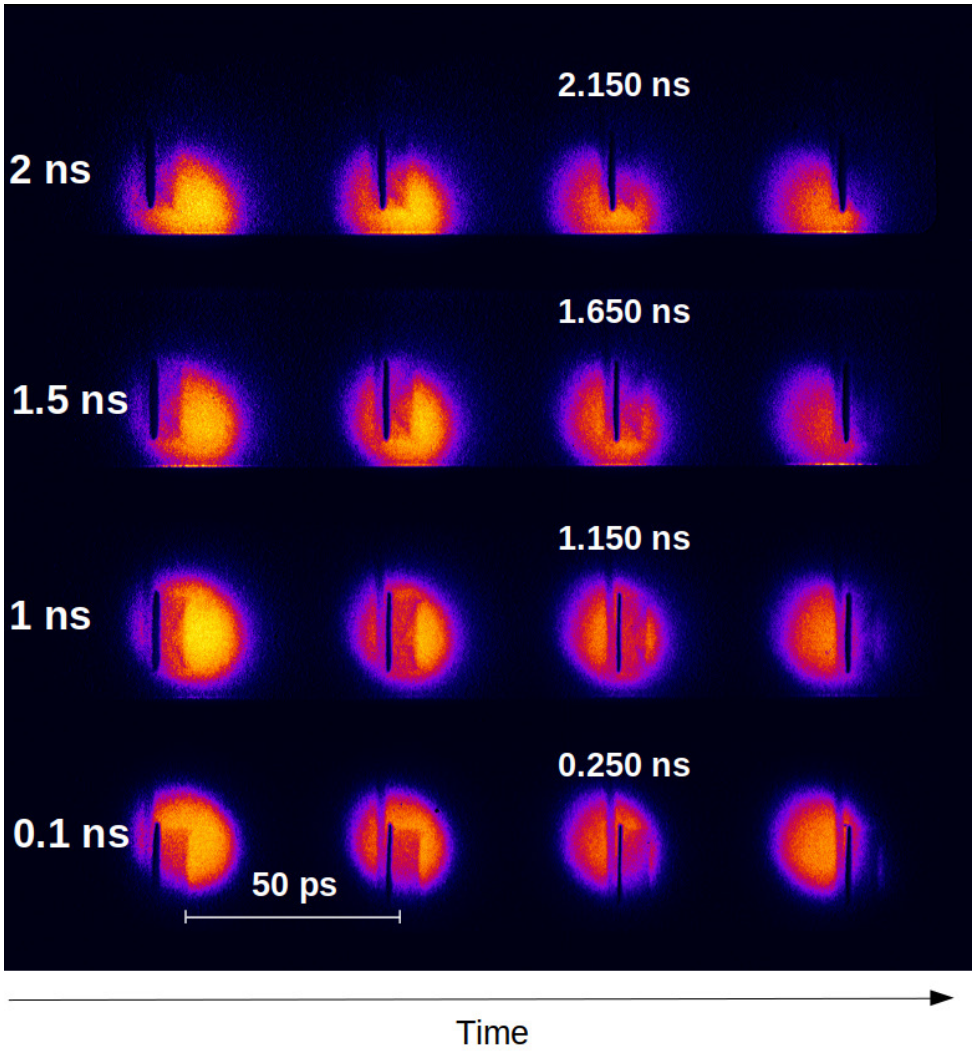

Figure 3.12: Array of 2-D radiographs captured at various times by the XRFC for shot #28407. Between each image on the line there are 50 ps.

the radiograph at 1.150 ns it is possible to discern the shock that propagates inside the ablator, although the poor contrast of the image makes the precise measurement of its position difficult. It is however clearly possible to see that the copper layer is thicker. Since at this time the shock did not reach the layer, such expansion has been attributed to the effect of hot electrons. The shock position and the copper plate expansion are the figures of merit considered to characterize the hot electron source. Different intensities and kinetic energies of the hot electron beam will strongly affect the variation in time of these two quantities.

The expansion of the plate is evaluated by referring to transmissivity profiles taken along the cylinder axis, as shown in Fig. 3.14. The minimum in the curves indicates the presence of the copper and the FWHM represents its thickness. The transmissivity values were then normalized by the values resulting from the plastic holder. The holder remains un-compressed during the radiography, and we can hence assume that the x-ray flux that goes through it is constant and proportional to the backlighter emission.

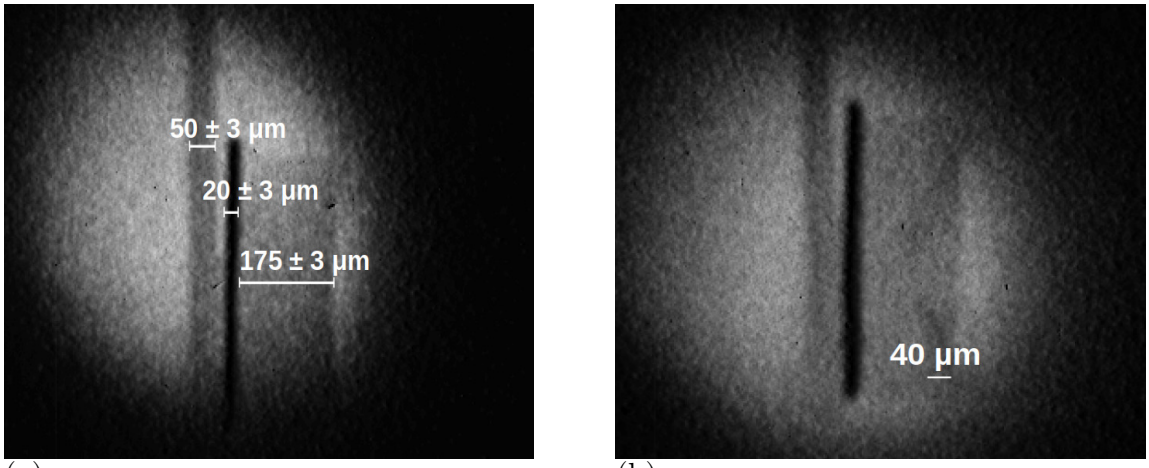

(a) (b)

Figure 3.13: Radiography of the target at 250 ps (a) and at 1.150 ns (b) for shot #28407. In the radiography (a) the thickness of the ablator, copper plate and holder are indicated. The laser impinges on the target from the right.

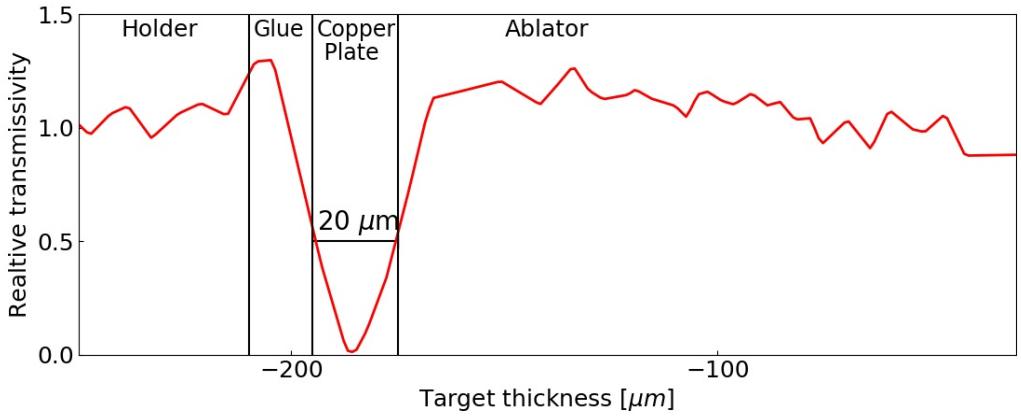

Figure 3.14: Transmissivity profile on the cylinder axis extracted from the radiography at 250 ps for shot #28407. The position of ablator, copper plate, glue and holder are indicated in the figure. The thickness of the copper is measured by the FWHM of the transmissivity profile.

Hydrodynamic simulations

Hydrodynamic simulations were performed with the 2D Hydrodynamic Code (CHIC) [37] developed at CELIA. The code describes single fluid two-temperatures hydrodynamics with thermal coupling between electrons and ions. Electron heat transport is described by the Spitzer-Harm model with flux limiter, while radiation transport is described by a multi-group approach using tabulated opacities. The calculation of hydrodynamic quantities relies on equations of state taken from the SESAME database, and the ionization is calculated according to the Thomas-Fermi theory. The laser propagation is modelled using ray tracing accounting for inverse bremsstrahlung absorption. Losses due to Stimulated-Brillouin Scattering (SBS) are not modelled. Since in our experiment the SBS reflected power was not directly measured, the experimental shape of the pulse was corrected by the amount of SBS evaluated by performing simulations with the time-enveloped wave

solver LPSE [197]. This code couples the equations that describe the pump wave with the equations for the Raman and Brillouin scattered light and plasma waves. Plasma waves equations are solved around a given plasma frequency ω_{pe0}, whereas the Raman scattered field is enveloped at $\omega_r = \omega_0 - \omega_{pe0}$. The fluid equations for the plasma density and velocity govern the plasma dynamics. Coronal plasma density, velocity profiles and electron temperatures at quarter critical density were extracted from an initial CHIC simulation with the experimental base pulse at four times: 0.3 ns, 0.5 ns, 0.9 ns and 1.3 ns. These parameters are then used as input for LPSE to calculate the percentage of SBS reflected light and study the Raman and the Brillouin scattering at quarter critical density in one-dimensional geometry. The LPSE simulations ran for 25 ps, which is long enough to observe the saturation of Raman and Brillouin instabilities. Discussion on the detailed results of these simulations, carried by A. Ruocco (Central Laser Facility, STFC Rutherford Appleton Laboratory, Harwell Oxford, Didcot, Oxford OX11 0QX, United Kingdom, at the moment of writing), lies beyond the purpose of this work. Here, we only retain the fraction of the Brillouin back-scattered light when the saturation of the instability is reached. The amount of the Brillouin reflected light obtained in the four simulations is the 2%, 7%, 46% and 2% of the incoming pump wave, respectively. The correction is done by interpolating linearly in time these percentages and subtracting the values to the base pulse. The total fraction of scattered power in the simulation is around 20%. The shapes of experimental (red line) and the SBS-corrected (orange line) pulses are shown in Fig. 3.15 (a).

Hot-electron propagation in the hydrodynamic simulation is modelled using the hot-electron transport package implemented in CHIC. Electrons propagate along straight lines depositing energy into the mesh according to the plasma stopping power formulas [123]. Straggling and blooming of the beam are taken into account by using the Lewis' model [125] (see appendix E). Electrons are described by a 2D Maxwellian function $f_e(N_e, T_h, E) = \frac{N_e}{T_h} e^{-E/T_h}$ in which the parameters N_e and T_h are taken from experimental

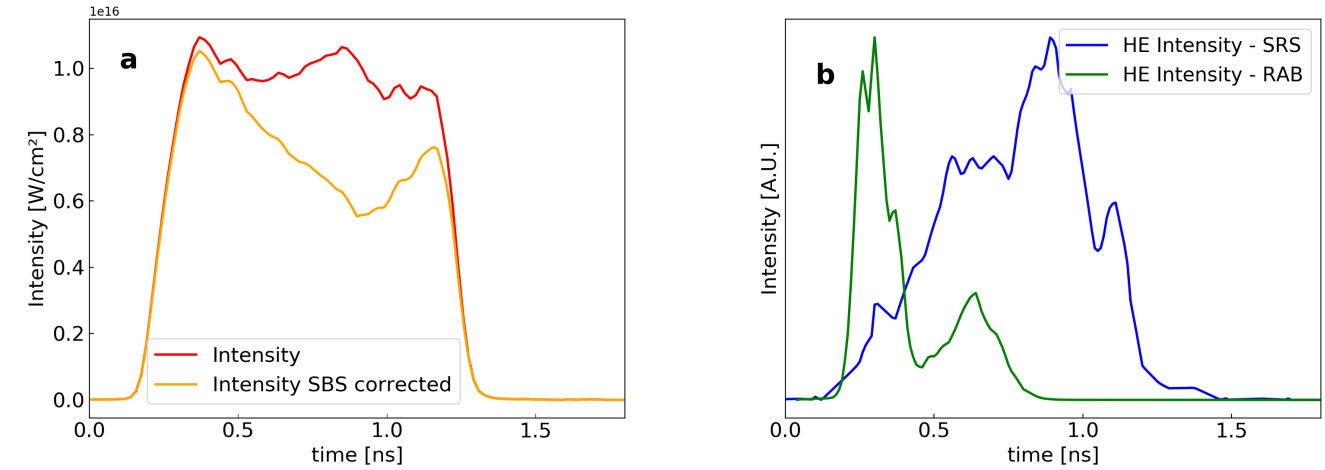

(a) (b)

Figure 3.15: (**a**) Experimental laser pulse shape (red) and SBS-corrected laser pulse shape (orange).(**b**) The intensity of HE beam is assumed to exactly follow either SRS reflected power measured by the SABS (blue) or RAB signal computed by CHIC (green).

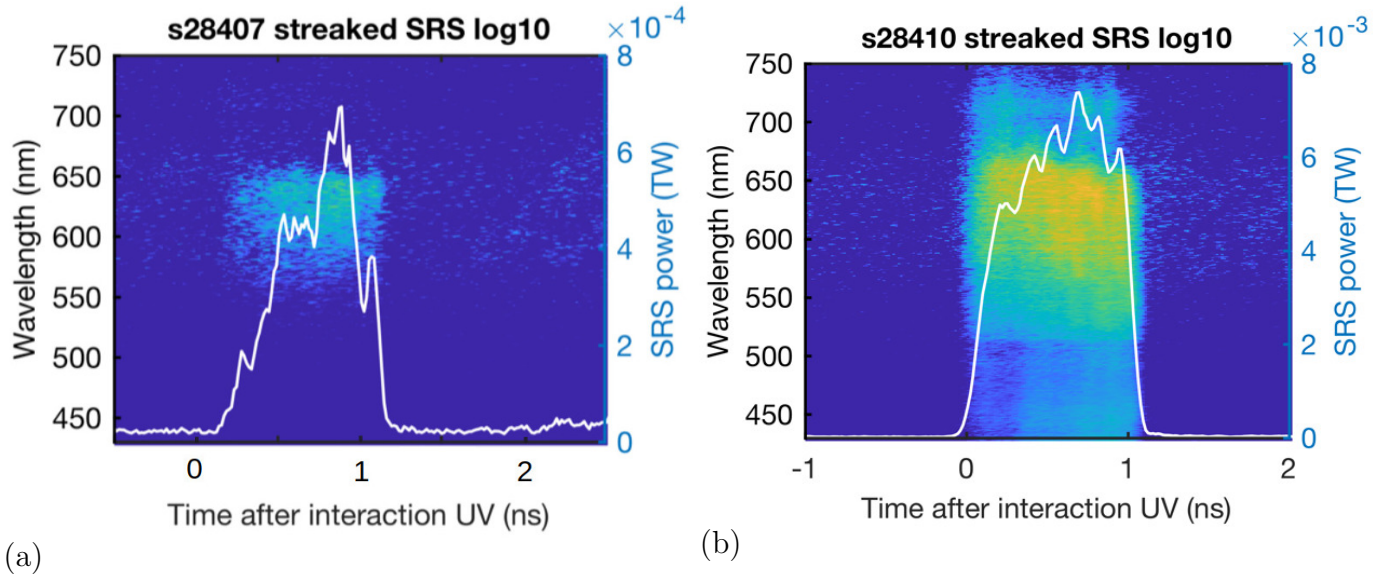

Figure 3.16: Reflected light due to SRS and TPD collected by the SABS for shot #28407 and #28410. The bandwidth of the diagnostic ranges from 400 nm up to 750 nm. The temporal profile of the signal is indicated by the white line. The values of the SRS power collected are not significative, since the diagnostic covers only the 6% of the beam solid angle.

data. The parameter N_e is related to laser to hot electron conversion efficiency η (see Sec. 3.1.2). This coefficient and the position where the hot electron source is initialized are modelled using the signal obtained by the SABS. As shown by Fig. 3.16, this diagnostic detects light generated by absolute and convective SRS and the $\omega/2$ TPD signal. From Fig. 3.16, it is possible to see that the strongest signal has the broad spectral features characteristics of convective SRS, while the $\omega/2$ signal produced by TPD is weaker. The centers of the convective SRS emissions are around 625 nm and 575 nm for shots #28407 and #28410, respectively. According to the relation between the wavelength of backward scattered SRS and the density at which the scattering occurs [46]:

$$\lambda_{\mathrm{SRS}} = \lambda_{\mathrm{L}} \left[1 - \sqrt{\frac{n_e}{n_{\mathrm{c}}} \left(1 + 3k^2 \lambda_{\mathrm{D}}^2\right)} \right]^{-1}, \tag{3.3}$$

we can estimated that the average SRS emission occurs in the range $0.14n_c$ - $0.18n_c$. In the simulations, electron beamlets are thus initialized at $0.14n_c$ with an initial divergence of $\pm$ 22°. This approach does not consider electrons generated at n_c by the Resonant Absorption (RAB) and at $n_c/4$ by the TPD. Nonetheless, different positions of the electron beam initialization do not influence the final results of the simulation. This is because electrons are initialized with a small angle of divergence and they will not lose a large amount of energy in the corona. The intensity of the electron beam is modelled in time considering the conversion efficiency $\eta(t)$ that follows temporally either the signal measured by the SABS or the RAB signal computed by CHIC, as shown in Fig. 3.15 (**b**). In particular, the signals were renormalised and rescaled using the conversion efficiency given by BMXS and ZNVH (11%, 6%, 3% for the shot #28407, see Sec. 3.1.2). A discussion on the mechanisms of hot electron generation is currently an open topic and it is out of the scope of the thesis work. Here we limit our analysis to the characterization of hot electrons, focusing our attention on their effects on the hydrodynamic evolution of

the target. Three different CHIC simulations are performed in order to determine which combination of conversion efficiency η and average temperature T_h better reproduces the experimental behaviour. This is done either for the one beam and the two beams cases.

Comparison between experimental and synthetic radiographs. One beam on target case

For the one beam case, referring to the shot #28407, the three corresponding $f_e(E)$ are reported in Tab. 3.4 and reported in Fig. 3.11 (a). The generation of synthetic radiographs from simulations is accomplished by reproducing the 3D cylindrical density profiles and then by calculating the theoretical transmissivity maps at the times of interest, according to the formula [198]:

$$T(t,x,y) = \exp\left[-\left(\frac{\mu}{\rho}\right)\int \rho(z)\mathrm{d}z\right]. \tag{3.4}$$

Here $\rho(z)$ is the density of the material along the radiography axis and $\frac{\mu}{\rho}$ is the mass absorption coefficient in plastic and copper. The images are then blurred with a 2D Gaussian convolution with standard deviation of 15 μm to take in account the spatial resolution of the pinhole array. Transmissivity profiles are then extrapolated along the cylinder axis to evaluate the copper plate expansion. The values are renormalized by the transmissivity of the holder to be consistent with the experimental analysis.

To retrieve information on the hot electron beam we rely on the radiography taken at 1.650 ns, when the laser interaction is finished and hot electrons have already deposited their energy in the target. The experimental thickness, evaluated from the transmissivity curves, is 34 $\pm$3 μm. Considering a diagnostic temporal resolution of $\pm$50 ps, Fig. 3.17 shows the superposition between the experimental curve at 1.650 ns and the simulation results for a time windows that spans from 1.600 ns up to 1.700 ns. Three hot electrons cases (denoted with the corresponding f_{e_i}) and the case without hot electrons (woHE) are reported. The figures report the simulations results in which the hot electron beam followed temporally the SRS signal (blue curve in Fig. 3.15 (**b**)). We do not report the figures in which hot electrons follow the RAB signal (green curve in Fig. 3.15 (**b**)), since the results are similar to the SRS case. This is likely due to the fact that we are considering the radiography at 1.650 ns, when the laser pulse is finished. At this time, the shock position and the copper thickness depend strongly on the intensity and on the mean kinetic energy of hot electrons (i.e. on their induced preheat), instead the temporal shape of the beam (i.e. the hot electron injection time) plays a second order effect.

The decrease of the synthetic transmissivity in the ablator is due to the presence of

f_e			
	T_h [keV]	η [%]	$N_e[10^{16}]$
$f_{e1}(E)$	26	11	3.4
$f_{e2}(E)$	35	6	1.4
$f_{e3}(E)$	45	3	0.5

Table 3.4: Parameters of Maxwellian functions $f_e(E)$ obtained from the post-process of BMXS and ZNVH for the shot #28407, used as input in CHIC.

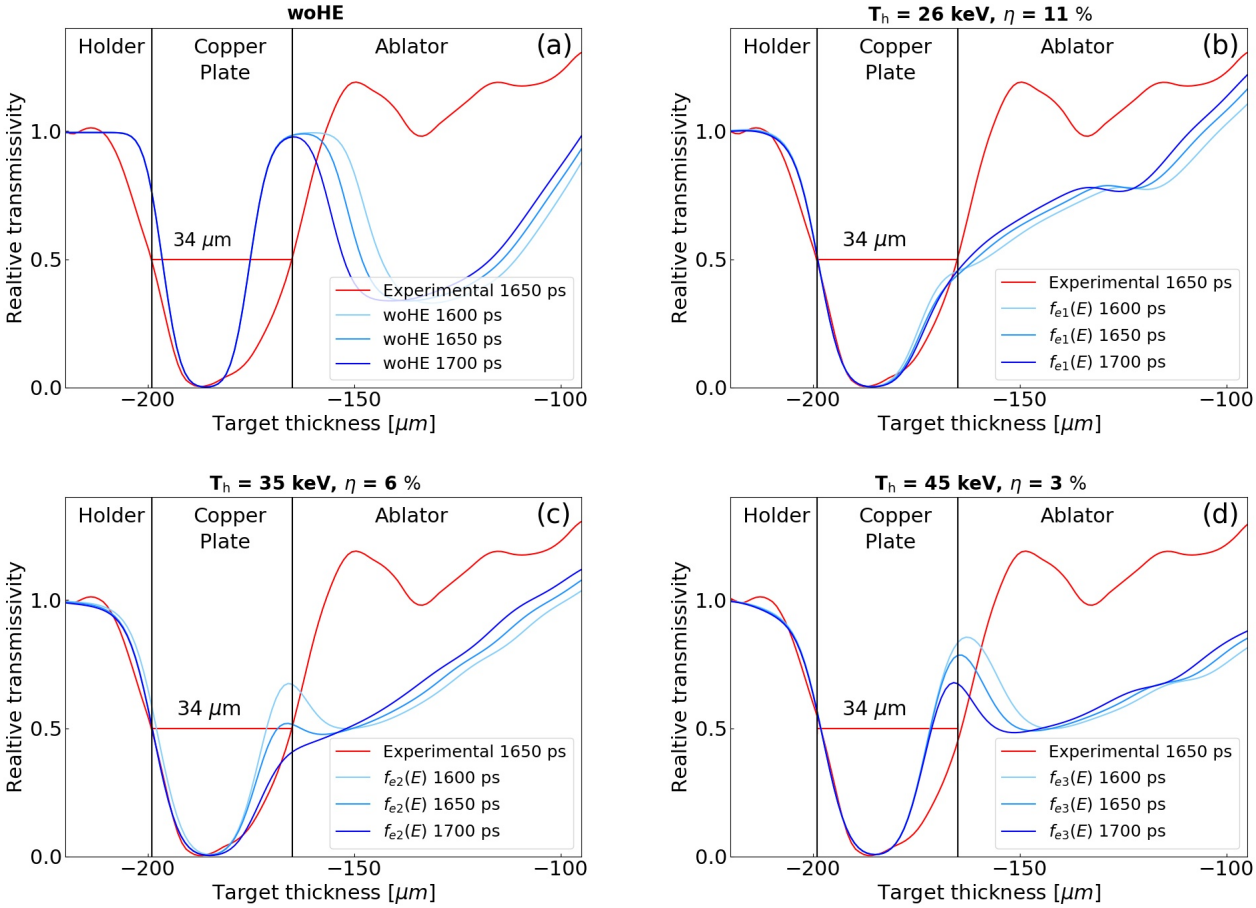

Figure 3.17: Transmissivity curves taken along the central axis. In red the experimental curve extracted from the radiography at 1.650 ns for shot #28407, in blue the synthetic curves for a time window that spans from 1.600 ns up to 1.700 ns. The four figures correspond to the four simulated cases: (a) case without hot electrons; (b) simulation with hot electron beam $f_{e1}(E)$; (c) simulation with hot electron beam $f_{e2}(E)$; (d) simulation with hot electron beam $f_{e3}(E)$. In these simulations the hot electron beam follows temporally the SRS signal (Blue curve in Fig. 3.15 (**b**))

the shock that compresses matter. This effect allows to see the shock front propagating in the ablator in the cases f_{e_3} and woHE, while in the other two cases the shock has already reached the copper plate at 1.650 ns. In the experimental curves this behaviour is not observed and, on the contrary, the values coming from the compressed ablator are slightly higher compared to the ones coming from the un-compressed holder. This is possibly due to non-uniformities in the x-ray backlighter source. While this issue makes the precise detection of the shock position difficult, it does not affect the information related to the copper thickness. From Fig. 3.17 it is possible to observe that the low temperature HE distributions (f_{e_1}, f_{e_2}) reproduce an expansion of the plate that approaches the experimental behaviour. For the other cases (f_{e_3}, woHE), the expansion is lower and not compatible with experimental results. For the case woHE, the shock front approaches the copper plate at t=1.900 ns. The copper expansion taken at this time for this particular case is $\sim$25 μm. This indicates that the copper expansion driven only by the radiative transport plays minor role compared to the expansion due to the hot electron energy deposition.

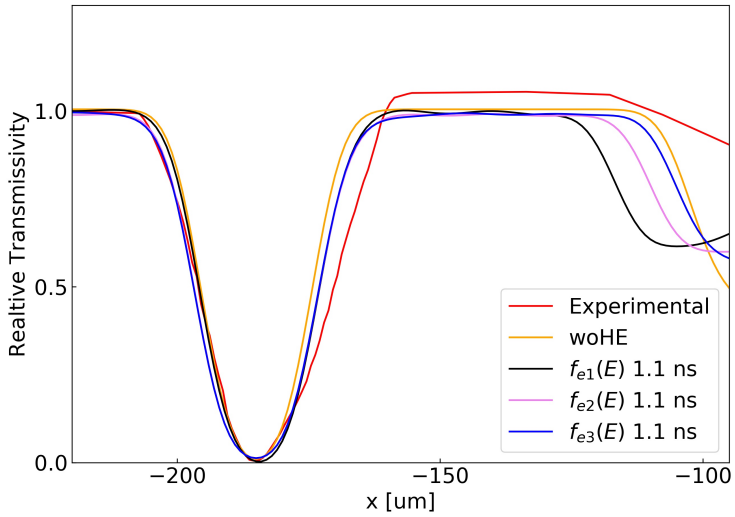

Figure 3.18: Transmissivity profile on the cylinder axis extracted from the radiography at 1100 ps for shot #28407. The red curve is the experimental transmissivity profile; the orange curve comes from the simulation without hot electrons; the black curve comes from the simulation with the hot electron beam $f_{e1}(E)$ (T_h= 26 keV, η = 11%); the violet curve comes from the simulation with the hot electron beam $f_{e2}(E)$ (T_h= 35 keV, η = 6%); the blue curve comes from the simulation with the hot electron beam $f_{e3}(E)$ (T_h= 45 keV, η = 3%);

Let us point out that it was necessary to rely on the radiography taken at 1.6 ns, because in the radiography at 1.1 ns the copper expansion is too weak and it is not possible to discriminate among the three cases which is the closer to the data. As shown in Fig. 3.18, the experimental copper plate thickness is around 26 ±3 μm, while the copper expansion predicted by the four simulations is around 23 μm. As such, it is not possible to exploit the radiography at 1.1 ns to constrain the problem.

The experimental radiography at 1.650 ns is illustrated in Fig 3.19. At that time, the shock front is into the copper plate. We report in the same figure the synthetic radiographs obtained from the simulations with $f_{e1}(E)$ and $f_{e2}(E)$ at 1.700 ns, considering as before the limit in the time resolution of the camera. In the case $f_{e2}(E)$ the shock is approaching the plate, while in the simulation with $f_{e1}(E)$ the shock is already propagating inside, in agreement with the experimental behaviour. In the other two cases (without HE and $f_{e3}(E)$) the shock at 1.700 ns has not yet reached the plate. As such, the 2D x-ray radiography suggests that the HE distributions $f_{e1}(E)$ and $f_{e2}(E)$ are more consistent with the experimental results.

The conclusions presented from the time-gated radiography are strengthened by results from the 1-D time-resolved radiography, shown in Fig. 3.20 for shot #28412. This figure shows the ablator of 175 μm, the ablation zone that grows in time and the copper plate. The progression of the shock into the target is indicated by the white-dashed line in Fig. 3.21, in which we compare the experimental radiography with the synthetic ones. Despite the large error bars due to low contrast of the experimental image, there is an indication

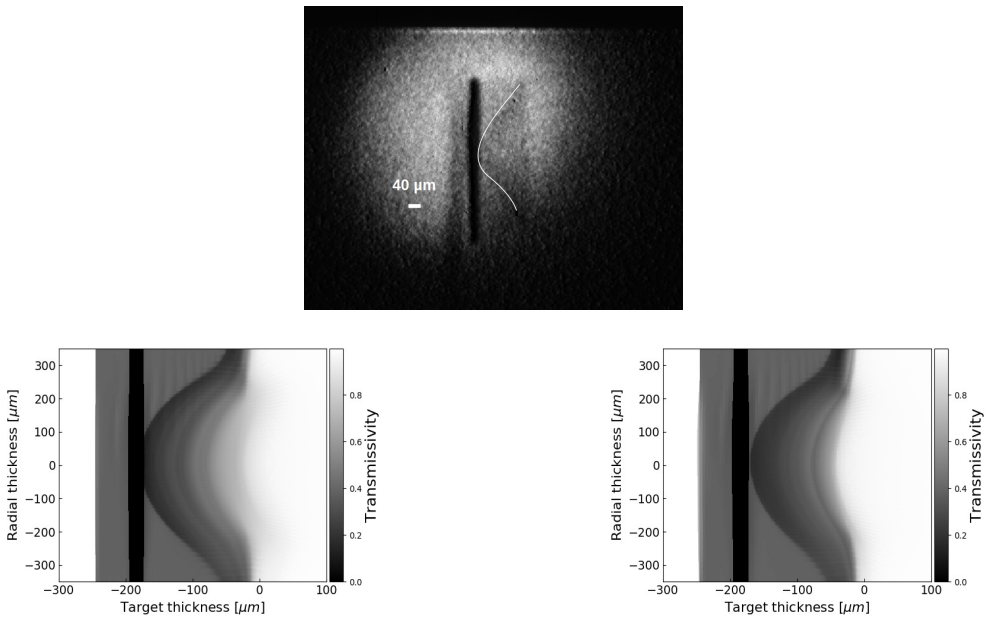

Figure 3.19: [Top] Experimental radiography of shot #28407 at 1.650 ns. The shock front is highlighted; [Bottom-left] synthetic radiography obtained by the simulation with $f_{e1}(E)$ at t= 1.700 ns; [Bottom-right] synthetic radiography obtained by the simulation with $f_{e2}(E)$ at t= 1.700 ns.

that lower temperatures and higher efficiencies are more appropriate to reproduce the experimental behaviour.

To summarize, the simulation with the distribution $f_{e1}(E)$ is better in agreement with experimental results, either considering the 2-D radiography and the 1-D time resolved radiography. The behaviour predicted by the simulation with $f_{e2}(E)$ approaches the experimental results, while the simulations with $f_{e3}(E)$ and without hot electrons are clearly not in agreement with experiment. Considering $f_{e1}(E)$ and $f_{e2}(E)$ as the closer to experimental results, we identify a hot electron temperature T_h = 27 keV ± 8 keV and a conversion efficiency η= 10% ± 4%. These ranges correspond to the first two zones (f_{e1} and f_{e2}) of figure 3.11(a).

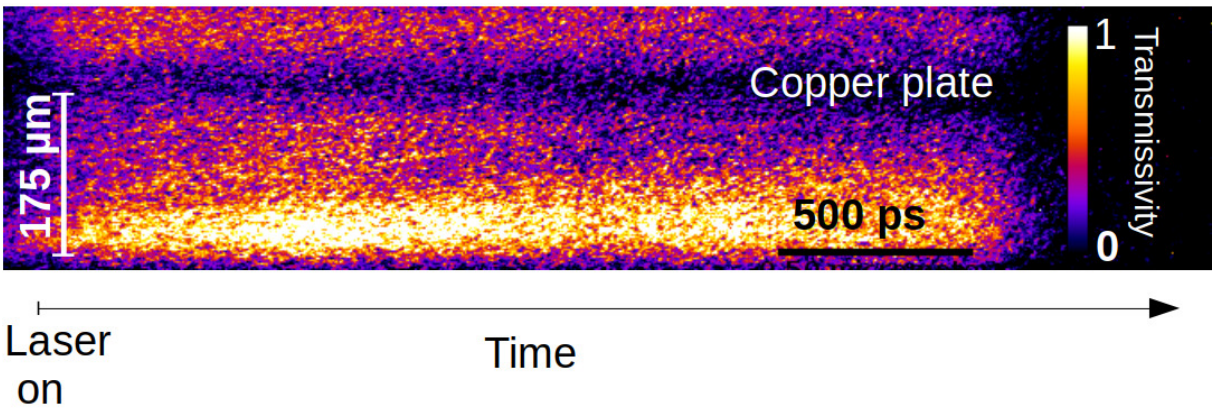

Figure 3.20: Experimental time resolved 1D radiography for the shot #28412. Time is on the x axis. In this figure, the laser is incident from the bottom.

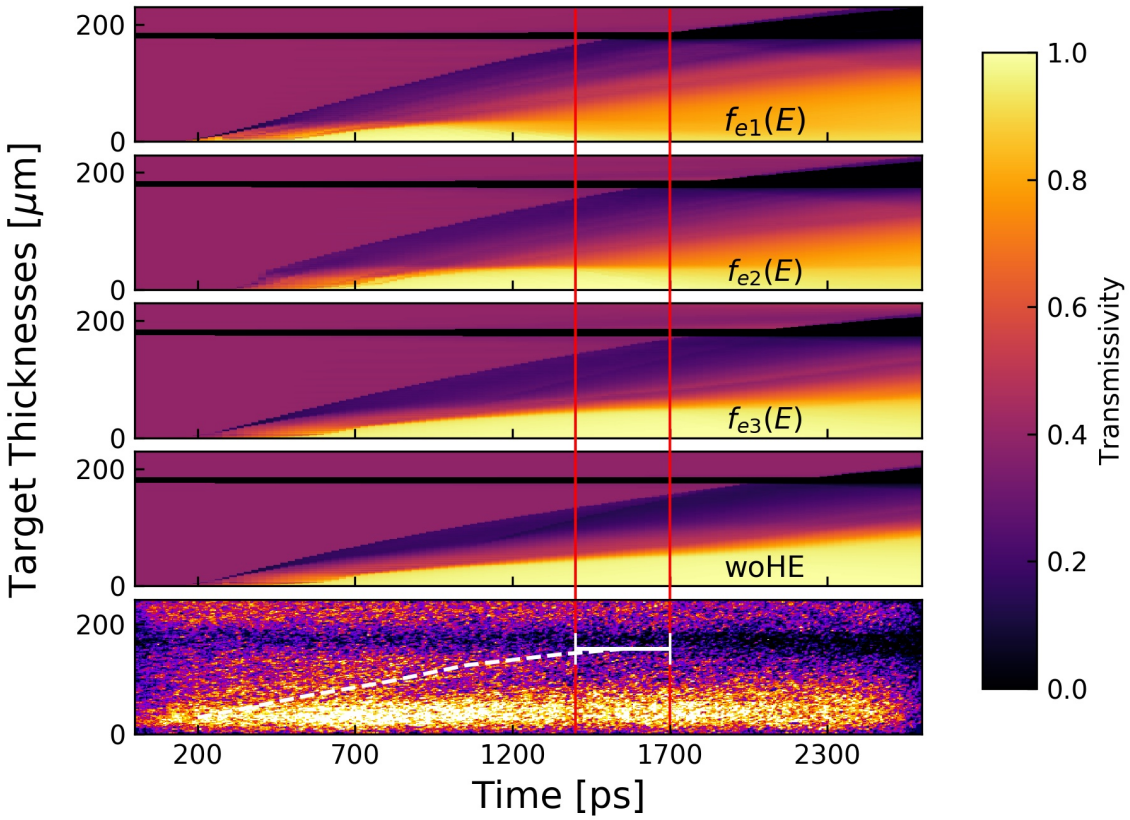

Figure 3.21: Comparison between the experimental 1D time resolved radiography of shot #28412 and the synthetic ones. The three hot electron cases (denoted f_{e_i}) and the case without hot electrons (woHE) are reported. The time at which the shock arrives on the plate is marked with red lines. The white dashed line indicates the progression of the shock.

Temperature of the copper layer

The K_α spectra measured by the HRS are used to estimate the electronic temperature reached by the copper layer during the irradiation. The spectrum measured by the HRS for shot #28407 is shown in Fig. 3.22 (red line). In the figure it is possible to see the two peaks related to the de-excitation of the copper K_α, namely $K_\alpha 1$ and $K_\alpha 2$, resolved by the instrument. The emission lines, in the case of cold material, are at 8.0478 keV for $K_\alpha 1$ and at 8.0278 keV for $K_\alpha 2$. The heating and the consequent ionization of the material due to the presence of hot electrons induces a wavelength shift of the emission that results in broadening of the peaks [152]. Since the position of the HRS pointed to the front side of the target, the measured temperatures are referred to the first layers of the plate. This is because the K_α signal coming from those layers is stronger and less attenuated by the target itself. The experimental broadening is compared with synthetic signals simulated using the PrismSpect code [199]. These synthetic signals are reproduced considering the emission of K_α at different copper temperatures (the simulations were conducted by S. Pikuz, Joint Institute for High Temperatures of Russian Academy of Sciences, 125412 Moscow, Russian Federation, at the moment of writing).

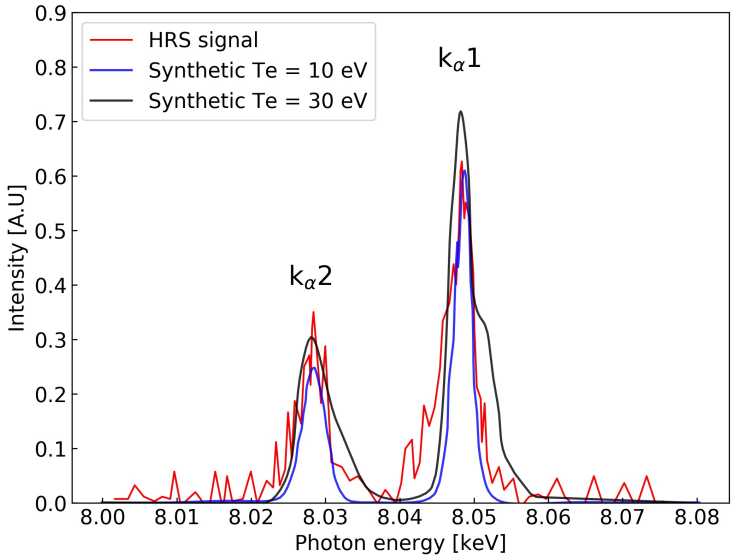

Figure 3.22: Experimental and synthetic K_α spectra superimposed. The experimental signal in red refers to the shot #28407. The synthetic signal are reproduced considering electronic copper temperatures between 10 eV (blue curve) and 30 eV (black curve), using the PrismSpect code [199].

As shown in Fig. 3.22, the broadening of the peaks indicates temperatures greater than 10 eV, but lower than 30 eV. The copper temperature computed by CHIC for simulations with hot electrons presents its maximum of 13 eV in the first part of the plate, decreasing down to 5 eV in the rear side. The values provided by the simulation without hot electrons are 0.2 eV. The values predicted by the simulations with hot electrons are thus in much better agreement with the experimental results.

Comparison between experimental and synthetic radiographs. Two beams on target case

As reported in Tab. 3.2, the radiographs of the shots 28140 and 28415 (the ones in which two laser beams were focused on the targets) are not exploitable. This issue is due to the low contrast of the images, that does not allow to retrieve the shock position or the copper expansion with sufficient accuracy.

Fig. 3.23 shows the 2D array of radiographs obtained in the shot 28410. In this array, the images in the first column are affected by a lower parallax, as can be observed from the transmissivity profiles extracted from the image at 200 ps, Fig. 3.24. Unfortunately, the times at which the radiographs were taken did not allow to constrain the hot electrons measurements. Fig. 3.25 reports the comparison between the experimental and the synthetic transmissivity profiles at 600 ps and at 1000 ps. The synthetic signals are extracted from three simulations considering the three different electron distribution functions, as done for the single beam case. The three electron distribution functions correspond to those reported in Fig. 3.11 (b) and in Tab. 3.5. We performed simulations in which electrons follow temporally the SABS or the RAB signal, as done for the single beam case (see Sec. 3.1.3). However, in Fig. 3.25, we report only the results coming from

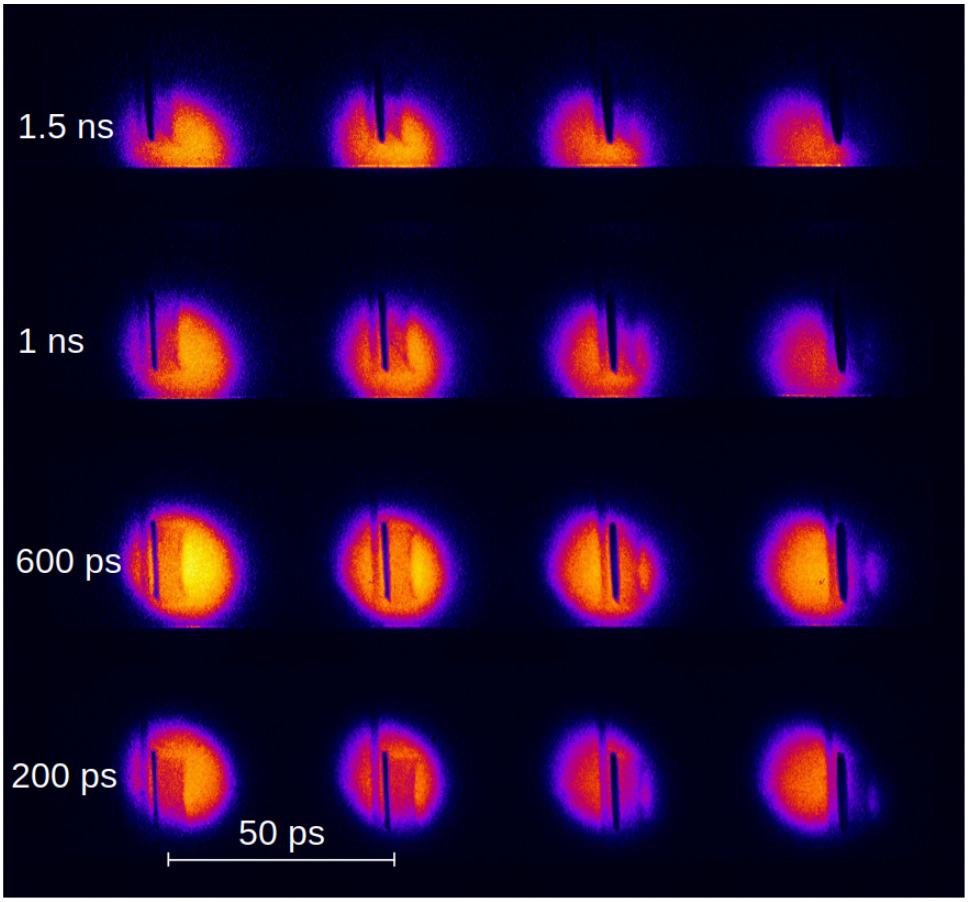

Figure 3.23: Array of 2-D radiographs captured at various times by the XRFC for shot #28410. Between each image on the line there are + 50 ps.

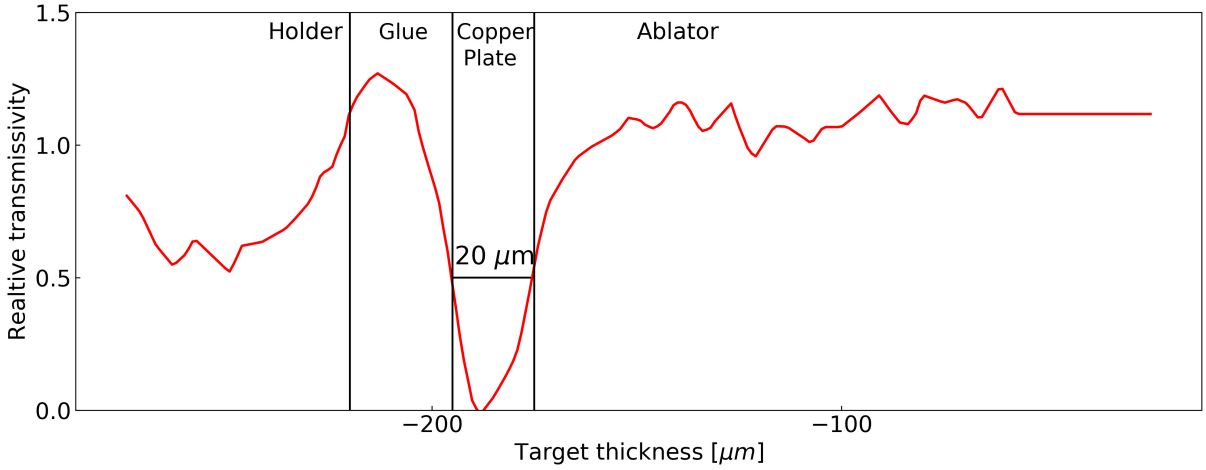

Figure 3.24: Transmissivity profile on the cylinder axis extracted from the radiography at 200 ps for shot #28410. The position of ablator, copper plate, glue and holder are indicated in the figure. The thickness of the copper is measured by the FWHM of the transmissivity profile.

the simulations in which hot electrons follow temporally the SABS signal, since the simulations considering the RAB signal predicted a similar copper thickness. As can be seen

f_e			
	T_h [keV]	η [%]	$N_e[10^{16}]$
$f_{e1}(E)$	32	10	5
$f_{e2}(E)$	37	7	3
$f_{e3}(E)$	43	5	2

Table 3.5: Parameters of Maxwellian functions $f_e(E)$ obtained from the post-process of BMXS and ZNVH for the shot #28410, used as input in CHIC.

from Fig. 3.25, experimentally at 600 ps the copper plate does not show any expansion, while at 1000 ps it is 30 $\pm$3 μm thick (i.e. with an expansion of 10 μm). Unfortunately, the simulations at 1000 ps predicted an expansion of only 2 μm (either considering the SABS or the RAB signal for the temporal generation of hot electrons). It is not clear whether this disagreement comes from issues in the hydrodynamic code or due to some parallax in the experimental radiography. Having at disposal only one shot, we do not have sufficient statistics to draw a conclusion.

Considering the shot 28415, the low contrast of the 1D radiography does not allow to locate correctly the shock position (Fig. 3.26).

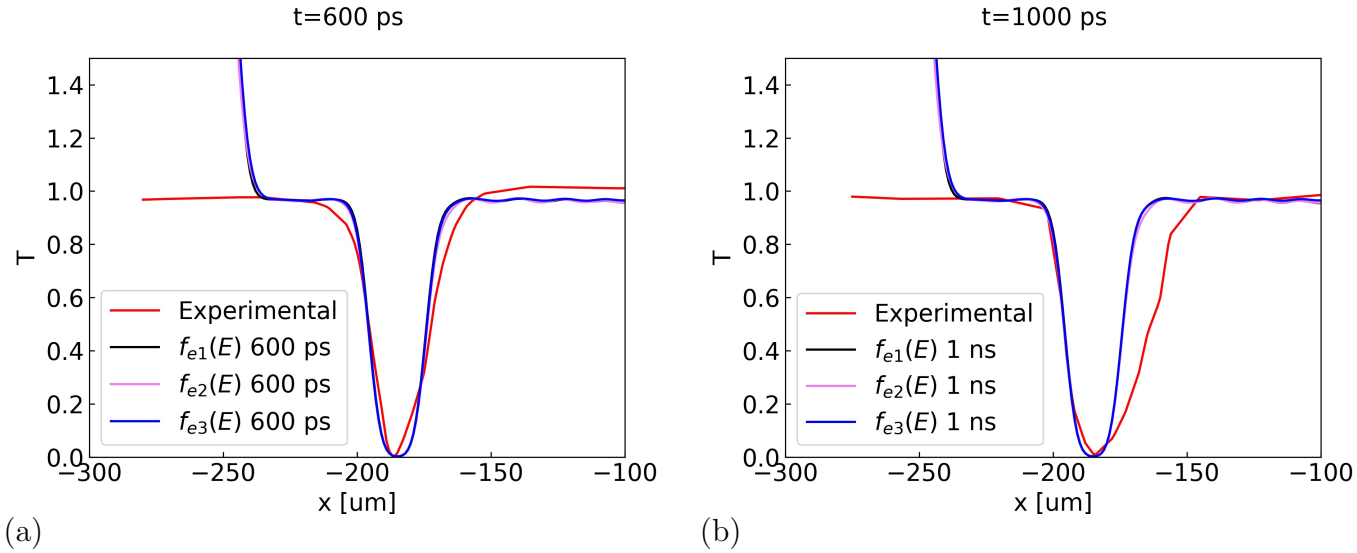

(a) (b)

Figure 3.25: Transmissivity profiles taken along the cylinder axis at (a) 600 ps and (b) 1000 ps. The red curve indicates the experimental transmissivity, while the black, the violet and the blue curves are the synthetic signals from CHIC, considering the scheme of the three representative points as done for the one beam case. The three electron distribution functions are listed in Tab. 3.5, and they correspond to the ones in the graph 3.11 (b).

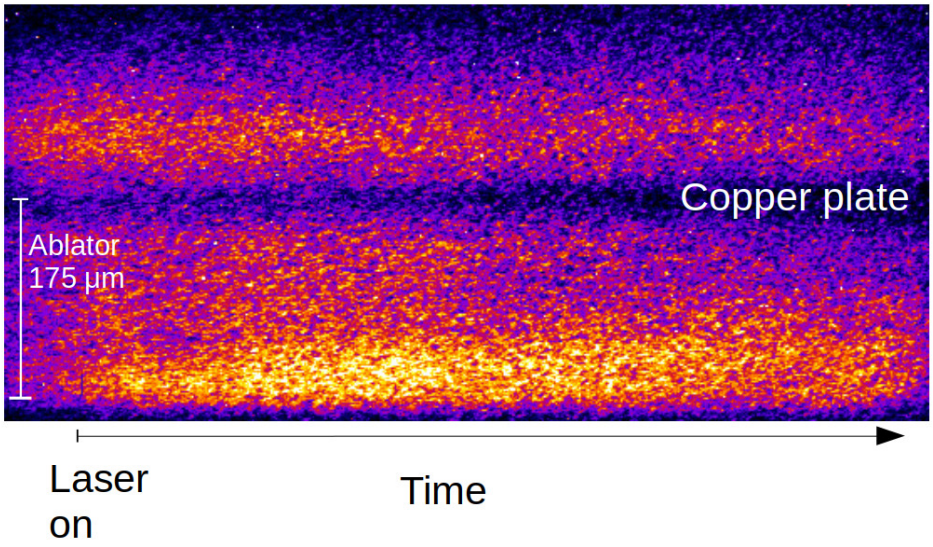

Figure 3.26: Experimental time resolved 1D radiography in the shot #28415. Time is on the x axis. Laser impinges from the bottom. The shock front is not visible.

3.1.4 Influence of hot electrons on the hydrodynamic

We now analyse the simulation results that match the experimental data for the single beam case. As explained in the previous section, the laser pulse used as input in the simulations follows temporally the experimental pulse, after a correction taking into account the SBS reflection. The SBS fraction was calculated performing LPSE simulations considering hydrodynamic profiles extracted by an initial CHIC simulation at different times (see Sec. 3.1.3). The SBS removed power corresponds to ∼20% of the total power. Hot electrons are generated at $0.14n_c$ following the temporal profile of the backscatterd light measured by the SABS instrument. Hot electron beams are energetically described by exponential distributions characterized by $T_h = 26$ keV and conversion efficiency with respect to the laser energy of $\eta \simeq 11\%$. We consider that an equal fraction of scattered light through SRS occurs, so an additional 11% of light at $0.14n_c$ is backscattered and subtracted from the laser. The RAB fraction computed by the code is only the 0.33%, while the collisional absorption is around ∼58%. In the simulation, electrons propagate according to straight lines, with an initial divergence of the beam of 22°. The hot electron beam widens during the propagation according to angular scattering. A simulation without hot electrons is also presented and, for this case, the fraction of collisional absorption computed by the code is ∼95% (after the subtraction of the SBS part).

Plasma Parameters

The $n_c/4$ density-scale length rises up to 150 μm in the first 0.8 ns, while the $n_c/4$ coronal electronic temperature reaches $\sim$ 2.1 keV in the first 0.6 ns, as shown in Fig. 3.27. Considering the temporal evolution of these parameters, the intensity threshold for SRS [77] and TPD [200] are exceeded after $\sim$ 200 ps, i.e. almost at the beginning of the drive laser pulse.

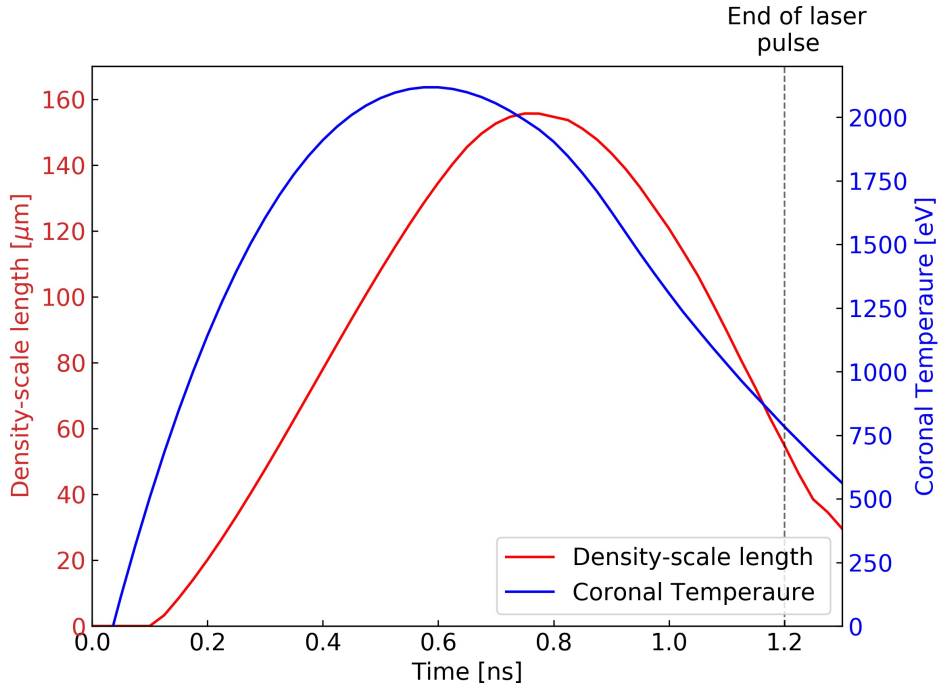

Figure 3.27: Evolution in time of the density-scale length and coronal electronic temperature computed at $n_c/4$. The time interval considered corresponds to the time of SRS activity observed in the SABS.

Shock characteristics

Fig. 3.28 shows the temporal progression of different hydrodynamic quantities around the shock front. Results from simulations with and without hot electrons are presented. The ablation pressure reaches a maximum of 100 MBar at 0.3 ns for the two cases, regardless of the presence of the hot electron beam. These values are four times less compared to the value of ∼400 MBar predicted by the scaling laws $p_{\mathrm{abl}} \propto \lambda^{-2/3} I_a^{2/3}$, observed for laser intensities of $10^{15}\mathrm{W/cm}^2$ [12]. This mismatch is due to the fact that the scaling law considers 1-D collisional laser absorption without parametric instabilities and non-thermal electrons. Despite this, these values of ablation pressure do not dramatically differ from the values obtained in other planar configurations experiments conducted at lower laser intensity[183], [174].

Considering that 175 μm of cold plastic stops electrons up to 100 keV, it is possible to estimate that 98% of electrons in the experiment are stopped in the ablator. This increases the electronic temperature and pressure reached by the ablator upstream of the shock, 9 eV and 11 MBar, respectively. The value of temperature is evaluated 50 μm upstream of the shock and the value of pressure is calculated considering the minimum around the shock front. The position of the shock front is computed considering the maximum of the derivative of the logarithm of the pressure. The downstream pressure reaches a maximum of 150 MBar, 25 MBar more than without hot electrons. The downstream pressure is calculated considering the maximum pressure after the shock front. The increase of the downstream pressure, driven by the presence of electrons, is beneficial for the SI scheme. The shock strength, which is the ratio between the downstream and the upstream pressures at the shock front, decreases dramatically from ∼700 for the case

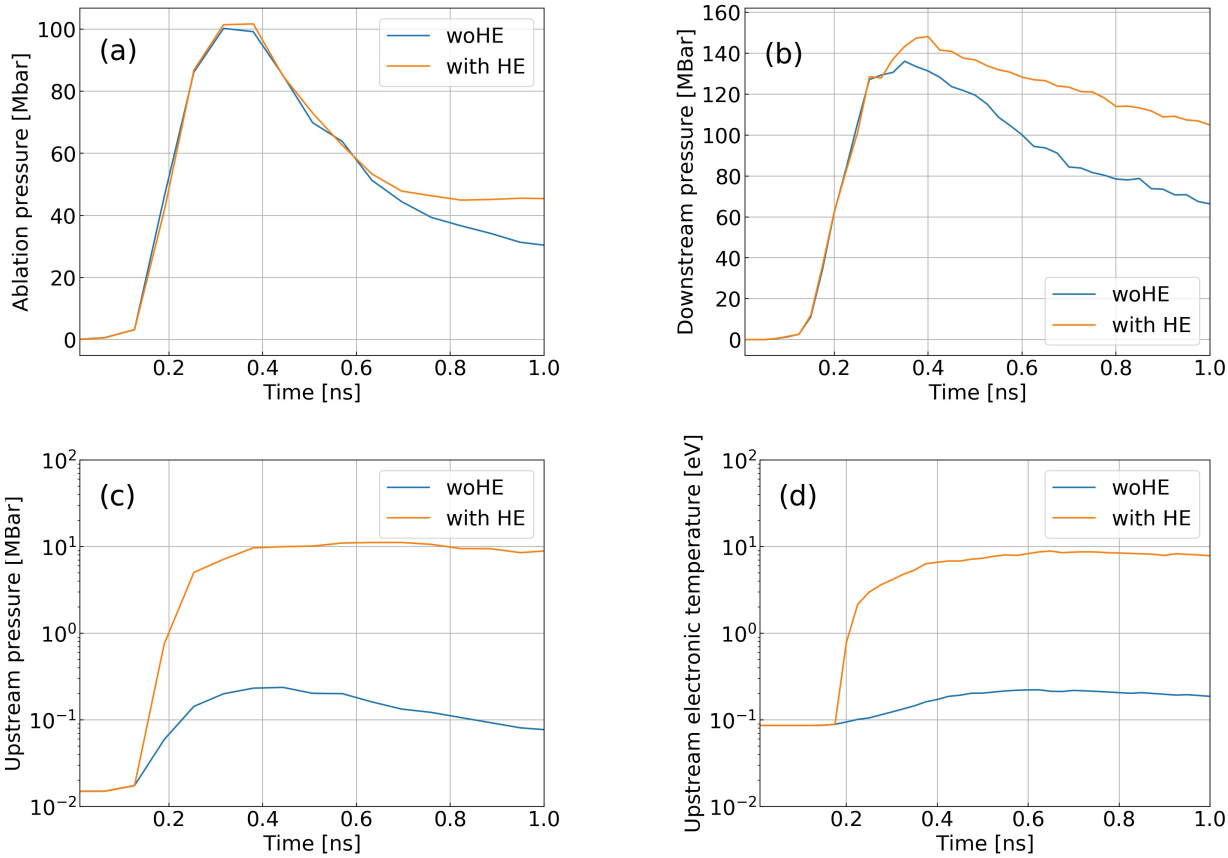

Figure 3.28: Evolution in time of hydrodynamic quantities around the shock position resulting from CHIC simulations. The simulation with hot electrons (orange) and without hot electrons (blue) are reported. (a) Ablation pressure; (b) downstream pressure; (c) upstream pressure; (d) upstream electronic temperature. Hot electrons are described by a Maxwellian function with T_h=26 keV and laser to hot electron conversion efficiency $\eta \sim 11\%$.

without hot electrons to ∼20 for the simulations with hot electrons. The shock velocity in presence of hot electrons increases from 100 km/s to 130 km/s.

3.1.5 Summary of the OMEGA-EP experiment

We reported, in this section, the analysis of an OMEGA experimental campaign aimed at characterizing the hot electrons and their influence in the shock dynamics, for interaction regimes relevant to SI. Despite the smaller density scale lengths and plasma coronal temperatures reached in this experiment, the laser intensity was of the same order of magnitude of the SI spike (I∼10^{16} W/cm^2).

The hot electron source was characterized in terms of Maxwellian temperature T_h and laser to hot electron energy conversion efficiency η using data from different x-ray spectrometers, specifically bremsstrahlung and K_α spectrometers. A post-processing methodology of the data coming from these diagnostics is presented, explaining in detail the numerical methods and the used procedure. In particular, the post processing of the bremsstrahlung spectrometer (BMXS) requires a first MC simulation in which the diag-

nostic response to monochromatic photon beams is computed. The photon distribution function detected by the diagnostic is then reconstructed by means of the reduced chi-square method (formula [3.2]). The figure of merit $\chi^2 \to 1$ allows to determine an ensemble of solutions which correspond to possible photon distribution functions detected by the instrument. The predicted energy deposition through the IPs by these photon distribution functions is consistent with the experimental measurements and their error (see Fig. 3.6).

To find the hot electron temperature T_h and intensity (related to the conversion efficiency η), Geant4 simulations of electron transport in targets are performed, aiming at reproducing the bremsstrahlung spectra and the K_α signal detected by the diagnostics. Here we explained in detail how these simulations are set up, showing that the initial geometric electron beam configuration does not affect the final result. The interval of T_h indicated by the spectrometers ranges from 20 up to 45 keV, with an energy conversion efficiency that goes from 13% down to 3%. These data are used as input in hydrodynamic simulations in order to reproduce the shock propagation and the Cu layer expansion observed in the radiographs. In this regard, hydrodynamic simulations suggested that an electron distribution function with temperature T_h=27±8 keV and conversion efficiency $\eta = 10 \pm 4\%$ better describes the problem.

Similar hot electron temperatures, but lower conversion efficiencies were observed in a recent OMEGA experiment [176]. Here the irradiation conditions were similar to our case: an UV laser beam with intensities around $\sim 10^{16}$ W/cm^2 was tightly focused on planar multilayer targets. In this case, the pulse was preceded by a pre-compression beam generating a pre-plasma with scale length of 380 μm and coronal temperature around 1.8 keV. The measured hot electron temperature and conversion efficiency were 27 keV and 1$\sim$ %, respectively. This low value of conversion efficiency may be related to the influence of a longer plasma-scale lengths on the LPI. Low hot electron temperatures of $\sim$ 30 keV are also reported in spherical configuration experiments [178] [32]. In this case, 40 of the 60 OMEGA beams were used to compress D2 filled plastic shells. The remaining 20 spike beams were delayed and tightly focused onto shell to deliver a late shock. The intensity of the single spike beam was several 10^{15} W/cm^2, interacting with a plasma characterized by L_n $\sim$170 μm and T_e $\sim$2 keV (see Tab. 2.5) . As such, we can observe that, in this particular regime, the hot electron temperature does not strongly depend on laser intensity.

In the last part of Sec, 3.1.4, we presented a brief discussion of the influence of hot electrons on the shock dynamics. In particular, the shock pressure increases because of the presence of the hot electrons, with beneficial effects on the SI scheme. Conversely, since hot electrons heat up the upstream region of the shock, the shock strength falls dramatically with detrimental effects for the scheme. We report, in the next chapters, a numerical study on the influence that hot electrons with these characteristics have on the shell adiabat of a typical SI implosion configuration.

3.2 Preliminary results from the PALS experiment on hot electrons characterization, in condition relevant to Shock Ignition.

We report on the preliminary results of an experimental campaign conducted at the PALS laser facility, aimed at characterizing the hot electrons and the shock dynamics for laser conditions relevant to the SI approach. As specified in Chapt. 2, the PALS laser system can provide a laser beam with an intensity that can reach values around 10^{16} W/cm^2, i.e. the same order of magnitude of the SI spike. In this experiment, targets were irradiated with the first harmonic 1ω ($\lambda = 1315$ nm) by a 300 ps FWHM Gaussian beam. The laser intensity was around 2×10^{16} W/cm^2, for a total laser energy of 700 J. As shown in Chapt. 1 and 2, in this condition the laser light is absorbed mainly by resonant effects which prevail over the bremsstrahlung absorption, generating a copious amount of hot electrons. The experiment aimed at studying the hot electron generation and their influence on the shock propagation. As shown in Chapt. 2, these electrons can contribute to the shock formation if they are at moderate kinetic energy, opening the possibility of using an IR laser beam for SI.

3.2.1 Experimental setup

Planar multilayer targets were irradiated by the 1ω ($\lambda = 1315$ nm) PALS laser beam with intensity around 1-2 $\times$ 10^{16} W/cm^2. Phase plates were used to obtain Gaussian spots with $\sim$100 μm diameter. The temporal pulse shape was a Gaussian function with FWHM around 300 ps and the total laser energy was $\sim$ 600 J. Measurements [164] show that about half of this energy arrives on targets. The pulse shape as a function of time is reported in Fig. 3.29 (f). Targets were 2x2 mm^2 planar multilayer foils composed of different ablators. The experiment aimed at studying how the hot electron conversion efficiency and temperature are affected by the ablator composition. In this regard, targets were composed by 20 μm ablators of different materials, as shown in Fig. 3.29. These were followed by a Polypropylene transport layer of 50 μm, a copper tracer of 10 μm and a final plastic layer of 20 μm, to avoid hot electron recirculation in the tracer. On the front side (where the laser impinges), all targets had an Aluminium flash protection of 41 nm deposited over the ablation layer. CHIC simulations (not presented in this work) predict a quarter critical plasma density scale length of $\sim$110 μm at 500 ps for all the targets. The quarter critical coronal temperatures are 2.9 keV for the target with plastic ablator, 3 keV in the case of Al ablator, 4.3 keV in the case of Ti ablator and 4.8 keV for Ni and C ablators.

The SRS and TPD backscattered emission were measured by using a near infrared spectrometer and an optical streak camera was used to perform time-resolved spectroscopy. The time evolution of hot electron generation was measured by detecting the time-resolved copper K_α emission using a X-ray streak camera with a suitable time fiducial. Furthermore, the CELIA bremsstrahlung spectrometer (see Sec. 2.3.2) detected the bremsstrahlung radiation generated by the propagation of the hot electrons in the target. The spectrometer was placed at 45° from the target normal, on the front side of the target (where laser impinges). The distance from TCC was of 0.22 m. Let us specify that the 11 cm lead collimator (see Fig. 2.8) was not used in this experiment. Measures of Shock Breakout time were performed to study the shock dynamics.

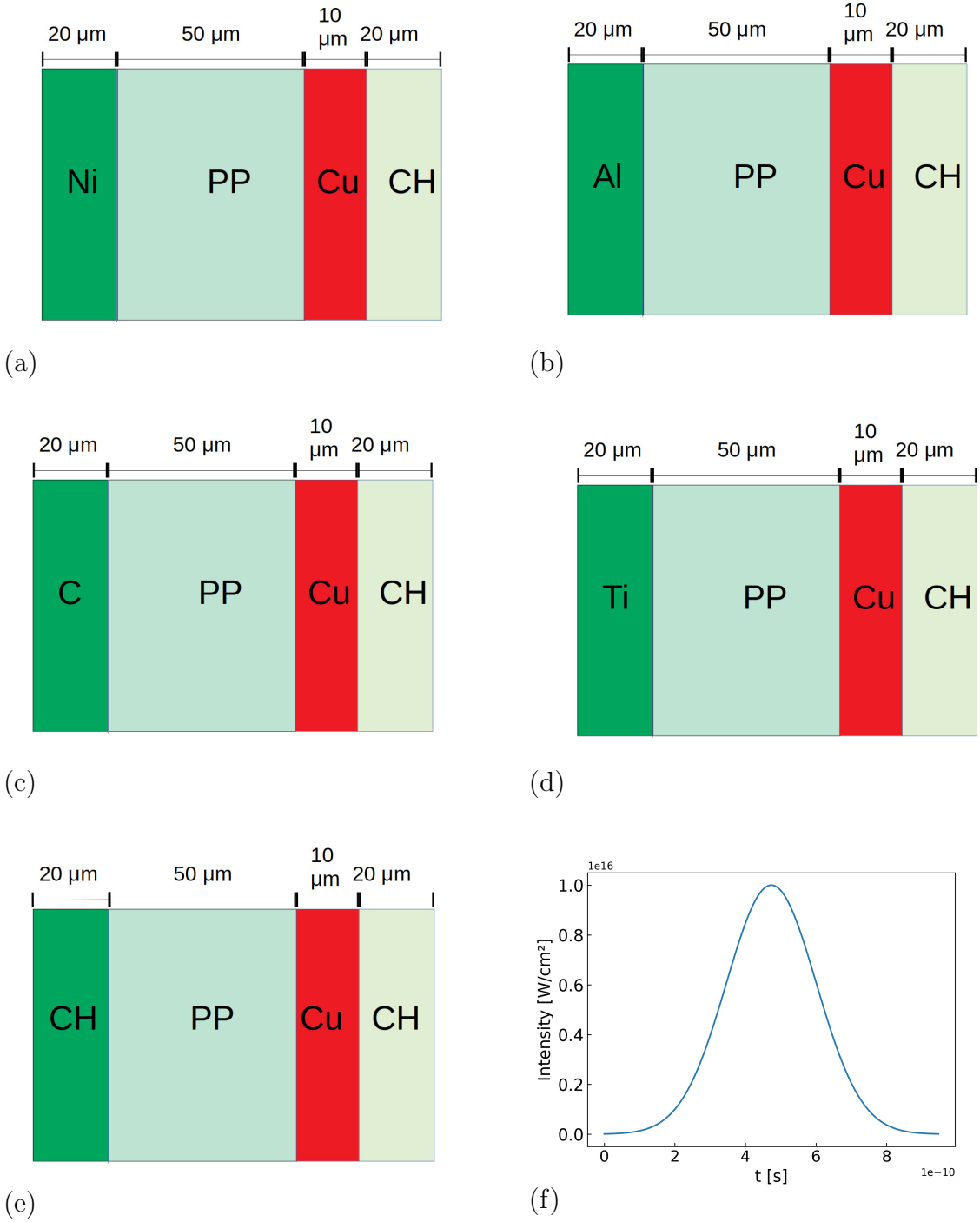

Figure 3.29: Composition of the planar multilayer targets used in the experimental campaign at PALS. Five different types of targets were used, composed of 20 μm ablators of (a) Ni, (b) Al, (c) C, (d) Ti and (e) CH. The ablator was followed by a Polypropylene transport layer (50 μm), a copper tracer (10 μm) and a final plastic layer of 20 μm to avoid hot electron recirculation in the tracer. (f) Laser intensity as a function of time. The temporal pulse shape was a Gaussian with a FWHM of 300 ps. In figures (a) to (e), the laser is incident on targets from the left.

3.2.2 Preliminary results from the CELIA Bremsstrahlung spectrometer

The experimental data of this experiment are being currently analysed. We report, in this section, the preliminary results coming from the post-processing of the CELIA bremsstrahlung spectrometer. As reported in Sec. 2.3.2, the CELIA spectrometer is composed by a stack of filters and IPs interleaved, encapsulated in a led case to reduce the background signal coming from the chamber fluorescence. The signal released through the IPS for the shot #55175 (CH ablator target) is shown in Fig. 3.30. Considering all the shots, a significant signal up to the seventh or the eighth IP was detected. The signal value in the first IP was around 10 - 11 PSL, below the saturation level of the scanner.

Similarly to what was done for the OMEGA experiment (Sec. 3.1.2), the diagnostic response is simulated by using the Geant4 MC code and the deposited energy in each IP per number of photon is calculated considering 72 x-ray monochromatic beams. The energy range covered by the simulations goes from 10 keV up to 10 MeV and in each simulation we launch 10^6 photons. This high number of particles is adequate to obtain a reduced statistical noise. In reality, for our purposes, it is redundant to calculate the response curves considering photons energies up to 10 MeV. As done for OMEGA, an upper limit of 1 MeV is sufficient. The simulations are performed considering four different electromagnetic physics libraries contained in Geant4 MC code: Penelope [194], Livermore [195], electromagnetic standard opt3 and electromagnetic standard opt4 [201]. As can be seen from figure 3.31, the four libraries predict the same energy deposition through the IPS, giving us more confidence on the final result.

The steps followed to post-process the experimental data are similar to what was done for the OMEGA experiment, Sec. 3.1.2. The experimental energy release through the IPS is reproduced by considering a photon distribution function of the type $f_{\mathrm{ph}}(\mathrm{A_{ph}}, \mathrm{T_{ph}}, E) = \frac{\mathrm{A_{ph}}}{E} e^{-E/\mathrm{T_{ph}}}$, and the free parameters $\mathrm{A_{ph}}$ and $\mathrm{T_{ph}}$ are retrieved by performing the chi-square analysis with the experimental data, eq. (3.2). The results for the shot #55175 are shown in Fig. 3.32. In particular, Fig. 3.32 (a) represents the map of the parameters $\mathrm{A_{ph}}$ and $\mathrm{T_{ph}}$ which satisfy the condition $\chi^2 \to 1$, while Fig. 3.32 (b) shows the energy deposition through the IPs considering the photon distribution function that minimizes the χ^2, i.e. the one with $\mathrm{T_{ph}}$ ~30 keV. As for the BMXS in OMEGA, the χ^2 function finds its minimum well below 1, and the scheme of the three representative points should

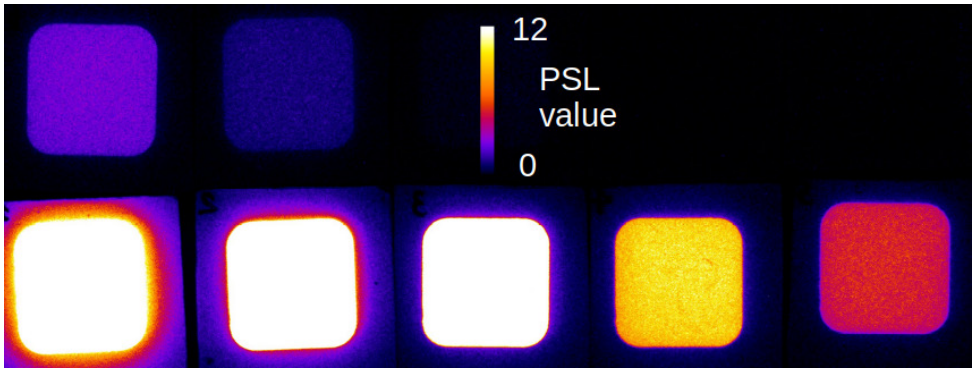

Figure 3.30: Signal in PSL values released through the IPS detected by the CELIA spectrometer for the shot #55175. In this shot, the target had a CH ablator.

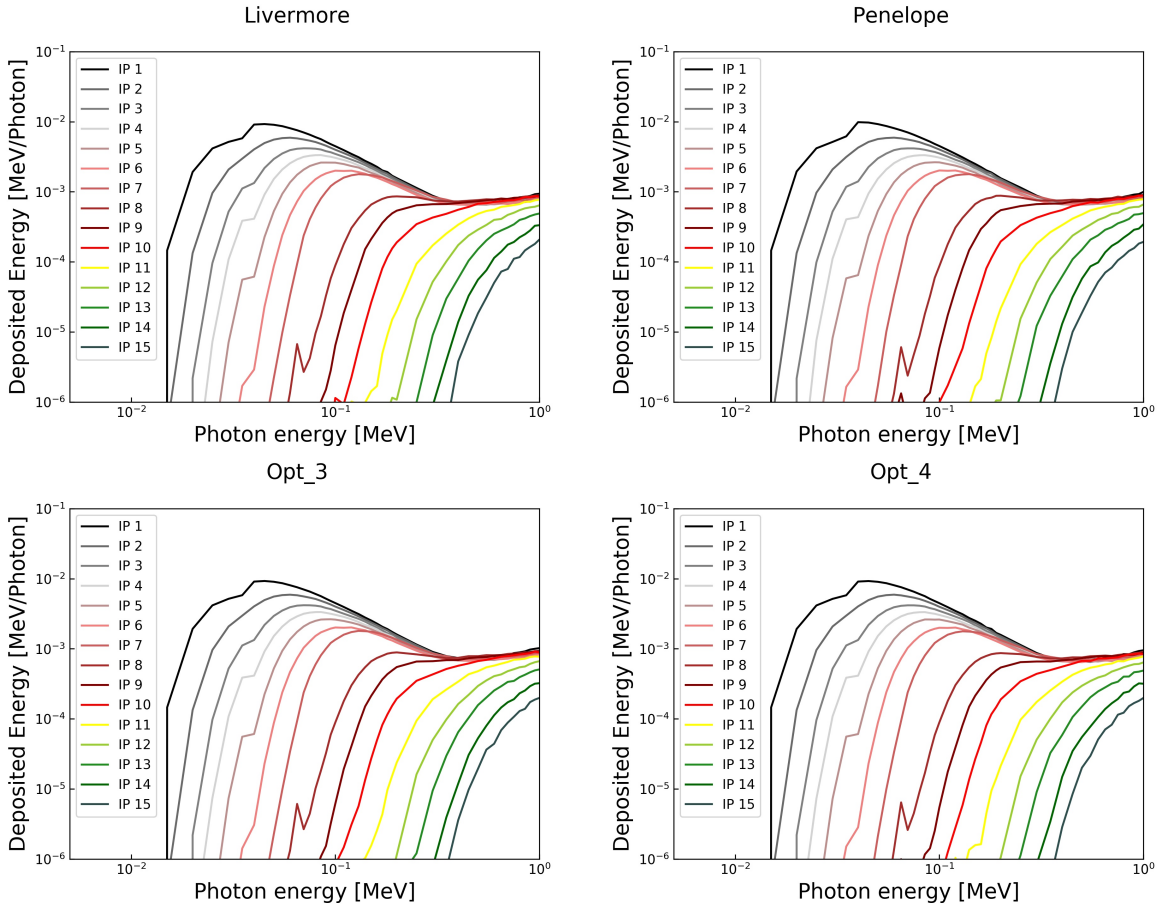

Figure 3.31: Response curves of each IP in the CELIA bremsstrahlung spectrometer calculated using four different libraries: [Upper-Left] Livermore; [Upper-Right] Penelope; [Bottom-Left] electromagnetic standard opt-3; [Bottom-Right] electromagnetic standard opt-4.

be consider also here. However, for the moment, we will consider only the points which minimize the χ^2, ($A_{ph} \sim 3 \times 10^{11}$ [ph/Sr] and $T_{ph} \sim 32$ keV for this shot).

To find the population of hot electrons that generated the bremsstrahlung spectrum detected by the spectrometer, we performed Geant4 simulations of electron propagation as already shown in Sec. 3.1.2. In these simulations, the 3D target geometry and material composition were reproduced, while the detector was simulated considering a spherical corona at the right distance and angle from the TCC (see Fig. 3.8). Let us specify that the Al layer (41 nm) placed before the ablator was not simulated, since Geant4 does not accept such small thicknesses as input. However, the fact that we neglect such thin layer, should not cause an appreciable error in the simulations. As done in Sec. 3.1.2, hot electrons are modelled energetically considering 2D Maxwellian distribution functions $f_e(N_e, T_h, E) = \frac{N_e}{T_h} e^{-E/T_h}$ with free parameters N_e and T_h. The results of these simulations are presented in Fig. 3.33, where we reported the conversion efficiency of laser energy into hot electron energy as a function of the hot electron temperature. The values are calculated considering the mean among the shots. Overall, the temperature spans in a range that goes from ∼25 up to ∼ 45 keV, with conversion efficiencies around the 1-2%. These quantities were calculated considering the real laser energy delivered on targets, around 250-300 J [164]. In particular, for the Aluminium ablator target, the hot electron

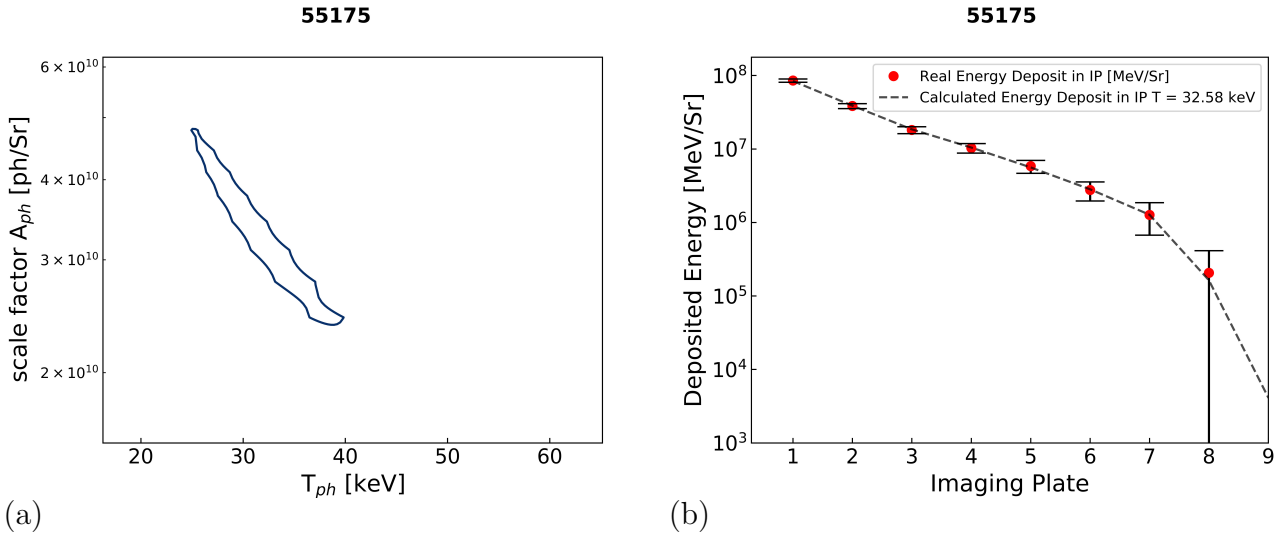

(a) (b)

Figure 3.32: (a) Contours of parameters A_{ph} and T_{ph} leading to a reduced χ^2 of 1 in the post processing of data from the CELIA bremsstrahlung spectrometer, for shot #55175. (b) Experimental deposited energy in the IPs (red dots) and theoretical energy deposition expected considering the f_{ph} that minimizes the chi-square (dashed lines), for the shot #55175.

temperature goes from 25 up to 35 keV, while for carbon, titanium and plastic ablator targets the temperature is slightly higher (up to 45 keV). These differences could be due to the different plasma conditions created by the laser interacting with different ablators (including different EPW and IAW damping rate). This effect is currently under inves-

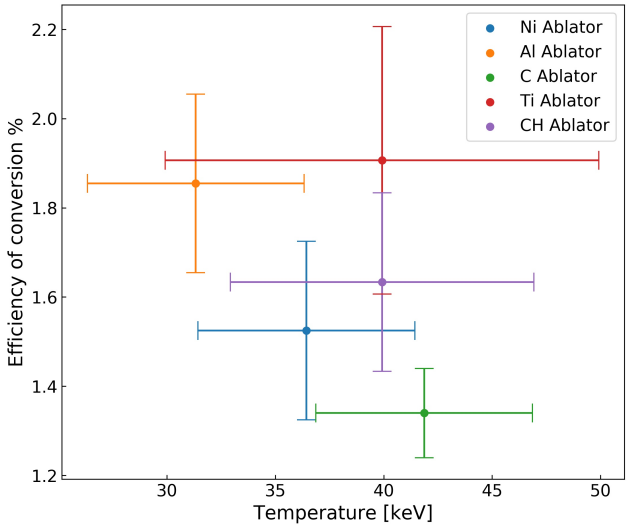

Figure 3.33: Conversion efficiencies of laser energy into hot electron energy as a function of the hot electron temperature that reproduce the experimental bremsstrahlung spectra detected by the CELIA spectrometer. The values are retrieved by performing Geant4 simulations of hot electron propagation in targets. Results for the four target types are reported.

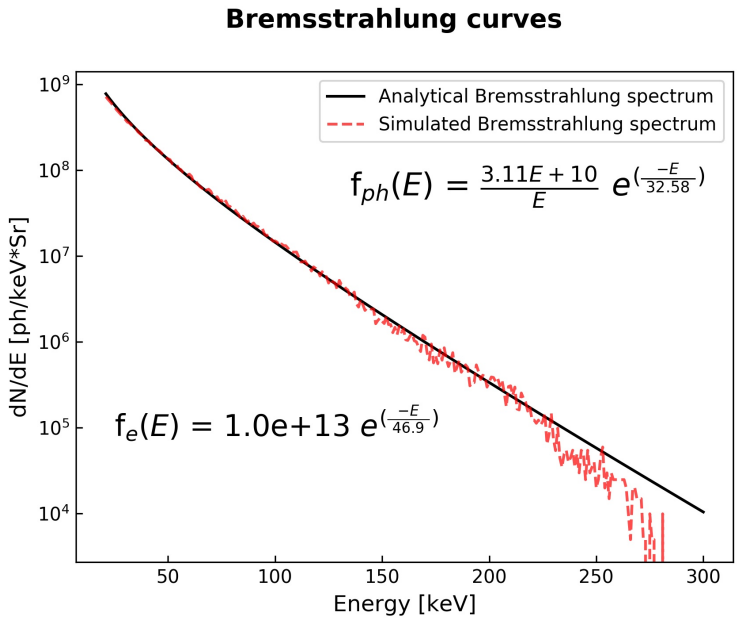

Figure 3.34: Comparison of the bremsstrahlung spectra $f_{\mathrm{ph}}(E)$ in black and simulated one resulting from $f_{\mathrm{e}}(E)$ reported in the figure. The bremsstrahlung spectra comes from the post-processing of the CELIA bremsstrahlung spectrometer for the shot #55175. The laser to hot electrons energy conversion efficiency is ∼1.4% for the curve $f_{\mathrm{e}}(E)$.

tigation by means of CHIC simulations [37] and a post processing of the SRS and TPD signal is being done to evaluate the contribution of the different phenomena to the hot electron generation. Let us also mention that, in this particular configuration, the photon distribution function generated on the bremsstrahlung spectrometer by a 2D Mawellian electron distribution function corresponds to $f_{\mathrm{ph}}(\mathrm{A_{ph}}, \mathrm{T_{ph}}, E) = \frac{\mathrm{A_{ph}}}{E} e^{-E/\mathrm{T_{ph}}}$, similarly to the OMEGA experiment, Sec. 3.1.2. This is shown in Fig. 3.34 for the shot #55175.

3.2.3 Conclusion

We reported, in this section, the preliminarily results of an experiment conducted at PALS aimed at characterizing the hot electrons and their influence on shock dynamics, in condition relevant to SI. Despite the lower density scale lengths and plasma coronal temperatures reached in this experiment, the used laser intensity was of the same order of magnitude of the SI spike (I∼10^{16} W/cm^2).

Hot electrons were characterized in terms of Maxwellian temperature and laser to hot electron energy conversion efficiency η using the CELIA bremsstrahlung spectrometer. Following the same methodology presented in the analysis of the OMEGA experiment (see Sec. 3.1), the diagnostic response is simulated using Geant4 and the photon distribution function detected by the instrument is retrieved using the chi-squared analysis. Overall, we can observe a hot electron temperature that ranges from 20 up to 45 keV and conversion efficiencies around ∼ 1-2%. The hot electron temperatures found in this experiment are similar to the ones obtained in other 1ω experiments [165] [166] (reported in Tab. 2.3 of Chap. 2.4.1), but our conversion efficiencies are lower, despite the irradiation condition being similar. The origin of this mismatch should be due to the fact that we considered only the photon distribution function that minimizes the chi-square,

while as shown in the OMEGA analysis (Sec. 3.1.2), one should consider the a system of degenerate solutions and then constrain the problem.

Considering the influence of the ablator on the hot electron generation, lower values of hot electron temperature are found for the Al and the Ni targets, compared to the CH and C cases. This is consistent with recent experimental and theoretical studies reported in the literature [36] [177], even if these were conducted in spherical geometry and considering an irradiation wavelength of 351 nm.

The origin of this hot electron population is being investigated by comparing the backscattered light spectra with the temporally resolved K_α signal. This will give some information about the predominant mechanism among RAB, SRS and TPD in the generation of hot electrons. Furthermore, the influence of the hot electrons on the shock dynamics will be evaluated using CHIC [37]. Finally, LPSE simulations could be conducted to evaluate the influence of different ablators on the hot electron generation.

3.3 Preliminarily results from the LMJ-Petal experiment on hot electrons characterization, in condition relevant to Shock Ignition

We report, in this section, the preliminary results of an experiment conducted at the LMJ-PETAL facility aimed at characterizing hot electrons and the shock propagation in laser condition relevant to the SI approach to ICF. Contrary to the experiments presented in Sec. 3.1 and 3.2, LMJ allows to achieve plasma scale lengths and coronal temperatures characteristic of SI, thanks to the possibility of using a long pulse profile. As such, the hot electron features observed in this experiment should be similar to the ones present in SI, with some differences due to the high value of the laser beam incidence angle.

The experiment is currently being analysed and its preliminarily results can be found in Ref. [202]. Here we report on the post-processing of the bremsstrahlung spectrometer data, retrieving the intensity and the temperature of the hot electrons emitted in two shots.

3.3.1 Experimental setup

The experiment was conducted in planar geometry and three LMJ UV beams were used to deliver a total energy of 20 kJ on the target. The focal spot of each beam was Gaussian with a radius around 300 μm. The pulse consisted in a 3 ns pre-compression beam, aimed at producing a long scale length plasma, followed by a high-intensity spike of 1.3 ns. Because of the high incidence angle of the beams ($\sim 50^\circ$), the overlapped intensity of the spike reached 2×10^{15} W/cm^2. The temporal evolution of the beam power is shown in Fig. 3.35 (a). For the shots presented in this work, the laser beams were not equipped by Smoothing by Spectral Dispersion (SSD) phase plates.

According to CHIC simulations [37], the quarter critical coronal temperature reached the value of 1.7 keV at the end of the pre-pulse (3.2 ns) and a peak of 4.5 keV during the main pulse, at 4.3 ns. The quarter critical density scale lengths were 390 μm at the end

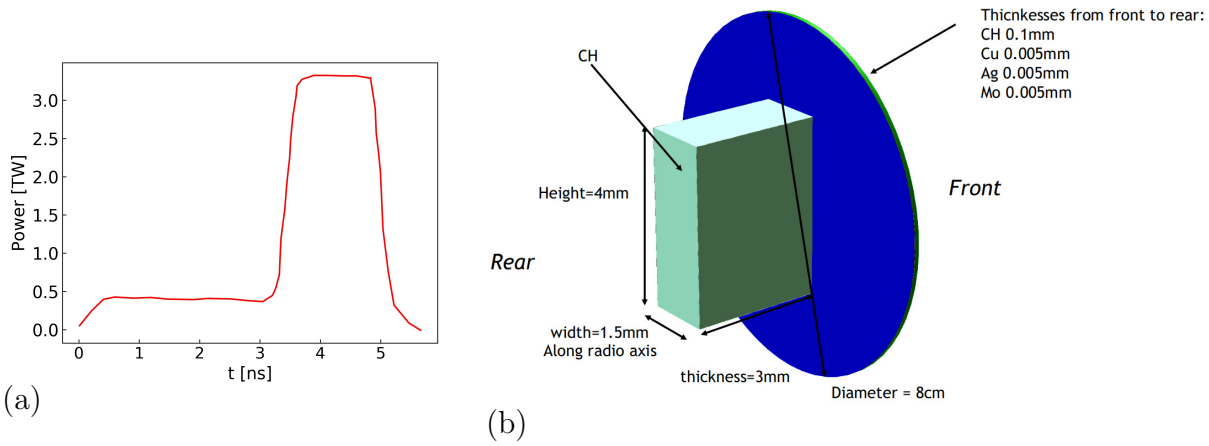

Figure 3.35: (a) Laser power as a function of time used in the experiment. A low intensity pre-compression beam of 3 ns is followed by a high intensity spike of 1.3 ns. (b) Target configuration used in the experiment. The laser impinges on the front side of the target. The Au shield is not reported in the figure.

of the pre-pulse and 480 μm during the spike pulse.

Targets were made of a plastic ablator disk 100 μm thick, followed by three 5 μm thick disks made of copper, silver and molybdenum, respectively. These were used as hot electron tracers. The disk diameter was 8 cm, and they were followed by a 3 mm plastic (CH) parallelepiped to diagnose the shock propagation. Finally, an Au shield was placed around the disks to prevent x-ray spectrometers from strong emission of the coronal plasma. The target configuration is reported in Fig. 3.35 (b).

A Full Aperture Backscattered Station (FABS) detected the backscattered light measuring with two different spectrometers the SRS and the SBS signal, with a temporal resolution of 100 ps [203]. The hot electron population was characterized using two x-rays spectrometers: SPECTIX [204] and CRACC-X [143]. SPECTIX is a k-alpha spectrometer used to detect the k-shell radiation emitted by the passage of hot electrons in the tracers. CRACC-X is a bremsstrahlung spectrometer consisting of a stack of filters and IP interleaved, similar to the ones used at OMEGA and at PALS. Finally, shock radiography was performed by coupling a hard X-ray imager to a framing camera (GXI) [205]. The backlighter source used for this purpose was a Fe foil irradiated by two supplementary beams.

3.3.2 Preliminary results from the CRACC-X spectrometer

The experiment is currently being analysed (at the moment of writing), and we report on the post-processing of the Bremsstrahlung spectrometer CRACC-X. As reported in Ref. [143], CRACC-X is a x-ray spectrometer composed by a stack of 25 disk-shaped IPs alternated by filters of different materials and thicknesses. As the BMXS (Sec. 3.1.2) and the CELIA spectrometers (Sec. 3.2), it detects and deconvolutes the bremsstrahlung spectrum emitted by the passage of hot electrons in target. The filter configuration is shown in Tab. 3.6. The instrument was located in the equatorial plane at 58° from the shock propagation axis, and its distance from the TCC was 22 cm. The stack was divided

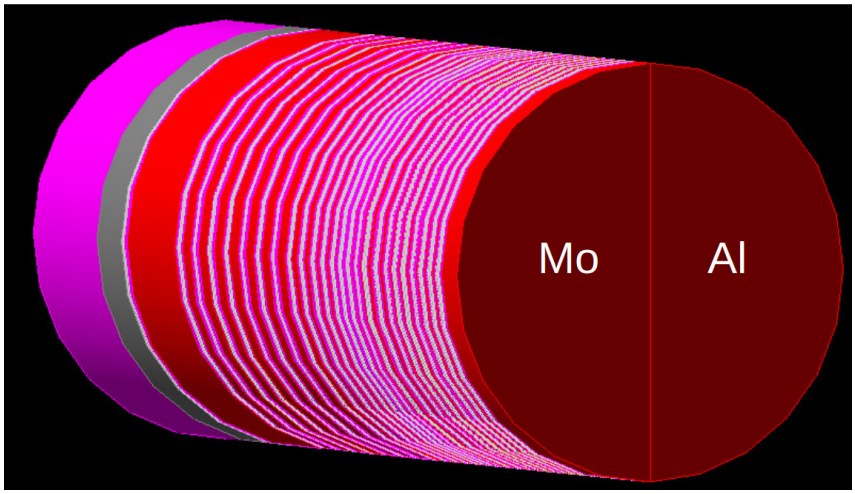

Figure 3.36: Schematic representation of the stack of filters and IPs adopted in CRACC-X. Two half circle filters (Al and Mo 2 mm thick) are used at the entrance of the stack to widen the dynamic range of the diagnostic. In this way, the spectrometer response is split into two channels. Filters are coloured in red, while the sensitive part of the IP is indicated in light-grey.

Filter	Material	Thickness [mm]	Filter	Material	Thickness [mm]	Filter	Material	Thickness [mm]
1	Al/Mo	2.0/2.0	10	Ta	0.100	19	Pb	1
2	Al	0.09	11	Ta	0.100	20	Pb	1
3	Ti	0.125	12	Au	0.250	21	Pb	1
4	Fe	0.125	13	Au	0.250	22	Pb	1
5	Cu	0.100	14	Pb	0.250	23	Pb	1
6	Mo	0.100	15	Pb	0.250	24	Pb	1
7	Ag	0.150	16	Pb	0.500	25	Pb	6
8	Ag	0.300	17	Pb	0.500			
9	Ag	0.300	18	Pb	1			

Table 3.6: Material and thicknesses of the filters used in the CRACC-X stack. The x-ray radiation impinges on the Al/Mo filter.

Figure 3.37: Signal in PSL values released through the IPS detected by the CRACC-X spectrometer in shot #1.

into two channels by placing two different half circle filters at the entrance. One consisting of 2 mm Al (Al filter channel) and the other of 2 mm Mo (Mo filter channel), as shown by the schematic representation of the stack in Fig. 3.36. These two thick filters prevent photons with energy less than ∼15 keV from entering the stack. The effect of these two different filtering can be seen in the energy deposition through the IPs in Fig. 3.37: the

brighter half circle represents the signal released in the Al channel, while the other half is the signal released in the Mo channel. Either for the Al and the Mo channel, we had a signal up to the tenth - eleventh IP, for the two shots reported. The background signal is $\sim 1\%$ of the signal of the tenth-eleventh IP, and it does not influence the measure. Because of the proximity of the instrument to the TCC and because of the high radiation fluxes generated by the laser-plasma interaction, the signal in the first five IPs of the Al channel was saturated, achieving a maximum value of ∼135 PSL. It was necessary to scan the IPs eleven times to obtain a non saturated level of signal (i.e. < 135 PSL) in the first IP. The real value of signal in the first five IPs was reconstructed considering the simple proportion:

$$\mathrm{PSL}(k)_{\mathrm{real}} = \frac{\mathrm{PSL}(j)_{\text{first scan}}}{\mathrm{PSL}(j)_{\text{last scan}}} \mathrm{PSL}(k)_{\text{last scan}}, \tag{3.5}$$

where $\mathrm{PSL}(k)$ is the signal in the k-th saturated IP and $\mathrm{PSL}(j)$ the signal in the j-th not saturated IP. Usually j is chosen considering the first not saturated IP. "Last scan" refers to a scan in which the signal in the k-th IP was not saturated. Conversely, the signal in the Mo channel was not saturated, and the maximum value in the first IP was around $\sim$ 13 PSL. This is the same order of magnitude of the signal obtained in the OMEGA (Sec. 3.1) and in the PALS (Sec. 3.2) experiments.

To reconstruct the photon distribution function detected by the diagnostic, we proceed as done in the previous sections. The spectrometer is first simulated with Geant4 [193] and the response curves are calculated. In particular, here we divided the IPs into two half circles (corresponding to the two channels) and the energy deposition per photon in each half IP is calculated considering 45 monochromatic photon beams. The response curves for the two channels are shown in Fig. 3.38. After that, the experimental energy release through the IPS is reproduced by considering a photon distribution function of the type $f_{\mathrm{ph}}(\mathrm{A_{ph}}, \mathrm{T_{ph}}, E) = \frac{\mathrm{A_{ph}}}{E} e^{-E/\mathrm{T_{ph}}}$, and the free parameters $\mathrm{A_{ph}}$ and $\mathrm{T_{ph}}$ are retreived

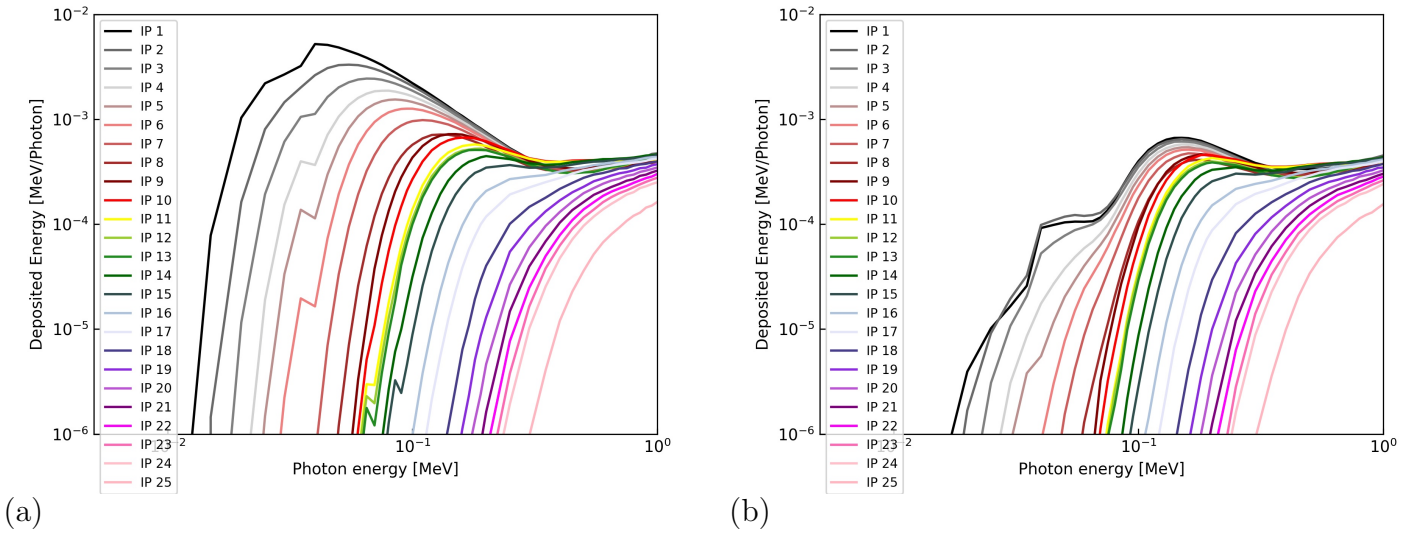

(a) (b)

Figure 3.38: Response curves of each IP in the CRACC-X spectrometer, calculated using Geant4 MC code [193] with the library Penelope [194]. (a) Response curves of the Al channel; (b) Response curves of the Mo channel.

Al channel Shot 1		
Distribution Function	Scale Factor [ph/Sr]	T_{ph} [keV]
$f_{ph} = {}^{N_{ph}}/_{T_{ph}} e^{-E/T_{ph}}$	$N_{ph} = 2.6 \times 10^{13}$	16
$f_{ph} = {}^{A_{ph}}/_{E} e^{-E/T_{ph}}$	$A_{ph} = 2.6 \times 10^{13}$	25

Table 3.7: Values of the parameters N_{ph} (A_{ph}) and T_{ph} coming from the minimization of the chi-square considering the two photon distribution functions $f_{ph} = {}^{N_{ph}}/_{T_{ph}} e^{-E/T_{ph}}$ and $f_{ph} = {}^{A_{ph}}/_{E} e^{-E/T_{ph}}$. Let us notice that N_{ph} represents the number of photon per steradian that reached the diagnostic, while A_{ph} is related to this quantity through a normalization constant. As such, the number of photon per steradian predicted by the minimization procedure, considering the function $f_{ph} = {}^{A_{ph}}/_{E} e^{-E/T_{ph}}$, is around $\sim 9 \times 10^{12}$ ph/sr. Data refer to shot 1, Al channel of the CRACC-X.

by performing the chi-square analysis with the experimental values (eq. (3.2)) (As shown in Sec. 3.1.2). In this case, a 2D Maxwellian photon distribution function of the type $f_{ph}(N_{ph}, T_{ph}, E) = \frac{N_{ph}}{T_{ph}} e^{-E/T_{ph}}$ was also used.

The results for the Al channel are shown in Fig. 3.39 and in Tab. 3.7 for the shot 1. From the analysis, the χ^2 function presents a minimum much greater than 1. In particular, the minima are around 390 and 270 for the two cases $f_{ph} = {}^{N_{ph}}/_{T_{ph}} e^{-E/T_{ph}}$ and $f_{ph} = {}^{A_{ph}}/_{E} e^{-E/T_{ph}}$, respectively. According to common statistics references [206] [207], such high values of χ^2 imply that the found distributions are unlikely to be correct. These high values of the chi-square could come from the fact that these single-temperature photon distribution functions fail in fitting the signal of deeper IPs. As shown in Fig. 3.39, the predicted energy deposition in the IPs 8-11 is lower compared to the experimental values. A two-temperature photon distribution function could solve this issue and further

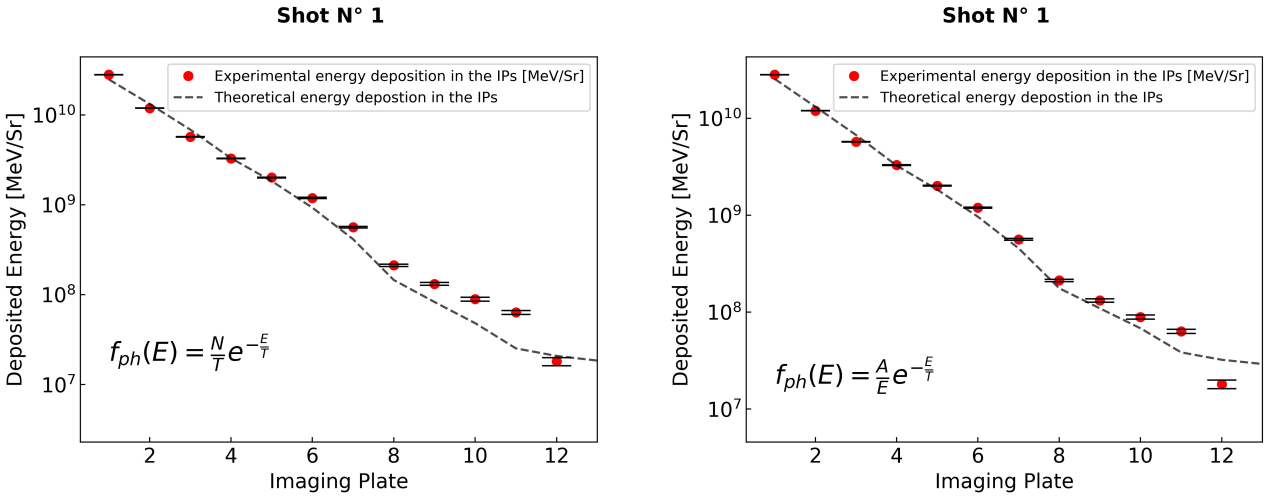

Figure 3.39: [Left] Experimental (red dots) and theoretical (dashed line) energy deposition through the IPs in the Al channel, computed considering the function $f_{ph} = {}^{N_{ph}}/_{T_{ph}} e^{-E/T_{ph}}$ in which the values of the parameters N_{ph} and T_{ph} are taken from Tab. 3.7. [Right] Experimental (red dots) and theoretical (dashed line) energy deposition through the IPs in the Al channel, computed considering the function $f_{ph} = {}^{A_{ph}}/_{E} e^{-E/T_{ph}}$ in which the values of the parameters A_{ph} and T_{ph} are indicated in Tab. 3.7

Mo channel Shot 1		
Distribution Function	Scale Factor [ph/Sr]	T_{ph} [keV]
$f_{ph} = {}^{N_{ph}}/_{T_{ph}} e^{-E/T_{ph}}$	$N_{ph} = 3.5 \times 10^{12}$	26
$f_{ph} = {}^{A_{ph}}/_{E} e^{-E/T_{ph}}$	$A_{ph} = 4.7 \times 10^{12}$	35

Table 3.8: Values of the parameters N_{ph} (A_{ph}) and T_{ph} coming from the minimization of the chi-square considering the two photon distribution functions $f_{ph} = {}^{N_{ph}}/_{T_{ph}} e^{-E/T_{ph}}$ and $f_{ph} = {}^{A_{ph}}/_{E} e^{-E/T_{ph}}$. Let us notice that N_{ph} represents the number of photon per steradian that reached the diagnostic, while A_{ph} is related to this quantity through a normalization constant. As such, the number of photon per steradian predicted by the minimization procedure considering the function $f_{ph} = {}^{A_{ph}}/_{E} e^{-E/T_{ph}}$ is around $\sim 1.5 \times 10^{12}$ ph/sr. Data refer to shot 1, Mo channel of the CRACC-X.

investigation is required. In this thesis, we will consider only single-temperature photon distribution functions. Given this, the number of photon per steradian that reached the instrument predicted by the chi-square analysis are 2.6×10^{13} ph/sr for the case $f_{ph} = {}^{N_{ph}}/_{T_{ph}} e^{-E/T_{ph}}$ and 9×10^{12} ph/sr for the $f_{ph} = {}^{A_{ph}}/_{E} e^{-E/T_{ph}}$ (let as notice that N_{ph} represents the number of photon per steradian, while A_{ph} is related to this quantity through a normalization constant).

Considering now the Mo channel, the results are presented in Tab. 3.8 and in Fig. 3.40. In the fitting process, the first IP was discarded because of the strong diffused light from the Al part. As can be seen from the figures, in this case the chi-square analysis offers more reliable results, having the χ^2 function reached minimum around 1.6-2 in the two cases. The photon number per steradian is 3.5 and 1.5×10^{12} ph/sr for the two cases, respectively, one order of magnitude less compared to what predicted using the Al channel. The photon temperatures go from 26 keV for the function $f_{ph} = {}^{N_{ph}}/_{T_{ph}} e^{-E/T_{ph}}$ up to 35 keV for $f_{ph} = {}^{A_{ph}}/_{E} e^{-E/T_{ph}}$.

Considering the shot #2, the results from the Mo channel are shown in Fig. 3.41. Here the χ^2 function finds its minimum at values less than one ($\sim$0.088 for $f_{ph} = {}^{N_{ph}}/_{T_{ph}} e^{-E/T_{ph}}$ and $\sim$0.064 for $f_{ph} = {}^{A_{ph}}/_{E} e^{-E/T_{ph}}$). The contour for the parameters N_{ph} (A_{ph}) T_{ph} that satisfies the condition $\chi^2 \to 1$ is shown in the two right graphs of Fig. 3.41. Here we report also the scheme of the three representative points, as done in the analysis of the OMEGA experiment. We thus consider three possible photon distribution functions detected by the diagnostic: f_{ph1}, f_{ph2} and f_{ph3} as reported by the figure. This is done both for $f_{ph} = {}^{N_{ph}}/_{T_{ph}} e^{-E/T_{ph}}$ and $f_{ph} = {}^{A_{ph}}/_{E} e^{-E/T_{ph}}$.

Proceeding as done in the analysis of OMEGA and PALS experiments, we performed Geant4 simulations in order to find the characteristics of the hot electron beam that generated these bremsstrahlung spectra on the instrument. In particular, we consider electrons energetically described by a 2D Maxwellian distribution function $f_e(E) = {}^{N_e}/_{T_h} e^{-E/T_h}$, with free parameters N_e and T_h. In the simulations, the real target geometry is reproduced, while the detector is simulated considering a circular corona placed at the right angle and distance from the TCC (see Fig. 3.8). As done in the analysis of OMEGA experiment, we calculate the parameters N_e and T_h considering the three possible photon distribution functions detected by the diagnostic. We rely only on the data coming

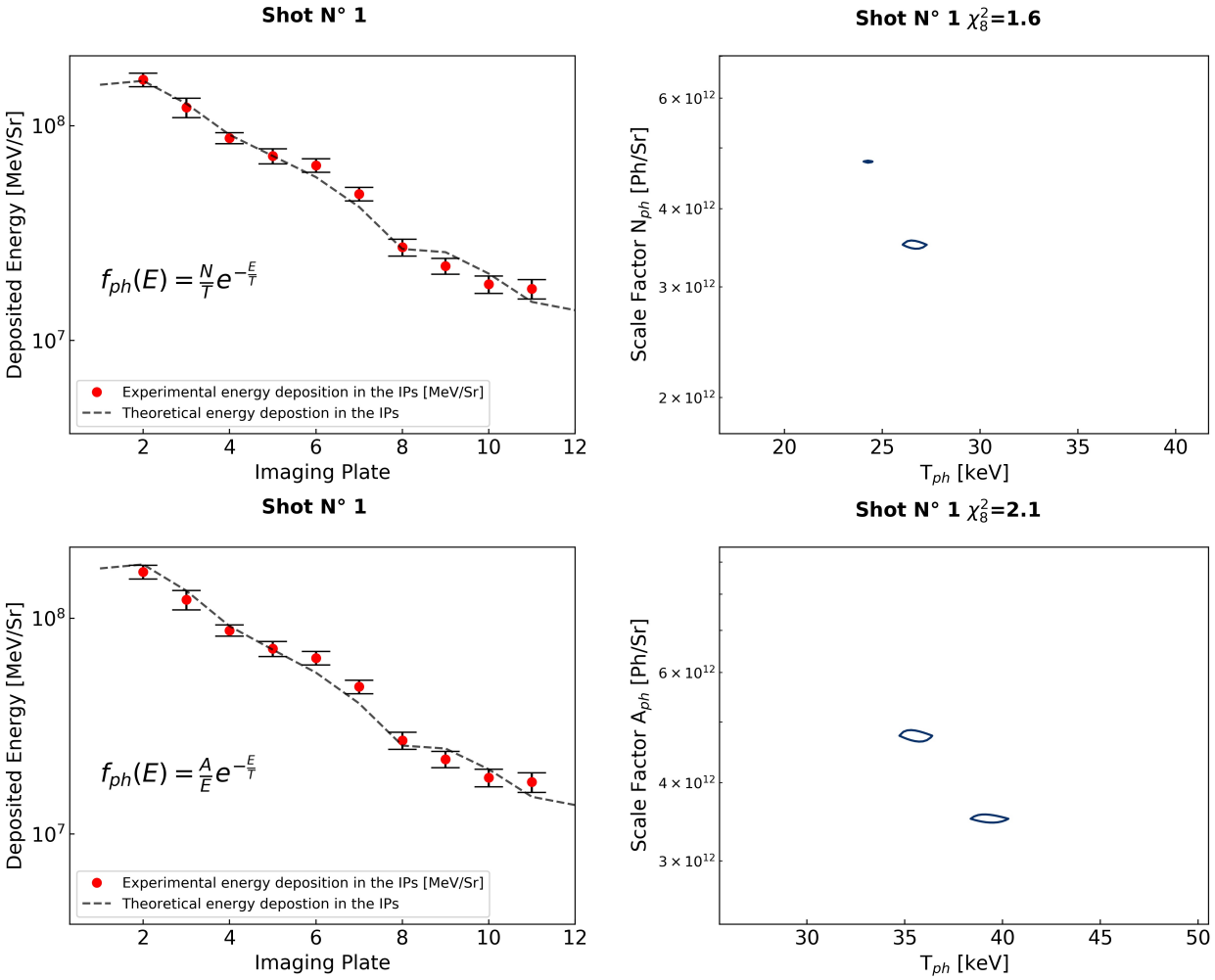

Figure 3.40: [Top-left] Experimental (red dots) and theoretical (dashed line) energy deposition through the IPs in the Mo channel considering the function $f_{\mathrm{ph}} = {}^{\mathrm{N_{ph}}}/_{\mathrm{T_{ph}}} e^{-E/\mathrm{T_{ph}}}$. The values of the parameters $\mathrm{N_{ph}}$ and $\mathrm{T_{ph}}$ are indicated in Tab. 3.8. [Top-right] Couple of parameters $\mathrm{N_{ph}}$ and $\mathrm{T_{ph}}$ that minimizes the chi-square. The minimum of the χ^2 is around ∼1.6 and the subscript 8 indicates the number of degrees of freedom. [Bottom-left] Experimental (red dots) and theoretical (dashed line) energy deposition through the IPs in the Mo channel considering the function $f_{\mathrm{ph}} = {}^{\mathrm{A_{ph}}}/_{\mathrm{E}} e^{-E/\mathrm{T_{ph}}}$. The values of the parameters $\mathrm{A_{ph}}$ and $\mathrm{T_{ph}}$ are indicated in Tab. 3.8.[Bottom-right] Couple of parameters $\mathrm{A_{ph}}$ and $\mathrm{T_{ph}}$ that minimizes the chi-square. The minimum of the χ^2 is around ∼2.1 and the subscript 8 indicates the number of degrees of freedom.

from the Mo channel, since the Al channel presented too high values of the χ^2 function in the minimization. Furthermore, we consider both the photon distribution functions $f_{\mathrm{ph}} = {}^{\mathrm{N_{ph}}}/_{\mathrm{T_{ph}}} e^{-E/\mathrm{T_{ph}}}$ and $f_{\mathrm{ph}} = {}^{\mathrm{A_{ph}}}/_{\mathrm{E}} e^{-E/\mathrm{T_{ph}}}$. The results are reported in Tab. 3.9 and Tab. 3.10 for the first and the second case, respectively, for the shot #2. As can be seen from these tables, the photon distribution functions at lower temperatures and higher number of photon per steradian (f_{ph1}) require an elevated conversion efficiencies of laser energy into hot electron energy (58 and 28%). These values are not consistent with the values commonly found in the literature and are clearly incorrect. Also the conversion efficiency predicted using the function f_{e2} of Tab. 3.9 reaches value which may be unrealistic. Note that, if one considers the photon distribution function retrieved by the Al

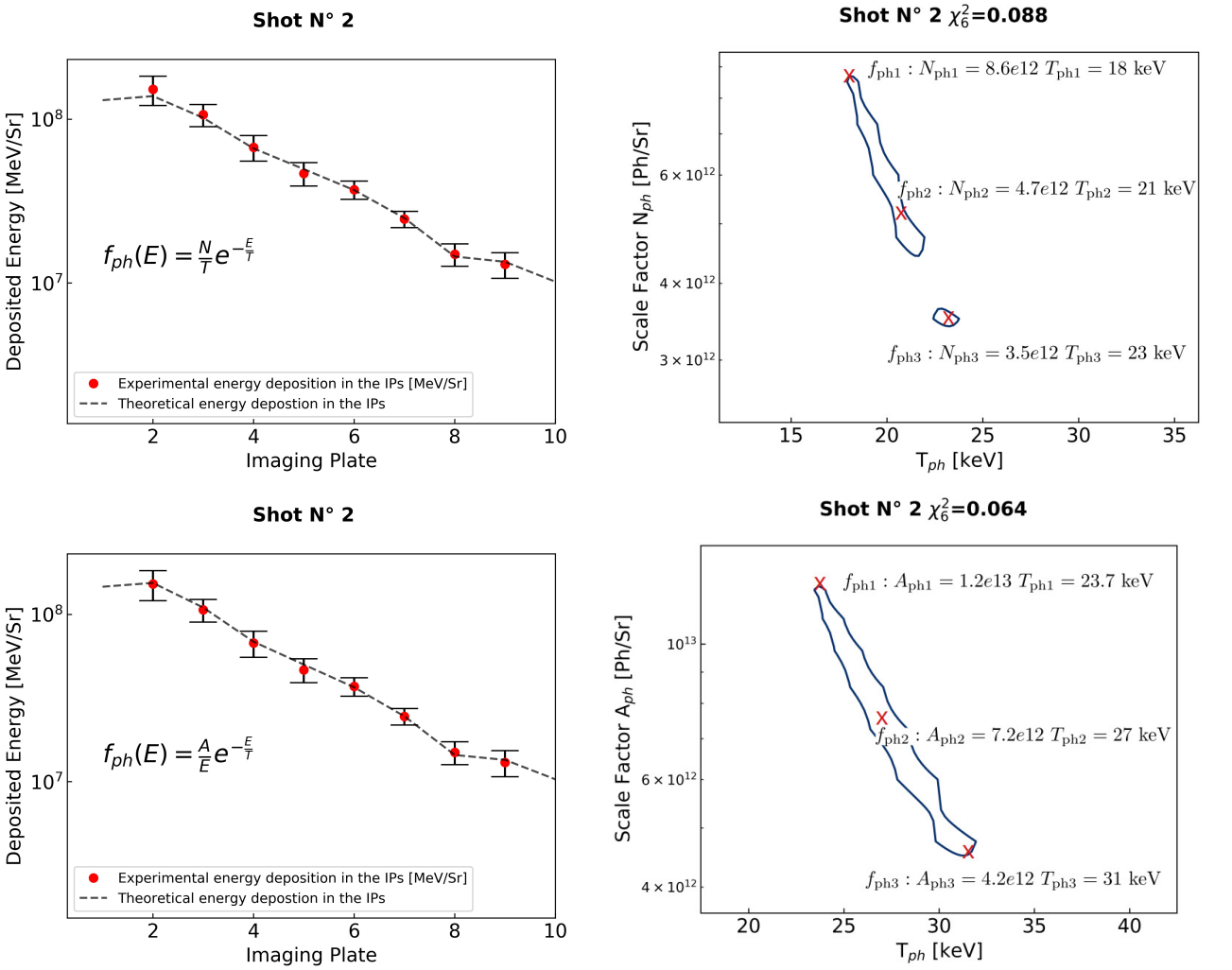

Figure 3.41: [Top-left] Experimental (red dots) and theoretical (dashed line) energy deposition through the IPs in the Mo channel considering the function $f_{\mathrm{ph}} = {}^{\mathrm{N_{ph}}}/_{\mathrm{T_{ph}}} e^{-E/\mathrm{T_{ph}}}$ which minimizes the chi-square (i.e. f_{ph2} indicated in the [Top-Right] figure). [Top-right] Couple of parameters $\mathrm{N_{ph}}$ and $\mathrm{T_{ph}}$ that satisfies the condition $\chi^2 \to 1$. The minimum of the χ^2 is around ∼0.088 and the subscript 6 indicates the number of degrees of freedom. [Bottom-left] Experimental (red dots) and theoretical (dashed line) energy deposition through the IPs in the Mo channel considering the function $f_{\mathrm{ph}} = {}^{\mathrm{A_{ph}}}/_{\mathrm{E}} e^{-E/\mathrm{T_{ph}}}$ which minimizes the chi-square (i.e. f_{ph2} indicated in the [Bottom-Right] figure). [Bottom-right] Couple of parameters $\mathrm{A_{ph}}$ and $\mathrm{T_{ph}}$ that satisfies the condition $\chi^2 \to 1$. The minimum of the χ^2 is around ∼0.064 and the subscript 6 indicates the number of degrees of freedom.

channel, even higher conversion efficiency (over the 100%) are found. This is because the number of photons and the temperature retrieved ($\mathrm{N_{ph}} \sim 2 \times 10^{13}$ ph/sr, $\mathrm{T_{ph}} \sim 26$ keV) from the diagnostic post processing are higher compared to what is obtained in the Mo channel. This is further confirmation of the unreliability of the data coming from the Al channel.

The bremsstrahlung spectra f_{ph3} and the computed bremsstrahlung spectra generated by the electron distribution function f_{e3} on the diagnostic are shown in Fig. 3.42. In particular, Fig. 3.42 (a) shows the functions $f_{\mathrm{ph3}} = {}^{\mathrm{N_{ph3}}}/_{\mathrm{T_{ph3}}} e^{-E/\mathrm{T_{ph3}}}$ and the bremsstrahlung

$f_e \rightarrow f_{\mathrm{ph}} = {}^{N_{\mathrm{ph}}}/_{T_{\mathrm{ph}}} e^{-E/T_{\mathrm{ph}}}$			
	$f_{e1} \rightarrow f_{\mathrm{ph1}}$	$f_{e2} \rightarrow f_{\mathrm{ph2}}$	$f_{e3} \rightarrow f_{\mathrm{ph3}}$
N_e	$4.2{\times}10^{18}$	$1{\times}10^{18}$	$4.2{\times}10^{17}$
$\mathrm{T_h}$ [keV]	16	20	23
η [%]	58	17.6	8.05

Table 3.9: Coefficients $\mathrm{N_e}$ and $\mathrm{T_h}$ of the electron distribution functions $f_{\mathrm{e}}(E)$ that generate the three $f_{\mathrm{ph}} = {}^{\mathrm{N_{ph}}}/_{\mathrm{T_{ph}}} e^{-E/\mathrm{T_{ph}}}$ detected by the Mo channel of the CRACC-X spectrometer for shot #2. η is the conversion efficiency of laser energy into hot electron energy.

$f_e \rightarrow f_{\mathrm{ph}} = {}^{A_{\mathrm{ph}}}/_{E} e^{-E/T_{\mathrm{ph}}}$			
	$f_{e1} \rightarrow f_{\mathrm{ph1}}$	$f_{e2} \rightarrow f_{\mathrm{ph2}}$	$f_{e3} \rightarrow f_{\mathrm{ph3}}$
N_e	$1.8{\times}10^{18}$	$3.8{\times}10^{17}$	$1.9{\times}10^{17}$
$\mathrm{T_h}$ [keV]	19	22	27
η [%]	28.5	6.38	4.27

Table 3.10: Coefficients $\mathrm{N_e}$ and $\mathrm{T_h}$ of the electron distribution functions $f_{\mathrm{e}}(E)$ that generate the three $f_{\mathrm{ph}} = {}^{\mathrm{A_{ph}}}/_{\mathrm{E}} e^{-E/\mathrm{T_{ph}}}$ detected by the Mo channel of the CRACC-X spectrometer for shot #2. η is the conversion efficiency of laser energy into hot electron energy.

spectra computed by Geant4 generated by the electron distribution function f_{e3} indicated in Tab. 3.9 (and in red the figure). Analogously, Fig. 3.42 (b) shows the functions $f_{\mathrm{ph3}} = {}^{\mathrm{A_{ph3}}}/_{\mathrm{E}} e^{-E/\mathrm{T_{ph3}}}$ and the bremsstrahlung spectra computed by Geant4 generated by the electron distribution function f_{e3} indicated in Tab. 3.10 (and in red in the same figure). As it can be observed, in this particular target configuration, the photon distribution function produced on the diagnostic by a 2D electron Maxwellian distribution function is most likely a 2D Maxwellian photon distribution function (i.e. $f_{\mathrm{ph}} = {}^{\mathrm{N_{ph}}}/_{\mathrm{T_{ph}}} e^{-E/\mathrm{T_{ph}}}$). This is due to the fact that photons at low energy ($\leq$ 40 keV) are reabsorbed by the thick target, that has dimensions of the order of mm. The function $f_{\mathrm{ph}} = {}^{\mathrm{N_{ph}}}/_{\mathrm{T_{ph}}} e^{-E/\mathrm{T_{ph}}}$ predicts a lower number of low energy photons compared to $f_{\mathrm{ph}} = {}^{\mathrm{A_{ph}}}/_{\mathrm{E}} e^{-E/\mathrm{T_{ph}}}$, which diverges for $E \rightarrow 0$. As such, the 2D Maxwellian photon function better matches the simulation prediction.

Overall, considering also the results from the first shot, the hot electron distributions that are the closest to the data range from a temperature of $\sim$ 23 keV with conversion efficiency of $\sim$8%, up to a temperature of 38 keV with conversion efficiency of $\sim$3%. As done for the OMEGA experiment, the problem should be constrained considering other experimental data and figures of merits.

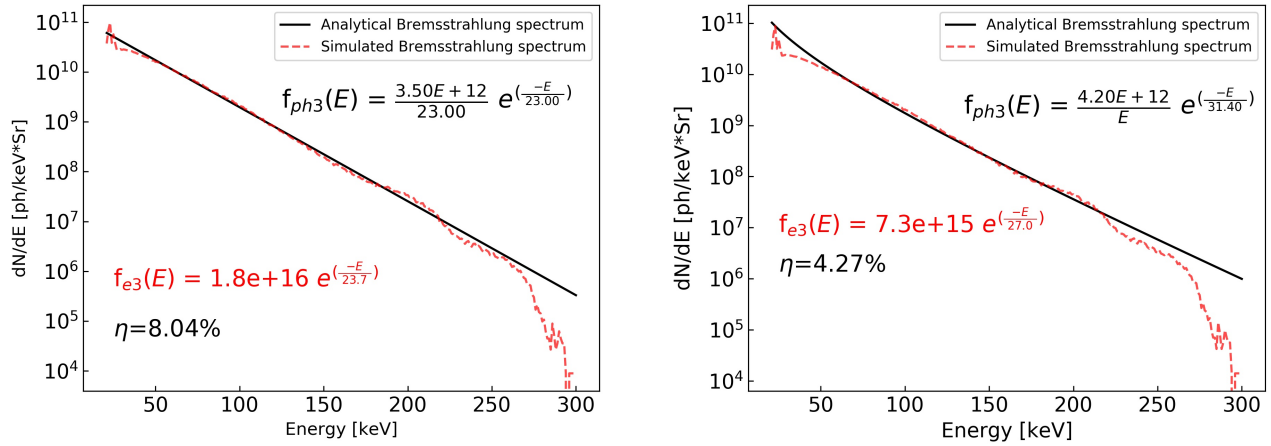

(a) (b)

Figure 3.42: (a) Comparison of the analytical form of the bremsstrahlung spectrum $f_{\mathrm{ph3}} = {}^{\mathrm{N_{ph3}}}/_{\mathrm{T_{ph3}}} e^{-E/\mathrm{T_{ph3}}}$ (black curve) with the one generated by the electron distribution function $f_{\mathrm{e3}}(E)$ reported in Tab. 3.9 (and written red in the figure), according to Geant4 (red curve). The bremsstrahlung spectrum comes from the post-processing of the Mo channel of the CRACC-X spectrometer for the shot #2. The laser to hot electron energy conversion efficiency is ∼8% for the curve $f_{\mathrm{e3}}(E)$. (b) Comparison of the analytical form of the bremsstrahlung spectrum $f_{\mathrm{ph3}} = {}^{\mathrm{A_{ph3}}}/_{\mathrm{E}} e^{-E/\mathrm{T_{ph3}}}$ (black curve) with the one generated by the electron distribution function $f_{\mathrm{e3}}(E)$ reported in Tab. 3.10 (and written red in the figure), according to Geant4 (red curve). The bremsstrahlung spectrum comes from the post-processing of the Mo channel of the CRACC-X spectrometer for the shot #2. The laser to hot electron energy conversion efficiency is ∼4% for the curve $f_{\mathrm{e3}}(E)$.

3.3.3 Summary of the LMJ experiment

We presented, in this section, the analysis of an LMJ experimental campaign aimed at characterizing hot electrons and their influence on the shock dynamics, for interaction regimes relevant to SI. Thank to the facility capabilities, planar targets were first irradiated by a long pre-compression beam, creating a plasma density scale length and a coronal temperature characteristic of SI (480 μm and 4.5 keV during the spike). The spike intensity was around $2 \times 10^{15} \mathrm{W/cm^2}$. Therefore, the hot electrons generated by this scheme should have features similar to the ones generated during a SI implosion.

Hot electrons were characterized in terms of Maxwellian temperature and laser to hot electron energy conversion efficiency η using the CRACC-X bremsstrahlung spectrometer. The experimental data were analysed following the procedure presented in Sec. 3.1.2, finding a hot electron temperature ranging from ∼ 23 up to 38 keV, with conversion efficiency going from ∼8% down to ∼3%. These values are retrieved considering the scheme of the three representative points, as done in Sec. 3.1.

Comparing these results with the ones obtained in similar interaction conditions, references [188] [189] report a planar target experiments conducted at the NIF. Here planar targets were irradiated using the 64 outers or the 32 inner beams configurations for an

overlapped intensity ranging from ∼4 up to 15 $\times 10^{14}$ W/cm^2. The $n_{c/4}$ density scale length and coronal temperature reached in these conditions were ∼500 - 700 μm and 3 - 5 keV, respectively. Hot electron temperatures of ∼40 to 60 keV with conversion efficiencies of ∼0.5% up to 5% were obtained when the laser intensity increased from 4 up to 15 $\times$ 10^{14} W/cm^2 (see Sec. 2.4.3). The temperature range obtained in this experiment is higher compared to our case, but the conversion efficiency of 5% at the laser intensity of 15 $\times$ 10^{14} W/cm^2 is similar to our findings. These values were obtained from the x-ray radiation emitted by the hot electrons propagation in targets, similarly to our procedure. However, the authors omit a detailed description of the post-processing of their diagnostics. As such, it is not clear whether they considered the degeneracy of the solutions, and thus the possibility of obtaining higher conversion efficiencies and lower temperatures. Furthermore, it is important to remark that the NIF experiment was conducted in the frame of the classical approach to ICF, i.e. using a flattop laser beam with 7.5 ns duration. On the contrary, the LMJ experiment was conducted in the SI ignition framework, i.e. considering a pre-compression beam followed by a high intensity spike of 1 ns.

Let us mention that we presented the results considering only two shots. Other shots have been performed in 2020 and they are being nowadays analysed, allowing to access better statistics.

3.4 Conclusion

In this chapter, we have presented the results of three experimental campaigns aimed at characterizing the hot electrons in condition relevant to the SI approach to ICF. These experiments were conducted in different laser facilities, allowing access to different laser-plasma conditions.

A detailed description of the x-ray spectrometer post processing was presented, describing how to retrieve a hot electron temperature T_h and number N_e. Let us mention that the figure of merit $\chi^2 \to 1$, in the bremsstrahlung spectrometer analysis, allows to find an ensemble of possible photon distribution functions detected by the diagnostic. This fact is reflected by an uncertainty on the parameters T_h and N_e (or η, the conversion efficiency of laser energy into hot electron energy). This uncertainty can be reduced exploiting information coming from other diagnostics.

In Sec. 3.1, we presented the analysis of an experiment conducted at OMEGA-EP laser facility. Here an UV laser beam with intensity around 10^{16} W/cm^2 for a 1 ns pulse duration was focused on planar multilayer targets, generating a copious amount of hot electrons and a strong shock propagating in matter. The plasma scale length and the coronal temperature reached after ∼0.7 ns were 150 μm and 2 keV, respectively. According to the spectrometer post-processing, a range of possible values for the parameter T_h and η is found (i.e. $T_h \in [20, 45]$ keV and $\eta \in [3\%, 13\%]$). These values are used as input in hydrodynamic simulations to reproduce the results obtained in radiographs, thus constraining the range for the hot electron measurements. According to this procedure, we found that the laser converts $\sim 10\% \pm 4\%$ of energy into hot electrons with $T_h = 27 \pm 8$ keV. This value of temperature is consistent with other OMEGA experiments in which a laser beam (the main driver) was tightly focused on the target, while the value of the conversion efficiency is slightly higher (in the experiments reported in Sec. 2.4.2 the con-

version efficiencies were around the 1-2%). This mismatch could be due to the fact that the experiments reported in 2.4.2 did not consider the possibility of having a degenerate solution in the bremsstrahlung spectrometer analysis. However, further experimental investigations will be required to confirm or not our findings.

In Sec. 3.2, the preliminary results of an experiment conducted at the PALS with the aim similar to the one conducted in OMEGA are presented. In this case, an IR laser beam with intensity $\sim 10^{16}$ W/cm^2 and pulse duration of 300 ps (FWHM of a Gaussian beam) was focused on planar multilayer targets composed of different ablators. The plasma scale length reached after 0.5 ns was around 110 μm and the coronal temperatures ranged from 3 up to 5 keV, according to the ablator composition. The hot electron temperature measured considering all the shots ranges from 20 up to 45 keV and the conversion efficiency is around 1-2%. The values of temperature found are consistent with the previous experimental findings at PALS, presented in Tab. 2.3, but our conversion efficiencies are lower. This mismatch cold be due to the fact that, in the bremsstrahlung spectrometer analysis, we did not consider the possibility of degenerate solutions, relying only on the photon distribution function that minimizes the chi-square. For what concerns the behaviour of the hot electrons considering different ablators, Al and Ni ablator targets present lower values T_h, compared to CH and C ablators. This is consistent with recent experimental studies [36] [177] [185] presented in Sec. 2.4.2, in which the effect of the mid-Z ablator on the hot electron production was investigated. This fact is related to different intensity threshold of SRS and TPD and to different damping mechanisms that arise in the corona because of different Z. A reduced hot electron temperature is positive for the SI scheme, though particular care should be given in choosing a high Z ablator, which can enhance the radiative preheating with deleterious effects.

In Sec. 3.3, the preliminary results of an experiment conducted at the LMJ facility are presented. LMJ allows to reach plasma scale lengths and coronal temperatures characteristic of SI thanks to the presence of a long low intensity pre-pulse. This pre-pulse had a duration of 3 ns, followed by a high intensity (2×10^{15} W/cm^2) UV spike of 1 ns. The plasma scale length and the coronal temperature reached during the spike were 480 μm and 4.5 keV, respectively. In this case, the spectrometer analysis gave $T_h \in [23-38]$ keV and $\eta \in [3\%, 8\%]$. Compared to the recent NIF experiment presented in Sec. 2.4.3, the conversion efficiencies are similar, but our temperatures are lower. It is however important to specify that our LMJ experiment was conducted in the SI framework, while the NIF experiment considered the classical ICF approach. As such, the laser intensity as a function of time was different in the two experiments.

Tab. 3.11 shows the results of the three experiments, listing also the experimental configuration and the condition achieved by the laser interaction. Let us notice that the measured hot electron temperature is similar for the three experiments: it ranges from 20 up to 45 keV, with a mean value around 30 keV. Conversely, the conversion efficiencies are similar in OMEGA and LMJ experiments (from 3 to $\sim$10%), while in PALS we obtained values around 1-2%. This difference is likely due to the different absorption mechanisms that develop in the interaction region, triggered by different laser-plasma conditions and the longer laser wavelength. A detailed discussion on the hot electron generation itself is out of the scope of the thesis work, and we prefer to not enter into details.

Facility	Target	I [W/cm^2]	λ [μm]	$L_{n_c/4}$ [μm]	T_e [keV]	T_h [keV]	η[%]
OMEGA	CH-Cu-CH	1×10^{16}	0.351	150	2	20 - 45	13 - 3
PALS	Ni-PP-Cu-CH	2×10^{16}	1.314	110	4.8	25 - 45	1.3 - 1.7
PALS	Al-PP-Cu-CH	2×10^{16}	1.314	110	3	20 - 35	1.6 - 2
PALS	C-PP-Cu-CH	2×10^{16}	1.314	110	4.8	35 - 45	1.2 - 1.4
PALS	Ti-PP-Cu-CH	2×10^{16}	1.314	110	4	30 - 50	1.6 - 2.2
PALS	CH-PP-Cu-CH	2×10^{16}	1.314	110	2.9	32 - 47	1.4 - 1.8
LMJ	CH-Cu-Ag-Mo-CH	2×10^{15}	0.351	380 - 480	1.7-4.5	23 - 38	8 - 3

Table 3.11: Summary of the relevant quantities and results of the experiments presented in the chapter. The laser facility and the target compositions are listed in the first two columns. Then the laser intensity and wavelength are reported in the third and the fourth column. The quarter critical density scale lengths and coronal temperatures reached in the experiments are reported in the columns five and six. In the last two columns we report the range of the hot electron temperature and conversion efficiency obtained. This range comes either from the degenerate solution of the chi-square analysis (OMEGA and LMJ) or from the results considering multiple shots (PALS).

In the next chapter, we report a theoretical investigation on the effects that hot electrons with such characteristics have on a typical SI implosion scheme. We also discuss the validity of using a cold target MC approach, as is done here and in the literature, to analyse the x-ray spectrometers data.

Chapter 4

A 3D Monte-Carlo method to study the transport of hot electrons in the context of Inertial Confinement Fusion

We report, in this section, a 3D Monte-Carlo (MC) method aimed at simulating the hot electron propagation in laser irradiated targets. As explained in the previous chapters, the role of hot electrons in ICF is controversial. Notably, as shown in Chap. 2, hot electrons can either preheat the inner part of the in-flight shell, compromising the compression, or they can enhance the shock pressure with beneficial effects for the implosion scheme. The studies reported in Chap. 2 were based on 1D or 2D hydrodynamic codes in which a module of hot electron propagation was included, or considering simplified analytical models to describe the hot electron effect. Over the last years, with the increase of the computational power at disposal, 3D hydrodynamic codes have been developed and, with them, the necessity of developing a 3D hot electron transport model. The possibility of performing inline 3D hydrodynamic simulations in which the hot electron generation and propagation is simulated will allow to better interpret future experiments and to propose more robust implosion schemes.

Moreover, as shown in Chap. 3, the analysis of the laser-plasma experiments aimed at characterizing hot electrons is based on cold MC methods, which do not account for the hydrodynamic evolution and the ionization state of the irradiated targets. An important step forward is thus to understand the margin of error introduced in using these cold MC codes in the interpretation of such experiments.

On this basis, we report on a 3D MC method to study the propagation of hot electrons in ionized or partially ionized fusion targets, with the aim of future implementation in hydrodynamic codes. Differently from ordinary cold MC methods, here electrons will propagate in a material which is in plasma state and whose density strongly varies in space (because of the ablation and compression wave). Notably, it will be necessary to consider appropriate scattering formulas (differential cross sections and stopping powers) and to compute correctly the mean free paths, i.e. considering the material density gradients. For what concerns the electron stopping power in plasmas, the subject has been widely studied during the last years, motivated by the interest in fast ignition concept of inertial confinement fusion [123] [208] [209]. We will report these studies, discussing critically the

regime of validity of the formulas involved. Regarding the differential cross sections, again the literature reports some models suitable in the context of fast ignition fusion [210]. In this case, hot electrons propagate in completely ionized targets colliding with free plasma electrons and with screened DT nuclei. However, the elastic scattering with the nucleus of a partially ionized atom, screened by the residual electronic structure and by other plasma particles, has not been addressed yet in the literature (at the moment of writing). As such, an analytical differential cross section suitable at describing this phenomenon is derived and proposed. Finally, also an algorithm to calculate the mean free path in density varying targets is proposed.

4.1 Introduction: general picture of Monte-Carlo methods: detailed and condensed algorithms

Monte-Carlo simulations are accurate methods to solve the problem of particle transport in matter. Considering charged particles (electrons in our case), the literature suggests two possible approaches: the *detailed* or the *condensed* methods [211] [212]. In the detailed method, all the collisions experienced by the particle are simulated. The particle history is composed of a succession of connected straight segments of free flight between each collision. Direction changes are sampled from scattering cross sections that account for the physical properties of the scattering centers. The simulated tracks can be considered as the real electron tracks. Apart from statistical uncertainties, the spatial distribution obtained coincides with the one obtained from a rigorous solution of the transport equation (eq. (1.30)). Despite the high precision of the model, detailed simulations are feasible only for a limited number of collisions, i.e. for low energy electrons (up to $\sim$ 100 keV) and for thin target geometries. Highly energetic electrons moving in thick targets will experience a large number of collisions, and the detailed algorithm becomes very inefficient.

In order to reduce the required computational time, condensed MC methods were formulated [212]. Here, the particle moves according to distances (steps) much greater than its mean free path. Because of this, during the step, a large number of collisions is experienced by the particle itself and the new direction is calculated according to multiple-scattering theories. The accuracy of these algorithms is related to the hypothesis on which these theories are based.

Another possibility suggested by the literature is the so-called "*mixed*" algorithm [213] [214] [212]. Here "soft" collisions are described according to multiple-scattering theories, while "hard" collisions are simulated individually, i.e. considering a two-bodies interaction. These algorithms are implemented in widely used MC codes such as Geant4 [193] and Penelope [215] [216] [217] [194] [212].

In this chapter, we report on a model for a mixed MC simulation to study the transport of hot electrons in ionized or partially ionized matter. This model is developed with the aim of future implementation in hydrodynamic codes, and it will be particularly useful to investigate the role of hot electrons in ICF implosion. In particular, in the code developed, the electron slowing down and direction changes due to scattering on plasma particles are simulated separately. The electron slowing down is computed considering collisions with other electrons (free or bound). Also the excitation of electron plasma waves is considered as possible source of energy loss. Hot electron direction

changes are simulated considering elastic scattering on plasma nuclei and on free plasma electrons. Direction changes due to collisions with bound electrons are neglected. This does not introduce a great error in the model, since the electron beam diffusion is ruled mainly by collisions on massive nuclei. Collisions with other electrons are less effective in deviating the beam. Adequate stopping power formulas and differential cross sections (DCSs) should be considered, taking into account the plasma state of the irradiated target.

The chapter is structured as follows: the physical picture of the entire problem is given in the first four sections, introducing the quantities of interest and discussing the validity of the used models. In particular, the physical description of a laser irradiated target is described in Sec. 4.2. In Sec. 4.3, we list the differential cross sections used to describe the electron scattering in ionized or partially ionized targets. In particular, we derive and propose an analytical form for the elastic scattering cross section to model the interaction between an electron and a partially ionized atom screened by plasma particles. A description on how the scattering phenomena (soft and hard) are simulated is presented in Sec. 4.4. Sec. 4.5 is devoted to the discussion on the electron stopping power in plasma and cold matter. Finally, the algorithm implementation is shown in Sec. 4.6 and the code benchmark in Sec. 4.7.

4.2 Physics of background material: non-ideal plasma

As mentioned in Sec. 1.3, a solid target hit by a laser in ICF regime heats up and starts vaporizing. Different regions characterized by different physical properties develop: the corona, the conduction zone, the shocked region and the "unperturbed" target. Apart from corona, the plasma generated in the solid target is non-ideal. It is characterized by a high density, partial ionization and strong Coulomb interactions. This happens in particular when high-Z materials are involved. As explained in Sec. 1.1, in a weakly coupled ideal plasma the electrical interactions between particles are weak, in the sense that the thermal energy is much grater compared to the binding energy (i.e. $T \gg e^2/r$). In this case, a large number of particles are involved in the screening (Debye-Huckel theory, see Chapt. 1). At high density, the screening length decreases and the statistical treatment of the equations on which the Debye theory is based cannot be justified. In this case, the screening effect is due to few neighbor ions that place themselves around a given charge. As such, literature suggests to describe the screening effect substituting the Debye length with the ion sphere radius [218] [219] [209]:

$$R_0 = \left(\frac{4}{3}\pi n_i\right)^{-1/3}, \tag{4.1}$$

where n_i is the ion density.

In non-ideal plasmas, atoms are strongly ionized and excited. Electronic levels are distorted by the impact of neighbour atoms. A mathematical treatment of this exotic conditions based on the Thomas-Fermi theory was developed by More, and it can be found in Refs. [208] [220] [41] [42]. A detailed discussion on these models is out of the scope of the thesis work, limiting ourselves in discussing only some result of interest like the ionization degree (or the number of free electrons per ion). According to the Thomas-Fermi theory, More [208] proposed an analytical algorithm to evaluate the ionization degree q as a function of material density and temperature. For a given element with atomic number Z, the

ρ = mass density in g/cm^3		
T = temperature in eV		
Z = atomic number		
A = atomic mass		
Let	$R = \rho/(ZA)$	$T_0 = T/Z^{4/3}$
	$\alpha = 14.3139$	$\beta = 0.6624$
	$f(x) = x/\left(1 + x + \sqrt{1+2x}\right)$	
$T_F = \frac{T_0}{1+T_0}$		
$A_m = a_1 T_0^{a_2} + a_3 T_0^{a_4}$		
$a_1 = 3.323 \times 10^{-3}$	$a_2 = 0.971832$	$a_3 = 9.26148 \times 10^{-5}$
$a_4 = 3.10165$		
$B_m = -\exp(b_0 + b_1 T_F + b_2 T_F^7)$		
$b_0 = -1.7630$	$b_1 = 1.43175$	$b_2 = 0.315463$
$C_m = c_1 T_F + c_2$		
$c_1 = -0.366667$	$c_2 = 0.983333$	
$Q_1 = A_m R^{B_m}$	$Q = \left(R^{C_m} + Q_1^{C_m}\right)^{1/C_m}$	$x = \alpha Q^\beta$
$Z^* = f(x)Z$		

Table 4.1: The average ionization Z^* of an element of atomic number Z as a function of electron temperature T and material density ρ. Algorithm proposed by More in [208].

ionization degree is defined as the ratio between the number of free electrons per atom Z^* and the atomic number itself, i.e. $q = {}^{Z^*}/_Z$. The More's algorithm approximates the values of Z^* for all elements to an accuracy of a few percent. It is reported in Tab. 4.1, but it can also be found in books like Salzmann [42] and Drake [41]. As an example, the number of free electrons per atom for a carbon plasma as a function of electron plasma temperature is reported in Fig. 4.1. Overall, the predicted Z^* is in agreement with other numerical studies available in the literature [221], even if some inaccuracies appear for $T_e \to 0$. In particular, for a cold material composed by carbon (i.e. a material in standard conditions at T=0.025 eV), the predicted Z^* is ~ 1.5 instead of 0. This is due to the fact that the Thomas-Fermi theory is adequate at describing conductors, while in the case of dielectric the model is not exact. Therefore, to overcome this issue, in case of dielectric material (such a common ICF plastic ablator) we chose as lower limit of algorithm validity $T_e = 1$ eV. For $T_e < 1$ eV the material is considered as cold, i.e. not ionized, while for $T_e > 1$ eV the algorithm calculates the ionization fraction. This discontinuity will not introduce a significant error in the simulation: as the target is hit by the laser, it suddenly heats up and this lower limit is overcame at the first stages of interaction. Considering as an example a common CH ablator hit by a laser in ICF regime, the solid to plasma transition occurs in a timescale of ~ 100 ps [222] [223], while we will be considering hot electrons generated during the main part of the pulse. The molecular dissociation of the CH molecule in carbon and hydrogen ions occurs in a temperature range included between 3 and 8 eV. As such, a lower temperature limit of 1 eV for the ionization is reasonable, considering the typical energies of chemical bonds (from $\sim$1 up to 10 eV).

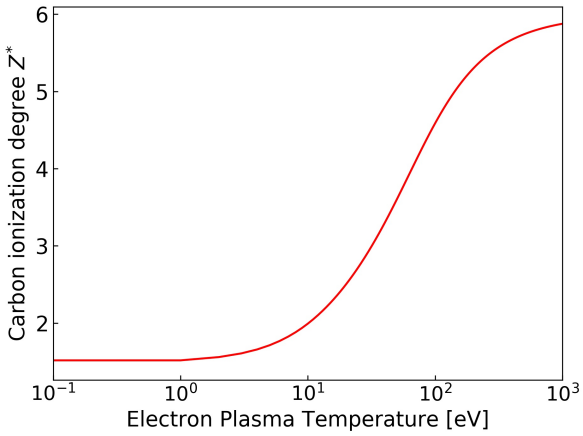

Figure 4.1: Evolution of the carbon ionization degree Z^* as a function of plasma electron temperature, for an electron density of $\sim 10^{23}\text{cm}^{-3}$. The values of Z^* are calculated considering the formulas reported in Tab. 4.1.

4.3 Cross sections

We report, in this section, a list of differential scattering cross sections (DSC), suitable at modelling the scattering phenomena which an electron that propagates in a plasma undergoes. In particular, the elastic scattering with atomic nuclei or with free plasma electrons and the inelastic scattering with the electronic structure of an atom are the processes that should be considered to describe the diffusion of the electron beam. The elastic electron-ion collisions are the main mechanisms responsible for the changes in the electron spatial distribution of the beam, because of the differences in the masses of the two interacting particles. As such, it will be necessary to consider adequate DCSs which model the collision between an electron and a ionized or partially ionized nucleus screened by its residual electronic structure and by other plasma particles. For this purpose an adequate DCS is proposed in this thesis, since the cross sections commonly used in cold MC methods [224][225] are not adequate (because the presence of a plasma is not accounted). Furthermore, to improve the accuracy of the model, we will also consider electron direction changes due to scattering with other free plasma electrons. Direction changes due to collisions with bond electrons of partially ionized atoms are neglected. This should not introduce a great error in the model, since the diffusion of the beam is mainly due to collisions with massive nuclei [226].

We propose, in the following, a list of differential elastic scattering cross sections (DCS) that are suitable for our purposes. These are the Moller DCS, which models the elastic scattering between two electrons; the Dalitz DCS, which models the elastic scattering between an electron and a completely ionized nucleus screened by plasma particles; we also propose a DCS to model the elastic collision between an electron and a partially ionized atom, screened by the plasma particles and by its residual electronic structure.

4.3.1 Electron - Electron scattering

The scattering between a hot electron and plasma electrons can be modelled considering the Moller cross-section [227][228][229][230][231]. In the center of mass frame, the cross

section writes:

$$\frac{\mathrm{d}\sigma}{d\Omega^*}_{ee} = \left(\frac{r_0}{\gamma\beta^2}\right)^2 2\left(\gamma+1\right)\left[\frac{4}{\sin^4\theta^*} - \frac{3}{\sin^2\theta^*} + \frac{\left(\gamma-1\right)^2}{4\gamma^2}\left(1+\frac{4}{\sin^2\theta^*}\right)\right]. \tag{4.2}$$

Here $r_0 = e^2/m_0c^2$ is the classical electron radius, θ^* the polar scattering angle in center of mass frame, $\beta = v/c$ the electron velocity normalized to the speed of light and $\gamma = \left(1-\beta^2\right)^{-1/2}$ the relativistic gamma factor. This formula is derived considering the quantum nature of the electron (i.e. a fermion with spin 1/2) and it is valid in the relativistic regime, but it neglects the motion of the target electron. Considering the relation between the scattering angle in center of mass and laboratory frame [232]:

$$\cos\theta^* = \frac{2m - m\left(\gamma+3\right)\sin^2\theta}{2m + m\left(\gamma-1\right)\sin^2\theta}, \tag{4.3}$$

it is possible to rewrite eq. (4.2) in laboratory frame [210]:

$$\frac{\mathrm{d}\sigma}{d\Omega}_{ee} = 4\left(\frac{r_0}{\gamma\beta^2}\right)^2 \cos\theta\left\{\frac{1}{\sin^4\theta} + \frac{\left(\gamma+1\right)^2}{4\cos^4\theta} + \frac{\left[\left(\gamma^2-1\right)/\gamma\right]^2}{\left[\left(\gamma-1\right)\sin^2\theta+2\right]^2} - \frac{\left(2\gamma-1\right)\left(\gamma+1\right)}{2\gamma^2\sin^2\theta\cos^2\theta}\right\}. \tag{4.4}$$

Here θ is the polar scattering angle in the laboratory frame.

4.3.2 Electron - Nucleus Scattering

When an electron propagates in matter, it undergoes several Coulomb collisions with the atomic nuclei of the material. The collision between a relativistic electron and a Z target nucleus is described by the Mott's DCS [233]:

$$\frac{\mathrm{d}\sigma}{\mathrm{d}\Omega}_{ei} = \left(\frac{Zr_0}{\gamma\beta^2}\right)^2 \frac{1}{4\sin^4\theta/2}\left(1-\beta^2\sin^2\frac{\theta}{2}\right). \tag{4.5}$$

Because of the higher ion mass ($m_i \sim 2000m_e$), the center of mass frame coincides with the laboratory frame and θ can be considered as the electron scattering angle in the laboratory frame. In cold condensed matter, nuclei are screened by their electronic structure which modifies the potential felt by the incident particle. A common way to describe this screening effect is to model the nuclear potential $V(r)$ felt by the incident particle taking into account the electronic density around the nucleus. The electronic density can be evaluated considering the Thomas-Fermi theory, as presented in the quantum mechanics literature [229][234]. In plasmas, the screening is due to the residual electronic structure and to other plasma particles around a given nucleus. We will propose, in the following, an analytical model to describe this effect.

Electron - Partially ionized screened ion scattering

In the case of a partially ionized atom in a plasma, the nuclear potential is screened by other plasma particles and by the remaining bound electrons around the nucleus. This condition is seldomly addressed in literature and no peer-reviewed articles that give a satisfactory discussion on this matter were found at the time of writing. As such, we derive and propose here an analytical DCS that describes this phenomenon.

To model the interaction between an electron and a partially ionized atom, we consider a potential $V(r)$ of the form:

$$V(r) = \frac{e^2}{r}\left(Z_b e^{-r/R} + Z^* e^{-r/D}\right). \tag{4.6}$$

Here Z_b is the number of bound electrons and Z^* is the number of free electrons. If the atom has atomic number Z, $Z^* = Z - Z_b$. In equation (4.6), R represents the distance at which the screening due to bound electrons is effective and reads:

$$R = 0.885 Z_b^{-1/3} a_0, \tag{4.7}$$

where a_0 is the Bohr radius:

$$a_0 = \frac{\hbar}{m_e c \alpha} = 5.29 \times 10^{-9}\text{cm}; \quad \alpha = \frac{1}{137}. \tag{4.8}$$

This parameter is derived considering the atomic structure described by the Thomas-Fermi theory, and it was firstly proposed by Stewart [235]. The complete treatment is also reported in widely known quantum mechanics references [229] [234] [212]. The screening effects due to plasma particles are modelled considering the Debye length or the ion sphere radius, as shown in Sec. 1.1. In particular, the screening length is set as the maximum between the Debye length and the ion sphere radius $D = \max[\lambda_D, r_i]$.

The potential (4.6) was proposed by Nardi and Zinamon [236], even if its explicit form is not written in the article, but it is described with the following sentence: *"it is assumed that the screening is due to the sum of two exponentials with characteristic lengths D and R"*. The explicit form is reported in the thesis works [237] [238] [239]. To better understand the model, we study its behaviour as a function of r:

$$\begin{cases} V(r) \simeq \frac{Ze^2}{r} & r \to 0 \\ V(r) \simeq \frac{e^2}{r}\left[Z_b e^{\left(-\frac{r}{R}\right)} + Z^*\right] & 0 < r < R \\ V(r) \simeq \frac{Z^* e^2}{r} e^{\left(-\frac{r}{D}\right)} & R \ll r \leq D \\ V(r) \simeq 0 & r \to \infty \end{cases}. \tag{4.9}$$

For $r \to 0$, i.e. in the closest range of the nucleus, the potential assumes the form of a Coulomb potential generated by a charge Z in vacuum. This is as expected, since in the proximity of the nucleus plasma or bound electrons do not screen the nuclear charge. For $0 < r < R$, the potential is given by the sum of the potential of a charge Z^* plus the potential of a screened Z_b charge . Here the screening effect is given only by bound electrons. The approximation introduced by the model is mainly contained in this region, since the electron should feel a potential generated by a charge Z screened by bound electrons. For $R \ll r \leq D$, the electron moves outside the screening sphere formed by bound electrons, and it actually feels the potential of a "macro-particle" of charge Z^* (the positively charged nucleus minus the charge of bound electrons). This macro-particle is screened by the presence of free-plasma particles and this is modeled by the exponential $e^{-r/D}$. For $r \to \infty$, the plasma charges screen completely the ion potential, and the value of $V(r)$ approaches 0. Fig 4.2 schematically shows the four limits.

Since the references reported do not propose a DCS considering the potential (4.6), we

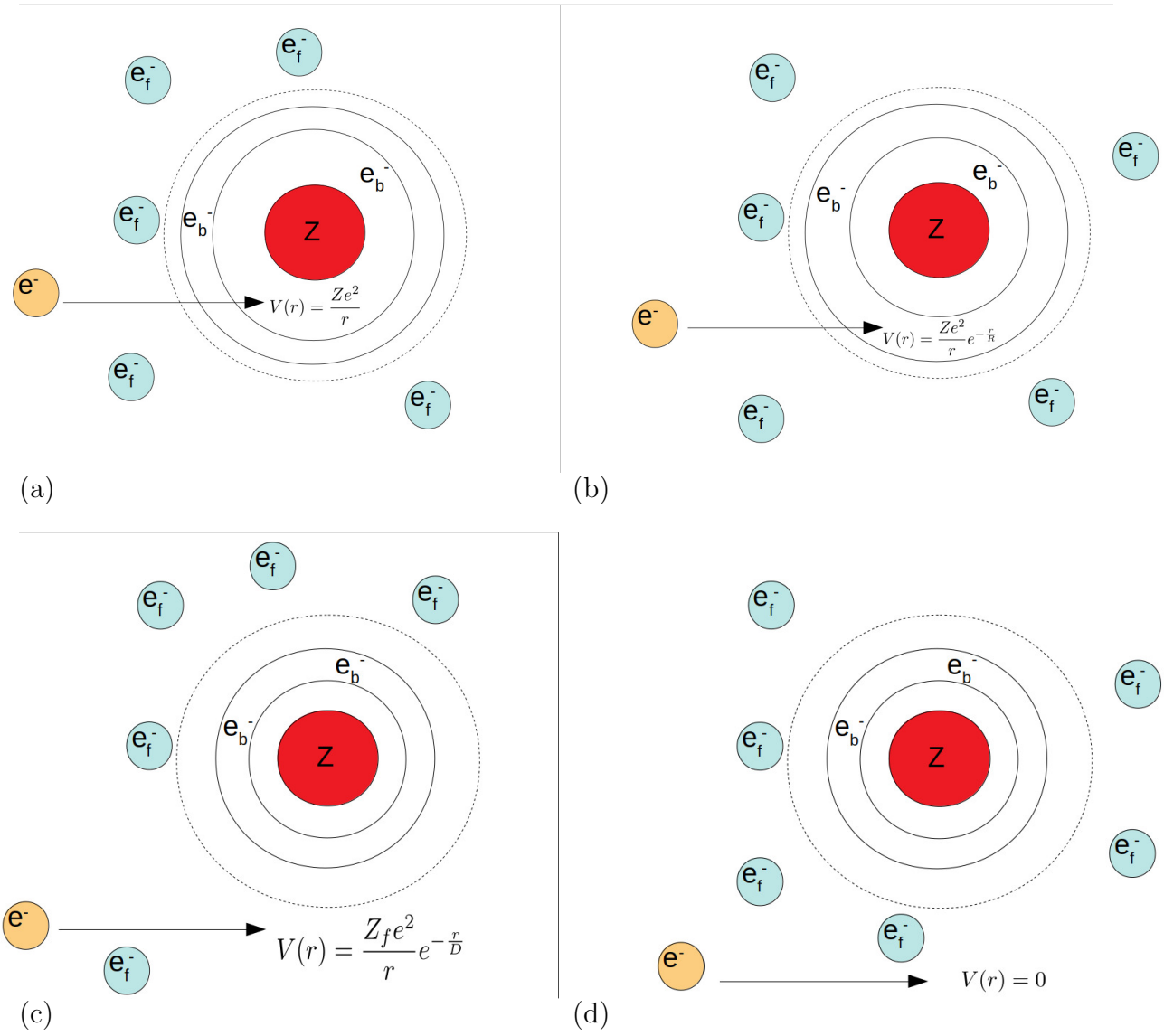

Figure 4.2: Value of the potential $V(r)$ felt by a hot electron that approaches a partially ionized nucleus. (a) The electron is near the nucleus and it feels a Coulomb potential of a charge Z in vacuum. (b) The electron is moving in the region where the screening due to bound electrons is effective. Here the electron should feel a potential of a charge Z screened by bound electrons. (c) The electrons moves in the Debye sphere. Here it feels the potential of a macro particle of charge Z^* screened by plasma particles. (d) The electron is outside the Debye sphere and it does not feel the presence of the nucleus.

will now derive it. According to the elastic diffusion theory in the *first Born approximation*, it is possible to derive an analytical form for the DCS from this potential [234][229]. The calculation is carried out considering the initial and the final states of the incident particle as free-particle wave function φ, perturbed by the presence of the potential $V(r)$. The initial state is represented by $\varphi_a = \exp(i\mathbf{k}_a \cdot \mathbf{r}_a)$ and the final by $\varphi_b = \exp(i\mathbf{k}_b \cdot \mathbf{r}_b)$. The momenta of the two states write $\mathbf{p}_a = \hbar\mathbf{k}_a$ and $\mathbf{p}_b = \hbar\mathbf{k}_b$. The transition from the state a to the state b is determined by the perturbation operator $\hat{V}(\mathbf{r})$. According to quantum mechanics, the probability of this transition per unit of time $\mathrm{d}P_{ba}$ is ruled by

the "*Fermi's golden rule*":

$$\mathrm{d}P_{ba} = \frac{2\pi}{\hbar} \mid< \varphi_b \mid \hat{V} \mid \varphi_a >\mid^2 \mathrm{d}\rho, \tag{4.10}$$

where $\mathrm{d}\rho$ is the number of final states per unit volume with momentum direction in the solid angle $\mathrm{d}\Omega$. According to statistical physics [240] [241], the density of states per unit volume for a free particle with kinetic energy E writes:

$$\rho = \frac{\mu^{3/2}}{\sqrt{2}\pi^2\hbar^3} E^{1/2}. \tag{4.11}$$

Considering that $E = \frac{\hbar^2 k^2}{2\mu}$, $v_b = \frac{\hbar k}{\mu}$ and dividing by 4π, the following expression for $\mathrm{d}\rho$ is obtained:

$$\mathrm{d}\rho = \frac{\mu^2 v_b \mathrm{d}\Omega}{(2\pi\hbar)^3}. \tag{4.12}$$

Here μ is the reduced mass of the electron-ion system and v_b the relative velocity after the collision. However, since the ion mass is much grater than the electron one, it is possible to write $\mu \simeq m_e$. Furthermore, the nucleus can be considered fixed during the collision, and v_b refers to the final electron velocity. Dividing eq. (4.10) by v_a (the flux of incident particles), we obtain an equation for the DCS:

$$\mathrm{d}\sigma = \frac{m_e^2 v_b}{(2\pi\hbar)^2 v_a} \mid< \varphi_b \mid \hat{V} \mid \varphi_a >\mid^2 \mathrm{d}\Omega. \tag{4.13}$$

Being an elastic diffusion, the electron does not change its velocity during the collision, i.e. $v_a = v_b$. The matrix element writes:

$$< \varphi_b \mid \hat{V} \mid \varphi_a >= \int V(\mathbf{r}) \exp\left[i\left(\mathbf{k}_a - \mathbf{k}_b\right)\cdot\mathbf{r}\right] \mathrm{d}^3\mathbf{r}, \tag{4.14}$$

i.e. it corresponds to the Fourier transform of the potential. Recasting the integral in spherical coordinates, one obtains:

$$< \varphi_b \mid \hat{V} \mid \varphi_a >= \int_0^{2\pi}\int_0^{\pi}\int_0^{\infty} V(\mathbf{r})\, e^{[i(\mathbf{k}_a-\mathbf{k}_b)\cdot\mathbf{r}]} r^2 \sin\theta \mathrm{d}r\mathrm{d}\theta\mathrm{d}\phi. \tag{4.15}$$

Introducing $q = \mid \mathbf{k}_a - \mathbf{k}_b \mid$ and considering that $(\mathbf{k}_a - \mathbf{k}_b)\cdot\mathbf{r} = (\mid \mathbf{k}_a - \mathbf{k}_b \mid) r\cos\theta$, eq. (4.15) becomes:

$$< \varphi_b \mid \hat{V} \mid \varphi_a >= \int_0^{2\pi}\int_0^{\pi}\int_0^{\infty} V(\mathbf{r})\, e^{[i(|\mathbf{k}_a-\mathbf{k}_b|)r\cos\theta]} r^2 \sin\theta \mathrm{d}r\mathrm{d}\theta\mathrm{d}\phi. \tag{4.16}$$

The integrals in the variables ϕ and θ are straightforward:

$$< \varphi_b \mid \hat{V} \mid \varphi_a >= 2\pi \int_0^{\infty} \mathrm{d}r V(r) r \left[-\frac{1}{iq}\left(e^{-iqr} - e^{iqr}\right)\right] = \frac{4\pi}{q}\int_0^{\infty} V(r) r \sin(qr). \tag{4.17}$$

If $V(r)$ is an even function, the integral could be extended to -∞ to +∞, and since $\int_{-\infty}^{+\infty} \mathrm{d}r V(r) r\cos(qr) = 0$ eq. (4.17) can be written as:

$$\begin{aligned} &< \varphi_b \mid \hat{V} \mid \varphi_a >= \frac{2\pi}{iq}\int_{-\infty}^{+\infty} \mathrm{d}r V(r) i r \sin(qr) + \frac{2\pi}{iq}\int_{-\infty}^{+\infty} \mathrm{d}r V(r) r\cos(qr) = \\ &= \frac{2\pi}{iq}\int_{-\infty}^{+\infty} \mathrm{d}r V(r) r e^{iqr} = \frac{2\pi}{i \mid \mathbf{k}_b - \mathbf{k}_a \mid}\int_{-\infty}^{+\infty} \mathrm{d}r V(r) r e^{i|\mathbf{k}_b-\mathbf{k}_a|r} = V\left(|\mathbf{k}_b - \mathbf{k}_a|\right). \end{aligned} \tag{4.18}$$

From this equation, it is clear that the Fourier transform of the potential depends only on the absolute value of the momentum exchanged, i.e.:

$$< \varphi_b \mid \hat{V} \mid \varphi_a >= V\left(|\mathbf{k}_b - \mathbf{k}_a|\right). \tag{4.19}$$

It is now possible to use these results to find a form for the DCS of an electron that scatters on a partially ionized atom. Using the potential (4.6) in eq. (4.18) and (4.13), after a simple Fourier transform of the exponential functions one obtains:

$$\frac{\mathrm{d}\sigma}{d\Omega} = \frac{e^4}{p^2v^2}\left\{\frac{Z^{*2}}{\left[1-\cos\theta+2\mathrm{F}\right]^2} + \frac{Z_b^2}{\left[1-\cos\theta+2\mathrm{B}\right]^2} + \frac{2Z_bZ^*}{\left[1-\cos\theta+2\mathrm{B}\right]\left[1-\cos\theta+2\mathrm{F}\right]}\right\}. \tag{4.20}$$

Here p and v are the momentum and the velocity of the incident electron. F and B are two coefficients that describe the screening effects due to free and bound electrons, respectively. They write:

$$F = \frac{1}{4}\left(\frac{\hbar}{p}\right)^2\left(\max[\lambda_D, r_i]^{-2}\right) \tag{4.21}$$

and

$$B = \frac{1}{4}\left(\frac{\hbar}{p}\right)^2 R^{-2}. \tag{4.22}$$

Eq. (4.23) represents the differential elastic scattering cross section that describes the collision between an electron and a partially ionized atom in a plasma.

Considering now the small scattering angle approximation ($\theta \to 0$), i.e. collisions at large impact parameter, it is possible to write a simpler form for the eq. (4.23) [242]:

$$\frac{\mathrm{d}\sigma}{d\Omega} = \frac{4e^4}{p^2v^2}\frac{Z^2}{(\theta^2+\theta_{min}^2)^2}, \tag{4.23}$$

where θ_{min} reads:

$$\theta_{min}^2 = 4\min\left[F, B\right]. \tag{4.24}$$

In the case of hard collisions, since $B \ll 1$ and $F \ll 1$, the cross section (4.23) reduces to the Rutherford cross section:

$$\frac{\mathrm{d}\sigma}{d\Omega} = \frac{e^4}{p^2v^2}\frac{Z^2}{4\sin^4\theta}. \tag{4.25}$$

As expected, the screening effects have influence on the collision at large impact parameter, while they do not play a role in a hard collision.

Regarding the regime of validity of the formula (4.23), the equation is derived on the basis of the first Born approximation. As such, the potential is seen as a perturbation compared to the electron kinetic energy ($V(r) \ll E$). This happens when the velocity of the incident electron is bigger compared to the velocity of a k-shell electron of the atom. Considering for simplicity an hydrogen-like atom, a k-shell electron has energy:

$$E_k = \frac{m_e e^4 Z^2}{\hbar^2} \Rightarrow v_k = \sqrt{\frac{E}{2m_e}} = \sqrt{\frac{e^4Z^2}{\hbar^2}} = \frac{cZ}{137}. \tag{4.26}$$

Considering now an electron incident with velocity v, the condition $v_k/v \ll 1$ is satisfied if:

$$\frac{v_k}{v} = \frac{cZ}{137v} = \frac{Z}{137\beta} \ll 1. \tag{4.27}$$

This is the figure of merit that should be satisfied for the first Born approximation to be valid. This conditions is no more valid for electrons at low energy (∼keV) interacting with high Z elements. In the context of ICF, hot electrons have usually kinetic energies of the order of tens or hundreds of keV, propagating in low Z materials (CH or DT). As such, the Born condition is usually fulfilled and the cross section (4.23) is adequate for our scope. Furthermore, eq. (4.23) is derived on the basis of quantum non-relativistic theory, and it should not be used to model relativistic electron collisions (i.e. $E \sim$ MeV). Again, our model is adequate, since typical hot electron mean kinetic energies go from ~ 30 up to 100 keV.

Electron - Not ionized atom collision

We also take into account the possibility for the electron of propagating in "cold" materials, i.e. in not ionized in materials. This will allow for an easier benchmark of the code with already existent and widely used MC codes, like Geant4 or Penelope.

As mentioned in Sec. 4.2, the material is assumed to ionize from $T_e > 1$eV. For lower temperatures, the material is considered as cold and the value of Z^* is zero. In this case, eq. (4.23) writes:

$$\frac{\mathrm{d}\sigma}{d\Omega} = \frac{e^4}{p^2 v^2} \frac{Z^2}{[1 - \cos\theta + 2\mathrm{B}]^2}. \tag{4.28}$$

This form coincides with the Wentzel's DCS [243] and it is commonly used in cold MC methods [212] [201]. This equation models the scattering between an electron and a non-ionized atom screened by its electronic structure. Here the screening factor is due only to bound electrons and it is modelled by the factor B.

4.3.3 Electron - Completely ionized atoms

As already mentioned, in ICF and in SI the generation of hot electrons happens after pre-compression laser pulses. In the compression phase, low Z atoms can be completely ionized. As such, hot electrons will interact with nuclei screened by plasma charges. This condition has been already considered in the literature, in particular to model the propagation of electrons in the fast ignition regime (i.e. electrons with energy of the order of MeV) [210]. A suitable DCS that describes the electron-ion interaction, considering the screening effects, is the Dalitz DCS [244] [245] [246] [210]:

$$\frac{\mathrm{d}\sigma}{\mathrm{d}\Omega} = \left(\frac{Z r_0}{\gamma\beta^2}\right)^2 \frac{1}{4\sin^4\theta/2} \left(1 - \beta^2 \sin^2\frac{\theta}{2}\right) \left(\frac{\Lambda^2 \sin^2\theta/2}{1 + \Lambda^2 \sin^2\theta/2}\right)^2. \tag{4.29}$$

Here Z is the atomic number of the scattering center, γ and β the electron relativistic kinematic quantities and θ the scattering angle in the laboratory frame. In this formula, it is possible to recognize a "Mott" part (4.5) multiplied by the screening term:

$$\left(\frac{\Lambda^2 \sin^2\theta/2}{1 + \Lambda^2 \sin^2\theta/2}\right)^2, \text{ where } \Lambda = 2\left(\frac{p}{\hbar}\right) \max[\lambda_D, r_i]. \tag{4.30}$$

Notice that in Ref. [246] there is a typo and the exponent of the screening term is missed. Recasting the formula (4.29) considering the relation $\Lambda^{-2} = F$, one obtains:

$$\frac{\mathrm{d}\sigma}{\mathrm{d}\Omega} = \left(\frac{r_0}{\gamma\beta^2}\right)^2 \left(1 - \beta^2 \mathrm{sin}^2\frac{\theta}{2}\right) \frac{Z^2}{\left[1 - \mathrm{cos}\theta + 2\mathrm{F}\right]^2}. \tag{4.31}$$

The non relativistic limit of this equation corresponds to eq. (4.23) in which $\mathrm{Z}_b = 0$.

Similarly to what shown for eq (4.23), the screening term plays an important role for the small angle collisions, (high impact parameters), while in case of hard collisions the cross section reduces to the Rutherford form.

Let us mention that eq. (4.29) reports only a part of the Dalitz DCS, neglecting a term. In reality the complete formula for the Dalitz's DCS is [245]:

$$\begin{aligned}\frac{\mathrm{d}\sigma}{\mathrm{d}\Omega} = \left(\frac{Zr_0}{\gamma\beta^2}\right)^2 \frac{1}{4\mathrm{sin}^4\theta/2} \left(\frac{\Lambda^2\mathrm{sin}^2\theta/2}{1 + \Lambda^2\mathrm{sin}^2\theta/2}\right)^2 \Bigg\{ \left(1 - \beta^2\mathrm{sin}^2\frac{\theta}{2}\right) \times \\ \left[1 - \left[\hbar^2\lambda^2 + 4p^2\mathrm{sin}^2\left(\frac{\theta}{2}\right)\right] \frac{\alpha}{\beta\pi^2} \mathrm{Re}\left(I + J\right)\right] \\ - \left(1 - \beta^2\right) \frac{\alpha}{\beta\pi^2} \left[\hbar^2\lambda^2 + 4p^2\mathrm{sin}^2\left(\frac{\theta}{2}\right)\right] \mathrm{Re}\left(I - J\right) \Bigg\}.\end{aligned} \tag{4.32}$$

where the terms $\mathrm{Re}(I \pm J)$ read:

$$\begin{aligned}\mathrm{Re}\left(I \pm J\right) = -\frac{1}{\mathrm{sin}\left(\frac{\theta}{2}\right)\left\{\hbar^4\lambda^4 + 4p^2\left[\hbar^2\lambda^2 + p^2\mathrm{sin}^2\left(\frac{\theta}{2}\right)\right]\right\}^{1/2}} \left[1 \pm \frac{\hbar^2\lambda^2 + 2p^2}{2p^2\mathrm{cos}^2\left(\frac{\theta}{2}\right)}\right] \times \\ \mathrm{tan}^{-1}\left(\frac{\hbar\lambda p \mathrm{sin}\left(\frac{\theta}{2}\right)}{\left\{\hbar^4\lambda^4 + 4p^2\left[\hbar^2\lambda^2 + p^2\mathrm{sin}^2\left(\frac{\theta}{2}\right)\right]\right\}^{1/2}}\right) \pm \frac{1}{2p^2\mathrm{cos}^2\left(\frac{\theta}{2}\right)} \\ \left[\mathrm{tan}^{-1}\left(\frac{2p}{\hbar\lambda}\right) - \frac{1}{\mathrm{sin}^2\left(\frac{\theta}{2}\right)} \mathrm{tan}^{-1}\left(\frac{p\mathrm{sin}^2\left(\frac{\theta}{2}\right)}{\hbar\lambda}\right)\right].\end{aligned} \tag{4.33}$$

As usual, λ is the maximum between the Debye length and the ion sphere radius. Eq. (4.37) is justified if the following two conditions are satisfied:

$$\begin{aligned}&\mathrm{I}: \quad \left[\hbar^2\lambda^2 + 4p^2\mathrm{sin}^2\left(\frac{\theta}{2}\right)\right] \frac{\alpha}{\beta\pi^2} \mathrm{Re}\left(I + J\right) \ll 1 \\ &\mathrm{II}: \ \left(1 - \beta^2\right) \frac{\alpha}{\beta\pi^2} \left[\hbar^2\lambda^2 + 4p^2\mathrm{sin}^2\left(\frac{\theta}{2}\right)\right] \mathrm{Re}\left(I - J\right) \ll 1.\end{aligned} \tag{4.34}$$

Fig. 4.3 shows the maps of the absolute values of the terms I and II as a function of the incident electron energy and scattering angle. As can be observed from the figure, these two terms are much less than 1 for the energy range of our interest. In particular, only for low electron kinetic energies ($\sim$ keV) and large angle deflection the two terms becomes important. However, electrons with energies around $\sim$ keV are suddenly absorbed in plasma, and this will not cause any appreciable error. As such, the formula (4.29) can be considered correct for our purposes and it is possible to neglect the terms (4.34).

Moreover, this DCS is derived according to the second Born approximation $(\frac{Z}{137\beta})^2 \ll 1$ and it is valid in relativistic regime.

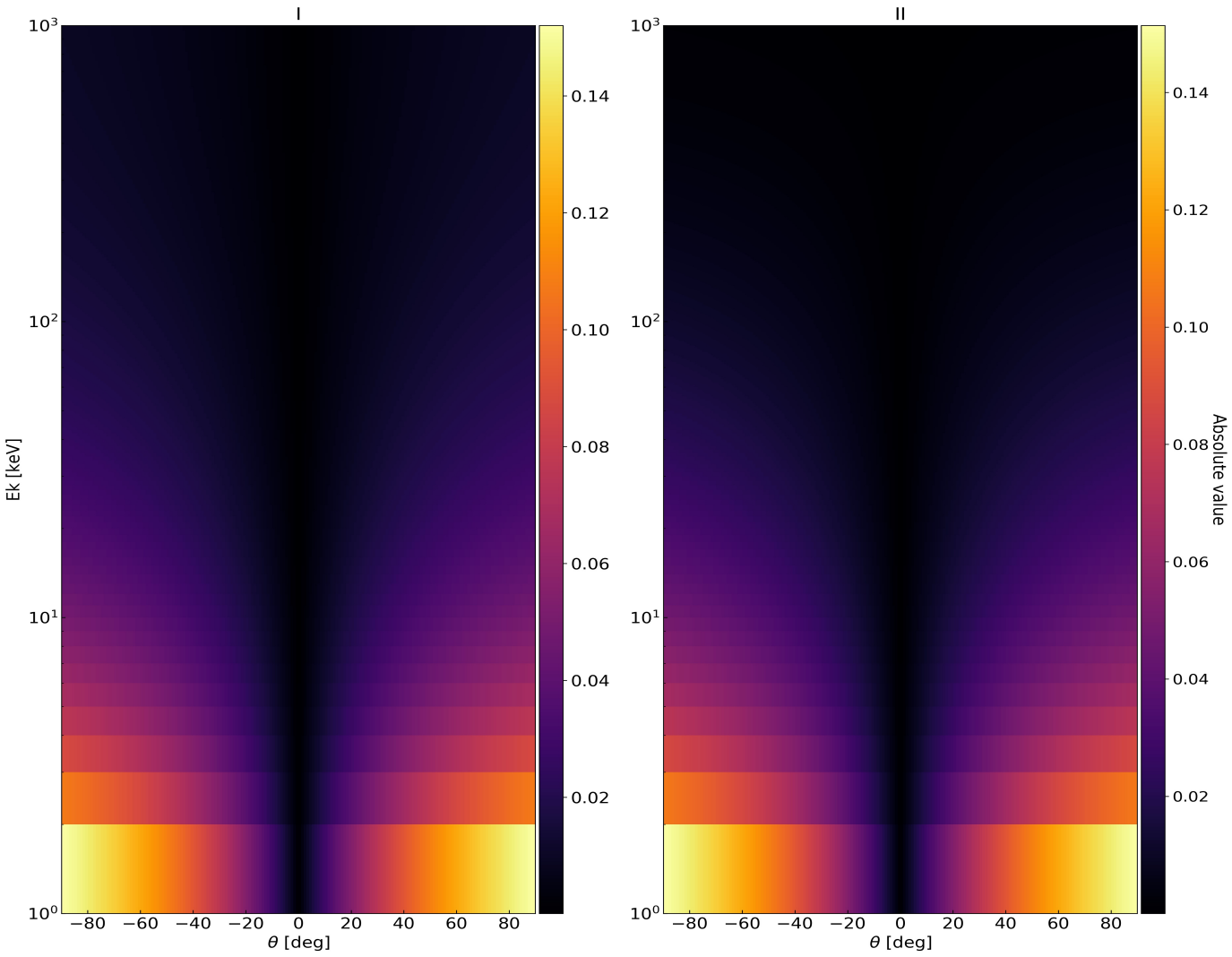

Figure 4.3: Maps of absolute values of the terms I and II of (4.34) as a function the incident electron energy and scattering angle. For the energy range of our interest, the terms I and II are much less than 1, justifying the form (4.29) for the DCS.

4.3.4 Summary of the differential elastic cross sections

To summarize, the three DCSs considered to model the hot electron propagation in ICF irradiated target are:

- The Moller cross section, which models the scattering between the hot electron and

a plasma electron:

$$\frac{\mathrm{d}\sigma}{d\Omega_{ee}} = 4\left(\frac{r_0}{\gamma\beta^2}\right)^2 \cos\theta \left\{ \frac{1}{\sin^4\theta} + \frac{(\gamma+1)^2}{4\cos^4\theta} + \frac{\left[(\gamma^2-1)/\gamma\right]^2}{\left[(\gamma-1)\sin^2\theta+2\right]^2} - \frac{(2\gamma-1)(\gamma+1)}{2\gamma^2\sin^2\theta\cos^2\theta} \right\}. \tag{4.35}$$

- The cross section we proposed to model the elastic scattering between the hot electron and a partially ionized atom screened by bound electrons and plasma particles:

$$\frac{\mathrm{d}\sigma}{d\Omega_{ei}} = \frac{e^4}{p^2v^2} \left\{ \frac{Z^{*2}}{\left[1-\cos\theta+2\mathrm{F}\right]^2} + \frac{Z_b^2}{\left[1-\cos\theta+2\mathrm{B}\right]^2} + \frac{2Z_bZ^*}{\left[1-\cos\theta+2\mathrm{B}\right]\left[1-\cos\theta+2\mathrm{F}\right]} \right\} \tag{4.36}$$

- The Dalitz's DCS to model the scattering between the hot electron and a nucleus screened by plasma particles:

$$\frac{\mathrm{d}\sigma}{\mathrm{d}\Omega_{ei}} = \left(\frac{Zr_0}{\gamma\beta^2}\right)^2 \frac{1}{4\sin^4\theta/2} \left(1-\beta^2\sin^2\frac{\theta}{2}\right) \left(\frac{\Lambda^2\sin^2\theta/2}{1+\Lambda^2\sin^2\theta/2}\right)^2. \tag{4.37}$$

Fig. 4.4 shows the behaviour of the cross sections considered as a function of the scattering angle, for a 30 keV incident electron. For the electron - ion cases, the target atom is Al. As can be observed, all the cross sections are peaked at low scattering angle. As such, low scattering angle phenomena are more probable than large deflection collisions. This encourage the use of the multiple scattering theories to model the hot electron transport, as it is shown in the next section.

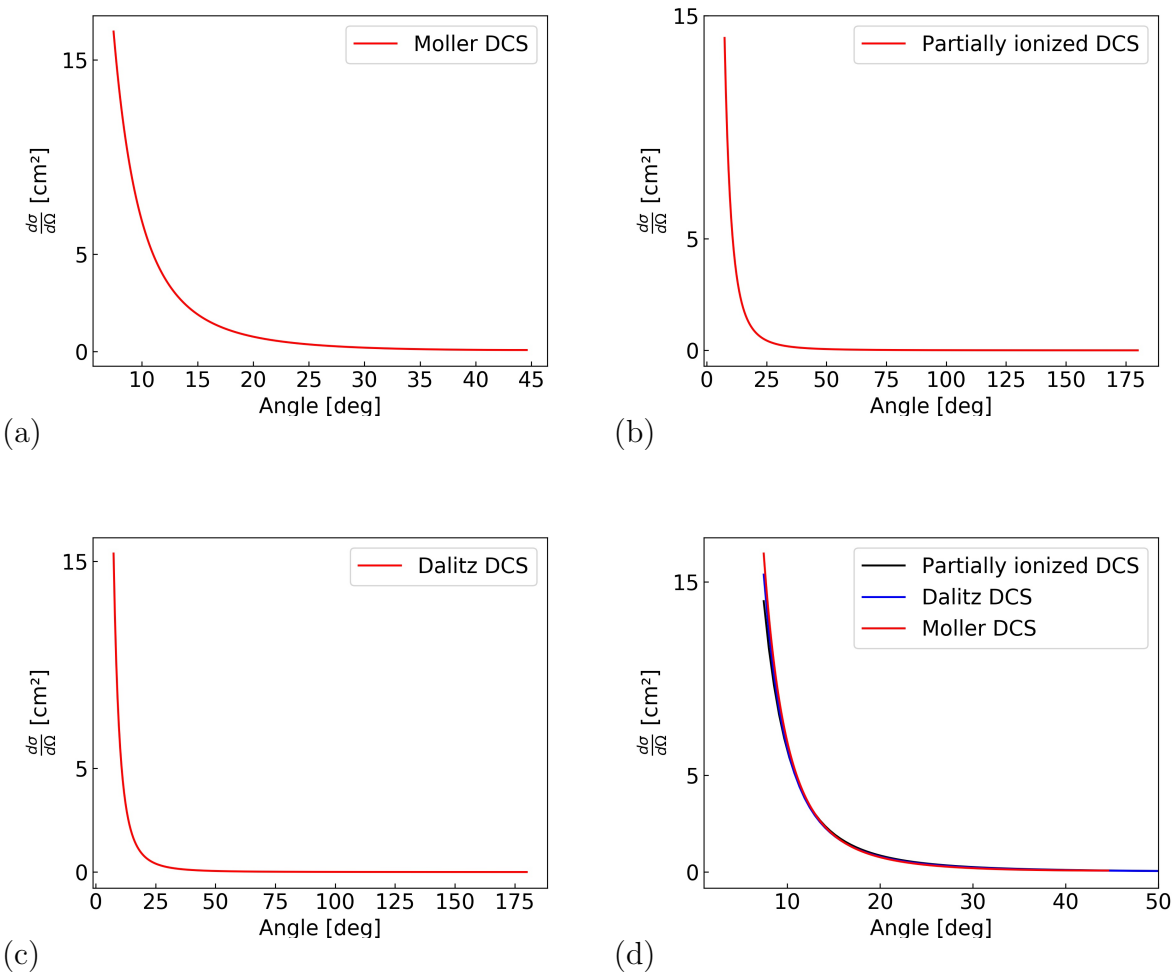

Figure 4.4: Cross sections as a function of the scattering angle for a 30 keV incident electron. (a) Moller DCS. (b) Patially ionzed DCS considering as target Al atoms at 50 eV ($Z^* \sim 5$). (c) Dalitz DCS considering complete ionized Al atoms as target. (d) The three cross sections.

4.4 Scattering theories: scattering polar angle distribution for soft and hard collisions

As mentioned in the introduction of this chapter, the MC method proposed here consists in a mixed algorithm in which soft and hard collisions are simulated separately. We identify as soft collisions such scattering events for which the polar scattering angle is less than a predetermine value θ_s, which is around 10° [212]. Evidently, hard collisions are that events with a scattering angle greater than θ_s. Soft scattering events are modelled according to the Goudsmit and Saunderson theory, while hard collisions are simulated considering a two-bodies interaction modelled considering the DCS listed in Sec. 4.3.

4.4.1 Soft collisions: Multiple Scattering Theory

The multiple scattering theories evaluate the global effect of the collisions that occur in a track segment of a given length travelled by the electron. An accurate simula-

tion procedure is based on the Goudsmit and Saunderson multiple scattering theory [247][248][249][212]. The most important result obtained in this theory is the fact that the soft collision polar angle can be sample from a Gaussian distribution. As shown in appendix C, the Goudsmit-Saunderson distribution function for the polar scattering angle θ reads:

$$F_{GS}\left(\theta, \Delta s\right) = \sum_{l=0}^{\infty} \left[\frac{(2l+1)}{4\pi}\right] P_l(\cos\theta) \exp\left(\frac{-\Delta s}{\lambda_l}\right), \tag{4.38}$$

where λ_l is the *transport mean free path* and Δs is the length of the path travelled by the particle. The transport mean free path reads:

$$\lambda_l^{-1} = 2\pi N \int_{\theta_{min}}^{\theta_{max}} \frac{\mathrm{d}\sigma(\theta)}{\mathrm{d}\Omega} \big[1 - P_l(\cos\theta)\big] \sin\theta \mathrm{d}\theta, \tag{4.39}$$

where N is the density of the scattering centers characterized by their DCS $\frac{\mathrm{d}\sigma(\theta)}{\mathrm{d}\Omega}$ (for simplicity here we are considering a medium composed by only one specie). Eq. (4.38) represents the probability density function for the particle to assume a final direction in the solid angle element $\mathrm{d}\Omega$, around a direction defined by the polar angle θ, after have travelled for a path Δs.

We now introduce an important approximation, the so-called *small scattering angle approximation*. In particular, we consider only collisions with scattering angle less than a given value θ_s. This allows to find an analytical form for the distribution function (4.38) that will be useful for our purposes. For $\theta \to 0$, the Legendre polynomial can be approximated according to [250]:

$$P_l\left(\cos\theta\right) \sim 1 - \frac{1}{4} l\left(l+1\right)\theta^2 = 1 - \frac{1}{2} l\left(l+1\right)\left(1-\cos\theta\right) \tag{4.40}$$

and the transport mean free path λ_l writes:

$$\lambda_l^{-1} = 2\pi N \frac{l\left(l+1\right)}{2} \int \frac{\mathrm{d}\sigma(\theta)}{\mathrm{d}\Omega} \left(1-\cos\theta\right) \sin\theta \mathrm{d}\theta = \frac{l\left(l+1\right)}{2} \frac{1}{\lambda_1^{(s)}}, \tag{4.41}$$

where $\lambda_1^{(s)}$ is the first transport mean free path computed considering a small collision angle:

$$\lambda_1^{(s)-1} = 2\pi N \int_{\theta_{min}}^{\theta_s} \frac{\mathrm{d}\sigma(\theta)}{\mathrm{d}\Omega} \big[1 - \cos\theta)\big] \sin\theta \mathrm{d}\theta. \tag{4.42}$$

Using this result in (4.38), the Goudsmit-Saunderson distribution function becomes:

$$F_{GS}\left(\theta, \Delta s\right) = \sum_{l=0}^{\infty} \frac{2l+1}{4\pi} \exp\left[-\frac{l\left(l+1\right)}{2} \frac{\Delta s}{\lambda_1^{(s)}}\right] P_l(\cos\theta). \tag{4.43}$$

At this point, we use the Moliere's approximation for the Legendre Polynomials [251] [252]:

$$P_l\left(\cos\theta\right) \simeq \left(\frac{\theta}{\sin\theta}\right)^{1/2} J_0\left(\left[l + \frac{1}{2}\right]\theta\right), \tag{4.44}$$

where J_0 is the Bessel function of the first kind. Eq. (4.43) becomes:

$$F_{GS}\left(\theta, \Delta s\right) = \sum_{l=0}^{\infty} \frac{2l+1}{4\pi} \exp\left[-\frac{l\left(l+1\right)}{2} \frac{\Delta s}{\lambda_1^{(s)}}\right] \left(\frac{\theta}{\sin\theta}\right)^{1/2} J_0\left(\left[l + \frac{1}{2}\right]\theta\right). \tag{4.45}$$

Now the sum is substituted by the integral introducing the variable $y = l + \frac{1}{2}$:

$$F_{GS}(\theta, \Delta s) = \frac{1}{2\pi} \int_0^\infty y J_0(y\theta) \exp\left[-\left(\frac{y^2 - \frac{1}{4}}{2} \right) \frac{\Delta s}{\lambda_1^{(s)}} \right] \left(\frac{\theta}{\sin\theta} \right)^{1/2} \mathrm{d}y. \tag{4.46}$$

This integral is tabulated in the Handbook of Mathematical Functions of Abramowitz (page 486, eq. (11.4.29)) [253] and it results:

$$F_{GS}(\theta, \Delta s) = \frac{1}{2\pi} \left(\frac{\theta}{\sin\theta} \right)^{\frac{1}{2}} \frac{\lambda_1^{(s)}}{\Delta s} \exp\left(\frac{\Delta s}{8\lambda_1^{(s)}} \right) \exp\left(-\frac{\lambda_1^{(s)}}{2\Delta s} \theta^2 \right). \tag{4.47}$$

We finally obtained an analytical form for the polar scattering angle probability. Let us notice that for $\theta \to 0$ $\sin\theta \to \theta$, and if:

$$\Delta s \ll \lambda_1^{(s)}, \tag{4.48}$$

this function does not differ significantly from the Gaussian distribution with variance $\Delta s / \lambda_1^{(s)}$:

$$F_{GS}(\theta, \Delta s) = \frac{1}{2\pi} \frac{\lambda_1^{(s)}}{\Delta s} \exp\left(-\frac{\lambda_1^{(s)}}{2\Delta s} \theta^2 \right). \tag{4.49}$$

This analytical distribution offers a simple tool to generate the angular deflection caused by soft collisions experienced by the hot electron. As shown in Sec. 4.6, it will be particularly useful in the building of the mixed algorithm.

4.4.2 Hard collisions

Hard collisions, i.e. the collisions that deviate the primary particle for a polar scattering angle greater than θ_s, are simulated considering a two-bodies interaction. In particular, the primary electron can scatter with other free plasma electrons or ions. The probability distribution for the polar scattering angle reads:

$$p^{(h)}(\theta_h) = c_n \frac{\mathrm{d}\sigma(\theta)}{\mathrm{d}\Omega} \sin\theta H(\theta - \theta_s), \tag{4.50}$$

where c_n is the normalization coefficient and $H(\theta - \theta_s)$ is the Heaviside function, since we want to exclude small scattering phenomena, already simulated according to the GS theory. Here $\frac{\mathrm{d}\sigma(\theta)}{\mathrm{d}\Omega}$ is the DCS related to the scattering center (free plasma electron or ion, see Sec. 4.3).

4.5 Stopping Power

The energy loss of a fast charged particle that propagates in matter has been widely discussed in the last century. The topic is particularly interesting in several fields such as radiotherapy, radiation protection, nuclear science or space engineering. The problem was firstly addressed by Bethe in 1930 [254] [255] and by Bohr in 1948 [256] [257] [258]. Thereafter, the theoretical comprehension of the phenomenon became more detailed thanks to contribution of Enrico Fermi and its studies on density effects [259] [260] [261]. Finally,

the bremsstrahlung energy losses were addressed by Seltzer and Berger [262] [263]. Nowadays, several numerical codes and tabulations are available. Regarding the loss of energy of electrons in matter, the ICRU report [264] summarizes the most important theoretical concepts and it tabulates the main physical quantities for several materials and energy ranges. For a practical application, the ESTAR program in the NIST website calculates the stopping power and the range of electrons in materials considering the ICRU's tabulation [265].

In the last decades, with the increasing interest in nuclear fusion, particular attention was devoted to the study of the energy loss of electrons in plasma [266] [267] [268] [123] [269]. As already mentioned in previous sections, a hot electron that propagates in plasma undergoes several collisions with other electrons (free or bound) or with ions. Collisions with free plasma electrons or with the remaining electronic structure of an atom are usually accompanied by energy transfer. Collisions with nuclei cause mostly changes in electron direction, while the energy transfer is limited because of the greater mass of the nucleus. Another source of energy loss is the excitation of plasma waves. In this case, the electric field generated by the hot electron makes plasma electrons oscillate, causing an energy transfer between the electron and the medium.

In this section, we describe with detail the different sources of energy loss for a hot electron that propagates in plasma, reporting the equations that rule the process.

4.5.1 Energy loss in electron-electron collision

While propagating in a plasma, a hot electron collides with other free plasma electrons [123]. Since the two colliding particles have the same mass, the primary particle may transfer part of its energy to the plasma electron. This energy transfer can be modelled considering the Moller cross section (4.2) recast in terms of energy loss ε:

$$\frac{\mathrm{d}\sigma}{\mathrm{d}\varepsilon} = \frac{2\pi r_0^2}{(\gamma-1)\,\beta^2}\left[\frac{1}{\varepsilon^2} + \frac{1}{(1-\varepsilon)^2} + \left(\frac{\gamma-1}{\gamma}\right)^2 - \frac{2\gamma-1}{\gamma^2\varepsilon\,(1-\varepsilon)}\right]. \tag{4.51}$$

In particular, ε is the ratio between the energy lost W by the primary particle and its kinetic energy T, i.e. $\varepsilon = W/T$. Let us notice that is possible to write this equation in terms of the polar scattering angle in center of mass θ^* (eq. (4.2)) using the formula:

$$W = \frac{T}{2}\left(1-\cos\theta^*\right) \Rightarrow \varepsilon = \frac{1}{2}\left(1-\cos\theta^*\right). \tag{4.52}$$

This formula relates the center of mass scattering angle θ^* with the energy transfer W in a binary collision. It is derived in Landau II [232], considering the conservation of the four-momentum in a scattering process between two relativistic particles.

The stopping power (i.e. the energy loss per unit length) of a hot electron due to binary collisions reads:

$$\begin{gathered}\frac{\mathrm{d}E}{\mathrm{d}S}_{ee} = -n_e T\int_{\varepsilon_{min}}^{\varepsilon_{max}} \varepsilon\left(\frac{\mathrm{d}\sigma}{\mathrm{d}\varepsilon}\right)\mathrm{d}\varepsilon = \\ -n_e T\frac{2\pi r_0^2}{(\gamma-1)\,\beta^2}\int_{\varepsilon_{min}}^{\varepsilon_{max}} \varepsilon\left[\frac{1}{\varepsilon^2} + \frac{1}{(1-\varepsilon)^2} + \left(\frac{\gamma-1}{\gamma}\right)^2 - \frac{2\gamma-1}{\gamma^2\varepsilon\,(1-\varepsilon)}\right]\mathrm{d}\varepsilon.\end{gathered} \tag{4.53}$$

The upper integration limit ε_{max} is taken as 1/2, because the higher energy electron after the collision is considered as the primary. If the incident electron transfers an half of its kinetic energy to a plasma electron, this latter will become the primary. ε_{min} is chosen according to the quantum theory of diffraction [123]. Expanding the cosine for $\theta^* \to 0$ in eq.(4.52) one obtains:

$$\varepsilon_{min} \sim \frac{\theta^{*2}_{min}}{4}. \tag{4.54}$$

Here, θ_{min} can be written in terms of variation of the particle momentum Δp from simple trigonometric considerations (see Fig. 4.5), i.e.:

$$\Delta p = p^* \sin\theta^*, \theta^* \to 0 \Rightarrow \Delta p \simeq p^* \theta^*_{min}. \tag{4.55}$$

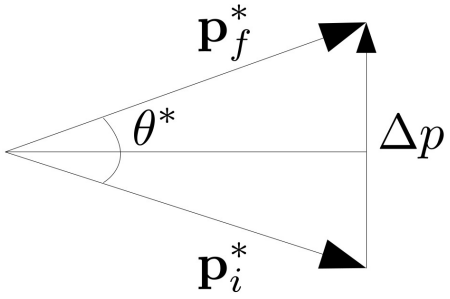

Figure 4.5: Directions of initial and final momentum $\mathbf{p}^*$ in the center of mass reference frame. Δp is the variation of the momentum due to the collision.

Substituting this result in the Heisenberg's uncertainty principle, and considering the maximum uncertainty on the particle position as the Debye length λ (or the ion sphere radius as explained in Sec. 4.2), the following relation for θ^*_{min} is obtained:

$$\Delta p \Delta x \simeq \hbar \Rightarrow \theta^*_{min} = \frac{\hbar}{p^* \lambda}. \tag{4.56}$$

Considering now the expressions for the electron momentum and the de Broglie wavelength in the center of mass:

$$p^* = \frac{mc\sqrt{2\left(\gamma - 1\right)}}{2}; \quad \lambda_{Dee} = \frac{\hbar}{mc\sqrt{2\left(\gamma - 1\right)}} = \frac{\hbar}{2p^*}, \tag{4.57}$$

from eq. (4.56) we obtain:

$$\theta^*_{min} = \frac{2\lambda_{Dee}}{\lambda}. \tag{4.58}$$

As such, from eq. (4.54):

$$\varepsilon_{min} = \frac{\theta^{*2}_{min}}{4} = \left(\frac{\lambda_{Dee}}{\lambda}\right)^2. \tag{4.59}$$

Considering these two integration limits (ε_{min} and ε_{max}) and the fact that $\varepsilon_{min} \ll 1$, the

result of the integral (4.53) is:

$$\frac{\mathrm{d}E}{\mathrm{d}S}_{ee} = \frac{2\pi r_0^2 mc^2 n_e}{\beta^2} = \left[\ln(\frac{1}{2}) + 2 + \ln(\frac{1}{2}) + \frac{1}{8}\Big(\frac{\gamma-1}{\gamma}\Big)^2 + \frac{2\gamma-1}{\gamma^2}\ln\frac{1}{2} - \ln\varepsilon_{min} - \frac{1}{1-\varepsilon_{min}}\right] = \frac{2\pi r_0^2 mc^2 n_e}{\beta^2}\left[2\ln(\Lambda) + \ln\left(\frac{1}{4}\right) + 1 + \frac{1}{8}\left(\frac{\gamma-1}{\gamma}\right)^2 - \left(\frac{2\gamma-1}{\gamma^2}\right)\ln(2)\right]. \tag{4.60}$$

Here Λ represents the so-called Coulomb logarithm, and it reads:

$$\Lambda = \frac{\max[\lambda_D, r_i]}{\lambda_{ee}^*}. \tag{4.61}$$

If the de Broglie length is smaller than the Landau impact parameter b_0, the quantum effects can be neglected and the plasma becomes classical [48]. As such, the literature suggests to use as Coulomb logarithm the expression[219] [121] [122]:

$$\Lambda = \frac{\max[\lambda_D, r_i]}{\max[\lambda_{ee}^*, b_0]}. \tag{4.62}$$

Let us notice that, in the case of a classical ideal plasma, the formula (4.62) corresponds to the classical formula of the Coulomb logarithm (1.17), as shown in Sec. 1.1.2.

4.5.2 Energy loss in electron-atom collision

A hot electron that propagates in a medium experiences collisions with atoms. In particular, the electron may undergo through an inelastic collision and transfer energy to the electronic structure of the atom. As remarked in Sec. 4.3, these collisions do not influence strongly the direction of the primary particle, but, conversely, they play an important role in the electron energy loss.

The energy transfer from a hot electron to the atomic structure is modelled with the mean excitation potential I. This quantity models the energy transfer between an electron and the atomic structure of an atom, and it is defined as the mean of the excitation energy E_n weighted by the oscillator strength f_n:

$$\ln I = \sum_n f_n \ln E_n. \tag{4.63}$$

In the case of non-ionized atom, the literature proposes a theoretical model [270] validated and refined by many experimental results. Nowadays, a detailed tabulation of I for elements and compounds is contained in the ICRU report [264]. The values of I contained in the ICRU report are implemented in the code for each element and they are used in the case of cold material (i.e. T$\leq$1 eV). Conversely, in case of ionized atoms, I is calculated according to the Thomas-Fermi theory[208]. In particular, More proposes a simple analytical formula that computes the values of I according to the ionization degree of an atom [271] [209]:

$$I = aZ\frac{\exp\left[1.294\left(\frac{Z^*}{Z}\right)^{0.72-0.18Z^*/Z}\right]}{\sqrt{1-\frac{Z^*}{Z}}}. \tag{4.64}$$

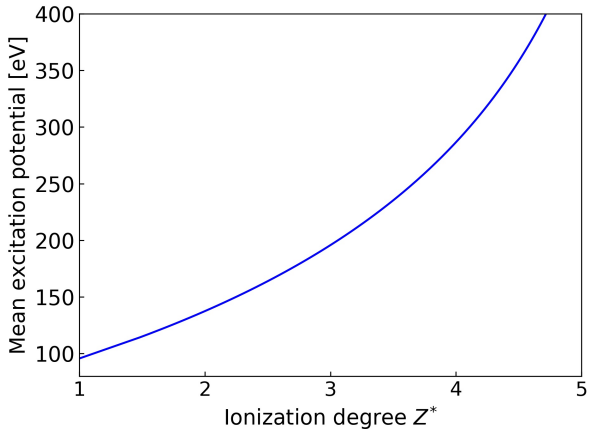

Figure 4.6: Evolution of the mean excitation potential for carbon as a function of ionization degree, according to the formula (4.64).

The constant a is set to ∼10 eV to fit the numerical calculations of I provided by McGuire [272] [273] (McGuire computed the values of I for several elements such as gold, aluminium and krypton using the Thomas-Fermi theory). Figure 4.6 shows the behaviour of I as a function of the ionization degree for carbon. For $Z^*=1$, I is equal to $\sim$ 95 eV, a value slightly greater compared to the value of 78 eV for the non-ionized atom. This is consistent with the fact that the values of I for ionized elements are in general greater compared to the non-ionized case. Qualitatively, this happens because the primary particle interacts with inner atomic electrons which feel a greater nuclear Coulomb potential.

To calculate the electron stopping power, I is used in the Bethe-Bloch formula [274]:

$$\frac{\mathrm{d}E}{\mathrm{d}S}_{ei} = \frac{2\pi r_0^2 mc^2 \left(Z - Z^*\right) n_i}{\beta^2} \left\{ \ln\left[\left(\frac{E}{I}\right)^2 \frac{(\gamma+1)}{2} \right] + \frac{1}{\gamma^2} + \frac{1}{8}\left(\frac{\gamma-1}{\gamma}\right)^2 - \left(\frac{2\gamma-1}{\gamma^2}\right)\ln(2) \right\}. \tag{4.65}$$

Here E represents the electron kinetic energy and n_i the atomic density of the i-specie. Let us remark that, in the classical Bethe-Bloch formula, i.e. the one commonly used for cold materials, the term $(Z - Z^*)$ in the coefficient is substituted by Z. Here we used $(Z - Z^*)$ since the impact of the primary particle in the plasma case is with the remaining bound electrons, thus $Z_b = Z - Z^*$.

In the case of several ion species, it is assumed that the stopping power additivity rule is a good approximation. For a plasma containing N ion species, this rule reads:

$$\frac{\mathrm{d}E}{\mathrm{d}S}_{ej} = \sum_j^N \left(\frac{\mathrm{d}E}{\mathrm{d}S}_{ei}\right)_j, \tag{4.66}$$

where j is the sum over all the species. This can be considered correct in plasma, since ions are free and molecular binding is absent. However, in cold materials (T < 1 eV), the molecular bond should be considered: the interaction of the hot electron is no more with atoms seen as single identity, but rather with the entire molecule. As such, the additivity rules of stopping power should break. Fig. 4.7 reports the comparison between the stopping power of an electron moving in polystyrene computed by ESTAR [265] or using the additivity rule. In particular, the mean ionization potential of polystyrene used

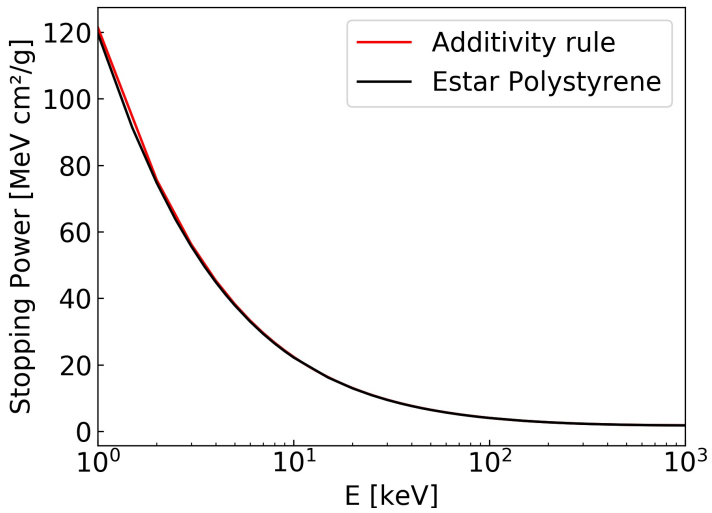

Figure 4.7: Comparison between the stopping power of electron in polystyrene computed using ESTAR [265] and using the additivity rule. The value of I used in Estar is 68.7 eV, while the values used in the additivity rule are 19.2 and 78 eV (hydrogen and carbon, respectively).

in ESTAR is $I = 68.7$ eV, while the values of I used for carbon and hydrogen in the additivity rule are 19.2 and 78 eV, respectively. As can be seen from the figure, there is not an important difference between the two cases. Only for electron energy less than 10 keV the two curves show a slightly different behaviour, but at this point the electron is almost stopped and it will propagate only few micrometers in the target. As such, the additivity rule is adequate for our purposes, either for the plasma and the cold case.

4.5.3 Energy loss due to plasmon excitation

The formulas reported in Sec. 4.5.1 and 4.5.2 describe the electron energy loss due to binary collisions with other free plasma electrons or with partially ionized atoms (or with non ionized atoms in the cold case). These interactions verify if the electron passes at distances from the target particle less than the Debye length (or ion sphere radius). For greater interaction distances, the plasma acts as a continuous medium in which the charged particles participate in collective behaviour, responding to the electric field generated by the hot electron [275]. In particular, electron loses energy by exciting plasma oscillation. A non-relativistic treatment of the phenomenon is given in the second edition of Jackson [242] and the stopping power formula that describes the loss of energy due to plasma wave excitation is given by:

$$\frac{\mathrm{d}E}{\mathrm{d}S}_{ep} = \frac{2\pi r_0^2 mc^2 n_e}{\beta^2} \ln\left(1.123 \frac{\beta c}{\omega_p \max[\lambda_D, r_i]}\right)^2 . \tag{4.67}$$

The analytical derivation of this formula is given in appendix D.

4.5.4 Conclusion

The total stopping power for a hot electron moving in plasma is obtained by adding the three contributions: the energy loss due to collisions with free plasma electrons (4.60),

the energy loss due to collisions with partially ionized atoms (4.65) and the energy loss due to plasma wave excitation (4.67):

$$S_e(E) = \left(\frac{\mathrm{d}E}{\mathrm{d}S}\right)_{ee} + \left(\frac{\mathrm{d}E}{\mathrm{d}S}\right)_{ei} + \left(\frac{\mathrm{d}E}{\mathrm{d}S}\right)_{ep}. \tag{4.68}$$

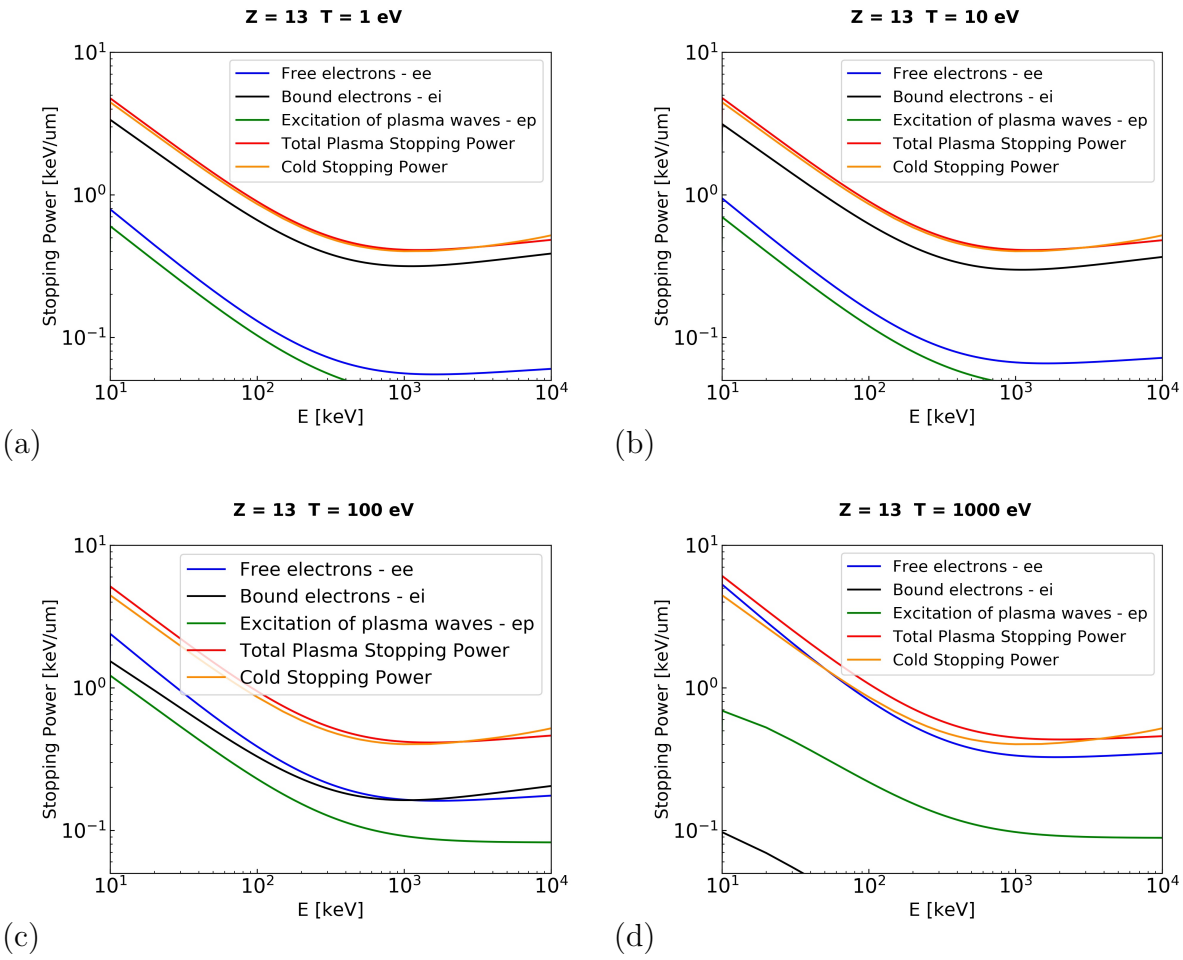

Figure 4.8: Different contributions to the stopping power for a hot electron moving in Aluminium plasma. The blue line is the contribution due to collisions with free electrons, the black line the contribution due to collisions with bound electrons and the green line is the contribution due to excitation of plasma waves. The red line is the sum of the three contributions, i.e. the total stopping power of the electron. The orange curve represent the stopping power in cold Aluminium, taken from ESTAR database [265]. (a) $T = 1$ eV,(b) $T = 10$ eV,(c) $T = 100$ eV, (d) $T = 1000$ eV.

Figure 4.8 shows the different contributions to the stopping power for a hot electron moving in Aluminium plasma, for T= 1, 10, 100, 1000 eV. The sum of the three components is indicated by the red line, while the stopping power for the cold material computed using ESTAR is represented by the orange line [265]. The contribution of bound electrons to the stopping power is predominant for lower plasma temperatures, when the degree of ionization is not high. For higher temperatures, the number of bound electrons decreases and the contribution due to free electrons becomes predominant. It is interesting to notice that the stopping powers of cold and plasma cases do not differ dramatically. Note that

in the case of cold material ($T < 1$ eV), only the second term $\left(\frac{\mathrm{d}E}{\mathrm{d}S}\right)_{ei}$ is considered.

In this description we did not mention the energy losses due to Bremsstrahlung generation. This effect is important for electron kinetic energy greater than ∼MeV and it can be neglected in our regime. In particular, the ratio between the collisional and the bremsstrahlung energy losses in cold material writes [276]:

$$\frac{(\mathrm{d}E/\mathrm{d}S)_b}{(\mathrm{d}E/\mathrm{d}S)_c} \sim \frac{TZ}{700}, \tag{4.69}$$

where T is the electron energy in MeV. As such, for an electron with average kinetic energy of ∼30 keV in CH ($Z = 3.5$), the collisional stopping power is four orders of magnitude greater compared to the bremsstrahlung stopping power.

Let us also mention that, in the cold case, the Fermi density effect is neglected. This effect reduces the values of the stopping power because of the atom polarization in the medium [242] and it becomes important for highly energetic electrons (∼ MeV).

4.6 Algorithm to build the MC code

After having described the physical phenomena of interest, we report in this section the practical implementation of the algorithm to simulate the hot electron propagation in plasma. The first part of this section is devoted to the description on how the transport paths are calculated, since these quantities play an important role. In the second part, the steps followed to implement the algorithm are listed. In the last part of the section, a discussion on the problematics related to the calculation of the mean free paths in an ICF irradiated target is presented.

4.6.1 Mean Free Path

In Sec. 4.4.1, we introduced the concept of the transport mean free path λ_l:

$$\lambda_l^{-1} = 2\pi N \int_{\theta_{min}}^{\theta_{max}} \frac{\mathrm{d}\sigma(\theta)}{\mathrm{d}\Omega}\big[1 - P_l(\cos\theta)\big]\sin\theta \mathrm{d}\theta, \tag{4.70}$$

where N is the number of scattering centers per unit volume, $\sigma(\theta)$ the differential cross section of elastic scattering and $P_l(\cos\theta)$ the unnormalized Legendre polynomials. According to the order of the Legendre polynomial, one has the "first, the "second" and so on transport mean free path. For our purposes, the first transport path λ_1 is particularly important, since it appears in the soft scattering polar angle distribution $F_{GS}(\theta, \Delta s)$, eq. (4.49):

$$\lambda_1^{-1} = 2\pi N \int_{\theta_{min}}^{\theta_{max}} \frac{\mathrm{d}\sigma(\theta)}{\mathrm{d}\Omega}\big[1 - \cos\theta\big]\sin\theta \mathrm{d}\theta. \tag{4.71}$$

Another important quantity is the *mean free path*, defined as:

$$\lambda^{-1} = 2\pi N \int_{\theta_{min}}^{\theta_{max}} \frac{\mathrm{d}\sigma(\theta)}{\mathrm{d}\Omega}\sin\theta \mathrm{d}\theta. \tag{4.72}$$

This quantity expresses the mean distance travelled by a particle before experiencing a collision.

Since these quantities are of practical importance for our purposes, we report, in this section, their analytical calculation. In particular, the evaluation of the integrals considering the three DCSs described in Sec. 4.3 is presented.

Let us also mention that, in the case of multi-specie medium like a plasma, the mean free paths are computed according to the additivity rule [201]:

$$\frac{1}{\lambda} = \sum_i \frac{1}{\lambda_i}. \tag{4.73}$$

Here the summation is over all the species: electrons and ions in the case of plasma, or different elements that compose the material in the cold case.

4.6.1.1 Electron - Electron transport paths

In case of electron-electron collision, the cross section to use in eqs. (4.71) and (4.72) to compute the paths is the Moller DCS in laboratory frame (4.4). We start considering the first transport mean free path λ_1:

$$\begin{aligned}\left(\frac{1}{\lambda_1}\right)_{ee} &= 2\pi n_e \int_{\theta_{min}}^{\theta_{max}} \frac{\mathrm{d}\sigma(\theta)}{\mathrm{d}\Omega}_{ee}\big[1-\cos\theta\big]\sin\theta \mathrm{d}\theta = \\ &8\pi n_e \left(\frac{r_0}{\gamma\beta^2}\right)^2 \int_{\theta_{min}}^{\theta_{max}} \cos\theta \Bigg\{ \frac{1}{\sin^4\theta} + \frac{(\gamma+1)^2}{4\cos^4\theta} \\ &+ \frac{\left[\left(\gamma^2-1\right)/\gamma\right]^2}{\big[(\gamma-1)\sin^2\theta+2\big]^2} - \frac{(2\gamma-1)(\gamma+1)}{2\gamma^2\sin^2\theta\cos^2\theta}\Bigg\}\big[1-\cos\theta\big]\sin\theta \mathrm{d}\theta.\end{aligned} \tag{4.74}$$

Here n_e is the free electron plasma density, r_0 the classical electron radius and β and γ the kinematic quantities related to the incident electron. The indefinite integral is solved by a change of variables:

$$x = \cos\theta \Rightarrow \mathrm{d}\theta = -\frac{\mathrm{dx}}{\sqrt{1-x^2}}, \tag{4.75}$$

which yields:

$$\begin{aligned}\left(\frac{1}{\lambda_1}\right)_{ee} &= -8\pi n_e \left(\frac{r_0}{\gamma\beta^2}\right)^2 \Bigg[-\frac{1}{2}\left(\frac{1}{1-x^2}\right) + \frac{1}{4}\ln\left(|1-x|\right) - \frac{1}{4}\ln\left(|1+x|\right) + \frac{1}{4}\frac{2x}{1-x^2} \\ &+\left(\frac{1}{2x^2}-\frac{1}{x}\right)\frac{(\gamma+1)^2}{4} + \Bigg(-\frac{1}{2}\frac{1}{a^2(1-x^2)+2a} - \frac{1}{2a^2c}\big(-\ln(|1-x/c|)+\ln(|1+x/c|)\big)+ \\ &\frac{1}{(4ca^2)}\Big(-\ln(|c-x|)+\ln(|c+x|)+\frac{2cx}{c^2-x^2}\Big)\Bigg)\left(\frac{\gamma^2-1}{\gamma}\right)^2 - \Bigg(\frac{1}{2}\ln(|1-x|) \\ &+\frac{1}{2}\ln(|1+x|)-\ln(|x|)+\frac{1}{2}\ln(|x+1|)-\frac{1}{2}\ln(|1-x|)\Bigg)\left(\frac{(2\gamma-1)(\gamma+1)}{(2\gamma^2)}\right)\Bigg]_{x_{min}}^{x_{max}},\end{aligned} \tag{4.76}$$

where $a = (\gamma-1)$, $b = \frac{2}{a}$ and $c = \sqrt{(1+b)}$.

The mean free path is calculated analogously:

$$\left(\frac{1}{\lambda}\right)_{ee} = 2\pi n_e \int_{\theta_{min}}^{\theta_{max}} \frac{\mathrm{d}\sigma(\theta)}{\mathrm{d}\Omega}_{ee} \sin\theta \mathrm{d}\theta = -8\pi n_e \left(\frac{r_0}{\gamma\beta^2}\right)^2 \left[-\frac{1}{2}\left(\frac{1}{1-x^2}\right) + \left(\frac{1}{2x^2}\right)\frac{(\gamma+1)^2}{4} - \left(\frac{1}{2}\frac{1}{a^2(1-x^2)+2a}\right)\left(\frac{\gamma^2-1}{\gamma}\right)^2 - \left(\frac{1}{2}\ln(|1-x|) + \frac{1}{2}\ln(|1+x|) - \ln(|x|)\right)\left(\frac{(2\gamma-1)(\gamma+1)}{(2\gamma^2)}\right)\right]_{x_{min}}^{x_{max}}. \tag{4.77}$$

The integration limits are set by the physics of the collision: x_{max} is related to θ_{min}, which is imposed by the diffraction theory, as explained in Sec. 4.5. In the laboratory frame θ_{min} reads:

$$\theta_{min} = \frac{\hbar}{p\lambda_D}. \tag{4.78}$$

x_{min} is equal to $\cos\theta_s$, where $\theta_s \sim 10°$ in the case of soft collisions, otherwise it writes:

$$x_{min} = \sqrt{\frac{\gamma+1}{\gamma+3}}. \tag{4.79}$$

This latter equation is obtained considering a collision in which the primary electron transfers half of its kinetic energy to the plasma electron [210][232].

4.6.1.2 Electron- Ions transport paths

The transport paths for the elastic electron-ion collisions are computed considering the two DCSs (4.36) or (4.37) and must be differentiated between partially and fully ionized atoms.

Partially ionized atoms

To compute the mean free paths considering collisions with partially-ionized atoms, in eq. (4.71) and (4.72) the DCS (4.36) must be used. The first transport path reads:

$$\left(\frac{1}{\lambda_1}\right)_{ei} = 2\pi n_i \int_{\theta_{min}}^{\theta_{max}} \frac{\mathrm{d}\sigma(\theta)}{\mathrm{d}\Omega}_{ei} \big[1-\cos\theta\big]\sin\theta \mathrm{d}\theta = 2\pi n_i \int_{\theta_{min}}^{\theta_{max}} \frac{e^4}{p^2v^2}\left\{\frac{Z^{*2}}{\left[1-\cos\theta+2\mathrm{F}\right]^2} + \frac{Z_b^2}{\left[1-\cos\theta+2\mathrm{B}\right]^2} + \frac{2Z_bZ^*}{\left[1-\cos\theta+2\mathrm{B}\right]\left[1-\cos\theta+2\mathrm{F}\right]}\right\}\times \big[1-\cos\theta\big]\sin\theta\mathrm{d}\theta, \tag{4.80}$$

where n_i is the ion density for the specie i. This integral is solved with the change of the integration variable:

$$1-\cos\theta = x \Rightarrow \mathrm{d}\theta = \frac{\mathrm{d}x}{\sqrt{1-(1-x)^2}}, \tag{4.81}$$

which yields:

$$\left(\frac{1}{\lambda_1}\right)_{ei} = \frac{2\pi n_i e^4}{p^2v^2}\left[\frac{2F}{2F+x} + \ln(|2F+x|) + \frac{2B}{2B+x} + \ln(|2B+x|) + \frac{1}{2(B-F)}\big(x-2F\ln(|2F+x|)\big) + \frac{1}{2(F-B)}\big(x-2B\ln(|2B+x|)\big)\right]_{x_{min}}^{x_{max}}. \tag{4.82}$$

Analogously, the mean free path is:

$$\left(\frac{1}{\lambda}\right)_{ei} = 2\pi n_i \int_{\theta_{min}}^{\theta_{max}} \frac{\mathrm{d}\sigma(\theta)}{\mathrm{d}\Omega}_{ei} \sin\theta \mathrm{d}\theta = \frac{2\pi n_i e^4}{p^2 v^2}\left[\frac{1}{2F+x} + \frac{1}{2B+x} + \frac{1}{2F-2B}\ln(|2B+x|) - \frac{1}{2F-2B}\ln(|2F+x|)\right]_{x_{min}}^{x_{max}}. \tag{4.83}$$

In the integrals, $\theta_{min} = 0$ and $\theta_{max} = \theta_s \sim 10^\circ$ or $\theta_{max} = \pi$ in the case we are considering soft collisions or not.

Ionized atoms

In case of completely ionized atoms, the Dalitz DCS (4.37) is used:

$$\left(\frac{1}{\lambda_1}\right)_{ei} = 2\pi n_i \int_{\theta_{min}}^{\theta_{max}} \frac{\mathrm{d}\sigma(\theta)}{\mathrm{d}\Omega}_{ei} \big[1-\cos\theta\big]\sin\theta \mathrm{d}\theta = 2\pi n_i \int_{\theta_{min}}^{\theta_{max}} \left(\frac{Zr_0}{\gamma\beta^2}\right)^2 \frac{1}{4\sin^4\theta/2}\left(1-\beta^2\sin^2\frac{\theta}{2}\right)\left(\frac{\Lambda^2\sin^2\theta/2}{1+\Lambda^2\sin^2\theta/2}\right)^2 \big[1-\cos\theta\big]\sin\theta \mathrm{d}\theta. \tag{4.84}$$

As before, the integral is carried out with the variable substitution:

$$1-\cos\theta = x \Rightarrow \mathrm{d}\theta = \frac{\mathrm{d}x}{\sqrt{1-(1-x)^2}}, \tag{4.85}$$

which yields:

$$\left(\frac{1}{\lambda_1}\right)_{ei} = 2\pi n_i \left(\frac{Zr_0}{\gamma\beta^2}\right)^2 \left[\ln\Big(x\Lambda^2+2\Big) + \frac{2}{(x\Lambda^2+2)} - \frac{\beta^2}{2}x + \frac{\beta^2}{\Lambda^2}\ln\Big(x\Lambda^2+2\Big)^2 + \frac{\beta^2 x}{\Lambda^2}\frac{2}{\Lambda^2 x+2}\right]_{x_{min}}^{x_{max}}. \tag{4.86}$$

The mean free path in this case writes:

$$\left(\frac{1}{\lambda}\right)_{ei} = 2\pi n_i \left(\frac{Zr_0}{\gamma\beta^2}\right)^2 \int_{\theta_{min}}^{\theta_{max}} \frac{\mathrm{d}\sigma(\theta)}{\mathrm{d}\Omega}_{ei} \sin\theta \mathrm{d}\theta = \left[-\frac{\Lambda^2}{2+\Lambda^2 x} - \frac{\beta^2}{2}\ln\big(2+\Lambda^2 x\big) - \frac{\beta^2}{2+\Lambda^2 x}\right]_{x_{min}}^{x_{max}}. \tag{4.87}$$

In the integrals, $\theta_{min} = 0$ and $\theta_{max} = \theta_s \sim 10^\circ$ or $\theta_{max} = \pi$ in the case we are considering soft collisions or not.

4.6.2 Numerical framework

The computation domain is divided in cells, which in turn are divided in tetrahedra. Each tetrahedron is defined by nodes. Fig. 4.9 shows, for example, the partition of a cubic domain into cubic cells, while Fig. 4.10 shows how each cell is divided in six tetrahedra. The lateral dimensions of these cells and tetrahedra are of the order of the μm or even less, in order to obtain a high precision. The values of the physical quantities that describe the material (densities, temperatures...) are given at each node.

In this structure, hot electrons propagate and the physical quantities of interest such as the cross sections or the stopping power formulas are computed locally considering the material properties in each cell. Let us also mention that each electron propagates independently and the code is parallelized using openMP. As such, the history of each electron is followed by one openMP thread, obtaining an efficient parallelization.

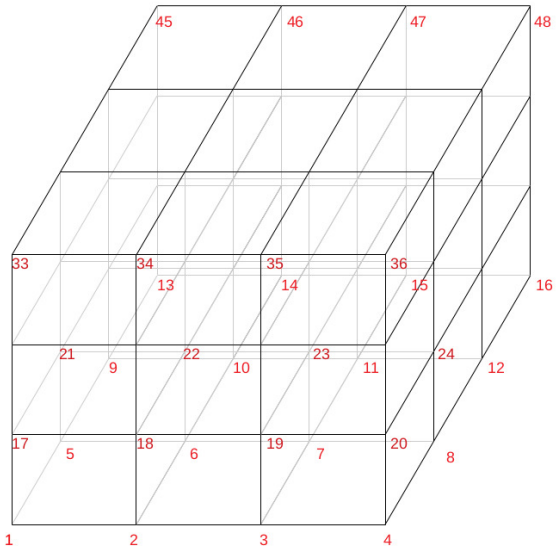

Figure 4.9: Partitioning of a cubic computational domain in cubic cells. The node number is indicated.

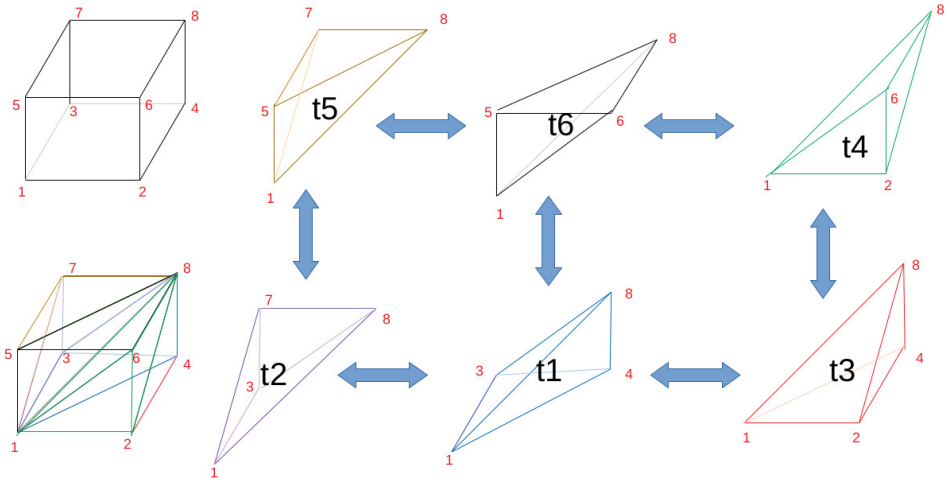

Figure 4.10: Partitioning of a cubic cell into six tetrahedra. The tetrahedron number is indicated by t-i and the node numbers are reported.

4.6.3 Propagation algorithm

As already mentioned, a mixed simulation algorithm was chosen to simulate the hot electron propagation. In particular, soft collisions are described by means of the multiple scattering theory, while hard collisions are individually simulated (see Sec. 4.4). The algorithm is implemented following closely the method used in the Penelope MC code [212] [194], even if some modifications are required because of the different nature of the

problem. Notably, in addition to the modifications in stopping powers and scattering cross sections, our numerical method implements the following differences with Penelope:

- unstructured tetrahedron grid framework, with spatial gradients and automatic update of $S_e(E)$.
- modification of free path probabilities considering inhomogeneous media.

The steps are listed as follows [212]:

- 1) Set the initial position and momentum direction $\mathbf{r}$ and $\mathbf{p}$ of the electron.

- 2) Sample the length of the step up to the following hard collision using the formula:

$$\Delta s = -\lambda^h \ln(\xi). \tag{4.88}$$

Here ξ is a random number between zero and 1 i.e. $\xi \in (0, 1]$. λ^h is the hard mean free path. The hard mean free path is computed according to:

$$\lambda^h = \max\{\lambda, C_s\lambda_1\}, \tag{4.89}$$

where λ is the mean free path (4.72) and λ_1 is the first transport path (4.71). If the medium is multi-specie, the two quantities are computed according to the additivity rule (4.73). C_s is a preselected small constant chosen by the user to control the computer time needed to simulate the electron history in a mixed algorithm. Its value should be small, in order to not have any influence on the simulation results. According to Penelope developers, simulation results are generally stable under variations of C_s within the interval (0,0.1) [215]. As in Penelope, we set C_s=0.05 [194] [212].

If $\lambda > C_s\lambda_1$ the simulation is detailed and the scattering phenomena are simulated individually (i.e. simulating a two-body interaction). Conversely, if $\lambda < C_s\lambda_1$, the simulation enters in the mixed mode, and soft and hard scattering phenomena are simulated separately. In our case, the simulation runs the most of the time in mixed mode. Only when the electron has energy around $\sim$ 10 keV the detailed algorithm comes into play, but, at this point, the electron will experience only few collisions before being completely stopped. The two algorithms are explained in the following.

4.6.3.1 Detailed Simulation

- 3a) If $\lambda > C_s\lambda_1$ the simulation becomes a detailed simulation. The particle is propagated for a step Δs and the collision is simulated. In case of multiple-species material, the probability of interacting with the i-th element is calculated according to the equation:

$$\mathrm{P}_i = \frac{\sigma_i}{\sigma_{tot}} = \frac{\lambda_i^{-1}}{\sum_j \lambda_j^{-1}}, \tag{4.90}$$

where the sum is over all the j elements and λ are the mean free paths considering the collisions with the j-th element:

$$\lambda_j^{-1} = 2\pi n_j \int_{\theta_{min}}^{\theta_{max}} \frac{\mathrm{d}\sigma_j(\theta)}{\mathrm{d}\Omega} \sin\theta \mathrm{d}\theta. \tag{4.91}$$

The probability for the electron of finding the i-th specie is sampled considering eq. (4.90) and using a random number $\xi \in (0, 1]$, according to the following algorithm:

$$\sum_{j=0}^{i-1} P(j) \leq \xi \leq \sum_{j=0}^{i} P(j). \tag{4.92}$$

The collision with the i-th component is simulated by sampling the scattering polar angle from the DCS of the i-th element:

$$p(\theta) = c_n \frac{\mathrm{d}\sigma_i(\theta)}{\mathrm{d}\Omega} \sin\theta, \tag{4.93}$$

where c_n is a normalization coefficient. The azimuthal angle φ is sampled from an uniform distribution from 0 to 2π. Let us notice that, since the algorithm is running in "detailed mode", the separation between hard and soft collision is not effective. The sampling is conducted from 0 to π in the case of collision with ions (considering the DCSs (4.29),(4.23) or (4.28), according to the ionization degree of the target atom), or from θ_{min} to θ_{max} in case the case of collisions with free electrons (using the Moller DCS (4.4) and considering the values of θ_{min} and θ_{max} dictated by the physics of the problem, as explained in Sec. 4.5.1). As such, contrary to formula (4.50), eq. (4.93) is not multiplied by the Heaviside function. As specified previously, directions changes due to collisions with bound electrons are not simulated.

4.6.3.2 Mixed Simulation

- 3b) If $\lambda < C_s\lambda_1$ the simulation uses the mixed algorithm. Soft collisions are treated using the Goudsmit-Saunderson theory (see Sec. 4.4.1) and hard collisions are simulated individually. In particular, the electron firstly moves for a distance $\tau = \Delta s\xi$, where ξ is a random number between 0 and 1. Here it experiences an artificial soft collision, and the polar angle θ_s that defines the new direction is sampled from the Goudsmit-Saunderson distribution function $F_{GS}(\theta_s, \tau)$ (4.49). The azimuthal angle φ is sampled from an uniform distribution between 0 and 2π. Let us notice that, for our purposes, $\tau \ll \lambda_1^{(s)}$ and the condition (4.48) is always valid.

  Finally, the electron moves for a distance $\Delta s - \tau$ where it will experience a single hard collision with a scattering center. As before, in the case of multi-species medium, the probability for the electron to collide with the i-th element is sampled according to eq. (4.92). After that, the scattering polar angle θ_h of the new direction is sampled from the DCS of the i-th scattering center, according to the distribution function (4.50). Fig. 4.11 represents schematically the two schemes: detailed and mixed.

- 4) The slowing down along the track is calculated considering the *continuous slowing down approximation*. With $S_e(E)$ (4.68) the stopping power, i.e. the energy loss

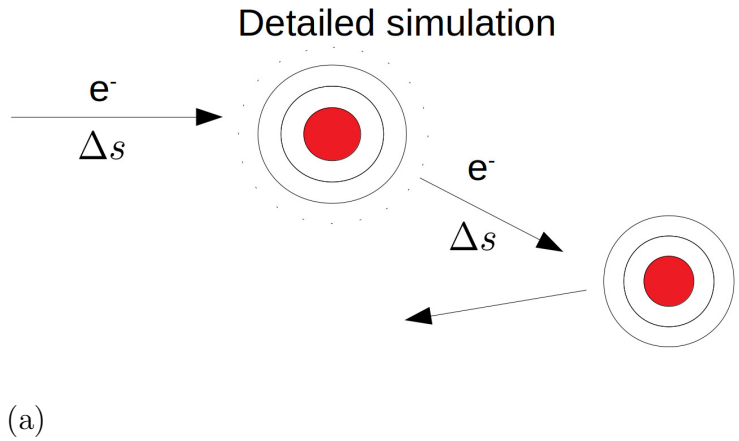

(a)

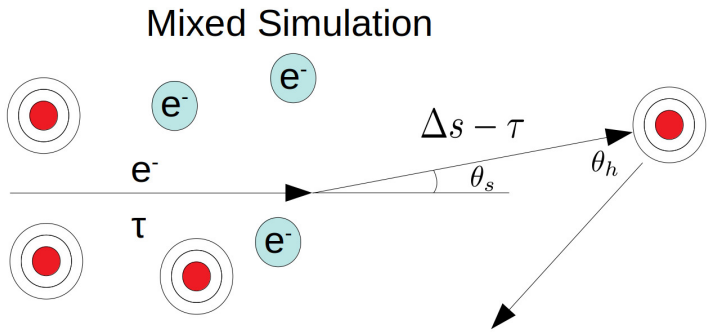

(b)

Figure 4.11: Schematic representation of the two algorithms: (a) detailed simulation algorithm; (b) mixed simulation algorithm. In a detailed simulation each scattering event is simulated individually in a two-bodies interaction. In the mixed algorithm soft and hard collisions are simulated separately.

per unit path length, the energy loss along the path Δr is simply $E_{loss} = S_e(E)\Delta r$, provided that $S_e(E)$ is constant along Δr. As mentioned in Sec. 4.6.2, this MC code will be implemented as a module of hydrodynamic codes and electrons move and deposit energy in 3D grid. If the electron enters the tetrahedron in the point $\mathbf{r}_0$ and it propagates for a path τ with direction $\mathbf{p}_0$, its position will be:

$$\mathbf{r}(\tau) = \mathbf{r}_0 + \mathbf{p}_0\tau, \tag{4.94}$$

as shown in Fig. 4.12. The energy loss is computed by integrating the stopping power S_e along the path τ:

$$\int_0^\tau \mathrm{d}t S_e(t) = \int_0^\tau \left[S(\mathbf{r}_1) + (\mathbf{r}(t) - \mathbf{r}_1)\cdot\nabla S\right]\mathrm{d}t, \tag{4.95}$$

where $\mathbf{r}_1$ is the position of the first node. The integral is analytically solvable and it yields:

$$E_{loss} = S(\mathbf{r}_1)\tau + \left[(\mathbf{r}_0 - \mathbf{r}_1)\,\tau + \frac{\mathbf{p}_0\tau^2}{2}\right]\cdot\nabla S. \tag{4.96}$$

Here we are assuming that the gradient is constant in each tetrahedron [277]. It is clear that large grid elements will cause greater error, while smaller grid elements

will allow for a more precise modelisation of the electron transport at the expense of computational time. In this regard, simulations are generally stable for tetrahedron lateral dimensions of the order of μm.

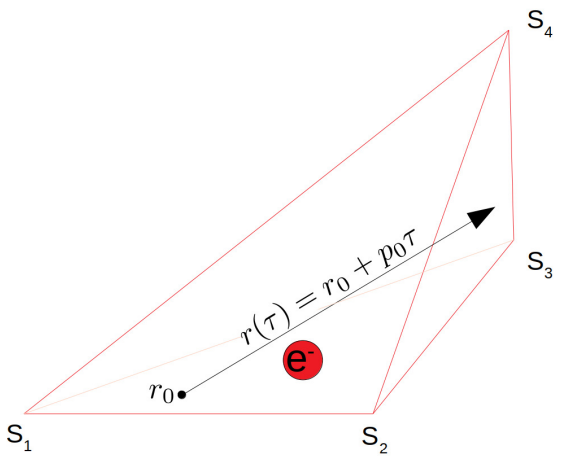

Figure 4.12: Grid element of the mesh in which the electron propagates. The four nodes are indicated. In each node, according to the material density and composition, the stopping power S_e assumes different values.

- 5) The process is repeated until the electron kinetic energy becomes lower than the electronic plasma temperature (i.e. the electron is thermalized) or until the electron exits from the computational domain.

Let us mention that, according to this algorithm, each electron history is followed individually and the electron scatters and loses energy according to the physical phenomena described in the precedent section. It is well known however, that the propagation of electrons emitted by laser-plasma interaction can be affected by the presence of collective effects and self-consistent electric and magnetic fields. These effects were neglected in previous studies of hot electron transport in fast ignition context [210] [278] [279]. Furthermore, in Ref [107], the authors evaluate the importance of the collective losses on the propagation of hot electrons in the context of SI, asserting that these are negligible because of the low intensities of the electron beam. The evaluation of the collective effects and the impact of the self generated electromagnetic fields on the hot electron propagation is an open topic and it can be the motivation for future works.

Another aspect that is not simulated by our model is the generation of secondary electrons. These electrons are generated by the hard collision of the primary particle with plasma or bound electrons, that become suprathermal. Hard collisions with a large energy exchange between two particles are less frequent compared to soft collisions (see 4.3). The fact that we are neglecting the secondary particle generation should not cause a great error in the model.

4.6.4 Calculation of mean free path in inhomogeneous media

In cold MC methods, the computation of the free path $\lambda(E, \rho)$ and the sampling of the collision distance Δs (eq. 4.88) is done at the beginning of electron history [194][212]. If the electron propagates in an heterogeneous medium and the collision distance Δs exceeds

the dimensions of the material in which the particle is propagating, at the discontinuity surface a new collision distance Δs is recalculated (see Fig. 4.13). A detailed discussion on the calculation of the mean free path in cold MC methods can be found in Refs. [194][212][216]. However, since these methods are not adapted to inhomogeneous media, we propose here an algorithm better suited to our case of interest.

In laser irradiated targets, the density can vary of orders of magnitude in several tens or hundreds of microns, as shown in Fig 4.14. In particular, the figure shows the density profile of a planar CH target irradiated with a laser of intensity 10^{16} W/cm^2, after 500 ps of irradiation. The density goes from 0.05 g/cm^3 at x=0 (coronal plasma) up to 4 g/cm^3 (shocked region) after 30 μm. An electron initialized at x=0 will be characterized by a large mean free path $\lambda(E, \rho)$, since the material density is very low. Because of this large mean free path, the electron propagates for the first 20-30 μm without experiencing any collision, but there it will find a different situation in terms of material density. The value of $\lambda(E, \rho)$ computed at the beginning of the electron history is no more valid in this new condition.

An approximate method to compute the mean free path in non homogeneous medium is presented in Ref [280]. This method is valid for neutral particles, but it is adequate for our purposes. Let us consider a neutral particle that propagates in a heterogeneous medium. In our case, this medium is composed by small volumes, the grid elements, within each the material is homogeneous, see Fig. 4.15. The probability for the particle to experience a collision in the cell 3, after having travelled a path $x = l_1 + l_2 + \Delta s_3$, is given by the product of the probabilities that the particle crosses the cell 1 and 2 and the probability of interacting after Δs_3:

$$P(x) = e^{-\frac{l_1}{\lambda_1} - \frac{l_2}{\lambda_2} - \frac{\Delta s_3}{\lambda_3}}. \tag{4.97}$$

As such, the probability of interacting after $x = l_2$ but before $x = l_2 + \Delta s_3$ reads:

$$P(x) = 1 - e^{-\frac{l_1}{\lambda_1} - \frac{l_2}{\lambda_2} - \frac{\Delta s_3}{\lambda_3}}. \tag{4.98}$$

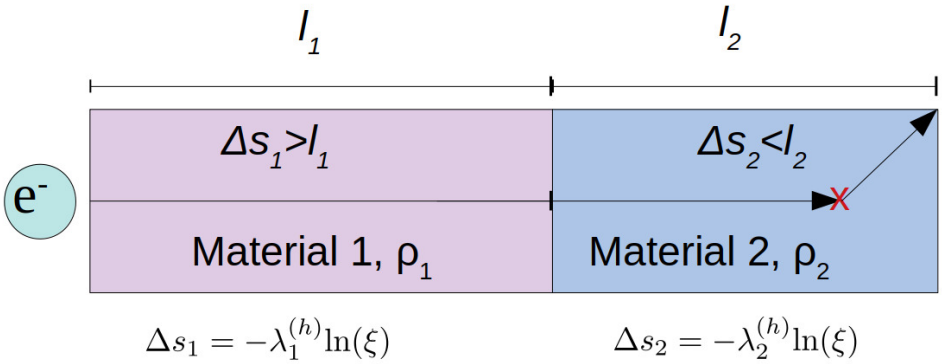

Figure 4.13: Calculation of collision distance and mean free path in cold MC methods. The electron enters in the material 1 and a collision distance Δs_1 is computed according to the law (4.88). If Δs_1 is greater than the material dimension l_1, the particle does not experience any collision in material 1 and it reaches the surface discontinuity between the two materials. Here a new collision distance Δs_2 is computed considering the properties of material 2.

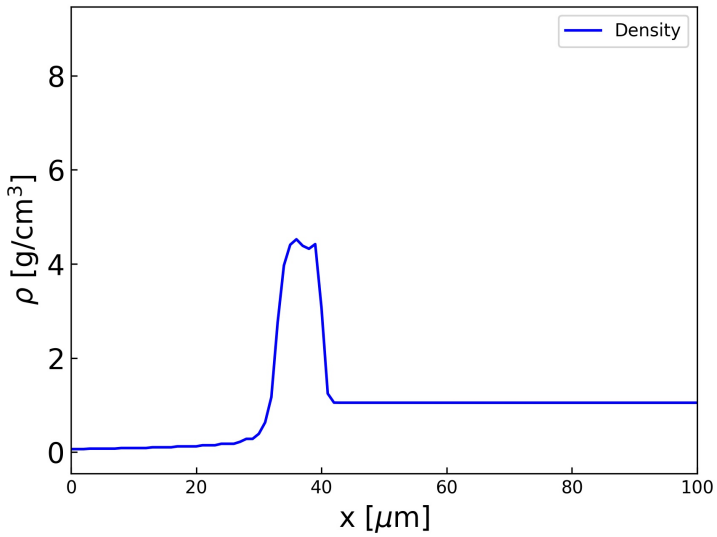

Figure 4.14: Density profile of a CH planar target irradiated with a laser of intensity 10^{16} W/cm^2. The density profile is extracted from hydrodynamic simulation using the CHIC code, after 500 ps of irradiation.

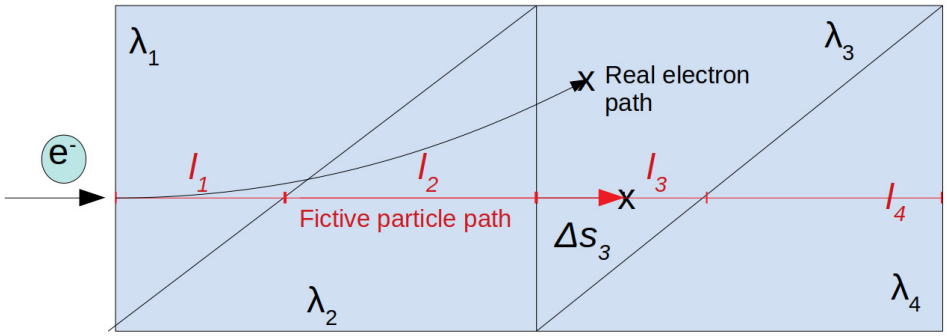

Figure 4.15: Calculation of the collision distance for an electron moving in a computation domain subdivided in triangular cells. In each k-th cell the medium density is constant, and the electron will be characterized by a mean free path λ_k. The path travelled by the electron before reaching the boundary of the k-th cell is l_k. Both the path of the fictive particle and of the electron are indicated by the red and the black arrows, respectively. The collision point for the two particles is indicated by **x**.

From this equation, using the inverse transform, it is possible to sample the collision distance Δs_3 that accounts for the path done by the particle in the first two cells:

$$\Delta s_3 = -\lambda_3^{(h)} \ln(\xi) - \frac{l_1}{\lambda_1^{(h)}} \lambda_3^{(h)} - \frac{l_2}{\lambda_2^{(h)}} \lambda_3^{(h)}. \tag{4.99}$$

If $\Delta s_3 < l_3$ the particle is transported in $x = l_2 + \Delta s_3$ and the collision is simulated. Conversely, if $\Delta s_3 > l_3$, the particle is propagated up to the boundary of the cell 3 and Δs_4 is computed by adding the term $-\frac{l_3}{\lambda_3^{(h)}} \lambda_4^{(h)}$ on the right-hand side of eq. (4.99) and substituting $\lambda_3^{(h)}$ with $\lambda_4^{(h)}$.

From a practical point of view, the collision distance Δs is calculated by launching a

"fictive" particle before the real electron track. These fictive particles have the same kinetic energy of the electron and they propagate following straight lines in the grid, as shown in Fig. 4.15. Referring to the figure, the particle starts in the tetrahedron 1, where the collision path is computed according to the formula (4.88):

$$\Delta s_1 = -\lambda_1^{(h)} \ln(\xi). \tag{4.100}$$

If $\Delta s_1 < l_1$, the real electron is launched and propagated up to x = Δs_1, where it experiences a collision. Conversely, if $\Delta s_1 > l_1$, the fictive particle arrives at the boundary between tetrahedrons 1 and 2 and Δs is recalculated considering eq. (4.99). This process is repeated i-times until $\Delta s_i < l_i$. At this point the collision path writes:

$$\Delta s = \sum_{i=0}^{i-1} l_i + \Delta s_i \tag{4.101}$$

and the real electron track starts. The main approximation introduced using this method is the fact that the fictive particle does not experience soft scattering events. Soft scattering events cause the electron to not follow exactly the straight lines travelled by the fictive particle. However, since the soft scattering events should not dramatically change the electron direction, the cells crossed by this latter are in the proximity of the ones crossed by the fictive particle. As such, the material density seen by the electron are similar to those seen by the fictive particle. To speed up the simulation and to reduce code complexity, one can also neglect the loss of energy of the fictive particle while propagating in the grid. This will play a second order effect in the computation of the collision path.

4.7 Benchmark against Geant4

We report, in this section, a benchmark of our 3D MC code against Geant4 used with the library Penelope. This benchmark was done by performing simulations in which the same target geometry and electron beam characteristics were applied and by comparing the responses of the two codes. In these simulations, our model worked according to the "cold model", i.e. considering electrons propagating in cold materials (see the previous sections). Let us recall that, in these conditions, atoms are not ionized and electrons scatter with nuclei screened by their complete electronic structure. In this case, the scattering cross sections are modelled according to the Wentzel model, eq. (4.28) (Sec. 4.3.2). Furthermore, electrons lose energy according to the continuous slowing down approximation considering the NIST stopping power formulas, eq. (4.65) (see Sec. 4.5.2). In Geant4, the models implemented to simulate the electron propagation in this condition are more detailed compared to ours. The scattering cross sections are computed according to accurate relativistic (Dirac) partial-wave calculations of elastic scattering of electrons by free atoms [194] [212] [281]. Moreover, the electron slowing down is calculated considering the soft and the hard scattering events separately [194]. This allows to compute the energy transfer from the primary particle to atomic shell electrons and the consequent emission of secondary particles. On the contrary, in our model, the emission of secondary electrons is not accounted.

A first benchmark between the two codes was performed by comparing the energy deposition of electrons in the matter. This quantity plays a primary role in the calculation of the shell preheat in the SI scheme and it is thus necessary to be sure about the reliability

of our numerical method. The benchmark was done as follows: monochromatic electron beams were injected in a 200 μm thick 0.4×0.4 mm^2 slab and the total energy deposit was computed. Electrons were initialized considering a 100 μm diameter spot with an initial beam divergence of 22°. The initial beam energy ranged from 20 up to 800 keV and each run consisted of 10000 particles. Several materials were considered, in order to evaluate the reliability of the model for different atomic numbers Z: Beryllium, Aluminium, Titanium, Copper, Tungsten and Gold. The results are shown in Fig. 4.16.

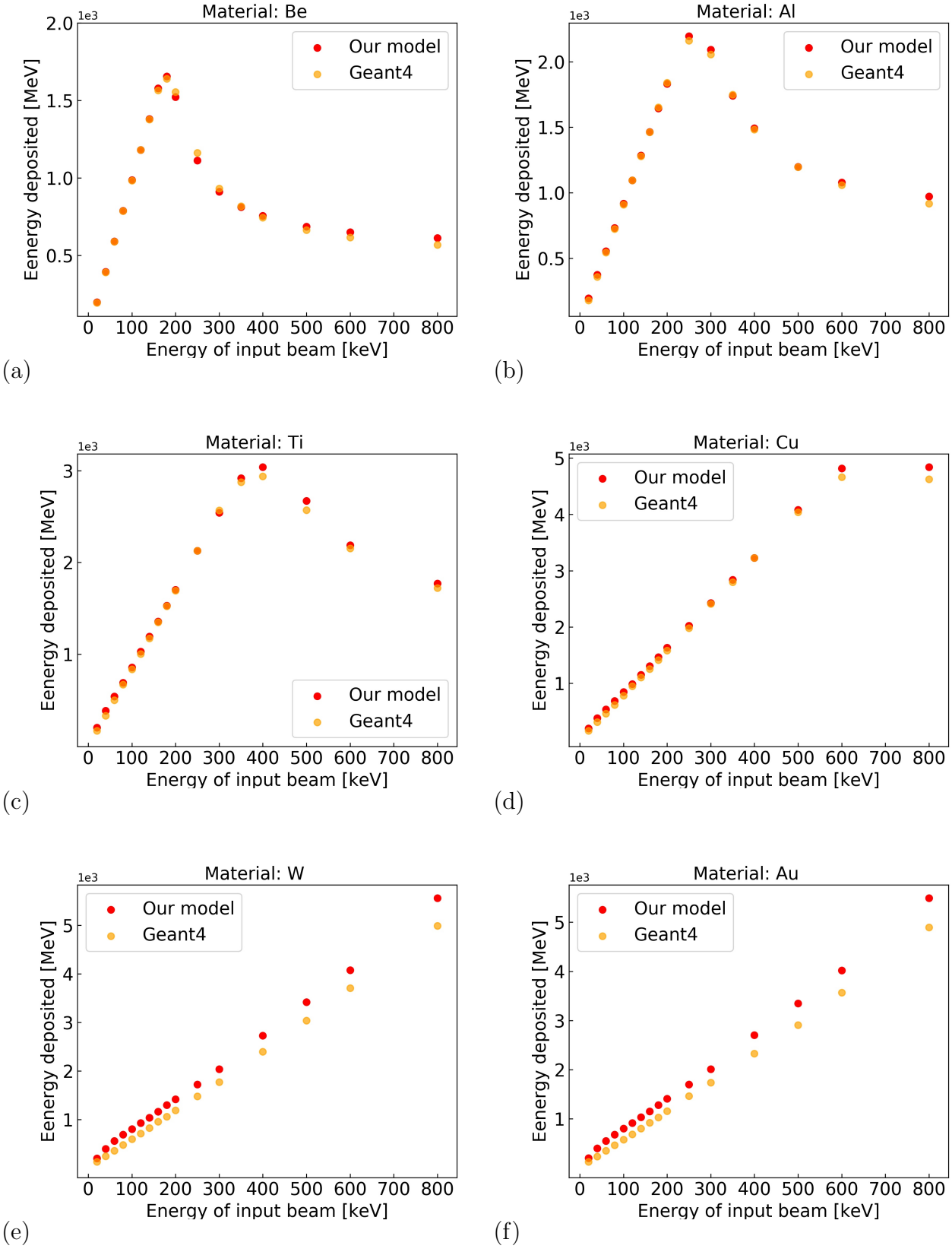

Figure 4.16: Energy deposition in the slab as a function of the initial monochromatic electron beam energy, computed by our model (red dots) and by Geant4 with the library Penlope (orange dots). The simulated slab was composed of: (a) Beryllium; (b) Aluminium; (c) Titanium; (d) Copper; (e) Tungsten; (f) Gold.

For low Z materials (Be and Al), our model reproduces the Geant4 energy deposition with an error that does not overcome the 10%. For the cases Ti and Cu the discrepancy between the two codes remains below the 20%, while for the highest Z (W and Au) the error does not exceed the 50%. The agreement between the two codes is particularly good for electron energy that ranges from 40 up to 180 keV, especially for the low Z materials, where it shows an error around the 1%. The discrepancies between the two codes at lower energies, especially for high Z materials, may be due to the fact that, in this regime, the first Born approximation does not hold anymore (see eq. (4.27)). As such, the stopping power formulas and the Wentzel DCS used in our model are not accurate. Moreover, for higher electron energies ($\geq$ 600 keV), the disagreement between the codes may be due to the fact that the bremsstrahlung energy losses, the Fermi density effect and the secondary electron emission are not accounted in our case. These discrepancies, however, should not represent a big issue. First of all, in ICF hot electrons propagate in low Z materials (plastic ablator and DT cryogenic shell). Furthermore, low energy electrons ($\sim$ 10 - 20 keV) will be suddenly stopped in the compressed shell and do not represent a preheat concern. Conversely, electrons with energy greater than 40 keV can penetrate deeper in the cryogenic shell, preheating the fuel. The fact that our model reproduces the Geant4 results in this energy range with an error around the 1% is an important achievement that gives us more confidence on the reliability of the code.

A second benchmark is done comparing the electron transport in CH targets. We considered in particular 0.4 $\times$ 0.4 mm^2 plastic slabs with variable thicknesses. Electrons are launched inside the target, considering a 2D Maxwellian distribution function with 26 keV temperature. This value was chosen according to the last experimental findings on the hot electron characterization in the context of SI, as presented in Chapt. 2 and 3. The particles are initialized in 100 μm diameter spot with an initial beam divergence of

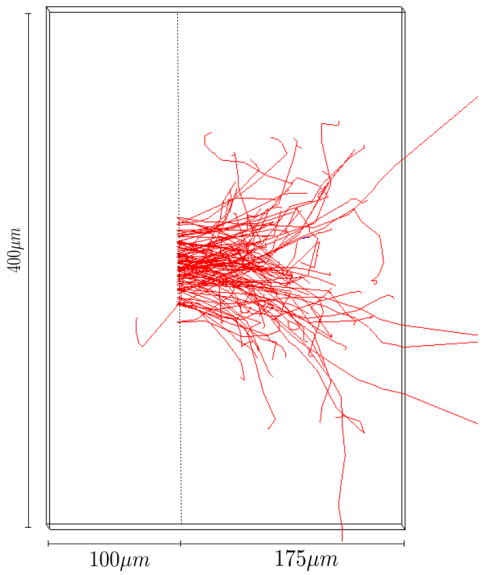

Figure 4.17: Schematic representation of the simulations performed to benchmark our MC model with Geant4. Electrons are injected in a 0.4×0.4 mm^2 CH slab at 100 μm from the left side. In this case, the simulated slab was 275 μm thick. The energy spectrum of the electrons that comes out of the slab is considered, as well as the energy deposition in the target.

±22°. As figure of merit for the benchmark, we compared the electron energy spectrum that exits the target and the energy deposition. Different target thicknesses are tested and the electrons are initialized at a distance of 100 μm from the left side of the target, as shown by Fig. 4.17. In order to maximize the statistics, the distribution function was sampled starting from 80 or 90 keV, since low energy electrons are stopped in the target and not counted. Three different CH density are tested: 0.1, 1 and 2 g/cm^3. The results are shown in Fig 4.19, 4.20 and 4.21 for the three cases, respectively. In these figures, we compare the electron spectra that come out from the target predicted by our model and by Geant4. Furthermore, the deposited energy in the targets predicted by the two codes is presented in Fig. 4.18, for the two cases at density 1 and 2 g/cm^3, respectively. Overall, we can observe a very good agreement between the two codes in the prediction of the electron spectrum that exits the target. Moreover, the differences in the energy deposition is less than 1%. This is a further important validation of our model, stating its reliability for the energy range considered.

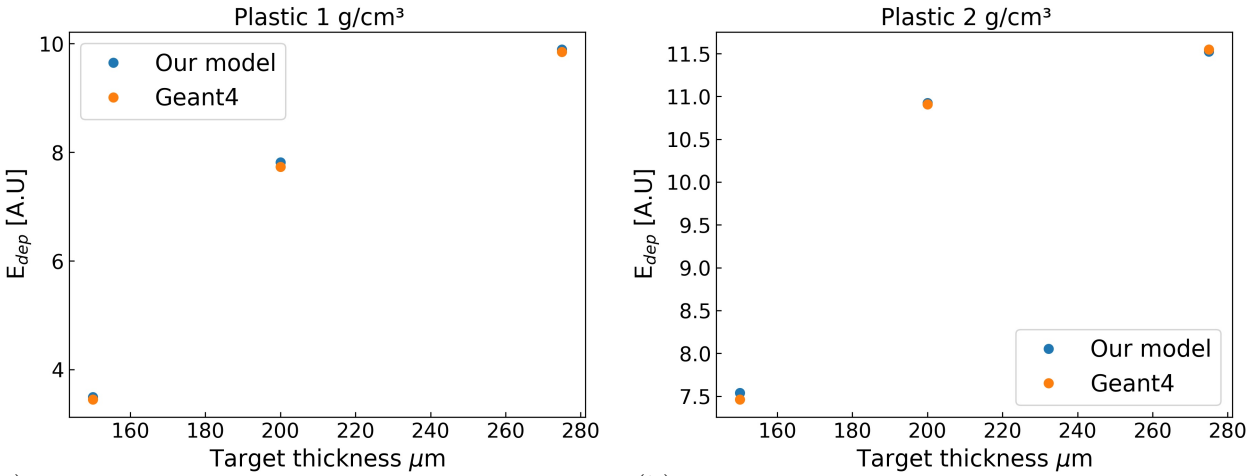

(a) (b)

Figure 4.18: Comparison between the energy deposition in the targets predicted by Geant4 (orange dots) and by our model (blue dots), as a function of the target thickness. (a) CH target 1 g/cm^3 dense. (b) CH target 2 g/cm^3 dense.

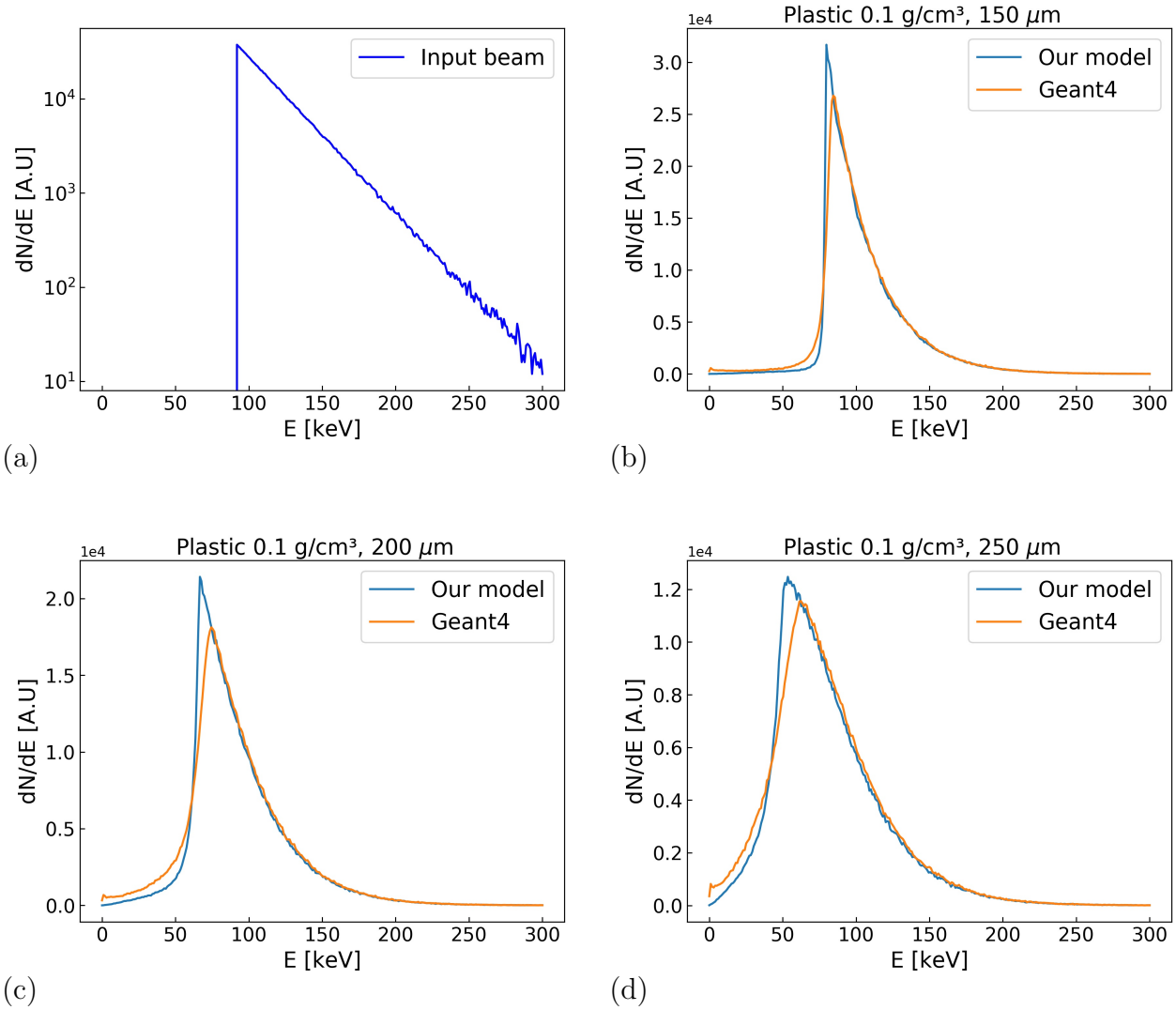

Figure 4.19: (a) Energy spectrum of the input electron beam used in the simulations. Electrons are distributed energetically according to a 2D Maxwellian function with temperature of 26 keV. The sampling starts from 90 keV, in order to increase the statistics (electrons initialized with a low energy will not exit the target). (b) Electron energy spectrum that exits the target considering an initial target thickness of 150 μm, as predicted by Geant4 (orange curve) and by our model (blue curve). (c) Electron energy spectrum that exits the target considering an initial target thickness of 200 μm, as predicted by Geant4 (orange curve) and by our model (blue curve). (d) Electron energy spectrum that exits the target considering an initial target thickness of 250 μm, as predicted by Geant4 (orange curve) and by our model (blue curve). The target is composed by CH with density of 0.1 g/cm^3.

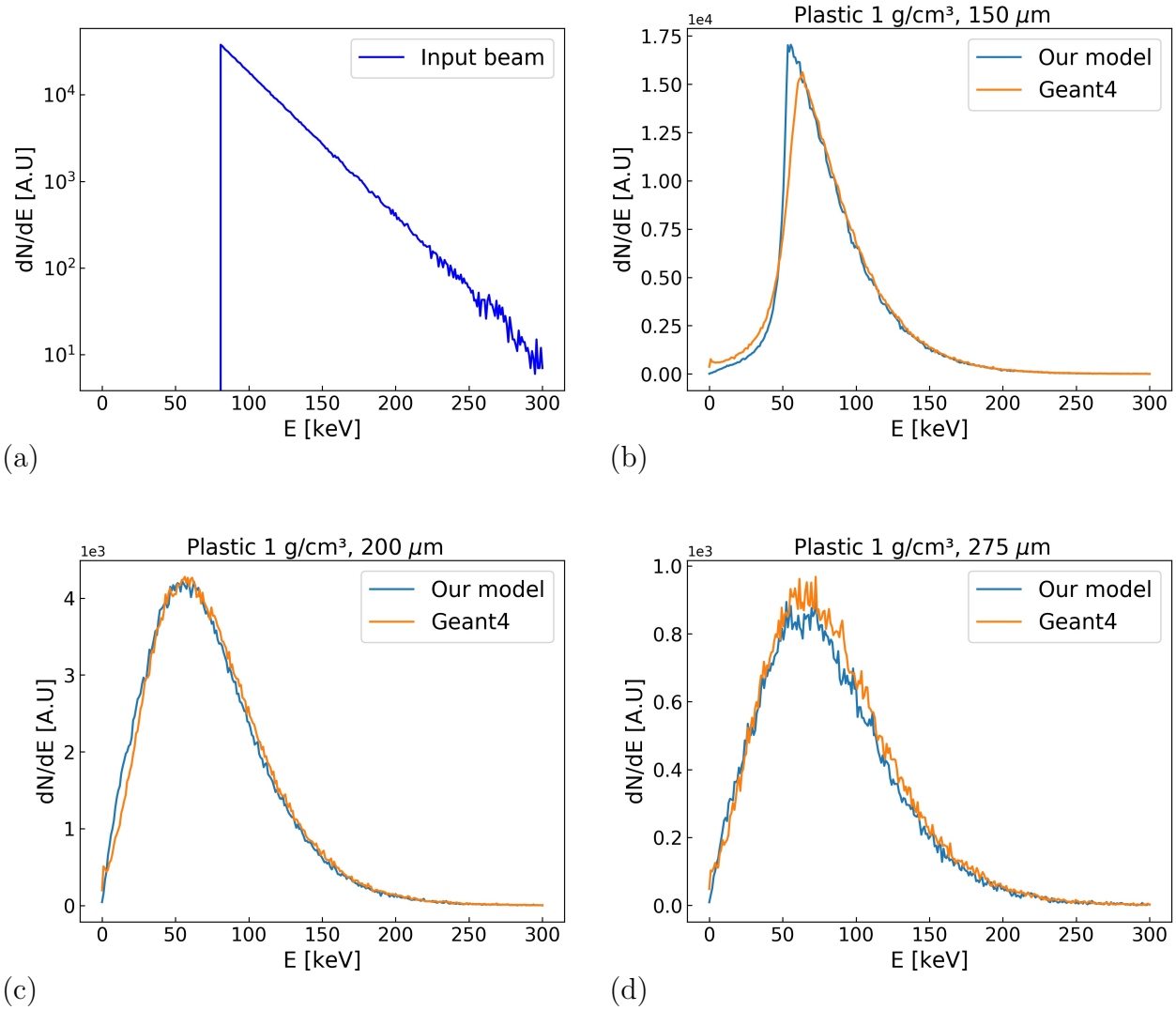

Figure 4.20: (a) Energy spectrum of the input electron beam used in the simulations. Electrons are distributed energetically according to a 2D Maxwellian function with temperature of 26 keV. The sampling starts from 80 keV in order to increase the statistics (electrons initialized with lower energy will not exit the target). (b) Electron energy spectrum that exits the target considering an initial target thickness of 150 μm, as predicted by Geant4 (orange curve) and by our model (blue curve). (c) Electron energy spectrum that exits the target considering an initial target thickness of 200 μm, as predicted by Geant4 (orange curve) and by our model (blue curve). (d) Electron energy spectrum that exits the target considering an initial target thickness of 250 μm, as predicted by Geant4 (orange curve) and by our model (blue curve). The target is composed by CH with density of 1 g/cm^3.

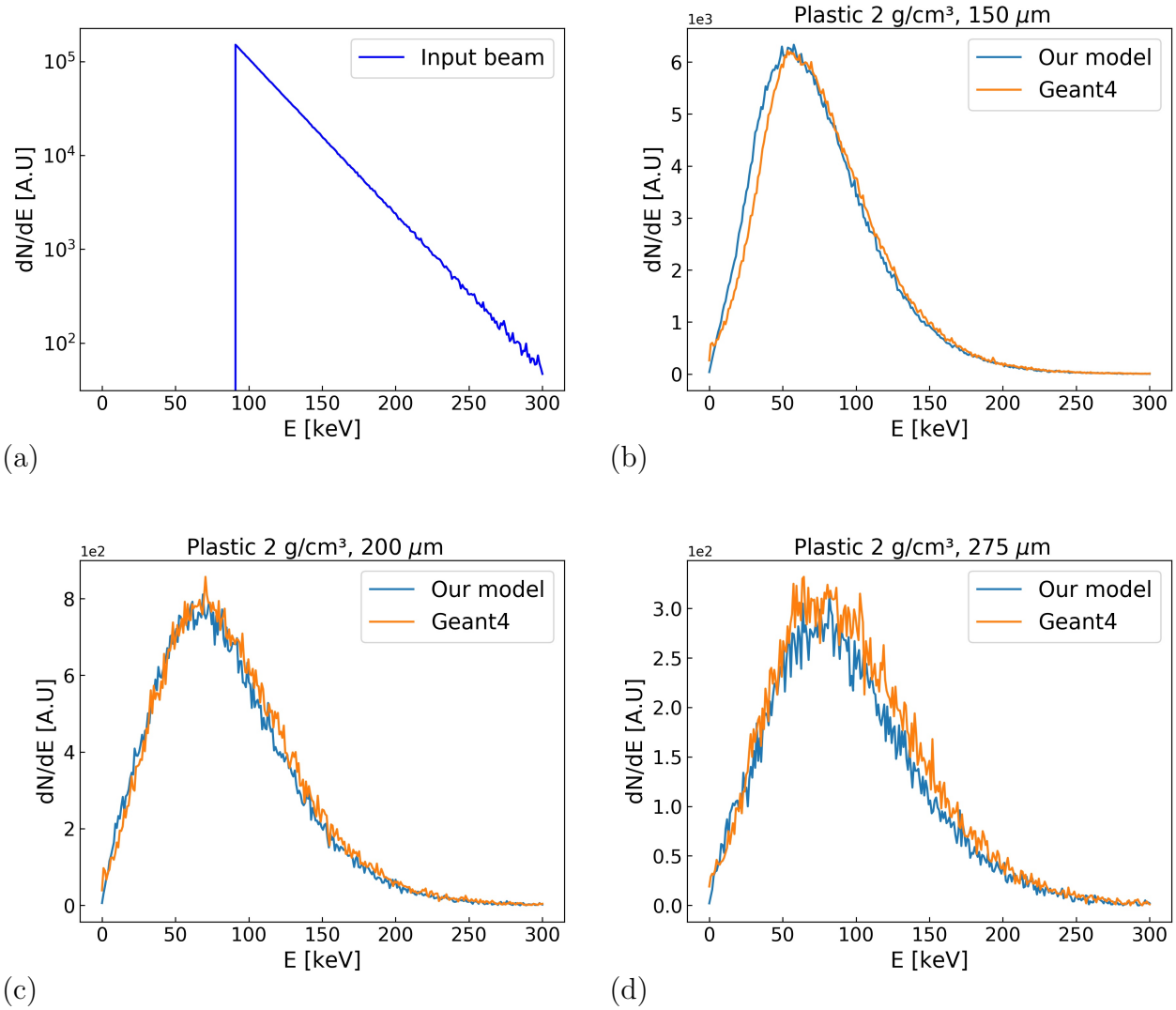

Figure 4.21: (a) Energy spectrum of the input electron beam used in the simulations. Electrons are distributed energetically according to a 2D Maxwellian function with temperature of 26 keV. The sampling starts from 90 keV in order to increase the statistics (electrons initialized with lower energy will not exit the target). (b) Electron energy spectrum that exits the target considering an initial target thickness of 150 μm, as predicted by Geant4 (orange curve) and by our model (blue curve). (c) Electron energy spectrum that exits the target considering an initial target thickness of 200 μm, as predicted by Geant4 (orange curve) and by our model (blue curve). (d) Electron energy spectrum that exits the target considering an initial target thickness of 250 μm, as predicted by Geant4 (orange curve) and by our model (blue curve). The target is composed by CH with density of 2 g/cm^3.

4.8 Conclusion

This chapter was devoted to present the physics and the development of a 3D plasma MC method suitable at simulating the hot electron propagation in plasmas. Conversely to common MC methods, in this model electrons propagate in ionized or partially ionized laser irradiated targets and it will be implemented in hydrodynamic codes. It will be

particularly useful to study the problematic of the hot electron transport in the context of ICF, allowing to perform numerical simulations aimed at proposing robust implosion schemes. Moreover, once implemented in hydrodynamic codes, this method will be useful to interpret ongoing ICF experiments conducted in the different laser facilities around the world.

In Sec. 4.2, we presented the physics of a laser irradiated target in ICF regime, considering in particular the model to calculate the ionization state. In Sec. 4.3, a list of scattering differential cross sections suitable at describing the hot electron scattering in plasma is presented. These cross sections were: the Moller's cross section, to model the electron - electron scattering; the Dalitz's cross section, to model the electron - completely ionized ion scattering (the ion is screened by plasma particles); a cross section to model the elastic scattering between an electron and a partially ionized atom. In this latter case, the ion is screened by other plasma particles and by its residual atomic structure. Since this condition was never addressed in the literature (at the moment of writing), we derived and proposed an analytical form of a differential cross section to describe this phenomenon. Considering these results, the diffusion is modelled considering a mixed algorithm in which soft scatterings are simulated according to the Goudsmit and Saunderson multiple scattering theory, while hard collisions are modelled simulating a two-bodies interaction 4.4. In Sec. 4.5 we presented the theory of electron stopping power in plasmas, discussing the regime of validity of the formula used. Let us remark that all the listed formulas and the differential cross section derived are valid in the considered regime, i.e. to describe the propagation of non-relativistic electrons (tens or hundreds of keV) in low Z materials. Finally, the algorithm implementation is shown in Sec. 4.6 and the code benchmark in Sec. 4.7. Since hot electrons propagate in materials characterized by strong density gradients, we propose a suitable algorithm to calculate the mean free paths in this conditions.

The code implements also a "cold" module, in which electrons scatter with non ionized atoms (i.e. with nuclei screened by their electronic structure) and lose energy according to the cold stopping power formulas.

The code is benchmarked against Geant4, comparing different figures of merit such as the energy deposition in targets or the electron spectra that exit from different target geometries. Overall, the code presents a very good agreement with Geant4 in the description of the hot electron transport and the energy deposition.

Compared to other plasma MC methods recently developed by Atzeni et al. [210], the MC code developed in this work implements the possibility to simulate the propagation of hot electrons in partially ionized materials. This is particularly useful in the analysis of the laser-plasma experiments in which the interaction conditions do not allow to obtain a complete target ionization. Furthermore, an important improvement is the simulation of hard collisions. As pointed out in 1.1.2, hard collisions become important when the Landau logarithm is bigger than $\sim$4, condition usually fulfilled in laser-irradiated targets in ICF regime. Hard collisions strongly modify the spatial distribution of the electron beam, causing its diffusion. Further investigations can be done in order to understand the importance of their presence, evaluating the possibility of neglecting them. Simulating an hard collisions requires a significant amount of computational power and the increase of code complexity. Therefore, the possibility of neglecting these phenomena, will remarkably simplify and speed up the code.

Chapter 5

Plasma MC method: Two cases of study

We report, in this chapter, two numerical studies using the 3D plasma MC code developed in Chap. 4. Let us briefly remind that the hot electron diffusion is modelled considering scattering with plasma electrons and elastic collisions with ionized or partially ionized atoms, Sec. 4.3. The Goudsmit Saunderson multiple scattering theory is used to model soft collisions (i.e. the collisions characterized by a polar scattering angle $\theta < 10°$), while hard collisions are simulated considering a two-bodies interaction (Sec. 4.4). The plasma stopping power formulas are used to compute the electron slowing down and the energy deposition in the target (Sec. 4.5). Also a cold part is implemented in the code, considering scattering with atoms and the stopping power formulas taken from the NIST library [265].

As shown in Chap. 2 and 3, the analysis of laser plasma-experiments aimed at characterizing hot electrons is based on cold MC methods, in which the hydrodynamic evolution and the plasma state of the irradiated target are not accounted. In this chapter, we present a numerical study aimed at understanding the margin of error introduced in using cold MC methods to analyse these experiments. In particular, a detailed investigation on how the electron propagation differs considering cold and irradiated target is conducted, with the aim of understanding which are the relevant phenomena that rule the process.

In the second part of the chapter, we present a numerical study on the preheat effect driven by the presence of hot electrons considering a typical SI scheme. In particular, the plasma MC code is used to simulate the electron energy deposition through an imploded ICF target, with the aim of calculating the inner DT shell adiabat before the shock convergence. Since the MC method has not yet been implemented in hydrodynamic codes (at the moment of writing), target hydrodynamic profiles are extracted from a 1D CHIC simulation and used as input in our plasma code. In doing this, we are neglecting the effects of hot electrons on the target hydrodynamic evolution, but it is however possible to obtain a first assessment on which are the hot electron characteristics that can be a concern for SI.

5.1 Hot electron transport in laser irradiated planar targets

5.1.1 Motivation

We report, in this section, a numerical study on the hot electron propagation in planar targets irradiated by laser beams with characteristics relevant to ICF. In Chap. 3 the results of different planar experimental campaigns, aimed at characterizing hot electrons, are presented. In particular, in these experiments, planar targets were irradiated by a laser beam with characteristics relevant to SI, generating a copious amount of hot electrons which propagated into the targets. The hot electron characteristics (temperature and intensity) were retrieved by reproducing the experiment by means of cold MC methods (Geant4), simulating the x-ray generation on the diagnostics. However, as explained in Chap. 4, a cold MC method does not consider several peculiar aspects of a laser irradiated target. First of all, the hydrodynamic evolution of the target, i.e. the ablation and the compression waves, can not be reproduced. Therefore, the target is simulated considering its nominal dimensions, i.e. its configuration before being shot. As explained in Sec. 3.1.2, this is justified considering the assumption that the product ρr has the same values both for the irradiated and the cold targets. This assumption holds considering 1D geometry and electrons that propagate according to straight lines and it is usually justified considering a 1D plasma plume expansion driven by big laser spots [108]. Moreover, a cold MC method does not account for the ionization state of atoms that compose the material. As such, as explained in Chap. 4, the primary particle scatters with atoms screened by their complete electronic structure. Conversely, in laser irradiated targets, hot electrons scatter with partially or completely ionized atoms and with other free plasma electrons. Given that, we present in this chapter a numerical study that allows to understand what is the margin of error introduced in using a cold MC method to reproduce a laser-plasma experiment. In particular, the plasma MC code developed in Chap. 4 is used to investigate the electron transport in laser irradiated targets and the results are compared with Geant4 simulations. In this way, it is possible to better understand which are the phenomena that rule the hot electron transport in laser irradiated targets and the differences compared to the cold case.

5.1.2 Reinterpretation of the OMEGA experiment using our plasma MC method: how the hot electron transport changes in laser irradiated targets

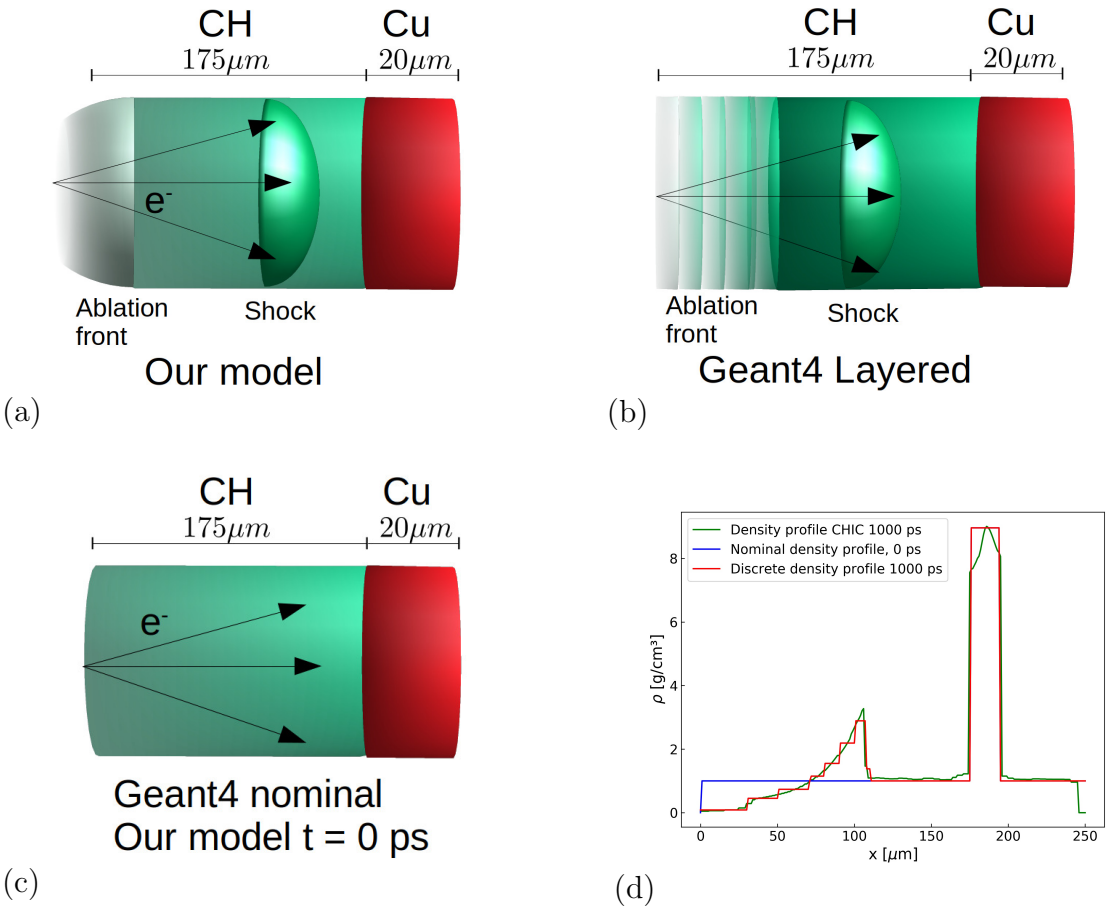

Figure 5.1: Schematic representations of the target configuration used in the simulations performed: (a) schematic representation of the target used in the simulations 1, 2 and 3 performed with our MC model. The target configuration is extracted from CHIC simulations at three different times (500, 750 and 1000 ps) and electrons are launched at the critical density. (b) Schematic representation of the layered target used in the simulations 4 performed with Geant4. The target is composed by several layers with an increasing density, in order to reproduce the ablated and the shocked region. The density profile along the cylinder axis reproduces discretely the profile extracted by CHIC, as shown by the red curve in Fig. (d), for the case at 1000 ps. (c) Schematic representation of the target used in the nominal Geant4 simulation and in the simulation with our MC code at 0 ps. Here the target is composed by a CH ablator of 175 μm at density 1 g/cm^3, followed by a 20 μm copper plate, as in the OMEGA experiment presented in Sec. 3.1 and in the article [190]. The density profile along the cylinder axis of this target is shown by the blue curve in Fig. (d). (d) Density profiles along the cylinder axis considered in the four simulations. The density profile used in simulations 1, 2 and 3 is indicated by the green curve; the density profile used in simulation 4 is indicated by the red curve; the density profile considered in the nominal Geant4 simulation and in the simulation at 0 ps using our model is indicated by the blue curve.

Let us reconsider the configuration and the results of the OMEGA experiment presented in Chap. 3, Sec. 3.1. In this experiment, planar multilayer targets were irradiated by a 1 ns UV laser beam with an intensity of 10^{16} W/cm^2. The targets consisted in 500 μm diameter disks composed by a 175 μm CH ablator, followed by a 20 μm copper plate used as tracer for the hot electrons. These were mounted on a 50 μm plastic slab to avoid hot electron recirculation. Hot electrons are generated in the coronal plasma and they propagate into the target, emitting bremsstrahlung and copper K_α radiation that is collected by the x-ray spectrometers. As shown in Chap. 3, the hot electron temperature and intensity were retrieved by simulating with Geant4 the generation of the bremsstrahlung and the K_α signals on the diagnostics. In the simulations, the nominal target geometry (175 CH - 20 Cu - 50 CH) was used (Fig. 5.1(c)).

We would like now to study the electron propagation considering the hydrodynamic evolution of the target and its ionization state, comparing then the results with the Geant4 predictions. For this purpose, target hydrodynamic profiles were extracted from CHIC simulations at four different times: 0, 500, 750 and 1000 ps. In particular, the electronic temperature, the mass density and the ion density profiles were extracted from CHIC and a 3D map of this quantity was created, generating a 3D target profile used as input for the plasma MC code. The plasma MC code calculates the target ionization degree according to the Thomas-Fermi theory, computing the local electron density (see Chap. 4). Simulations were performed by launching electrons at the critical density, with an initial spot of 100 μm diameter and a beam divergence of $\pm 22°$. Energetically, electrons are described by a 2D Maxwellian function with a temperature of 26 keV, which corresponds to the function found in Sec. 3.1. In each simulation, we lunched 4×10^6 particles, sampling the Maxwellian from a minimum value of 90 keV. Geant4 simulations in similar conditions were also performed with the aim of comparing its prediction with the plasma case. The figure of merit chosen to compare the two codes was the electron energy spectrum that arrives on the copper plate. This quantity is directly related to the K_α generation and the comprehension of its behaviour considering cold or warm targets will allow to better understand the reliability of the experimental data analysis presented in Chap. 3. Except for the case t = 0 ps, we performed four different simulations for each time considered (500, 750 and 1000 ps).

1. A 3D simulation in which the target is modelled considering hydrodynamic profiles extracted from CHIC, but the scattering processes are turned off. In this case, the ablator density is not constant along the electron path and it varies according to the profile extracted from the CHIC simulation. As an example, the green curve in Fig. 5.1 (d) shows the density profile along the cylinder axis extracted from the simulation at 1000 ps. The electrons move according to straight lines, loosing energy according to the stopping power formulas.

2. A full 3D plasma MC simulation in which the target is modelled considering hydrodynamic profiles extracted from CHIC and its warm state is considered. In this case, the ablator density is not constant along the electron path and it varies according to the profile extracted from the CHIC simulation (for example the green curve in Fig. 5.1 (d)). Electrons scatter with ionized or partially ionized atoms and with other free plasma electrons and they lose energy according to the plasma stopping power formulas. A schematic representation of the target configuration adopted in this configuration is shown in Fig. 5.1 (a).

3. A 3D MC simulation in which the target is modelled considering hydrodynamic profiles extracted from CHIC, but it is considered as in a "cold" state. In this case, the ablator density is not constant along the electron path and it varies according to the CHIC profile (for example the green curve in Fig. 5.1 (d)). Contrary to the previous case, here electrons scatter with non-ionized atoms and lose energy according to the cold stopping power formula. These simulations allow to study the effect of the ρr conservation on the propagation of hot electrons, excluding the effects related to the ionization state of target. A schematic representation of the target configuration adopted in this configuration is shown in Fig. 5.1 (a).

4. A Geant4 simulation in which the ablator is divided in CH layers with an increasing density, conserving the ρr as predicted by the CHIC simulation. These layers have thicknesses of several microns, allowing to study the effect of the ablated and the shocked region considering discrete density steps. For example, the density profile considered at 1000 ps is shown by the red curve in Fig. 5.1 (d). In this way, it is possible to reproduce the effect of the ablation and the compression wave on the electron propagation in Geant4. Evidently, the target plasma state is not simulated. A schematic representation of the target configuration adopted in this configuration is shown in Fig. 5.1 (b).

For the case t=0 ps, the target profile extracted from CHIC corresponds to the unablated target configuration, referred here as "nominal target case", i.e. 175 μm CH ablator 1 g/cm^3 dense, followed by the copper plate (blue curve in Fig. 5.1 (d)). Evidently, in this case our MC code works according to the cold model, considering the cold stopping power formulas and scattering models.

The obtained results are compared each time with the nominal Geant4 simulation, i.e. the one used in the experimental analysis presented in Sec. 3.1, in which the target was composed by 175 μm CH ablator followed by 20 μm Cu plate.

Figure 5.2 shows the electron spectra that impinge on the copper plate predicted by the simulations 1, in which the scattering effects were turned off (electrons propagate according to straight lines slowing down according to the stopping power formulas). The electrons propagate in targets whose density profiles were extracted from CHIC simulations at 0, 500, 750 and 1000 ps. In particular, in the simulation at 0 ps electrons slow down according to the cold stopping power formulas, while at other times they will follow the plasma stopping power formulas. As can be seen from the figure, these simulations predict an electron number on the copper plate that is approximately one order of magnitude greater compared to what is predicted by the nominal Geant4 simulation, even considering the cold non-ablated target (0 ps). This dramatic difference tells that, in this regime, it is not possible to neglect the beam diffusion due to scattering phenomena, in order to correctly model the hot electron propagation in matter.

Let us now consider the simulations in which the diffusion of the hot electron beam is considered. Fig. 5.3 (a) shows the comparison between the electron spectra that reach the copper plate as predicted by our model at t = 0 ps and by Geant4. These two simulations are equivalent, since both the two codes simulate the nominal target configuration (i.e. 175 μm CH - 20 μm Cu, density profile indicated by the blue line in Fig. 5.1 (d)). Our model works according to the cold scattering and stopping power formulas. As can be seen for the figure, there is a very good agreement between the spectra predicted by

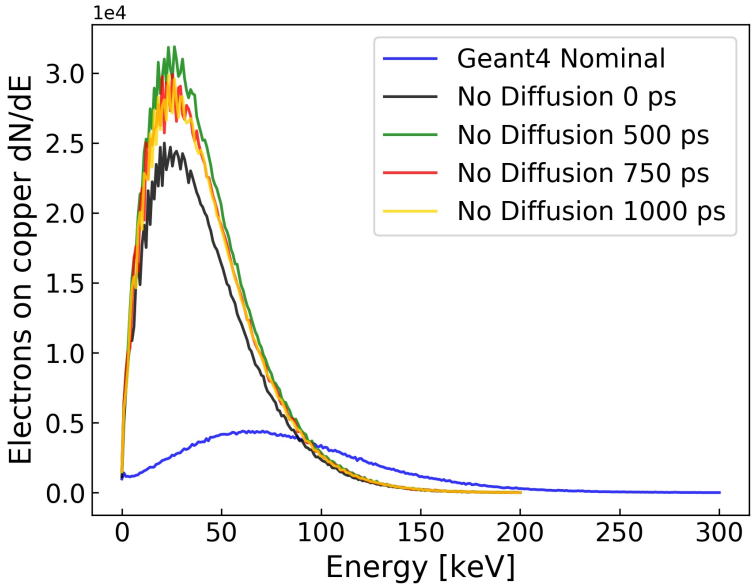

Figure 5.2: Electron spectra the impinge on the copper plate as predicted by the four simulations using our MC model in which the scattering effects are turned off (simulation 1 in the list above). As such, electrons propagate along straight lines slowing down according to the stopping power formulas. The target hydrodynamic profiles are extracted from CHIC simulations at 0 ps (black curve), 500 ps (green curve), 750 ps (red curve) and 1000 ps (yellow curve). These spectra are compared to the spectrum predicted by the nominal Geant4 simulation (blue curve).

the two codes. A small difference is seen in the low energy part and it may be due to the fact that our model does not simulate the secondary electron emission. This good agreement offers another evidence on the reliability of our code.

Fig. 5.3 (b) (c) and (d) report the results considering the other times (500, 750 and 1000 ps). When the plasma models are turned off (simulations 3 in the previous list), our model (black curve) predicts a higher number of electrons that reaches the copper compared to the nominal case (blue curve). This behaviour is also confirmed by the Geant4 layered target simulations (red curve, simulations 4 in the previous list), which agree with our MC method run in cold mode. In particular, the predicted electron spectrum increases as a function of the irradiation time. The more the target is ablated, the less electrons are stopped in the ablator and reach the copper. This is due to the fact that the electrons, propagating in the coronal plasma and in the ablated region, are not subjected to a severe scattering phenomena because of the low density of the material. As such, they tend to keep their directionality for tens of μm, until they reach the shocked region. In the shocked region, the scattering phenomena are more severe, but they are not sufficient to compensate for the fact that the electrons have travelled for tens of μm without experiencing collisions. For this reason, the number of electrons that impinges on the copper plate is greater in the ablated targets compared to the nominal case. As such, the 1D hypothesis of the ρr conservation seems to not be confirmed by our calculations. However, when the plasma effects are turned on (simulation 2, green curve), a lower number of electrons arrives on copper. Notably, it seems that a target in plasma state absorbs and slows down electrons with more efficacy compared to the cold case.

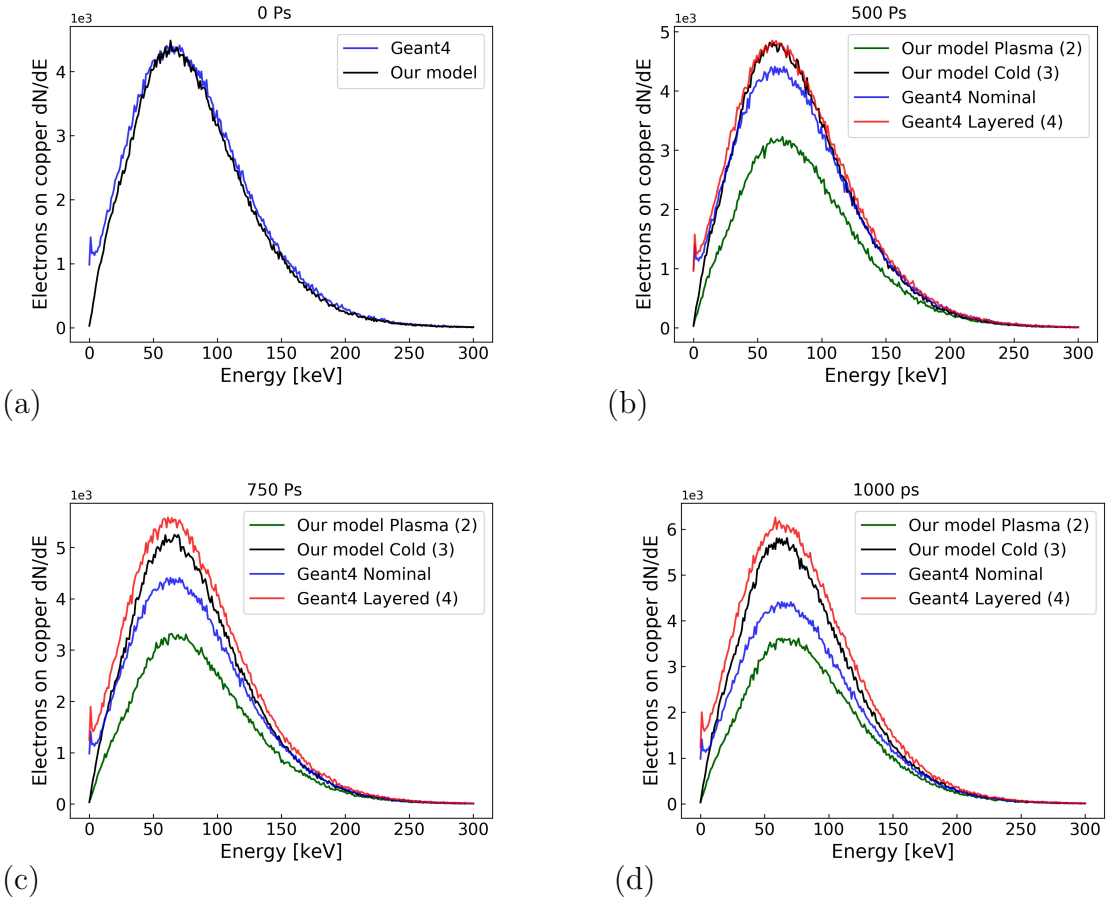

Figure 5.3: Energetic electron spectra that impinge on the copper plate predicted by the four simulations at the four different times. Electrons described energetically by a 2D Maxwellian function are launched at the critical density with an initial divergence of $\pm 22°$. The green curve is the spectrum predicted by our plasma MC code (simulation 2 in the list above). The black curve is the spectrum predicted by our MC model in which the plasma effects have been turned off and electrons propagate according to the cold stopping power and scattering formulas (simulation 3 in the list above). The blue line is the spectrum predicted by Geant4 considering the nominal target configuration (175 μm, 1g/cm^3 CH - 20 μm Cu). The red line is the spectrum predicted by Geant4 considering a layered target which reproduces the density profile extracted from CHIC (simulation 4 in the list above). (a) 0 ps (cold non-irradiated target); (b) 500 ps; (c) 750 ps; (d) 1000 ps.

There are two reasons which explain this fact. First of all, the stopping power in plasma presents greater values compared to cold materials, as shown by Fig. 5.4. In particular, the figure reports the value of the stopping power as a function of the electron kinetic energy in cold and in warm (T = 10 eV) polystyrene. The plasma stopping power has values greater compared to the cold case, in particular for electron energies lower than $\sim$100 keV, our regime of interest (this is expected, since an electron which moves with high values of kinetic energy collides and loses energy with other electrons in the medium, not distinguishing their bound or free state). Another difference between the propagation in cold or in plasma targets is in the scattering with nuclei. In the cold case, the nuclear potential is screened by the electronic cloud of the atom, while in plasma the screening is given by the residual electronic structure and by other plasma particles. In particu-

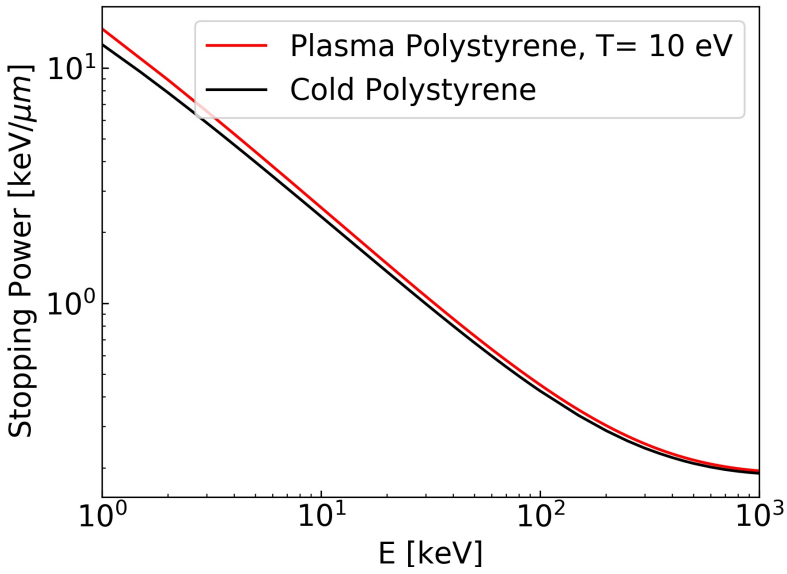

Figure 5.4: Stopping power in polystyrene (1.05 g/cm^3) as a function of electron kinetic energy considering the plasma (T=10 eV) and the cold case, red and black lines, respectively. The plasma stopping power is computed according to the formulas presented in Chap. 4, while the cold stopping power is taken from the NIST database [265].

lar, in this regime, the characteristic screening lengths in plasmas are greater compared to the screening distances of cold atoms. As such, the effective distances of the nuclear potentials are greater in plasma, enhancing the scattering phenomena and the diffusion of the electron beam, which is prevented from arriving at the copper plate. Overall, the reduction in the number of hot electrons that arrives on the copper plate is around the ∼30% for the simulations at 500 and 750 ps and around the ∼20% in the simulation at 1000 ps.

From this analysis, it seems that the justification based on the ρr conservation, used in Sec. 3.1 to justify the use of cold MC methods to analyse planar target experiments, is not completely exact. The effect of the ρr conservation (i.e. the formation of an ablated and compressed zone) increases the number of electrons that impinges on copper, as shown by the red and the black lines in the graphs of Fig. 5.3. However, this effect is counterbalanced by the fact that the target is in plasma state and the different nuclear screening mechanism causes a strong diffusion of the hot electron beam, reducing the number of hot electrons that arrives on copper.

5.1.3 Reinterpretation of the OMEGA experiment using our plasma MC method: how the K_α yield changes considering cold or irradiated targets

Let us now reconsider the K_α spectrometer (ZNVH) post processing, presented in Chap. 3 Sec. 3.1.2. Now our 3D plasma MC method is used to calculate the electron spectrum that arrives on the copper plate. In Sec. 3.1, the parameters N_e and T_h of a 2D electron Maxwellian function $f_e(E) = {}^{N_e}/_{T_h} e^{-E/T_h}$ were retrieved by simulating the K_α detected by the diagnostic. In particular, for this purpose, we performed 45 simulations considering

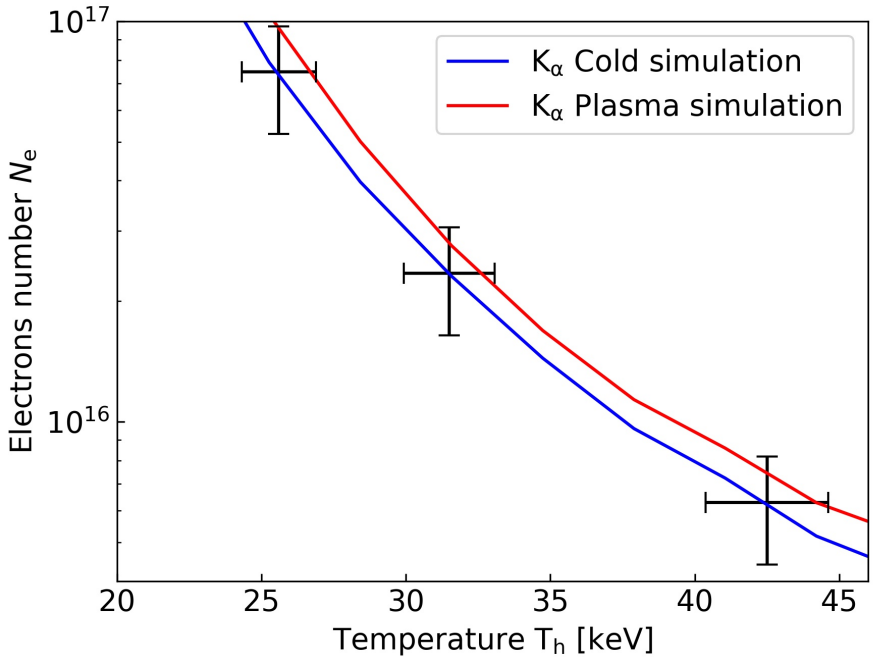

Figure 5.5: Couple of parameters T_h and N_e that reproduces the K_α signal on the ZNVH in the OMEGA experiment presented in Chap. 3, Sec. 3.1.2 according to Geant4 simulations. The blue line refers to the nominal Geant4 simulation (i.e. cold target composed by 175 μm CH - 20 μm Cu). The red line indicates the couple of parameters T_h and N_e obtained by using as input electron spectra on the copper plate obtained from the plasma simulations. The Geant4 library used to compute the K_α is Livermore. The predicted hot electron temperatures are $\sim$ 5% greater for the plasma case compared to the cold case, while the difference in the parameter N_e does not exceed the 30%. These percentage are indicated by the error bars.

monochromatic electron beams propagating in the target (see Sec. 3.1.2). The target configuration used in these simulations was the nominal one (175 μm CH, 20 μm Cu) and the electron energies used ranged from 90 keV up to 300 keV (electrons with energy less than 90 keV do not arrive on the copper plate and do not generate K_α signal). These simulations are re-performed using our plasma MC code, taking now into account the hydrodynamic evolution and the plasma state of the target. The temporal evolution of the system is reproduced by weighing the signal of the plasma simulations at the three chosen times (500, 750 and 1000 ps) according to the SABS curve (Fig. 3.16). In this way, we are considering the hot electron flux to follow the SABS signal, along the lines of what was done in analysis of the experiment in Chap. 3.1, Sec. 3.1.2. The electron spectra that impinge on the copper plate are then used as input in Geant4 simulation in order to compute the K_α signal, since in our plasma MC code the K_α generation is not modelled. Both for the cold and the plasma simulations, the library used to compute the K_α de-excitation was the library Livermore. Let us recall that, in Sec. 3.1.2, also the library Penelope was used, showing an $\sim$ 25% of discrepancy in the K_α yield compared to Livermore. Fig. 5.5 reports the values of the parameters N_e and T_h which reproduce the K_α signal on the ZNVH, considering the nominal Geant4 simulation (i.e. cold target composed by 175 μm CH - 20 μm Cu) and the plasma simulations. The discrepancies between the two cases are less than the 5% and 30%, considering the values of T_h and

N_e, respectively, as indicated by the error bar. Reasonably, since as shown in Fig. 5.3 the plasma target stops electrons more efficiently than the cold one, higher values of T_h and N_e are required to obtain the same K_α yield. Overall, the discrepancy between the cold and the plasma models is not dramatic and it is similar to the uncertainty found in simulations using the two libraries Livermore and Penelope (see Chap. 3.1, Sec. 3.1.2). As such, considering also the experimental uncertainty in the K_α detection ($\sim 20\%$), we can conclude that the use of a cold MC method to interpret the K_α measurement of laser plasma experiments is adequate.

5.2 Effect of hot electron on a typical implosion scheme

We report on a numerical study conducted with our 3D plasma MC method on the effect of hot electrons on a typical SI implosion scheme. We consider, in particular, the scheme proposed in the numerical study of Ref. [33], reported also in Chap. 2, Sec. 2.2.2. Here, a SI capsule composed by a 31 μm CH ablator (1.05 g/cm^3), 220 μm DT shell (0.253 g/cm^3) and 737 μm DT-gas (10^{-4} g/cm^3) is imploded by the laser pulse reported in Fig. 5.6. The laser pulse consisted in a low-intensity pre-compression beam followed by an 1 ns high intensity spike launched at 13.6 ns. The total energy delivered on the capsule is around ∼350 kJ and the energy contained in the spike is ∼290 kJ. Let us specify that, in Ref. [33], the effect of hot electrons on the implosion scheme was calculated according to a 2D simplified hot electron transport model (see appendix E). We will reconsider the results of this paper using our 3D plasma MC method, in order to check the margin of error introduced by using this model. Since our MC model has not been implemented in hydrodynamic codes yet, we performed offline simulations in which the target hydrodynamic profiles were extracted from a 1D CHIC implosion simulation, in which the propagation of hot electrons was not accounted. From these 1D profiles, exploiting the spherical symmetry of the problem, 3D spherical targets were generated.

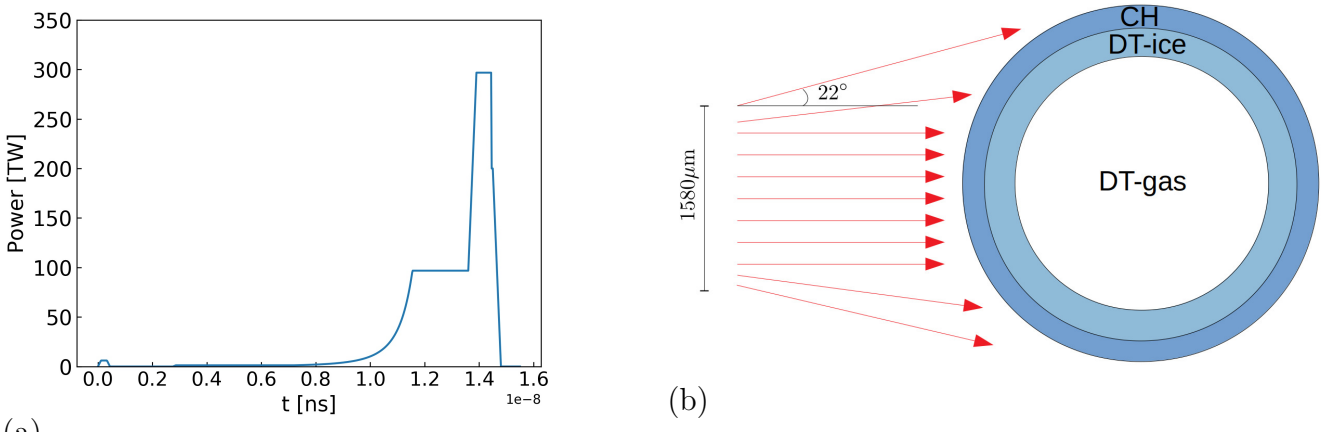

Figure 5.6: (a) Laser pulse used to implode the capsule. The laser pulse consists in a low intensity pre-compression beam followed by a high intensity spike launched at 13.6 ns. The spike has duration of 1 ns. The total energy contained in the beam is around ∼350 kJ. (b) Schematic representation of the setting of the MC simulation and geometric characteristics of the hot electron beam.

Because of the decoupling between the two codes, it was not possible to evaluate the hot electron effect on the hydrodynamic evolution of the target. Our analysis was limited in computing the energy deposition in the inner part of DT shell and in evaluating its consequent increase of the adiabat according to the perfect gas model. As introduced in Chap. 0, we define the adiabat as the ratio of the plasma pressure to the Fermi pressure of an electron degenerate gas [22]:

$$\alpha = \frac{p}{p_f}. \tag{5.1}$$

Since we are interested in the preheat of the inner part of the DT shell, the value of the adiabat in this region (α_{inn}) is computed considering the minimum of the adiabat along the shell radius, as shown in Fig. 5.7 for the simulation at 13.6 ns. The CHIC simulation predicts an initial value of α_{inn} around ~1.7 at 13.6 ns, before the spike. We compute, by means of our plasma MC code, the increase of α_{inn} before the shock convergence, considering different hot electron beams. An increase of the adiabat is related to the fact that hot electrons are sufficiently energetic to penetrate the inner part of the cryogenic shell, crossing the compressed plastic ablator and the external part of the DT shell itself. If this happens, the implosion could be compromise because of the preheat effects. Notably, not only the compression will require more energy, but the preheat causes also the global expansion of the shell, increasing its thickness and temperature and decreasing its density. Therefore, the alpha particle energy deposition which generates the burning wave will be less effective. In Ref. [26] [22] one can find a series of scaling laws that show that a high areal densities require a low adiabat implosions to minimize the laser energy invested (in the context of the conventional ICF and SI). To calculate the inner DT shell adiabat before the shock convergence, we considered the hydrodynamic profiles of the imploding capsule at four different times during the spike pulse: 13.6, 13.85, 14.1 and 14.35 ns. For each time, a plasma MC simulation is conducted by launching the hot electron beam at the critical density considering a circular spot of 1580 μm diameter (~

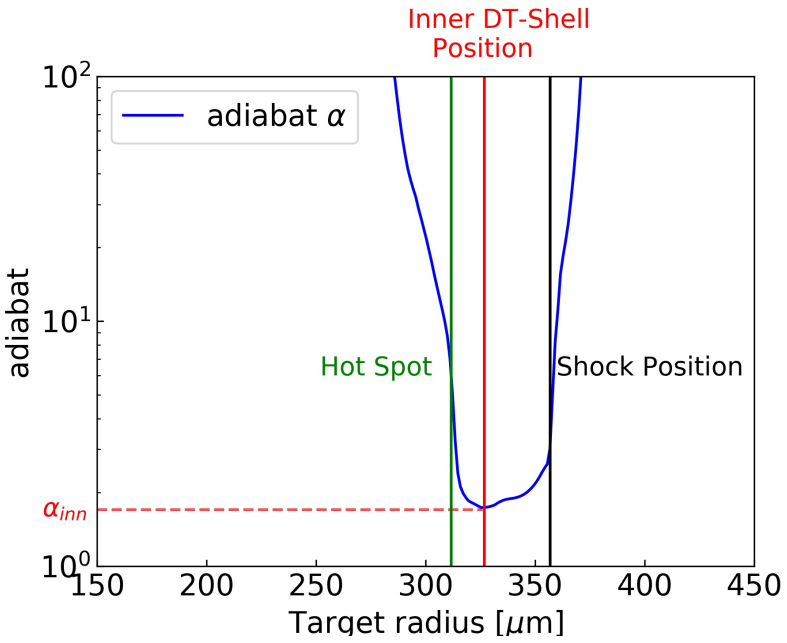

Figure 5.7: Adiabat as a function of the shell radius, computed from the CHIC simulation at 13.6 ns. The position of the shock front, the inner shell and the hot-spot are indicated by the black, the red and the green lines, respectively.

Distribution function	f_{e1}	f_{e2}	f_{e3}	f_{e4}
T_h [keV]	26	35	45	43 - 98
η[%]	11	6	3	1.2 - 0.94
α_{inn}	1.8	1.9	1.93	2.14 (2.3*)

Table 5.1: Hot electron temperatures T_h and laser to hot electron conversion efficiencies η used as input in the simulations. We performed four different simulations considering the hot electron beam characteristics found in the OMEGA experimental campaign (Chap. 3, Sec. 3.1) and used in Ref. [33]. The values of α_{inn} are the results computed according to our MC simulations. The asterisked value (2.3) is the adiabat of the inner DT shell at the shock convergence reported in Ref. [33]

the 80% of the initial target radius) and an initial beam divergence of $\pm 22°$. A schematic representation of the simulation settings is shown in Fig. 5.6 (b). Let us specify that, exploiting the spherical symmetry of the problem, only one electron beam is launched and the energy deposition along the capsule radius is computed. We are thus assuming that, in an hypothetical NIF or OMEGA implosion, each laser beam acts independently in generating hot electrons. This is not completely exact, since there are phenomena like the cross beam energy transfers that make the laser beams not independent. Electrons launched in simulations are energetically described by 2D Maxwellian functions considering different temperatures and conversion efficiencies in relation to the total spike energy. In particular, the set of parameters T_h and η found in the OMEGA experiment (Chapt. 3, Sec. 3.1) and the ones used in Ref. [33] were chosen. Notably, we considered four different cases reported in Tab. 5.1.

The calculation of the shell adiabat is conducted as explained in the following. The laser spike duration is divided in four steps of 250 ps each and a MC simulation is conducted at each step, considering the correspondent hydrodynamic profile. In each simulation, we launched an electron beam whose energy is calculated in relation to the spike energy delivered on the target in the time windows selected (250 ps), using the parameters indicated in Tab. 5.1. In order to reduce the computational time demand, the simulations were conducted by launching 10^6 particles and then by rescaling the values considering the real laser energies and conversion efficiencies. This low number of particles was sufficient to reduce the statistical noise in the quantities considered. The volumetric energy deposition in concentric spheric shells with radius $\sim$10 μm was therefore computed. The pressure induced by hot electrons is then calculated considering the law of a perfect diatomic gas:

$$p_{HE} = (\gamma - 1) e_{HE}, \tag{5.2}$$

where p_{HE} is the pressure, $\gamma = 7/5$ for a perfect gas and e_{HE} is the volumetric energy deposited by hot electrons. The adiabat at the end of the spike pulse is computed according to the formula:

$$\alpha = \frac{p}{p_f} + \Delta\alpha_1 + \Delta\alpha_2 + \Delta\alpha_3 + \Delta\alpha_4 = \frac{p}{p_f} + \frac{p_{HE1}}{p_f} + \frac{p_{HE2}}{p_f} + \frac{p_{HE3}}{p_f} + \frac{p_{HE4}}{p_f} \tag{5.3}$$

where p is the sum of the electron and ion pressure as predicted by CHIC at the shock launching time (13.6 ns), p_f is the Fermi pressure and p_{HEi} is the pressure generated by the hot electrons in the i-th time step. The Fermi pressure writes:

$$p_f = \frac{(3\pi^2)^{2/3}\hbar^2}{5m_e} n_e^{5/3}, \tag{5.4}$$

where n_e is the electron density and m_e the electron mass. By using the formula (5.3), we are assuming that the ratio p/p_f in the base CHIC simulation remains constant during the spike. This assumption was made necessary because of the decoupling between the hydrodynamic and the MC codes.

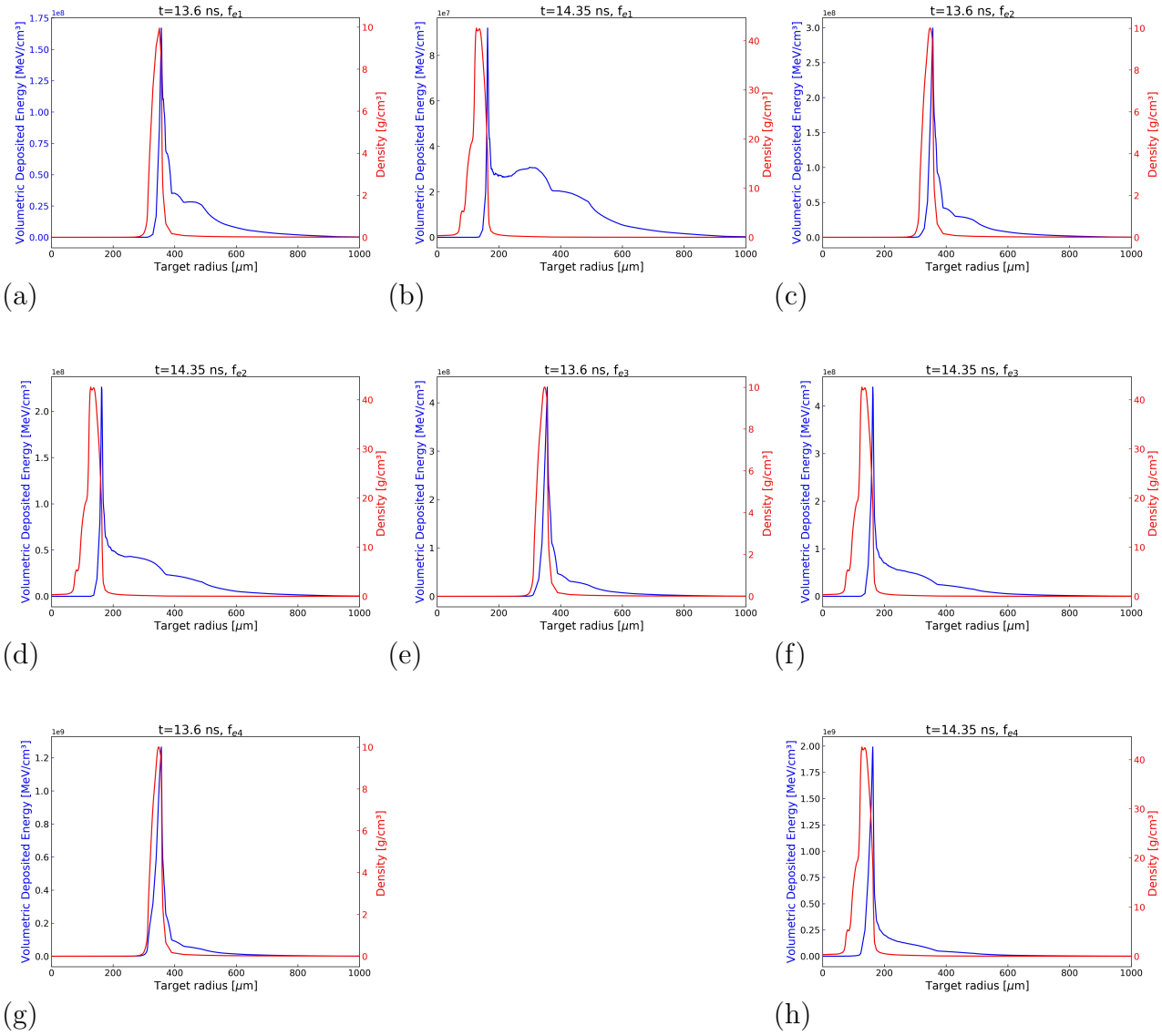

Figure 5.8: Blue curve: volumetric energy deposition along the capsule radius. Red curve: density profile of the imploding capsule as a function of the radius. The capsule center is at $r = 0$ μm and the shock is moving from the right to the left. (a) and (b): simulations performed with f_{e1} (see Tab. 5.1) and considering the target hydrodynamic profiles extracted from the CHIC simulation at 13.6 ns and 14.35 ns, respectively. (c) and (d): simulations performed with f_{e2} and considering the target hydrodynamic profiles extracted from the CHIC simulation at 13.6 ns and 14.35 ns, respectively. (e) and (f): simulations performed with f_{e3} and considering the target hydrodynamic profiles extracted from the CHIC simulation at 13.6 ns and 14.35 ns, respectively (g) and (h): simulations performed with f_{e4} and considering the target hydrodynamic profiles extracted from the CHIC simulation at 13.6 ns and 14.35 ns, respectively.

The values of α_{inn} before the shock convergence (after 14.35 ns) are indicated in the last row of Tab. 5.1, for the four cases. Here it is possible to see that the simulation with f_{e1} (T_h = 26 keV, η=11%) does not predict a significant increase of α_{inn}, despite the high intensity of the electron beam (around the 11% of the total spike energy). Conversely, the simulation with f_{e4} (T_h = 43 keV, η=1.2% - T_h = 98 keV, η=0.94%) predicts an $\alpha_{inn} \sim 2.14$, and thus a greater shell preheat. This effect could be explained considering the graphs in Fig. 5.8. In particular, the figures show the hot electron energy deposition and the target density profile as a function of the sphere radius, for two different times (13.6 and 14.35 ns) and for the four studied cases (see Tab. 5.1). The red line represents the target density profile along the shell radius, where it is possible to recognize the shocked region identified by the maximum of the function (around 10 g/cm^3 at 13.6 ns and 40 g/cm^3 at 14.35 ns). Considering the hot electron energy deposition, represented by the blue lines, it is possible to realize that in the cases f_{e1}, f_{e2} and f_{e3} both at 13.6 and at 14.35, the majority of hot electrons is stopped in the shocked region. This happens because the hot electron temperatures are low and the electrons are not sufficiently energetic to reach the inner part of the DT-shell. On the contrary, in the case f_{e4}, at 13.6 ns, the compressed part of the capsule has not sufficiently high values of ρr to stop the hot electron population at T_h= 98 keV, which can propagate up to the inner part of DT-shell. This causes a preheat effect, raising the shell adibat at ∼2.14. At 14.35 ns, in all the four cases, the target ρr is sufficient to stop the electrons. As such, in the design of SI implosion schemes, one should pay attention that the capsule has reached sufficient values of compression before launching the ignitor spike, to avoid DT-shell preheat. This is consistent with recent OMEGA experiments ([32], Sec. 2.2) in which a ρr degradation was evaluated as a function of the spike launching time. Finally, let us notice that the value of α_{inn} found in our calculation does not differ dramatically from the value computed in Ref. [33], that was 2.3. In particular, with such high value of shell adiabat, the paper predicted the ignition failure for this particular scheme.

Let us now consider the same simulation setup to evaluate the variation of the shell adiabat considering a range for the parameters η and T_h. In particular, several simulations are performed varying T_h from 20 up to 150 keV and η from 1 up to 20 % (considering the laser spike energy). Fig. 5.9 shows the inner shell adiabat α_{inn} as a function of the parameters η and T_h. The red line delimits the region of the map for which $\alpha_{inn} \leq 1.8$, the blue line the region for which $\alpha_{inn} < 2$ and the green line the region for which $\alpha_{inn} \leq 2.3$. The condition $\alpha_{inn} \leq 1.8$ is the most strict condition, which minimizes the preheat effect. The condition $\alpha_{inn} \leq 2$ was chosen because, as indicated by the Tab. 5.1 and Fig. 5.8, with such value of α_{inn} the majority of hot electrons does not penetrate in the inner DT shell. Finally, the condition $\alpha = 2.3$ is chosen because this level of preheat leads to the ignition failure, as predicted by in Ref. [33]. To evaluate which is the level of preheat that can be tolerated by the scheme, it will be necessary to conduct inline 3D hydrodynamic simulations in which the effect of the hot electrons on the shock propagation and on the hydrodynamic evolution of the capsule is accounted.

From the figure, it is possible to see that hot electrons with temperatures in the range $T_h \in [30, 50]$ keV should be limited at few precent of the spike energy, in order to satisfy the condition $\alpha \leq 1.8$. Furthermore, with this condition, the presence of more energetic electrons ($T_h > 50$ keV) should be suppressed. Considering now the experimental findings reported in Chap. 3 for the OMEGA-EP and the LMJ experiments ($T_h \in [20, 45]$ keV and $\eta \in [13, 3]$%, see Tab. 3.11), only the lower temperature - high intensity electron

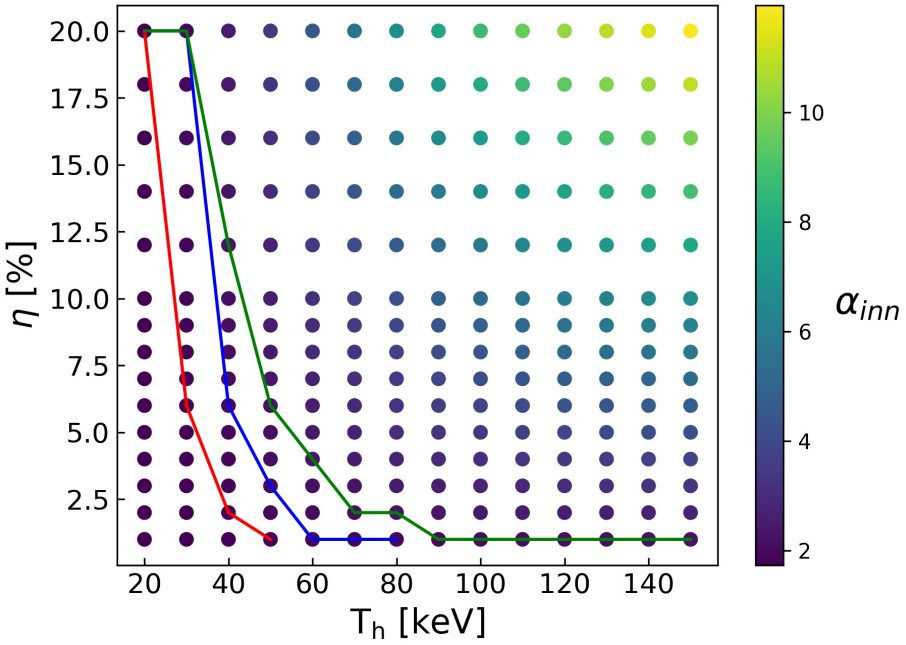

Figure 5.9: Inner shell adiabat α_{inn} as a function of the hot electron temperature T_h and laser to hot electron energy conversion efficiency η. The values of α_{inn} are calculated at the end of the implosion according to the formula (5.3), after having performed MC plasma simulations as explained at the beginning of the section. The red line indicates the points for which $\alpha_{inn} \leq 1.8$, the blue the points for which $\alpha_{inn} < 2$ and the green the points for which $\alpha_{inn} < 2.3$.

distribution functions (T_h= 20 - 25 keV, $\eta \sim 10\%$) are tolerated by the scheme. Conversely, if the condition on the α_{inn} is softened, the hot electron characteristics found in that experiments should not represent an issue. It remains to understand the role of hot electron populations at higher temperatures. As explained in Sec. 1.2.6 of Chap. 1, recent numerical simulations predicted TPD generated hot electrons with temperatures ranging from 60 up to 90 keV. According to our study, to obtain $\alpha_{inn} < 2$ these populations should be limited at $\eta \sim 1\%$.

5.3 Conclusion

This chapter reports two numerical studies, conducted with the plasma MC code presented in Chap. 4, considering planar and spherical targets. In Sec. 5.1, we showed that the interpretation of laser-plasma experiments using cold MC codes is appropriate, despite these methods neglect several features characteristic of a laser irradiated target. In particular, the target ablation causes the electrons to keep their directionality, reducing their angular spreading. This effect is however counterbalanced by the fact that targets are in plasma state and the screening lengths of nuclear potentials of plasma ions are greater compared to the cold case. As such, in plasma the scattering is enhanced and the electron beam is more diffused, compared to the cold case. Because of the competition of these two effects, the propagation of hot electrons in cold or in laser ablated planar targets does not differ dramatically. As such, cold MC methods can be considered adequate to

interpret laser-plasma experiments. This is further confirmed by the recomputation of the K_α signal done considering hot electrons propagating in laser irradiated targets. The differences on the parameters T_h and N_e for the cold and the irradiated targets are of $\sim 5\%$ and $\sim 30\%$, respectively. Considering the typical experimental uncertainties in the K_α and bremsstrahlung measurements (see Sec. 3.1.2), these differences are acceptable.

In the second part of the chapter, we presented a numerical investigation aimed at evaluating the effect of the hot electrons on a typical SI implosion scheme. The hot electron energy deposition in the inner part of the DT shell is computed considering different hot electron characteristics (temperature and conversion efficiencies with respect to the laser energy). The study shows that low hot electron temperatures (20-25 keV) do not cause a preheat concern, even at high conversion efficiencies. Conversely, the presence of electrons at temperatures around 30 - 40 keV should be limited at few percent of the laser energy, while hot electron populations with temperatures greater than 50 keV should be suppressed.

Chapter 6

Conclusion

The characterization of the hot electrons and the comprehension of their role in ICF are critical steps for assessing the feasibility of the implosion schemes, in particular the shock ignition approach. On this basis, the thesis work developed having several objectives:

1. Characterize hot electrons in conditions relevant to ICF and in particular to SI. This is accomplished by analysing experimental data obtained in several experiments conducted in different laser facilities. The capability of each facility allowed access to different plasma conditions, exploring different interaction regimes.

2. Develop a 3D hot electron propagation model with the aim of future implementation in hydrodynamic codes. This model considers the propagation of hot electrons in plasmas, taking into account their collisions with other free plasma electrons and with ions.

3. Evaluation of the margin of error introduced by using cold Monte-Carlo methods to interpret laser-plasma experiments aimed at characterizing hot electrons. This is done by comparing the hot electron transport in cold and in laser irradiated targets, using the plasma Monte-Carlo code developed.

4. Evaluation of the hot electron preheat effect on a typical SI implosion scheme. The energy deposition in the inner DT shell of a typical implosion scheme is evaluated using the plasma MC code developed, considering hot electrons with different characteristics.

We present here the conclusions of this work.

6.1 Experimental characterization of hot electrons

We presented the results of three experimental campaigns aimed at characterizing hot electrons, conducted in three different laser facilities: OMEGA-EP, PALS and LMJ. According to the capabilities and the laser parameters of each facility, different interaction conditions were explored. Several diagnostics were used in each experiment, notably, backscattered laser light spectrometers, x-ray spectrometers and x-ray streaked cameras. The spectrometers allowed to obtain information on hot electrons, while the streak cameras were involved to perform shock radiographs or shock breakout pyrometry.

In this thesis, we focused our attention in particular on the post-processing of the x-ray spectrometers, used to detect the radiation emitted by the hot electron propagation in targets. In particular, the x-ray spectrometers considered in this work are the K_α and the bremsstrahlung spectrometers. Despite these diagnostics have been frequently used in the last decade, in the literature a detailed explanation on their post-processing techniques and the setup of the simulations is usually omitted. As such, we performed a detailed study on their behaviour, presenting a post-processing methodology.

The time integrated bremsstrahlung spectrometer is composed of a stack of filters and IPs that deconvolute the bremsstrahlung spectrum: the more a photon is energetic, the more it propagates inside the stack, depositing energy in deeper IPs. The bremsstrahlung spectrum detected by the diagnostic is retrieved by following these steps: at first, it is necessary to guess a form for the photon distribution function dependent on free parameters. In this regard, we considered single temperature exponential functions of the type $f_{\mathrm{ph}}(E) = \frac{\mathrm{A_{ph}}}{E} e^{-\frac{E}{\mathrm{T_{ph}}}}$ or $f_{\mathrm{ph}}(E) = \frac{\mathrm{N_{ph}}}{\mathrm{T_{ph}}} e^{-\frac{E}{\mathrm{T_{ph}}}}$, with free parameters $\mathrm{A_{ph}}$ ($\mathrm{N_{ph}}$) and $\mathrm{T_{ph}}$. Then the diagnostic response is simulated using a MC method, to calculate the theoretical energy deposition through the IPs as a function of the free parameters $\mathrm{A_{ph}}$ ($\mathrm{N_{ph}}$) and $\mathrm{T_{ph}}$. Finally, the values of the free parameters are calculated using the reduced chi-square analysis with the experimental data. In particular, we proposed not only to consider the solution that minimizes the chi-square function (as commonly done in the literature), but to take also into account a series of degenerate solutions coming from the figure of merit $\chi^2 \to 1$. This allows to find a map of possible photon distribution functions detected by the diagnostic.

In the analysis, hot electrons were assumed to be energetically described by 2D Maxwellian distribution functions $f_{\mathrm{e}}(E) = \frac{\mathrm{N_e}}{\mathrm{T_h}} e^{-\frac{E}{\mathrm{T_h}}}$. The parameters $\mathrm{N_e}$ and $\mathrm{T_h}$ are retrieved by performing MC simulations of electron propagation in the targets, reproducing the bremsstrahlung and the K_α signal on the diagnostics. These MC simulations are performed using cold MC codes (Geant4), which do not account for the hydrodynamic evolution and the ionization state of the target. Despite this, these methods are appropriate for the interpretation of the experiments.

This post-processing methodology is applied in the analysis of the experimental campaigns cited above. In particular, in the OMEGA and in the LMJ experiments hot electrons were found to have values of $\mathrm{T_h}$ ranging from 20 up to 45 keV, with conversion efficiency with respect to the laser energy going from 3% up to 13%. Considering the OMEGA experiment, the range of temperature found is similar to what reported by previous experiments in similar conditions, but the obtained values of conversion efficiency are slightly higher. Further experimental investigations will be required to understand the origin of this mismatch and to confirm our findings. One possibility is the fact that previous experiments did not consider the degenerate solutions coming from the bremsstrahlung spectrometer post-processing, considering only the function that minimizes the chi-square. Concerning the LMJ experiment, other shots will allow to confirm or not our findings, giving a better statistics.

In the PALS experiment, the values of temperature found were similar to the ones obtained in the OMEGA and LMJ experiments (i.e. $\mathrm{T_h} \in [25, 50]$ keV), but accompanied by lower conversion efficiencies ($\eta \sim 1 - 2\%$). This range of temperature is consistent

with previous PALS experiments conducted in analogous conditions, but our conversion efficiency was slightly lower. This could be due to the fact that, in the analysis, we considered only the photon distribution function that minimizes the chi-square, neglecting the possibility of a degenerate solution. For what concerns the influence of the ablator composition on the hot electrons, consistently to what found in the literature, mid-Z ablators seemed to reduce the hot electron generation. Lower hot electron temperatures were found for the Al and the Ni cases, compared to the CH and C ablators. This is a positive effect for the SI scheme, however particular care should be given in choosing a high Z ablators, because of the enhance preheat effects due to the radiative transport.

The large uncertainty in the values of T_h and η, measured by the spectrometers can be reduced constraining the problem using other experimental data, relying for example on shock measurements. In particular, this is done for the OMEGA experiment by performing hydrodynamic simulations aimed at reproducing the target hydrodynamic evolution observed in the shock radiographs. For this purpose, hydrodynamic simulations were conducted using as input different electron distribution functions, characterized by different values of T_h and η as retrieved by the spectrometers. We finally find that lower hot electron temperatures and higher conversion efficiencies ($T_h \sim$27 keV, $\eta \sim 10\%$) allow to better reproduce the experimental data.

6.2 3D Monte-Carlo method to simulate the hot electron propagation in ionized targets

With the increase of the computational power at disposal, during the last few years 3D hydrodynamic codes have been developed. Having in mind of simulating the entire implosion process, a module of hot electron propagation should be implemented in these codes. As such, part of the thesis work was devoted to the developing of a hot electron transport model, with the aim of future implementation in hydrodynamic codes.

In this regard, a Monte-Carlo (MC) approach was chosen to simulate the hot electron propagation in fusion targets. Differently from common MC methods (e.g. Geant4), this model simulates the hot electron propagation in ionized or partially ionized targets, taking into account the presence of the plasma state. As such, in this condition, the electron diffusion is ruled by elastic scattering with other plasma electrons and by collisions with nuclei screened by their residual electronic structure and by other plasma particles. These phenomena are modelled according to suitable scattering differential cross sections, as the Moller's cross section for the electron-electron scattering and the Dalitz's formula, which models the collisions between an electron and a completely ionized nucleus screened by plasma charges. The collision between an electron and a partially ionized nucleus, screened by its residual electronic structure and by other plasma particles, is a phenomenon rarely addressed in the literature, for which it was not possible to find an adequate differential cross section. As such, we derived and we proposed an analytical form of scattering differential cross section aimed at modelling this collision.

The MC method is developed following the so-called mixed algorithm approach. Here, electrons propagate for distances greater than their mean free paths, and the new directions are evaluated according to multiple scattering theories. In particular, soft collisions are modelled according to the Goudsmit and Saunderson theory, while hard collisions are

simulated considering two-bodies interaction. The electron slowing down and the energy deposition are computed according to plasma stopping power formulas.

An important difference with the cold MC methods is the fact that electrons propagate in targets in which strong density gradient are present. Notably, the ablation and compression waves generated by the laser interaction. As such, a new algorithm to evaluate the electron mean free path in inhomogeneous materials is developed and presented.

6.3 Comparison between cold and plasma MC methods

The MC code is used at first to reconsider the interpretation of the laser-plasma experiments aimed at characterizing hot electrons, presented in this work. In particular, these experiments are interpreted by means of cold MC methods, i.e. codes in which the ionization state of the targets and their hydrodynamic evolution are not accounted. To better understand which is the margin of error introduced by using these codes, the propagation of hot electrons in cold and in laser irradiated targets is compared. From this comparison, it comes that a laser irradiated target absorbs and stops more efficiently the electron beam. This effect is due to the competition between two effects: the variation of the ρr (i.e. the formation of an ablated and a shocked region) and the presence of longer screening lengths of nuclear potentials in plasma. In particular, the presence of the ablated region causes the electron beam to be more collimated, while the fact that the screening lengths are grater enhances the beam diffusion. The net effect of these two competitive phenomena is the fact that electrons diffuse more in ionized targets than in a cold ones. However, the difference between the two cases is not dramatic, leading to an error of ~ 5 and 30 % in the computation of the parameters T_h and N_e of the electron distribution function. These errors are comparable with the experimental uncertainty of the measurements, and we can consider appropriate to interpret a laser-plasma experiment using a cold MC method.

6.4 Hot electron induced preheat effect on a typical SI implosion scheme

The plasma MC code is finally used to evaluate the preheat effect induced by the hot electrons on a typical SI implosion scheme. In particular, the increase of the inner shell adiabat driven by hot electrons is evaluated considering different hot electron temperatures and laser to hot electron energy conversion efficiencies. The study suggests that the implosion scheme can tolerate low values of hot electron temperatures (20 - 25 keV) up to high conversion efficiencies ($\sim 10\%$). More energetic electron populations should be limited as much as possible. Therefore, considering the range of the values T_h and η retrieved in the experimental campaigns presented in this work ($T_h \in [20, 50]$ keV, $\eta \in [3, 13]$ %), only the lower hot electron temperatures will be tolerated (by the scheme proposed).

6.5 Perspectives

For what concerns the experimental characterization of hot electrons, further efforts will be required in the near future to refine the experimental techniques and to obtain more precise results. In particular, the scientific community is working at developing diagnostics that can give more precise information on hot electrons, trying in particular to detect the presence of highly energetic populations. The choice of using single temperature electron distribution functions to interpret the experiments was dictated by the nature of the signal collected through the IPs in the bremsstrahlung spectrometers. Notably, only the first seventh or tenth IPs collected a significant level of energy deposition in the experiments analysed in this work. These signal was adequately fitted with single temperature photon distribution functions, which were generated by single temperature electron distribution functions. Having at our disposal other diagnostic techniques, such as electron spectrometers, or refining the filtering of the bremsstrahlung spectrometers will allow to detect also higher energy electron populations. This is particularly important, since these highly energetic hot electron populations represent a preheat concern. Having information on their intensity and energy will allow to design robust implosion schemes. Let us also mention that the development of the diagnostics should be accompanied by the development of the numerical methods to analyse them. As we showed in the thesis, the analysis of the bremsstrahlung spectrometers relies on complex MC simulations coupled with a fitting numerical procedure. In the case of a multiple temperatures distribution functions, the fitting procedure will become more complex, since four or six free parameters will have to be considered.

Still considering the diagnostic development, a great effort is being made by the scientific community to develop time resolved spectrometers. The possibility of resolving the x-ray radiation emitted by the propagation of hot electrons in time will give important information on the laser-plasma mechanisms which are responsible of the electron acceleration.

Finally, other experiments should be conducted to characterize hot electrons in real SI conditions, exploiting laser facilities such as the NIF or the LMJ. Since, however, having access at such large facilities is relatively difficult, other experiments can be conducted in smaller installations like PALS or OMEGA. This will allow to refine the diagnostic techniques and to obtain more precise information on hot electrons, trying to reduce the large ambiguity on the parameters T_h and η reported in our analysis. An adequate characterization of hot electrons in SI conditions is a critical step for answering the feasibility of the scheme and to propose robust implosion configurations.

Considering now the theoretical part of the thesis, other physical phenomena could be added to the plasma MC method. In particular, it will be necessary to evaluate the effect of the collective effects and of the self generated electromagnetic fields on the hot electron propagation, trying to understand if they are really negligible. Furthermore, the generation of secondary electrons, generated by hard collisions, should be simulated.

Another interesting feature that could be added to the MC code is the generation of the x-ray radiation due to the hot electron propagation. In this way, once implemented in hydrodynamic codes, it will be possible to perform hydrodynamic simulations in which the bremsstrahlung and the K_α emission are simulated. This will allow to interpret future planar and spherical experiments with more confidence, without relying on cold MC methods.

However, the code is ready to be implemented in hydrodynamic codes and, in the near future, it will be possible to perform several theoretical studies and to propose robust SI implosion schemes. In particular, it will be possible to perform simulations considering different ablators and to evaluate the effects of hot electrons on different schemes. As mentioned in the last chapter of the thesis, the spike launching time is a crucial parameter to be chosen in order to avoid shock collision mismatch and hot electron preheat. As such, several implosion schemes can be studied, varying the initial target configuration or the spike launching time, in order to find out which is the most robust solution.

Appendices

Appendix A

Chi-squared analysis

The chi-squared test is a statistical procedure to determine whether an observed distribution is consistent with the expected theoretical distribution. Namely, the test is used to determine if there is a statistically significant difference between the expected frequencies and the observed frequencies [206] [207].

Let us consider to have a set of measurements $x_1, x_2 ... x_N$ (the signals deposited through the IPs) and let us assume that each measurement is characterized by a Gaussian distribution with mean value $\langle x_i \rangle$ and variance σ_i^2:

$$p(x_i) = \frac{1}{\sigma_i \sqrt{2\pi}} \exp\left[-\frac{(x_i - \langle x_i \rangle)^2}{2\sigma_i^2} \right]. \tag{A.1}$$

Considering N points, the total proability reads:

$$P(x_i, \langle x_i \rangle, \sigma_i) = \frac{1}{(2\pi)^{N/2} \Pi_i \sigma_i} \exp\left[-\sum_i^N \frac{(x_i - \langle x_i \rangle)^2}{2\sigma_i^2} \right]. \tag{A.2}$$

Introducing now a distribution function $f(y)$ which predicts the mean for each data point ($f(y) \sim \langle x_i \rangle$), eq. (A.2) becomes:

$$P(x_i, \langle x_i \rangle, \sigma_i) = \frac{1}{(2\pi)^{N/2} \Pi_i \sigma_i} \exp\left[-\sum_i^N \frac{(x_i - f(y_i))^2}{2\sigma_i^2} \right]. \tag{A.3}$$

This function will find its maximum when the argument of the exponent is minimum. From this consideration, a new variable is introduced, the so-called chi-squared statistic:

$$\chi^2 = \sum_i^N \frac{(x_i - f(y_i))^2}{\sigma_i^2}. \tag{A.4}$$

In statistics, the method of least squares is built on the hypothesis that the distribution function which better describes a set of data is the one that minimizes function χ^2. Note that, ideally, given the fluctuations of the values of x_i about their mean values $\langle x_i \rangle$, each term in the sum will be of order unity. As such, $\chi^2 \sim N$, and a first figure of merit to evaluate if a distribution function fits the data is to obtain $\chi^2 \ll N$. However, according to the statistics literature, a more exact procedure relies on considering the *reduced chi-squared*, defined as:

$$\chi^2_\nu = \frac{\chi^2}{\nu}, \tag{A.5}$$

where ν is the number of *degrees of freedom*. The number of degrees of freedom is defined as the number of observed data minus the number of parameters used in the calculation [282] [283]. As such, considering our problem of fitting the signal through the IPs, ν would be defined as the number of IPs in which the signal was deposited minus 2, the number of free parameters of the photon distribution function. The χ^2 (or the χ^2_ν, the two variables differ only because of a multiplication factor) is a random variable and it will be described by an adequate distribution function. The probability density for the variable χ^2, considering ν degrees of freedom reads [206]:

$$p_\nu(\chi^2) = C_\nu(\chi^2)^{\frac{\nu}{2}-1}\exp\left(-\frac{\chi^2_\nu}{2}\right), \tag{A.6}$$

where C_ν is a normalization constant. From this, it is possible to derive that $\langle\chi^2\rangle = \nu$ and, as such, $\langle\chi^2_\nu\rangle = 1$.

Let us now consider an experiment in which a set of data is described by a given distribution function and the fit is characterized by $\chi^2_\nu = \chi^2_{\nu 0}$. If one reperforms the experiment, the probability of having a worse result is equal to $P(\chi^2_\nu > \chi^2_{\nu 0})$, i.e. to the probability of obtaining a value of χ^2_ν greater than $\chi^2_{\nu 0}$. Mathematically, this concept writes:

$$P(\chi^2_\nu > \chi^2_{\nu 0}) = \int_{\chi^2_{\nu 0}}^{\infty} p(\chi^2_\nu)\mathrm{d}\chi^2_\nu. \tag{A.7}$$

The literature reports a tabulation for which the condition $P(\chi^2_\nu > \chi^2_{\nu 0})$ is evaluated as a function of ν and $\chi^2_{\nu 0}$. This means to look at the probability of finding a distribution function that fits the data worse than the distribution used to obtain a reduced chi-squared equal to $\chi^2_{\nu 0}$. Considering now, as we did in the analysis of the bremsstrahlung spectrometer, $\chi^2_{\nu 0} = 1$ and typical values of $\nu \in [5, 8]$ the probability of findings photon distribution functions that fit the data worse than the found distributions is around the 40%. This is a quite fair result. A low value of this probability would mean that the distribution function found is not adequate in fitting the data, since it would indicate that there are many other distribution functions that work better. Conversely, a high value of probability indicates that the fitting function is correct, but "suspicious", since there is the possibility that other distribution functions would work. As reported in Fig. 3.6, $\chi^2_{\nu 0} = 1$ is a good figure of merit to retrieve a series of photon distribution functions that deposit energy through the IPs consistently with the experimental error of the measure.

Appendix B

Scanner calibration

When imaging plates are red in the scanner, the blue light generated by the de-excitation of metastable centres is collected by a photomultiplier tube (PMT) and digitized in a 2D image. Since different laser facilities posses scanner from different manufacturers, an universal calibration method has been adopted. This method consisted in using a radioactive source of known activity (radiocarbon), or pre-calibrated scanners with radioisotopes for which the activity was not known. As an example, at the NIF, imaging plates were exposed to a radiocarbon source for a fixed time to yield a known absorbed dose. After that, the IPs were scanned considering different photomultiplier gain voltage from 500 up to 1000 V. With this procedure, it is possible to obtain a calibration curve for which the PSL values are correlated to the signal recorded by the scan considering different parameters. In particular, the formula reported in the literature is [136]:

$$PSL = \left(\frac{G}{2^{16}-1}\right)^2 \left(\frac{R_{\mu\mathrm{m}}}{100}\right)^2 h(V) 10^{L/2} \tag{B.1}$$

Here $\mathrm{R}_{\mu\mathrm{m}}$ is the spatial resolution in μm, L is the dynamic range latitude (4 or 5 according to the scanner), G is the recorder signal and $h(V)$ is an empiric function related to the chosen value of voltage. In Ref. [136], empirical laws and graphs on the behaviour of $h(V)$ with the voltage are reported. These curves are reported for the scanners placed at the NIF, at the LLE and at GEKKO. Scan calibrations were also done at the LMJ laser facility, and the information is contained in an internal report.

We considered these calibrations to calculate the PSL values in the IPs, for the experiments conducted at OMEGA and at LMJ.

Appendix C

Derivation of the Goudsmit and Saunderson distribution function

We report here the analytical derivation of the Goudsmit and Saunderson distribution function. These calculations are based on the works of Lewis [250] and Bethe [284] [285]. As reported in Chap. 1, the Boltzmann equation that describes the evolution of the distribution function $f_e(\mathbf{r}, \mathbf{v}, t)$ is:

$$\frac{\partial f_e}{\partial t} + \mathbf{v} \cdot \nabla f_e - \frac{e}{m_e}\left(\mathbf{E} + \frac{\mathbf{v} \times \mathbf{B}}{c}\right) \cdot \frac{\partial f_e}{\partial \mathbf{v}} = C_e. \tag{C.1}$$

Here $f_e(\mathbf{r}, \mathbf{v}, t)$ denotes the probability density of finding the electron at the position $\mathbf{r}$ moving with velocity $\mathbf{v}$ in the direction given by the unit vector $\mathbf{u}$, i.e. $\mathbf{v}$=$v\mathbf{u}$. In spherical coordinates, $\mathbf{u}$ is represented by polar and azimuthal angles θ and φ.

Considering elastic scattering and the absence of electric and magnetic fields, eq. (C.1) reads:

$$\frac{\partial f_e}{\partial t} + \mathbf{v} \cdot \nabla f_e = N \int \left[f_e(\mathbf{r}, \mathbf{v'}, t) - f_e(\mathbf{r}, \mathbf{v}, t)\right] \frac{\mathrm{d}\sigma(\theta, v)}{\mathrm{d}\Omega} v \, \sin\theta \mathrm{d}\theta \mathrm{d}\varphi \tag{C.2}$$

where N is the number of scattering centers per unit volume, σ is the elastic scattering cross section, $\mathbf{v}$ is the incident electron velocity and θ and φ are the polar and the azimuthal scattering angles. Here we are assuming that the incident particle moves along the z-axis, i.e. with θ=0. Dividing the equation by the modulus of the particle velocity v and introducing the arc length traversed by the particle $\mathrm{d}s = vt$, eq. (C.2) becomes (eq. (1) in Ref. [250]):

$$\frac{\partial f_e}{\partial s} + \mathbf{u} \cdot \nabla f_e = N \int \left[f_e(\mathbf{r}, \mathbf{u'}, s) - f_e(\mathbf{r}, \mathbf{u}, s)\right] \frac{\mathrm{d}\sigma(\theta, v)}{\mathrm{d}\Omega} \mathrm{d}\mathbf{u'}. \tag{C.3}$$

Let us notice that $\mathrm{d}\mathbf{u'} = \sin\theta \mathrm{d}\theta \mathrm{d}\varphi$. This equation is solved by Lewis by expanding the function $f_e(\mathbf{r}, \mathbf{u}, t)$ in spherical harmonics:

$$f_e(\mathbf{r}, \mathbf{u}, t) = \sum_{\lambda,\mu} f_{\lambda,\mu}(\mathbf{r}, s) \, Y_{\lambda,\mu}(\mathbf{u}) = \sum_{\lambda,\mu} f_{\lambda,\mu}(\mathbf{r}, s) \, Y_{\lambda,\mu}(\theta, \varphi), \tag{C.4}$$

where

$$f_{\lambda,\mu}(\mathbf{r}, s) = \int Y^*_{\lambda,\mu}(\mathbf{u}) \, f_e(\mathbf{r}, \mathbf{u}; s) \, \mathrm{d}\mathbf{u}. \tag{C.5}$$

Using this in Eq. (C.3) we obtain:

$$\begin{aligned}\frac{\partial}{\partial s}\sum_{\lambda,\mu} f_{\lambda,\mu}\left(\mathbf{r},s\right) Y_{\lambda,\mu}\left(\mathbf{u}\right) + \sum_{\lambda,\mu} \mathbf{u}\cdot\nabla f_{\lambda,\mu}\left(\mathbf{r},s\right) Y_{\lambda,\mu}\left(\mathbf{u}\right) = \\ N\sum_{\lambda,\mu}\int f_{\lambda,\mu}\left(\mathbf{r},s\right)\left[Y_{\lambda,\mu}\left(\mathbf{u'}\right) - Y_{\lambda,\mu}\left(\mathbf{u}\right)\right]\frac{\mathrm{d}\sigma\left(\theta,v\right)}{\mathrm{d}\Omega}\mathrm{d}\mathbf{u'}.\end{aligned} \tag{C.6}$$

This equation is projected on a basis function $Y_{l,m}$ using the scalar product $\int Y^*_{l,m}\left(\mathbf{u}\right)\mathrm{d}\mathbf{u}$, i.e:

$$\begin{aligned}\sum_{\lambda,\mu}\frac{\partial}{\partial s} f_{\lambda,\mu}\left(\mathbf{r},s\right)\int Y^*_{l,m}\left(\mathbf{u}\right) Y_{\lambda,\mu}\left(\mathbf{u}\right)\mathrm{d}\mathbf{u} + \sum_{\lambda,\mu}\nabla f_{\lambda,mu}\left(\mathbf{r},s\right)\int Y^*_{l,m}\left(\mathbf{u}\right)\mathbf{u} Y_{\lambda,\mu}\left(\mathbf{u}\right) = \\ N\sum_{\lambda,\mu} f_{\lambda,\mu}\left(\mathbf{r},s\right)\int\int Y^*_{l,m}\left(\mathbf{u}\right)\left[Y_{\lambda,\mu}\left(\mathbf{u'}\right) - Y_{\lambda,\mu}\left(\mathbf{u}\right)\right]\frac{\mathrm{d}\sigma\left(\theta,v\right)}{\mathrm{d}\Omega}\mathrm{d}\mathbf{u}\mathrm{d}\mathbf{u'}.\end{aligned} \tag{C.7}$$

Considering the addition theorem of the spherical harmonics:

$$P_l\left(\cos\theta\right) = \frac{4\pi}{2l+1}\sum_{m=-l}^{+l} Y^*_{m,l}\left(\theta,\varphi\right) Y_{m,l}\left(\theta,\varphi\right), \tag{C.8}$$

and the orthogonality condition [242]:

$$\int_0^{2\pi}\mathrm{d}\varphi\int_0^{\pi}\mathrm{d}\theta\sin\theta Y^*_{m',l'}\left(\theta,\varphi\right) Y_{m,l}\left(\theta,\varphi\right) = \frac{4\pi}{2l+1}\delta_{l,l'}\delta_{m,m'}, \tag{C.9}$$

only terms indexed l, m will remain and eq. (C.7) writes:

$$\begin{aligned}\frac{\partial f_{lm}\left(\mathbf{r},s\right)}{\partial s} + 2\pi N f_{lm}\left(\mathbf{r},s\right)\int_0^{\pi}\frac{\mathrm{d}\sigma(\theta)}{\mathrm{d}\Omega}\Big[1 - P_l\left(\cos\theta\right)\Big]\sin\theta\mathrm{d}\theta = \\ -\sum_{\lambda,\mu}\nabla f_{\lambda,\mu}\left(\mathbf{r},s\right)\cdot\int Y^*_{l,m}\mathbf{u} Y_{\lambda,\mu}\mathrm{d}\mathbf{u}.\end{aligned} \tag{C.10}$$

In Lewis' paper [250], this equation is written in a more compact form:

$$\frac{\partial f_{lm}\left(\mathbf{r},s\right)}{\partial s} + \kappa_l f_{lm}\left(\mathbf{r},s\right) = -\sum_{\lambda,\mu}\nabla f_{\lambda,\mu}\left(\mathbf{r},s\right)\cdot\mathbf{Q}_{lm}{}^{\lambda\mu}, \tag{C.11}$$

introducing the quantities:

$$\kappa_l = 2\pi N\int_0^{\pi}\frac{\mathrm{d}\sigma(\theta)}{\mathrm{d}\Omega}\Big[1 - P_l\left(\cos\theta\right)\Big]\sin\theta\mathrm{d}\theta, \tag{C.12}$$

$$\mathbf{Q}_{lm}{}^{\lambda\mu} = \int Y^*_{l,m}\mathbf{u} Y_{\lambda,\mu}\mathrm{d}\mathbf{u}. \tag{C.13}$$

Eq (C.11) is integrated in the variable $\mathbf{r}$, yielding:

$$\frac{\partial F_l(s)}{\partial s} + \kappa_l F_l(s) = 0, \tag{C.14}$$

where $F_l(s) = \int f_{l,m}(\mathrm{r}, s)\,\mathrm{d}\mathbf{r}$. The right-hand side of equation (C.11) integrated over all space is zero, since $f(\mathbf{r} \to \infty, s) = 0$. Eq. (C.14) is solved considering the boundary condition:

$$f_{lm}(\mathbf{r}, 0) = \delta_{m0}\delta(\mathbf{r})\, Y_{l0}(0) = \left[\frac{(2l+1)}{4\pi}\right]^{1/2} \delta_{m0}\delta(\mathbf{r}). \tag{C.15}$$

For t=0, f_e is 0 except at $\mathbf{r}$=0 and the incident beam has initial direction θ=0. The condition δ_{m0} reflects the cylindrical geometry of the process. The solution of this equation considering the boundary condition is:

$$F_l(s) = \left[\frac{(2l+1)}{4\pi}\right]^{\frac{1}{2}} \exp\left(-\int_0^{\Delta s} \kappa_l \mathrm{d}s\right). \tag{C.16}$$

Considering the initial expansion of the distribution function f_e (C.4):

$$f_e(\mathbf{r}, \mathbf{u}, s) = \sum_{l=0}^{\infty} f_{l,0}(\mathbf{r}, s)\, Y_{l0}(\theta, \varphi), \tag{C.17}$$

we can introduce the distribution function $F_{GS}(\mathbf{u}, s)$, obtaining:

$$\begin{gathered} F_{GS}(\mathbf{u}, s) = \int f_e(\mathbf{r}, \mathbf{u}, s)\,\mathrm{d}\mathbf{r} = \sum_{l=0}^{\infty} \int f_{l,0}(\mathbf{r}, s)\, Y_{l0}(\theta, \varphi)\,\mathrm{d}\mathbf{r} = \\ \sum_{l=0}^{\infty} F_l(s) Y_{l0}(\theta, \varphi) = \sum_{l=0}^{\infty} \left[\frac{(2l+1)}{4\pi}\right] P_l(\cos\theta) \exp\left(-\int_0^{\Delta s} \kappa_l \mathrm{d}s\right) = \\ \sum_{l=0}^{\infty} \left[\frac{(2l+1)}{4\pi}\right] P_l(\cos\theta) \exp\left(-2\pi N \int_0^{\Delta s} \int_0^{\pi} \frac{\mathrm{d}\sigma(\theta)}{\mathrm{d}\Omega} \big[1 - P_l(\cos\theta)\big] \mathrm{d}s\right). \end{gathered} \tag{C.18}$$

Introducing the *transport mean free paths*:

$$\lambda_l^{-1} = 2\pi N \int_0^{\pi} \frac{\mathrm{d}\sigma(\theta)}{\mathrm{d}\Omega} \big[1 - P_l(\cos\theta)\big] \sin\theta \mathrm{d}\theta, \tag{C.19}$$

and integrating in the variable s we finally obtain:

$$F_{GS}(\theta, s) = \sum_{l=0}^{\infty} \left[\frac{(2l+1)}{4\pi}\right] P_l(\cos\theta) \exp\left(\frac{-\Delta s}{\lambda_l}\right). \tag{C.20}$$

Eq. C.20 represents the probability density function for the particle to assume a final direction in the solid angle element $\mathrm{d}\Omega$, around a direction defined by the polar angle θ, after have travelled for a path Δs. This distribution function does not depend on the azimuthal scattering angle φ, according to the cylindrical symmetry of the problem. This result was firstly derived by Goudsmit and Saunderson [248].

Appendix D

Derivation of the electron energy losses due to excitation of plasma waves

The analytical derivation of the formula (4.67) is presented in this appendix. The equation is derived in Jackson [242] by adapting the derivation of the Fermi's density effect for cold materials in plasma case.

Let us consider a fast charged particle ze that moves along the x-axis interacting with a plasma electron at impact parameter b (see Fig. D.1). If the distance between the particle and the electron is smaller than the plasma screening parameter D (i.e. the Debye length or the ion sphere radius), the individual-particle behaviour dominates and a two-body collision takes place. This is modelled by the formula (4.60). If $b > D$, the collective behaviour of plasma dominates and plasma oscillations develop because of the electric field generated by the fast particle. To calculate the energy transfer that takes place in this process, we consider the deflection of the incident particle due to these collisions to be negligible. I.e. the particle propagates according to straight lines. Furthermore, since the energy exchange is not large, the plasma electron oscillates around the equilibrium position with an amplitude much smaller than b. This is called *dipole approximation*. The energy exchanged between the fast particle and a plasma electron put in motion with velocity $\dot{\mathbf{x}}(t)$ is:

$$\Delta E = e \int_{-\infty}^{+\infty} \dot{\mathbf{x}}(t) \cdot \mathbf{E}(t) \mathrm{d}t, \tag{D.1}$$

where $\mathbf{E}(t)$ is the field of the incident particle on the electron. In the frequency domain ω this relation writes:

$$\Delta E = 2e \mathrm{Re} \int_{0}^{+\infty} i\omega \mathbf{x}(\omega) \cdot \mathbf{E}^*(\omega) \mathrm{d}\omega, \tag{D.2}$$

where we used the Fourier transform:

$$F(\mathbf{k}, \omega) = \frac{1}{4\pi^2} \int \mathrm{d}^3 k \int \mathrm{d}\omega F(\mathbf{x}, t) e^{(i\mathbf{x}\cdot\mathbf{k} - i\omega t)}. \tag{D.3}$$

Considering now the presence of many electrons that respond to the electric field, eq. (D.2) reads:

$$\Delta E = 2e \sum_j f_j \mathrm{Re} \int_{0}^{+\infty} i\omega \mathbf{x}_j(\omega) \cdot \mathbf{E}^*(\omega) \mathrm{d}\omega, \tag{D.4}$$

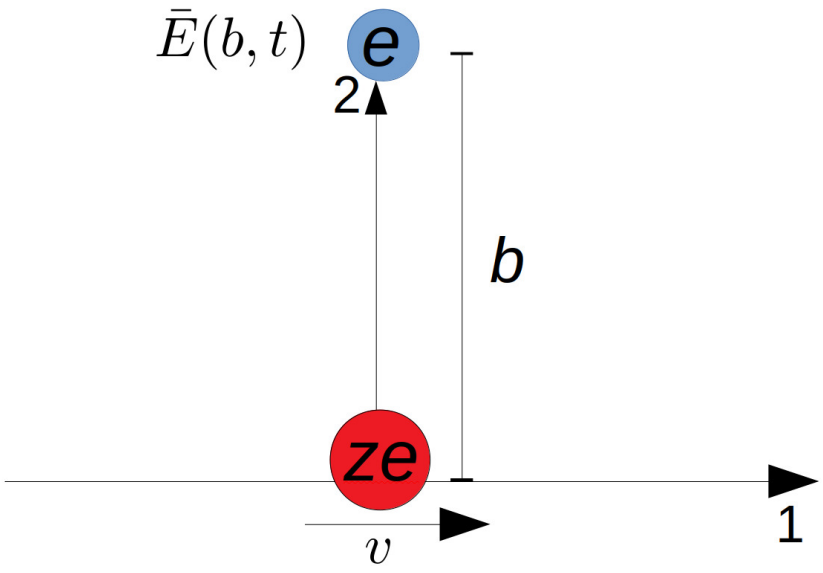

Figure D.1: Fast charged particle ze that interacts with an electron with impact parameter b. The electric field generated by the fast charged particle has value $\mathbf{E}(b,t)$ on the position of the electron.

where f_j and $x_j(\omega)$ are the intensity and amplitude of the j-th oscillator. Introducing now the continuum approximation, according to Maxwell's equations, the polarization $\mathbf{P}$ can be written as:

$$\mathbf{P}(\omega) = -eN\sum_j f_j \mathbf{x}_j(\omega) = \frac{1}{4\pi}\left[\varepsilon(\omega) - 1\right]\mathbf{E}(\omega), \tag{D.5}$$

so that:

$$\sum_j f_j \mathbf{x}_j(\omega) = -\frac{1}{4\pi eN}\left[\varepsilon(\omega) - 1\right]\mathbf{E}(\omega). \tag{D.6}$$

Here N represents the electronic density and the medium is described by the dielectric function $\varepsilon(\omega)$. With this result eq. (D.4) writes:

$$\Delta E = \frac{1}{2\pi N}\mathrm{Re}\int_0^\infty -\varepsilon(\omega) i\omega |\mathbf{E}(\omega)|^2 \mathrm{d}\omega \tag{D.7}$$

(notice that only the term with $\varepsilon(\omega)$ was considered because of the reality condition).

The electric field $|\mathbf{E}(\omega)|$ generated by the incident fast particle moving at constant velocity v is found using the Fourier transform, starting from the Maxwell's equation for the scalar and the vector potentials ϕ and $\mathbf{A}$:

$$\begin{cases} \Delta\mathbf{A}(\mathbf{x},t) - \dfrac{1}{c^2}\dfrac{\partial^2\mathbf{A}(\mathbf{x},t)}{\partial t^2}\varepsilon(\mathbf{x}) = \dfrac{4\pi\mathbf{J}(\mathbf{x},t)}{c} \\ \Delta\phi(\mathbf{x},t) - \dfrac{1}{c^2}\dfrac{\partial^2\phi(\mathbf{x},t)}{\partial t^2}\varepsilon(\mathbf{x}) = \dfrac{4\pi\rho(\mathbf{x},t)}{\varepsilon(\mathbf{x})}. \end{cases} \tag{D.8}$$

Fourier transformed, these equations are:

$$\begin{cases} \left[k^2 - \dfrac{\omega^2}{c^2}\varepsilon(\omega)\right]\mathbf{A}(\mathbf{k},\omega) = \dfrac{4\pi}{c}\mathbf{J}(\mathbf{k},\omega) \\ \left[k^2 - \dfrac{\omega^2}{c^2}\varepsilon(\omega)\right]\phi(\mathbf{k},\omega) = \dfrac{4\pi}{\epsilon(\omega)}\rho(\mathbf{k},\omega). \end{cases} \tag{D.9}$$

The Fourier transform of the incident particle density and current write:

$$\begin{cases} \rho(\mathbf{k},\omega) = ze\delta(\mathbf{x}-\mathbf{v}t) \\ \mathbf{J}(\mathbf{x},t) = \mathbf{v}\rho(\mathbf{x},t), \end{cases} \tag{D.10}$$

where

$$\begin{cases} \rho(\mathbf{k},\omega) = \dfrac{ze}{2\pi}\delta(\omega-\mathbf{k}\cdot\mathbf{v}) \\ \mathbf{J}(\mathbf{k},\omega) = \mathbf{v}\rho(\mathbf{k},\omega). \end{cases} \tag{D.11}$$

Combining eq (D.9) and (D.11), the following relations for the scalar and the vector potentials are obtained:

$$\begin{cases} \phi(\mathbf{k},\omega) = \dfrac{2ze}{\varepsilon(\omega)}\dfrac{\delta(\omega-\mathbf{k}\cdot\mathbf{v})}{k^2-\frac{\omega^2}{c^2}\varepsilon(\omega)} \\ \mathbf{A}(\mathbf{k},\omega) = \varepsilon(\omega)\dfrac{\mathbf{v}}{c}\phi(\mathbf{k},\omega). \end{cases} \tag{D.12}$$

Considering the relation between the potentials and the electric and magnetic fields:

$$\begin{cases} \mathbf{B} = \nabla\times\mathbf{A} \\ \mathbf{E} = -\nabla\phi - \dfrac{1}{c}\dfrac{\partial\mathbf{A}}{\partial t} \end{cases}, \tag{D.13}$$

the following expression for $\mathbf{E}$ and $\mathbf{B}$ can be derived:

$$\begin{cases} \mathbf{E}(\mathbf{k},\omega) = i\left[\dfrac{\omega\varepsilon(\omega)}{c^2}\mathbf{v}-\mathbf{k}\right]\phi(\mathbf{k},\omega) \\ \mathbf{B}(\mathbf{k},\omega) = i\varepsilon(\omega)\mathbf{k}\times\dfrac{\mathbf{v}}{c}\phi(\mathbf{k},\omega) \end{cases}. \tag{D.14}$$

The component of the electric field $E_1(\omega)$ reads:

$$E_1(k_1,\omega) = \frac{2ize\omega}{(2\pi)^{3/2}}\left[\frac{\omega\varepsilon(\omega)}{c}\frac{v}{c}-k_1\right]\frac{\delta(\omega-vk_1)}{k^2-\frac{\omega^2}{c^2}\varepsilon(\omega)} \tag{D.15}$$

and the other component is:

$$E_2(k_2,\omega) = -\frac{2zei}{\varepsilon(\omega)(2\pi)^{3/2}}k_2\frac{\delta(\omega-k_1v)}{k^2-\frac{\omega^2}{c^2}\varepsilon(\omega)}. \tag{D.16}$$

Considering an electron distant $x(t)\sim b$ from the fast particle, the electric field $\mathbf{E}(\omega)$ is calculated by anti-transforming $\mathbf{E}(\mathbf{k},\omega)$ and considering $\mathbf{x}=(0,b,0)$:

$$\mathbf{E}(\omega) = \frac{1}{(2\pi)^{3/2}}\int \mathrm{d}k^3\mathbf{E}(\mathbf{k},\omega)e^{ibk_2}. \tag{D.17}$$

Let us firstly develop $E_1(\omega)$:

$$E_1(\omega) = \frac{2ize}{\varepsilon(\omega)(2\pi)^{3/2}}\int \mathrm{d}k_1\left(\frac{\omega\epsilon(\omega)v}{c^2}-k_1\right)\delta(\omega-k_1v)\int \mathrm{d}k_2e^{ik_2b}\int \mathrm{d}k_3\frac{1}{k^2-\frac{\omega^2}{c^2}\varepsilon(\omega)}. \tag{D.18}$$

The integral in k_1 is straightforward:

$$E_1(\omega) = \frac{2ize}{v\varepsilon(\omega)(2\pi)^{3/2}}\left(\beta^2 - \frac{1}{\epsilon(\omega)}\right)\int \mathrm{d}k_2 e^{ik_2 b}\int \frac{\mathrm{d}k_3}{k_3^2 + k_2^2 + \frac{\omega^2}{v^2} - \frac{\omega^2}{c^2}\varepsilon(\omega)}. \tag{D.19}$$

The integral in k_3 is solved using the Cauchy's residue theorem and it gives:

$$E_1(\omega) = \frac{2ize}{v\varepsilon(\omega)\sqrt{(2\pi)}}\left(\beta^2 - \frac{1}{\epsilon(\omega)}\right)\int_{-\infty}^{+\infty} \mathrm{d}k_2 \frac{e^{ibk_2}}{\sqrt{\mu^2 + k_2}}, \tag{D.20}$$

where $\mu^2(\omega) = \frac{\omega^2}{v^2}\left(1 - \epsilon(\omega)\beta^2\right)$. The last integral corresponds to the modified Bessel function K_0:

$$\int_{-\infty}^{+\infty} \mathrm{d}k_2 \frac{e^{ibk_2}}{\sqrt{\mu^2 + k_2}} = 2K_0(\mu b). \tag{D.21}$$

As such, $E_1(\omega)$ is:

$$E_1(\omega) = -\frac{ize\omega}{v^2}\left(\frac{2}{\pi}\right)^{1/2}\left[\frac{1}{\varepsilon(\omega)} - \beta^2\right]K_0(\mu(\omega)b). \tag{D.22}$$

Analogously, the integral (D.17) with $E_2(\omega)$ is:

$$E_2(\omega) = \frac{2ize}{\varepsilon(\omega)(2\pi)^{3/2}}\int_{-\infty}^{+\infty} \mathrm{d}k_2 k_2 e^{ibk_2}\int_{-\infty}^{+\infty} \mathrm{d}k_3 \frac{1}{k^2 - \frac{\omega^2}{c^2}\varepsilon(\omega)}\int_{-\infty}^{+\infty} \mathrm{d}k_1 \delta(\omega - k_1 v). \tag{D.23}$$

The integral in k_1 is straightforward and eq. (D.23) becomes:

$$E_2(\omega) = \frac{2ize}{v\varepsilon(\omega)(2\pi)^{3/2}}\frac{1}{i}\frac{\mathrm{d}}{\mathrm{d}b}\int_{-\infty}^{+\infty} e^{ik_2 b}\mathrm{d}k_2 \int_{-\infty}^{+\infty} \mathrm{d}k_3 \frac{1}{k_2^2 + k_3^2 + \mu^2}. \tag{D.24}$$

The other two integrals are similar to the ones performed to evaluate $E_1(\omega)$ and the result is:

$$E_2(\omega) = -\frac{ze}{v}\frac{\mu}{\varepsilon(\omega)}\left(\frac{1}{2\pi}\right)^{1/2}\frac{\mathrm{d}}{\mathrm{d}(\mu b)}K_0(\mu b). \tag{D.25}$$

Using a simple relation that relates the modified Bessel functions and their derivatives [253]:

$$\frac{\mathrm{d}K_0(z)}{\mathrm{d}z} = -K_1(z), \tag{D.26}$$

eq (D.25) becomes:

$$E_2(\omega) = \frac{ze}{v}\left(\frac{1}{2\pi}\right)^{1/2}\frac{\mu(\omega)}{\varepsilon(\omega)}K_1(\mu(\omega)b). \tag{D.27}$$

$|E_1(\omega)|^2$ and $|E_2(\omega)|^2$ are used in eq. (D.7) to evaluate the energy loss for collisions with impact parameter b. The two quantities write:

$$|E_1(\omega)|^2 = \left(\frac{ze}{\omega}\right)^2\left(\frac{2}{\pi}\right)\left|\frac{\mu^2}{\epsilon(\omega)}K_0(\mu b)\right|^2 \tag{D.28}$$

$$|E_2(\omega)|^2 = \left(\frac{ze}{\omega}\right)^2\left(\frac{2}{\pi}\right)\left|\frac{\mu^2}{\epsilon(\omega)}K_0(\mu b)\right|^2. \tag{D.29}$$

The stopping power is obtained by integrating $\Delta E(b)$ over all the possible impact parameters, i.e.:

$$\left(\frac{\mathrm{d}E}{\mathrm{d}x}\right)_{ep} = 2\pi N \int_D^{+\infty} \Delta E(b) b \mathrm{d}b \tag{D.30}$$

and using (D.28) (D.29) we obtain:

$$\begin{aligned}\left(\frac{\mathrm{d}E}{\mathrm{d}x}\right)_{ep} = -\mathrm{Re}\int \mathrm{d}\omega i\omega\varepsilon(\omega)\left(\frac{2}{\pi}\right)\left(\frac{ze}{v}\right)^2\left|\frac{\mu(\omega)}{\varepsilon(\omega)}\right|^2 \times \\ \int_D^{+\infty} b\left\{\left(\frac{v}{\omega}\right)^2 |\mu(\omega)|^2 |K_0(\mu b)|^2 + |K_1(\mu b)|^2\right\}\mathrm{d}b.\end{aligned} \tag{D.31}$$

This integral is solved as follows: first of all, let us notice that for a generic modified Bessel function the following relation holds:

$$|K_u(\mu b)|^2 = K_u(\mu b)K_u^*(\mu b) = K_u(\mu b)K_u(\mu^* b). \tag{D.32}$$

With this result, the two integrals in b that must be solved are:

$$I_0 = \int_D^{+\infty} bK_0(\mu b)K_0(\mu^* b)\mathrm{d}b \tag{D.33}$$

and

$$I_1 = \int_D^{+\infty} bK_1(\mu b)K_1(\mu^* b)\mathrm{d}b. \tag{D.34}$$

The resolution of these integrals can be accomplished considering the formula 11.3.29 in Abramowitz [253]:

$$\begin{aligned}I_0 = \int_D^{+\infty} bK_0(\mu b)K_0(\mu^* b)\mathrm{d}b = -\frac{D}{\mu^2-\mu^{*2}}\left[\mu K_1(\mu D)K_0(\mu^* D) - \mu^* K_0(\mu D)K_1(\mu^* D)\right] = \\ -\frac{D}{\mu^2-\mu^{*2}} 2i\mathrm{Im}\Big\{\mu K_1(\mu D)K_0(\mu^* D)\Big\}\end{aligned} \tag{D.35}$$

$$\begin{aligned}I_1 = \int_D^{+\infty} bK_1(\mu b)K_1(\mu^* b)\mathrm{d}b = -\frac{D}{\mu^2-\mu^{*2}}\left[\mu K_2(\mu D)K_1(\mu^* D) - \mu^* K_1(\mu D)K_2(\mu^* D)\right] = \\ -\frac{D}{\mu^2-\mu^{*2}} 2i\mathrm{Im}\Big\{\mu K_0(\mu D)K_1(\mu^* D)\Big\},\end{aligned} \tag{D.36}$$

where we used:

$$K_2(\mu D) = K_0(\mu D) + \frac{2}{\mu D}K_1(\mu D). \tag{D.37}$$

Considering that:

$$\mu^2 - \mu^{*2} = -2i\beta^2\varepsilon_2\frac{\omega^2}{c^2}, \tag{D.38}$$

where ε_2 is the imaginary part of the dielectric tensor, after grouping $K_0(\mu D)K_1(\mu^* D)$, eq (D.31) writes

$$\left(\frac{\mathrm{d}E}{\mathrm{d}x}\right)_{ep} = \int \mathrm{d}\omega i\omega\frac{2}{\pi}\left(\frac{ze}{v}\right)^2\left|\frac{\mu(\omega)}{\varepsilon(\omega)}\right|^2\frac{Dc^2}{\omega^2 2i\varepsilon_2\beta^2}\left[\mathrm{Im}\left[\left(\left(\frac{v}{\omega}\right)^2|\mu|^2\mu^* - \mu\right)2iK_0(\mu D)K_1(\mu^* D)\right]\right]. \tag{D.39}$$

Considering that:

$$\begin{aligned}\left(\frac{v}{\omega}\right)|\mu|^2\mu^* - \mu &= -\mu\beta^2\varepsilon^* \\ |\mu|^2\mu = \left(\frac{\omega}{v}\right)^2\left(1-\beta^2\varepsilon\right)\mu^* &= \left(\frac{\omega}{c}\right)^2\varepsilon\left(\frac{1}{\varepsilon}-\beta^2\right)\mu^*\end{aligned}, \tag{D.40}$$

eq (D.39) becomes:

$$\left(\frac{\mathrm{d}E}{\mathrm{d}x}\right)_{ep} = \mathrm{Re}\int \mathrm{d}\omega i\omega\frac{2}{\pi}\left(\frac{ze}{v}\right)^2\frac{D\varepsilon}{\varepsilon_2}\mathrm{Im}\left[\left(\frac{1}{\varepsilon}-\beta^2\right)D\mu^*K_0(\mu D)K_1(\mu^* D)\right]. \tag{D.41}$$

Writing $\varepsilon = \varepsilon_1 + i\varepsilon_2$ eq (D.41) writes:

$$\left(\frac{\mathrm{d}E}{\mathrm{d}x}\right)_{ep} = \mathrm{Re}\int \mathrm{d}\omega i\omega\frac{2}{\pi}\left(\frac{ze}{v}\right)^2\left(\frac{\varepsilon_1}{\varepsilon_2}+i\right)\mathrm{Im}\left\{\left(\frac{1}{\varepsilon(\omega)}-\beta^2\right)D\mu^*K_0(\mu D)K_1(\mu^* D)\right\}. \tag{D.42}$$

Considering that only the real part of the integrand, we finally obtain:

$$\left(\frac{\mathrm{d}E}{\mathrm{d}x}\right)_{ep} = \frac{2}{\pi}\left(\frac{ze}{v}\right)^2\mathrm{Re}\int_0^{+\infty}\mathrm{d}\omega i\omega\mu(\omega)^* DK_1(\mu^* D)K_0(\mu D)\left(\frac{1}{\varepsilon(\omega)}-\beta^2\right). \tag{D.43}$$

This equation was firstly derived by Enrico Fermi in 1940 [259], and it describes the energy losses due to distant collisions of a fast charged particle ze that moves in a medium. The formula was originally derived for the case of cold material and it describe the density effect.

Jackson [242] readapts this formula for plasma case, considering an appropriate description of the dielectric tensor $\varepsilon(\omega)$. In doing this, the main approximation made by the author is to consider non relativistic electrons, i.e $\beta \to 0$. In this case the coefficient $\mu(\omega)$ becomes a real quantity, i.e.:

$$\lim_{\beta\to 0}\mu(\omega) = \lim_{\beta\to 0}\frac{\omega^2}{v^2}\left(1-\beta^2\varepsilon(\omega)\right) = \frac{\omega^2}{v^2}. \tag{D.44}$$

As such, the argument of the Bessel functions becomes real, and the formula (D.43) is:

$$\left(\frac{\mathrm{d}E}{\mathrm{d}x}\right)_{ep} = \frac{2}{\pi}\left(\frac{ze}{v}\right)^2\mathrm{Re}\int_0^{+\infty}\mathrm{d}\omega\frac{i\omega}{\varepsilon(\omega)}\left[\frac{\omega D}{v}K_1\left(\frac{\omega D}{v}\right)K_0\left(\frac{\omega D}{v}\right)\right]. \tag{D.45}$$

For electron velocities greater than thermal velocity the coefficient $\omega D/v$ leads to zero and the Bessel functions can be approximated considering the asymptotic formulas:

$$\begin{aligned}\lim_{z\to 0}K_0(z) &= \ln\left(\frac{1.123}{z}\right) \\ \lim_{z\to 0}K_1(z) &= \frac{1}{z} = \frac{v}{D\omega},\end{aligned} \tag{D.46}$$

where $z = \omega D/v$. Fig. D.2 shows the behaviour of the Bessel functions in the asymptotic limits. As can be seen, the approximation holds for electron kinetic energy greater than

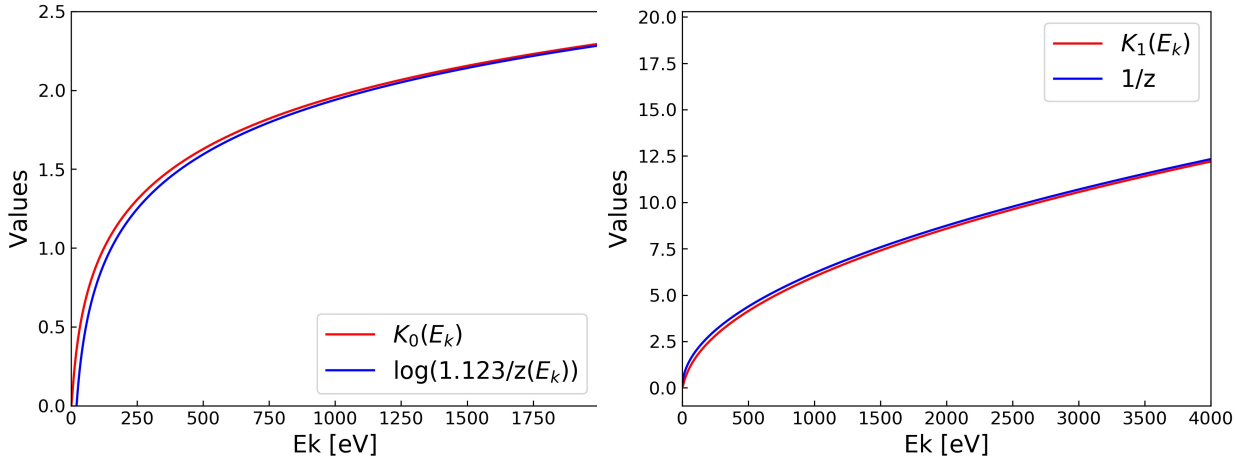

(a) (b)

Figure D.2: Asymptotic limits of the modified Bessel functions K_0 (a) and K_1 (b) as a function of the electron energy in eV.

few eV and it is suitable for our purposes. Substituting the asymptotic formulas in eq (D.45) we obtain:

$$\left(\frac{\mathrm{d}E}{\mathrm{d}x}\right)_{ep} = \frac{2}{\pi}\left(\frac{ze}{v}\right)^2 \int_0^{+\infty} \mathrm{d}\omega \mathrm{Re}\left(\frac{i\omega}{\epsilon(\omega)}\right) \ln\left(\frac{1.123v}{\omega}\right). \tag{D.47}$$

It is now necessary to give a form for the dielectric constant $\varepsilon(\omega)$. As shown in Sec. 1.2.3, in case of collisional plasma $\varepsilon(\omega)$ reads:

$$\epsilon\left(\omega\right) = 1 - \frac{\omega_{pe}^2}{\omega\left(\omega + i\nu_{ei}\right)}. \tag{D.48}$$

The real part of $\left(\frac{i}{\varepsilon}\right)$ that appears in (D.47) is:

$$\mathrm{Re}\left(\frac{i}{\varepsilon}\right) = \frac{\nu_{ei}\omega_{pe}^2}{(\omega^2 - \omega_{pe}^2)^2 + (\omega\nu_{ei})^2} \tag{D.49}$$

and it is similar to a Cauchy distribution:

$$f(x) = \frac{1}{\pi}\frac{y_0}{(x - x_0)^2 + y_0^2}. \tag{D.50}$$

This distribution is related to the Dirac delta according to the relation

$$\lim_{y_0 \to 0} f(x) = \delta\big((x - x_0)(x + x_0)\big) = \frac{\delta(x - x_0)}{2x_0} + \frac{\delta(x + x_0)}{2x_0} \tag{D.51}$$

and because of this, $\mathrm{Re}\left(\frac{i}{\varepsilon}\right)$ can be written as:

$$\left(\frac{i}{\varepsilon}\right) = \frac{\pi\omega_{pe}}{2}\Big[\delta(\omega - \omega_{pe}) + \delta(\omega - \omega_{pe})\Big]. \tag{D.52}$$

Using this result in eq (D.47) we can write:

$$\left(\frac{\mathrm{d}E}{\mathrm{d}x}\right)_{ep} = \left(\frac{ze}{v}\right)^2 \int_0^{+\infty} \mathrm{d}\omega\omega_{pe}\omega \ln\left(\frac{1.123v}{\omega}\right)\Big[\delta(\omega-\omega_{pe})+\delta(\omega-\omega_{pe})\Big]. \tag{D.53}$$

At this point the integral is straightforward and the formula (4.67) is finally obtained:

$$\left(\frac{\mathrm{d}E}{\mathrm{d}x}\right)_{ep} = \left(\frac{ze}{v}\right)^2 \omega_{pe}^2 \ln\Big(1.123\frac{v}{D\omega_{pe}}\Big) = \frac{4\pi z^2 e^4 n_e}{c^2\beta^2}\ln\Big(1.123\frac{\beta c}{D\omega_{pe}}\Big) \tag{D.54}$$

For an electron, obviously $z = 1$.

Appendix E

Modelization of hot electron transport in CHIC

Hot electrons propagate along straight lines, depositing energy in the mesh according to the plasma stopping power formulas (see Sec. 4.5) . Some angular scattering is however accounted for by widening the electron beam according the first transport scattering cross-section (see at the end of this appendix). This approach has been validated against the M1 code [286].

The stopping power formulas consider the loss of energy of the primary particle due to collisions with plasma free electrons (Sec .4.5.1, formula (4.60)), partially ionized atoms (Sec. 4.5.2, formula (4.65)) and excitation of plasma waves (Sec. 4.5.3, formula (4.67)).

The diffusion is modelled considering the mean diffusion angle obtained by the Lewis' theory [126]:

$$\langle \cos\theta \rangle (s) = \exp\left[- \int_0^s k_1(s) \mathrm{d}s \right], \tag{E.1}$$

where $k_1(s)$ is the inverse of the first transport path. Assuming that the particles in the beam propagate along straight line in the z direction, the energy loss rate reads:

$$\frac{\mathrm{d}E}{\mathrm{d}z} = -\frac{1}{\langle \cos\theta \rangle (s)} S_e(E). \tag{E.2}$$

Here $S_e(E)$ is the plasma stopping power, defined as the sum of the various components listed above. An additional energy loss is accounted in the transverse direction of thickness Δ:

$$\frac{\mathrm{d}\Delta}{\mathrm{d}z} = 2 \langle \tan\theta \rangle (s). \tag{E.3}$$

Bibliography

[1] British Petroleum Co. *"Bp Statistical Review of World Energy"*. Tech. rep. British Petroleum Co, 2021.

[2] Dr. Lana Aref, Profs. Patricia J. Culligan, Kenneth R. Czerwinski, and Heidi M. Nepf. *Nuclear Energy: the Good, the Bad, and the Debatable*. University Lecture.

[3] John Lindl et al. "Review of the National Ignition Campaign 2009-2012". In: *Physics of Plasmas* 21.2 (2014), p. 020501. eprint: https://doi.org/10.1063/1.4865400. URL: https://doi.org/10.1063/1.4865400.

[4] Dale Meade. "50 years of fusion research". In: *Nuclear Fusion* 50.1 (2009), p. 014004. URL: https://doi.org/10.1088/0029-5515/50/1/014004.

[5] Kenneth S. Krane. *"Introductory Nuclar Physics"*. JOHN WlLEY and SONS, 1955.

[6] J D Lawson. "Some Criteria for a Power Producing Thermonuclear Reactor". In: *Proceedings of the Physical Society. Section B* 70.1 (1957), pp. 6–10. URL: https://doi.org/10.1088/0370-1301/70/1/303.

[7] S Pfalzner. *"An Introduction to Inertial Confinement Fusion"*. Taylor and Francis Ltd, 2006.

[8] Stefano Atzeni. *"The physics of inertial fusion"*. Oxford: CLARENDON PRESS-OXFORD, 2004.

[9] Tjiessen A Nuckolls J. Wood L. "Laser Compression of Matter to Super High Densities: Thermonuclear (CTR) Applications". In: *Nature* 239 (1972), 139142.

[10] G. V. Sklizkov N. G. Basov O. N. Krokhin. "Heating of Laser Plasmas for thermonuclear fusion". In: *Laser Interaction and Related Plasma Phenomena* 2 (1972), p. 398.

[11] Mordecai D. Rosen. "The physics issues that determine inertial confinement fusion target gain and driver requirements: A tutorial". In: *Physics of Plasmas* 6.5 (1999), pp. 1690–1699. eprint: https://doi.org/10.1063/1.873427. URL: https://doi.org/10.1063/1.873427.

[12] J. Lindl. "Development of the indirect drive approach to inertial confinement fusion and the target physics basis for ignition and gain". In: *Physics of Plasmas* 2 (1995), pp. 3933–4024.

[13] Robert L McCrory. *"Laser Driven ICF Experiments"*. Tech. rep. University of Rochester Laboratory for laser energetics, 1992.

[14] P. W. McKenty et al. "Analysis of a direct-drive ignition capsule designed for the National Ignition Facility". In: *Physics of Plasmas* 8.5 (2001), pp. 2315–2322. URL: https://doi.org/10.1063/1.1350571.

[15] V N Goncharov et al. "Demonstration of the Highest Deuterium Tritium Areal Density Using Multiple Picket Cryogenic Designs on OMEGA". In: *Physical Review Letters* 104.16 (2010). ISSN: 0031-9007. URL: https://www.osti.gov/biblio/21410645.

[16] V. N. Goncharov et al. "Improved performance of direct drive inertial confinement fusion target designs with adiabat shaping using an intensity picket". In: *Physics of Plasmas* 10.5 (2003), pp. 1906–1918. eprint: https://doi.org/10.1063/1.1562166. URL: https://doi.org/10.1063/1.1562166.

[17] J. D. Lindl and W. C. Mead. "Two-Dimensional Simulation of Fluid Instability in Laser-Fusion Pellets". In: *Phys. Rev. Lett.* 34 (20 1975), pp. 1273–1276. URL: https://link.aps.org/doi/10.1103/PhysRevLett.34.1273.

[18] R. Betti et al. "Hot spot dynamics and deceleration-phase Rayleigh Taylor instability of imploding inertial confinement fusion capsules". In: *Physics of Plasmas* 8.12 (2001), pp. 5257–5267. eprint: https://doi.org/10.1063/1.1412006. URL: https://doi.org/10.1063/1.1412006.

[19] R. Betti et al. "Deceleration phase of inertial confinement fusion implosions". In: *Physics of Plasmas* 9.5 (2002), pp. 2277–2286. eprint: https://doi.org/10.1063/1.1459458. URL: https://doi.org/10.1063/1.1459458.

[20] J. Meyer-Ter-Vehn. "On energy gain of fusion targets: the model of Kidder and Bodner improved". In: *Nuclear Fusion* 22.4 (1982), pp. 561–565. URL: https://doi.org/10.1088/0029-5515/22/4/010.

[21] Mark C. Herrmann, Max Tabak, and John D. Lindl. "Ignition scaling laws and their application to capsule design". In: *Physics of Plasmas* 8.5 (2001), pp. 2296–2304. eprint: https://doi.org/10.1063/1.1364516. URL: https://doi.org/10.1063/1.1364516.

[22] C. D. Zhou and R. Betti. "Hydrodynamic relations for direct-drive fast-ignition and conventional inertial confinement fusion implosions". In: *Physics of Plasmas* 14.7 (2007), p. 072703. eprint: https://doi.org/10.1063/1.2746812. URL: https://doi.org/10.1063/1.2746812.

[23] V A Shcherbakov. "Ignition of a laser fusion target by a focusing shock wave". In: *Soviet Journal of Plasma Physics* 9 (1983). URL: https://www.osti.gov/biblio/5398617.

[24] R. Betti et al. "Shock Ignition of Thermonuclear Fuel with High Areal Density". In: *Phys. Rev. Lett.* 98 (15 2007), p. 155001. URL: https://link.aps.org/doi/10.1103/PhysRevLett.98.155001.

[25] L. J. Perkins, R. Betti, K. N. LaFortune, and W. H. Williams. "Shock Ignition: A New Approach to High Gain Inertial Confinement Fusion on the National Ignition Facility". In: *Phys. Rev. Lett.* 103 (4 2009), p. 045004. URL: https://link.aps.org/doi/10.1103/PhysRevLett.103.045004.

[26] S. Atzeni et al. "Shock ignition of thermonuclear fuel: principles and modelling". In: *Nuclear Fusion* 54.5 (2014), p. 054008. URL: https://doi.org/10.1088/0029-5515/54/5/054008.

[27] W. Theobald et al. "Initial experiments on the shock-ignition inertial confinement fusion concept". In: *Physics of Plasmas* 15.5 (2008), p. 056306. eprint: https://doi.org/10.1063/1.2885197. URL: https://doi.org/10.1063/1.2885197.

[28] X Ribeyre et al. "Shock ignition: modelling and target design robustness". In: *Plasma Physics and Controlled Fusion* 51.12 (2009), p. 124030. URL: https://doi.org/10.1088/0741-3335/51/12/124030.

[29] R. Nora and R. Betti. "One-dimensional planar hydrodynamic theory of shock ignition". In: *Physics of Plasmas* 18.8 (2011), p. 082710. eprint: https://doi.org/10.1063/1.3619827. URL: https://doi.org/10.1063/1.3619827.

[30] K. S. Anderson et al. "A polar-drive shock-ignition design for the National Ignition Facility". In: *Physics of Plasmas* 20.5 (2013), p. 056312. eprint: https://doi.org/10.1063/1.4804635. URL: https://doi.org/10.1063/1.4804635.

[31] R. S. Craxton et al. "Direct-drive inertial confinement fusion: A review". In: *Physics of Plasmas* 22.11 (2015), p. 110501. eprint: https://doi.org/10.1063/1.4934714. URL: https://doi.org/10.1063/1.4934714.

[32] J. Trela et al. "The control of hot-electron preheat in shock-ignition implosions". In: *Physics of Plasmas* 25.5 (2018), p. 052707. eprint: https://doi.org/10.1063/1.5020981. URL: https://doi.org/10.1063/1.5020981.

[33] A. Colatis et al. "Influence of laser induced hot electrons on the threshold for shock ignition of fusion reactions". In: *Physics of Plasmas* 23.7 (2016), p. 072703. URL: https://doi.org/10.1063/1.4958808.

[34] S. Gus'kov et al. "Ablation Pressure Driven by an Energetic Electron Beam in a Dense Plasma". In: *Phys. Rev. Lett.* 109 (25 2012), p. 255004. URL: https://link.aps.org/doi/10.1103/PhysRevLett.109.255004.

[35] R. K. Follett et al. "Thresholds of absolute instabilities driven by a broadband laser". In: *Physics of Plasmas* 26.6 (2019), p. 062111. eprint: https://doi.org/10.1063/1.5098479. URL: https://doi.org/10.1063/1.5098479.

[36] J. R. Fein et al. "Mitigation of hot electrons from laser-plasma instabilities in high-Z, highly ionized plasmas". In: *Physics of Plasmas* 24.3 (2017), p. 032707. eprint: https://doi.org/10.1063/1.4978625. URL: https://doi.org/10.1063/1.4978625.

[37] Maire P Breil J. Galera S. "Multi-material ALE computation in inertial confinement fusion code CHIC". In: *Computers and Fluids* 46.1 (2011). 10th ICFD Conference Series on Numerical Methods for Fluid Dynamics (ICFD 2010). ISSN: 0045-7930. URL: http://www.sciencedirect.com/science/article/pii/S0045793010001489.

[38] P. Debye and Hckel E. "Zur Theorie der Elektrolyte. Physikalische Zeitschrift". In: *Phys. Z.* 24 (1923), pp. 185–206.

[39] H. Yukawa. "On the Interaction of Elementary Particles. I". In: *Progress of Theoretical Physics Supplement* 1 (1955), pp. 1–10.

[40] Naval Research Laboratory. *"NRL Plasma Formulary"*. Tech. rep. Naval Research Laboratory, 2013.

[41] R. Paul Drake. *"High-Energy-Density Physics Second Edition"*. Springer, 2018.

[42] David Salzmann. *"Atomic Physics in Hot Plasmas"*. Oxford UNiversity Press, 1998.

[43] Sergio E. Segre G. Pucella. *"Fisica dei Plasmi"*. Zanichelli, 2010.

[44] Spitzer Lyman. *"Physics of Fully Ionized Gases"*. Dover Publications, 1962.

[45] John Wesson. *"Tokamaks"*. Oxford: CLARENDON PRESS-OXFORD, 2003.

[46] J.P. Watteau R. Dautray. *"FUSION THERMONUCLEAIRE INERTIELLE PAR LASER. Tome 1. 2, L'intraction laser- matire, 2me partie"*. CEA ditions, 1991.

[47] Ludwig Boltzmann. *"Lectures on Gas Theory"*. Dover Publications, 1964.

[48] L. D. Landau, E. M. Lifshitz, and L. P. Pitaevskii. *"Physical Kinetics. Vol. 10"*. Pergamon Press, 1981.

[49] Feugeas JL. Dubroca B. and Frank. "M. Angular moment model for the Fokker-Planck equation". In: *The European Physical Journal D* 60 (2010), pp. 301–307.

[50] A.I. Akhiezer et al. *"Plasma Electrodynamics: Volume I: Linear theory"*. Pergamon Press, 1975.

[51] J.J. Sanderson T.J.M. Boyd. *"The physics of plasmas"*. Cambridge university Press, 2003.

[52] William L. Kruer. *"The Physics Of Laser Plasma Interactions"*. Oxford: Westview Press; Reprint dition (29 janvier 2003), 2003.

[53] Ya. B. Zel'dovich Yu. P. Raizer. *"Phyisics of Shock Waves and High-Temperature Hydrodynamic Phenomena"*. Academic Press New York and London, 1966.

[54] Maire P Breil J. Galera S. "Multi-material ALE computation in inertial confinement fusion code CHIC". In: *Computers and Fluids* 46.1 (2011). 10th ICFD Conference Series on Numerical Methods for Fluid Dynamics (ICFD 2010). ISSN: 0045-7930. URL: http://www.sciencedirect.com/science/article/pii/S0045793010001489.

[55] V. L. Ginzburg, Walter L. Sadowski, D. M. Gallik, and Sanborn C. Brown. "Propagation of Electromagnetic Waves in Plasma". In: *Physics Today* 15.10 (1962), pp. 70–73. eprint: https://doi.org/10.1063/1.3057811. URL: https://doi.org/10.1063/1.3057811.

[56] A. Bruce Langdon. "Nonlinear Inverse Bremsstrahlung and Heated-Electron Distributions". In: *Phys. Rev. Lett.* 44 (9 1980), pp. 575–579. URL: https://link.aps.org/doi/10.1103/PhysRevLett.44.575.

[57] C. Garban-Labaune et al. "Effect of Laser Wavelength and Pulse Duration on Laser-Light Absorption and Back Reflection". In: *Phys. Rev. Lett.* 48 (15 1982), pp. 1018–1021. URL: https://link.aps.org/doi/10.1103/PhysRevLett.48.1018.

[58] W. Seka et al. "Measurements and interpretation of the absorption of 0.35 μm laser radiation on planar targets". In: *Optics Communications* 40.6 (1982), pp. 437–440. ISSN: 0030-4018. URL: https://www.sciencedirect.com/science/article/pii/0030401882900499.

[59] W. C. Mead et al. "Laser irradiation of disk targets at 0.53 μm wavelength". In: *The Physics of Fluids* 26.8 (1983), pp. 2316–2331. eprint: https://aip.scitation.org/doi/pdf/10.1063/1.864390. URL: https://aip.scitation.org/doi/abs/10.1063/1.864390.

[60] Shalom Eliezer. *"The Interaction of High-Power Lasers with Plasmas"*. Philadelphia: Institue of Physics Publishing Bristol and Philadelphia, 2002.

[61] Evgenij M. Lifsits Lev D. Landau. *"Course of Theoretical Physics: Electrodynamics of Continuous Media"*. Butterworth-Heinemann, 1984.

[62] Denisov N.G. "On a singularity of the field of an electromagnetic wave propagated in an inhomogeneous plasma". In: *JETP* 4 (1957), p. 544.

[63] V. L. Ginzburg B. N. Gershman and N. G. Denisov. *"THE PROPAGATION OF ELECTROMAGNETIC WAVES IN A PLASMA (IONOSPHERE)"*. UNITED STATES ATOMIC ENERGY COMMISSION, 1957.

[64] Thomas Speziale and P. J. Catto. "Linear wave conversion in an unmagnetized, collisionless plasma". In: *The Physics of Fluids* 20.6 (1977), pp. 990–997. eprint: https://aip.scitation.org/doi/pdf/10.1063/1.861987. URL: https://aip.scitation.org/doi/abs/10.1063/1.861987.

[65] J. P. Freidberg, R. W. Mitchell, R. L. Morse, and L. I. Rudsinski. "Resonant Absorption of Laser Light by Plasma Targets". In: *Phys. Rev. Lett.* 28 (13 1972), pp. 795–799. URL: https://link.aps.org/doi/10.1103/PhysRevLett.28.795.

[66] K. G. Estabrook, E. J. Valeo, and W. L. Kruer. "Two dimensional relativistic simulations of resonance absorption". In: *The Physics of Fluids* 18.9 (1975), pp. 1151–1159. eprint: https://aip.scitation.org/doi/pdf/10.1063/1.861276. URL: https://aip.scitation.org/doi/abs/10.1063/1.861276.

[67] I. V. Igumenshchev et al. "The effect of resonance absorption in OMEGA direct-drive designs and experiments". In: *Physics of Plasmas* 14.9 (2007), p. 092701. eprint: https://doi.org/10.1063/1.2768515. URL: https://doi.org/10.1063/1.2768515.

[68] Kent Estabrook and W. L. Kruer. "Properties of Resonantly Heated Electron Distributions". In: *Phys. Rev. Lett.* 40 (1 1978), pp. 42–45. URL: https://link.aps.org/doi/10.1103/PhysRevLett.40.42.

[69] D. W. Forslund, J. M. Kindel, and K. Lee. "Theory of Hot-Electron Spectra at High Laser Intensity". In: *Phys. Rev. Lett.* 39 (5 1977), pp. 284–288. URL: https://link.aps.org/doi/10.1103/PhysRevLett.39.284.

[70] R. A. Haas et al. "Irradiation of parylene disks with a 1.06 μm laser". In: *The Physics of Fluids* 20.2 (1977), pp. 322–338. eprint: https://aip.scitation.org/doi/pdf/10.1063/1.861870. URL: https://aip.scitation.org/doi/abs/10.1063/1.861870.

[71] K. R. Manes, H. G. Ahlstrom, R. A. Haas, and J. F. Holzrichter. "Light–plasma interaction studies with high-power glass laser$*$". In: *J. Opt. Soc. Am.* 67.6 (1977), pp. 717–726. URL: http://www.osapublishing.org/abstract.cfm?URI=josa-67-6-717.

[72] D. C. Slater et al. "Absorption and Hot-Electron Production for 1.05 and 0.53 μm Light on Spherical Targets". In: *Phys. Rev. Lett.* 46 (18 1981), pp. 1199–1202. URL: https://link.aps.org/doi/10.1103/PhysRevLett.46.1199.

[73] N.N. Demchenko. "Numerical Simulation of the Absorption of Laser Radiation in a Plasma Including the Resonance Mechanism and Generation of Fast Electrons for the Conditions of a Nuclear Fusion Target Ignition". In: *Soviet Journal of Experimental and Theoretical Physics* 130.6 (2020), pp. 945–954.

[74] J. R. Albritton and A. B. Langdon. "Profile Modification and Hot-Electron Temperature from Resonant Absorption at Modest Intensity". In: *Phys. Rev. Lett.* 45 (22 1980), pp. 1794–1797. URL: https://link.aps.org/doi/10.1103/PhysRevLett.45.1794.

[75] J. D. Hares and J. D. Kilkenny. "A demonstration of the decrease of fast electron preheat from laser produced plasmas with increasing pulse length". In: *Journal of Applied Physics* 52.10 (1981), pp. 6420–6422. eprint: https://doi.org/10.1063/1.328588. URL: https://doi.org/10.1063/1.328588.

[76] R.Z. Sagdeev M.N. Rosenbluth. *"Handbook of plasma physics Vol 3"*. Elsevier Science Publishers, 1991.

[77] B. B. Afeyan and E. A. Williams. "Stimulated Raman sidescattering with the effects of oblique incidence". In: *The Physics of Fluids* 28.11 (1985), pp. 3397–3408. eprint: https://aip.scitation.org/doi/pdf/10.1063/1.865340. URL: https://aip.scitation.org/doi/abs/10.1063/1.865340.

[78] D. W. Forslund, J. M. Kindel, and E. L. Lindman. "Theory of stimulated scattering processes in laser irradiated plasmas". In: *The Physics of Fluids* 18.8 (1975), pp. 1002–1016. eprint: https://aip.scitation.org/doi/pdf/10.1063/1.861248. URL: https://aip.scitation.org/doi/abs/10.1063/1.861248.

[79] Bedros B. Afeyan and Edward A. Williams. "A variational approach to parametric instabilities in inhomogeneous plasmas IV: The mixed polarization high-frequency instability". In: *Physics of Plasmas* 4.11 (1997), pp. 3845–3862. eprint: https://doi.org/10.1063/1.872507. URL: https://doi.org/10.1063/1.872507.

[80] R. P. Drake et al. "Efficient Raman Sidescatter and Hot-Electron Production in Laser-Plasma Interaction Experiments". In: *Phys. Rev. Lett.* 53 (18 1984), pp. 1739–1742. URL: https://link.aps.org/doi/10.1103/PhysRevLett.53.1739.

[81] Kent Estabrook, W. L. Kruer, and B. F. Lasinski. "Heating by Raman Backscatter and Forward Scatter". In: *Phys. Rev. Lett.* 45 (17 1980), pp. 1399–1403. URL: https://link.aps.org/doi/10.1103/PhysRevLett.45.1399.

[82] O Klimo, S Weber, V T Tikhonchuk, and J Limpouch. "Particle-in-cell simulations of laser–plasma interaction for the shock ignition scenario". In: *Plasma Physics and Controlled Fusion* 52.5 (2010), p. 055013. URL: https://doi.org/10.1088/0741-3335/52/5/055013.

[83] O. Klimo et al. "Laser plasma interaction studies in the context of shock ignitionTransition from collisional to collisionless absorption". In: *Physics of Plasmas* 18.8 (2011), p. 082709. eprint: https://doi.org/10.1063/1.3625264. URL: https://doi.org/10.1063/1.3625264.

[84] O Klimo and V T Tikhonchuk. "Laser–plasma interaction studies in the context of shock ignition: the regime dominated by parametric instabilities". In: *Plasma Physics and Controlled Fusion* 55.9 (2013), p. 095002. URL: https://doi.org/10.1088/0741-3335/55/9/095002.

[85] Francois Amiranoff. "Etude des electrons rapides dans l'interaction Laser Matiere". PhD thesis. Universit de Paris sud, 1984.

[86] C. S. Liu and Marshall N. Rosenbluth. "Parametric decay of electromagnetic waves into two plasmons and its consequences". In: *The Physics of Fluids* 19.7 (1976), pp. 967–971. eprint: https://aip.scitation.org/doi/pdf/10.1063/1.861591. URL: https://aip.scitation.org/doi/abs/10.1063/1.861591.

[87] A. Simon, R. W. Short, E. A. Williams, and T. Dewandre. "On the inhomogeneous two plasmon instability". In: *The Physics of Fluids* 26.10 (1983), pp. 3107–3118. eprint: https://aip.scitation.org/doi/pdf/10.1063/1.864037. URL: https://aip.scitation.org/doi/abs/10.1063/1.864037.

[88] N. A. Ebrahim, H. A. Baldis, C. Joshi, and R. Benesch. "Hot Electron Generation by the Two-Plasmon Decay Instability in the Laser-Plasma Interaction at 10.6 μm". In: *Phys. Rev. Lett.* 45 (14 1980), pp. 1179–1182. URL: https://link.aps.org/doi/10.1103/PhysRevLett.45.1179.

[89] M. C. Richardson et al. "Absorption Physics at 351 nm in Spherical Geometry". In: *Phys. Rev. Lett.* 54 (15 1985), pp. 1656–1659. URL: https://link.aps.org/doi/10.1103/PhysRevLett.54.1656.

[90] H. X. Vu, D. F. DuBois, J. F. Myatt, and D. A. Russell. "Hot-electron production and suprathermal heat flux scaling with laser intensity from the two-plasmondecay instability". In: *Physics of Plasmas* 19.10 (2012), p. 102703. eprint: https://doi.org/10.1063/1.4757978. URL: https://doi.org/10.1063/1.4757978.

[91] A. G. Seaton and T. D. Arber. "Laser-plasma instabilities in long scale-length plasmas relevant to shock-ignition". In: *Physics of Plasmas* 27.8 (2020), p. 082704. eprint: https://doi.org/10.1063/5.0010920. URL: https://doi.org/10.1063/5.0010920.

[92] C. S. Liu, Marshall N. Rosenbluth, and Roscoe B. White. "Raman and Brillouin scattering of electromagnetic waves in inhomogeneous plasmas". In: *The Physics of Fluids* 17.6 (1974), pp. 1211–1219. eprint: https://aip.scitation.org/doi/pdf/10.1063/1.1694867. URL: https://aip.scitation.org/doi/abs/10.1063/1.1694867.

[93] Seppo J. Karttunen. "Ion fluctuation effects on the two-plasmon decay and stimulated Raman scattering". In: *Phys. Rev. A* 23 (4 1981), pp. 2006–2010. URL: https://link.aps.org/doi/10.1103/PhysRevA.23.2006.

[94] S. Depierreux et al. "Langmuir Decay Instability Cascade in Laser-Plasma Experiments". In: *Phys. Rev. Lett.* 89 (4 2002), p. 045001. URL: https://link.aps.org/doi/10.1103/PhysRevLett.89.045001.

[95] L. D. Landau. "61 - ON THE VIBRATIONS OF THE ELECTRONIC PLASMA". In: *Collected Papers of L.D. Landau*. Ed. by D. TER HAAR. Pergamon, 1965, pp. 445–460. ISBN: 978-0-08-010586-4. URL: https://www.sciencedirect.com/science/article/pii/B9780080105864500663.

[96] Dieter Bauer Peter Mulser. *"High Power LaserMatter Interaction"*. Springer, 2010.

[97] R. Yan et al. "Generating energetic electrons through staged acceleration in the two-plasmon-decay instability in inertial confinement fusion". In: *Phys. Rev. Lett.* 108 (17 2012), p. 175002. URL: https://link.aps.org/doi/10.1103/PhysRevLett.108.175002.

[98] W. M. Manheimer, D. G. Colombant, and J. H. Gardner. "Steady state planar ablative flow". In: *The Physics of Fluids* 25.9 (1982), pp. 1644–1652. eprint: https://aip.scitation.org/doi/pdf/10.1063/1.863956. URL: https://aip.scitation.org/doi/abs/10.1063/1.863956.

[99] G H McCall. "Laser driven implosion experiments". In: *Plasma Physics* 25.3 (1983), pp. 237–285. URL: https://doi.org/10.1088/0032-1028/25/3/001.

[100] David C. Cartwright. *Summary of research for the Inertial Confinement Fusion Program at Los Alamos National Laboratory*. Tech. rep. Los Alamos National Laboratory, 1985.

[101] G H McCall. "Laser-driven implosion experiments". In: *Plasma Physics* 25.3 (1983), pp. 237–285. URL: https://doi.org/10.1088/0032-1028/25/3/001.

[102] P. P. Volosevich and V. B. Rozanov. "Conversion of laser radiation into fast electrons in the LTF problem". In: *ZhETF Pisma Redaktsiiu* 33 (1981), pp. 19–23.

[103] R G Evans. "Laser generation of ultra high pressure". In: *Plasma Physics and Controlled Fusion* 28.1A (1986), pp. 157–164. URL: https://doi.org/10.1088/0741-3335/28/1a/014.

[104] T. H. Tan et al. "CO2 laser driven high density implosion experiments". In: *The Physics of Fluids* 24.4 (1981), pp. 754–758. eprint: https://aip.scitation.org/doi/pdf/10.1063/1.863439. URL: https://aip.scitation.org/doi/abs/10.1063/1.863439.

[105] HELMUT; et. Al. (EDITORS) SCHWARTZ. *"Laser interaction and related plasma phenomena"*. Plenum Pub Corp, 1981.

[106] B. Yaakobi et al. "Preheat measurements in UV-laser target interaction". In: *Optics Communications* 41.5 (1982), pp. 355–359. ISSN: 0030-4018. URL: https://www.sciencedirect.com/science/article/pii/0030401882904126.

[107] X. Ribeyre et al. "Dense plasma heating and Gbar shock formation by a high intensity flux of energetic electrons". In: *Physics of Plasmas* 20.6 (2013), p. 062705. eprint: https://doi.org/10.1063/1.4811473. URL: https://doi.org/10.1063/1.4811473.

[108] Sergei Guskov et al. "Generation of shock waves and formation of craters in a solid material irradiated by a short laser pulse". In: *Quantum Electronics - QUANTUM ELECTRON* 34 (2004), pp. 989–1003.

[109] Sergei Yu Guskov et al. "Efficiency of ablative loading of material upon the fast-electron transfer of absorbed laser energy". In: *Quantum Electronics* 36.5 (2006), pp. 429–434. URL: https://doi.org/10.1070/qe2006v036n05abeh013242.

[110] S. Yu. Guskov et al. "Laser-driven ablation through fast electrons in PALS-experiment at the laser radiation intensity of 150 PW/cm2". In: *Laser and Particle Beams* 32.1 (2014), 177195.

[111] K. Jungwirth et al. "The Prague Asterix Laser System". In: *Physics of Plasmas* 8.5 (2001), pp. 2495–2501. eprint: https://doi.org/10.1063/1.1350569. URL: https://doi.org/10.1063/1.1350569.

[112] K S Guskov and Sergei Yu Guskov. "Efficiency of ablation loading and the limiting destruction depth of material irradiated by a high-power laser pulse". In: *Quantum Electronics* 31.4 (2001), pp. 305–310. URL: https://doi.org/10.1070/qe2001v031n04abeh001940.

[113] V. A. Smalyuk et al. "Role of Hot-Electron Preheating in the Compression of Direct-Drive Imploding Targets with Cryogenic D_2 Ablators". In: *Phys. Rev. Lett.* 100 (18 2008), p. 185005. URL: https://link.aps.org/doi/10.1103/PhysRevLett.100.185005.

[114] T.R Boehly et al. "Initial performance results of the OMEGA laser system". In: *Optics Communications* 133.1 (1997), pp. 495–506. ISSN: 0030-4018. URL: https://www.sciencedirect.com/science/article/pii/S0030401896003252.

[115] A. R. Christopherson et al. "Direct Measurements of DT Fuel Preheat from Hot Electrons in Direct-Drive Inertial Confinement Fusion". In: *Phys. Rev. Lett.* 127 (5 2021), p. 055001. URL: https://link.aps.org/doi/10.1103/PhysRevLett.127.055001.

[116] Ph. Nicolaï et al. "Deleterious effects of nonthermal electrons in shock ignition concept". In: *Phys. Rev. E* 89 (3 2014), p. 033107. URL: https://link.aps.org/doi/10.1103/PhysRevE.89.033107.

[117] S. Atzeni et al. "Studies on targets for inertial fusion ignition demonstration at the HiPER facility". In: *Nuclear Fusion* 49.5 (2009), p. 055008. URL: https://doi.org/10.1088/0029-5515/49/5/055008.

[118] B. Dubroca, J. L. Feugeas, and M. Frank. "Angular moment model for the Fokker-Planck equation". In: *European Physical Journal D* 60.2 (2010), pp. 301–307.

[119] A. Colaïtis, G. Duchateau, P. Nicolaï, and V. Tikhonchuk. "Towards modeling of nonlinear laser-plasma interactions with hydrocodes: The thick-ray approach". In: *Phys. Rev. E* 89 (3 2014), p. 033101. URL: https://link.aps.org/doi/10.1103/PhysRevE.89.033101.

[120] A. Colaïtis et al. "Coupled hydrodynamic model for laser-plasma interaction and hot electron generation". In: *Phys. Rev. E* 92 (4 2015), p. 041101. URL: https://link.aps.org/doi/10.1103/PhysRevE.92.041101.

[121] Michael Touati. "Fast Electron Transport Study for Inertial Confinement Fusion". PhD thesis. SPI University of Bordeaux, 2015. URL: http://www.theses.fr/2015BORD0076.

[122] Cyril Regan. "Modles rduits pour le transport de particules rapides dans le cadre de la fusion par confinement inertiel". Thse de doctorat dirige par Tikhonchuk, Vladimir et Feugeas, Jean-Luc Astrophysique, plasmas, corpuscules Bordeaux 1 2010. PhD thesis. SPI Universite de Bordeaux, 2010. URL: http://www.theses.fr/2010BOR14138.

[123] A. A. Solodov and R. Betti. "Stopping power and range of energetic electrons in dense plasmas of fast-ignition fusion targets". In: *Physics of Plasmas* 15.4 (2008), p. 042707. eprint: https://aip.scitation.org/doi/pdf/10.1063/1.2903890. URL: https://aip.scitation.org/doi/abs/10.1063/1.2903890.

[124] Arnaud Colaitis. "Multiscale description of the laser-plasma interaction : application to the physics of shock ignition in inertial confinement fusion". PhD thesis. SPI University of Bordeaux, 2015. URL: http://www.theses.fr/2015BORD0253.

[125] C Li and Richard Petrasso. "Stopping, Straggling, and Blooming of Directed Energetic Electrons in Hydrogenic and Arbitrary-Z Plasmas". In: *Physical review. E, Statistical, nonlinear, and soft matter physics* 73 (2006), p. 016402.

[126] C. K. Li and R. D. Petrasso. "Stopping of directed energetic electrons in high-temperature hydrogenic plasmas". In: *Phys. Rev. E* 70 (6 2004), p. 067401. URL: https://link.aps.org/doi/10.1103/PhysRevE.70.067401.

[127] S.Yu. Guskov, P.A. Kuchugov, R.A. Yakhin, and N.V. Zmitrenko. "The role of fast electron energy transfer in the problem of shock ignition of laser thermonuclear target". In: *High Energy Density Physics* 36 (2020), p. 100835. ISSN: 1574-1818. URL: https://www.sciencedirect.com/science/article/pii/S1574181820300793.

[128] S Yu Guskov, P A Kuchugov, R A Yakhin, and N V Zmitrenko. "Effect of fast electrons on the gain of a direct-drive laser fusion target". In: *Plasma Physics and Controlled Fusion* 61.10 (2019), p. 105014. URL: https://doi.org/10.1088/1361-6587/ab400e.

[129] S Yu Guskov, P A Kuchugov, R A Yakhin, and N V Zmitrenko. "Effect of fast electrons on the gain of a direct-drive laser fusion target". In: *Plasma Physics and Controlled Fusion* 61.10 (2019), p. 105014. URL: https://doi.org/10.1088/1361-6587/ab400e.

[130] W. L. Shang et al. "Electron Shock Ignition of Inertial Fusion Targets". In: *Phys. Rev. Lett.* 119 (19 2017), p. 195001. URL: https://link.aps.org/doi/10.1103/PhysRevLett.119.195001.

[131] E. Llor Aisa et al. "Dense plasma heating and shock wave generation by a beam of fast electrons". In: *Physics of Plasmas* 22.10 (2015), p. 102704. eprint: https://doi.org/10.1063/1.4933119. URL: https://doi.org/10.1063/1.4933119.

[132] A. Curcio et al. "Imaging plates calibration to X-rays". In: *Journal of Instrumentation* 11.05 (2016), pp. C05011–C05011. URL: https://doi.org/10.1088/1748-0221/11/05/c05011.

[133] B. R. Maddox et al. "High-energy x-ray backlighter spectrum measurements using calibrated image plates". In: *Review of Scientific Instruments* 82.2 (2011), p. 023111. eprint: https://doi.org/10.1063/1.3531979. URL: https://doi.org/10.1063/1.3531979.

[134] K. Zeil et al. "Absolute response of Fuji imaging plate detectors to picosecond-electron bunches". In: *Review of Scientific Instruments* 81.1 (2010), p. 013307.

[135] A. L. Meadowcroft, C. D. Bentley, and E. N. Stott. "Evaluation of the sensitivity and fading characteristics of an image plate system for x-ray diagnostics". In: *Review of Scientific Instruments* 79.11 (2008), p. 113102. eprint: https://doi.org/10.1063/1.3013123. URL: https://doi.org/10.1063/1.3013123.

[136] G. Jackson Williams et al. "Calibration and equivalency analysis of image plate scanners". In: *Review of Scientific Instruments* 85.11 (2014), 11E604. eprint: https://doi.org/10.1063/1.4886390. URL: https://doi.org/10.1063/1.4886390.

[137] Guillaume Boutoux et al. "Validation of modelled imaging plates sensitivity to 1-100 keV X-rays and spatial resolution characterisation for diagnostics for the " PETawatt Aquitaine Laser "". In: *Review of Scientific Instruments* 87 (2016).

[138] T. Bonnet et al. "Response functions of imaging plates to photons, electrons and 4He particles". In: *Review of Scientific Instruments* 84.10 (2013), p. 103510. eprint: https://doi.org/10.1063/1.4826084. URL: https://doi.org/10.1063/1.4826084.

[139] F. Ingenito et al. “Comparative calibration of IP scanning equipment”. In: *Journal of Instrumentation* 11.05 (2016), pp. C05012–C05012. URL: https://doi.org/10.1088/1748-0221/11/05/c05012.

[140] Thomas Bonnet. “Caractrisation et optimisation de sources d’lectrons et de photons produites par laser dans les domaines du keV et du MeV”. Thse de doctorat dirige par Gobet, Franck et Tarisien, Mehdi Astrophysique, Plasmas et Corpuscules Bordeaux 1 2013. PhD thesis. SPI University of Bordeaux, 2013. URL: http://www.theses.fr/2013BOR15248.

[141] Nesrine Rabhi. “Charged particle diagnostics for PETAL, calibration of the detectors and development of the demonstrator”. PhD thesis. SPI University of Bordeaux, 2016. URL: http://www.theses.fr/2016BORD0339.

[142] C. D. Chen et al. “A Bremsstrahlung spectrometer using k-edge and differential filters with image plate dosimeters”. In: *Review of Scientific Instruments* 79.10 (2008), 10E305.

[143] P. Koester et al. “Bremsstrahlung cannon design for shock ignition relevant regime”. In: *Review of Scientific Instruments* 92.1 (2021), p. 013501. eprint: https://doi.org/10.1063/5.0022030. URL: https://doi.org/10.1063/5.0022030.

[144] O Klimo, J Psikal, V T Tikhonchuk, and S Weber. “Two-dimensional simulations of laser–plasma interaction and hot electron generation in the context of shock-ignition research”. In: *Plasma Physics and Controlled Fusion* 56.5 (2014), p. 055010. URL: https://doi.org/10.1088/0741-3335/56/5/055010.

[145] C. Stoeckl, W. Theobald, S. P. Regan, and M. H. Romanofsky. “Calibration of a time-resolved hard-x-ray detector using radioactive sources”. In: *Review of Scientific Instruments* 87.11 (2016), 11E323. eprint: https://aip.scitation.org/doi/pdf/10.1063/1.4960599. URL: https://aip.scitation.org/doi/abs/10.1063/1.4960599.

[146] C. Stoeckl et al. “Hard x-ray detectors for OMEGA and NIF”. In: *Review of Scientific Instruments* 72.1 (2001), pp. 1197–1200. eprint: https://doi.org/10.1063/1.1322621. URL: https://doi.org/10.1063/1.1322621.

[147] M. Hohenberger et al. “Time-resolved measurements of the hot-electron population in ignition-scale experiments on the National Ignition Facility (invited)”. In: *Review of Scientific Instruments* 85.11 (2014), p. 11D501. eprint: https://doi.org/10.1063/1.4890537. URL: https://doi.org/10.1063/1.4890537.

[148] A. Morace and D. Batani. “Spherically bent crystal for X-ray imaging of laser produced plasmas”. In: *Nuclear Instruments and Methods in Physics Research Section A: Accelerators, Spectrometers, Detectors and Associated Equipment* 623.2 (2010). 1rs International Conference on Frontiers in Diagnostics Technologies, pp. 797–800. ISSN: 0168-9002. URL: https://www.sciencedirect.com/science/article/pii/S0168900210003864.

[149] L. C. Jarrott et al. “Calibration and characterization of a highly efficient spectrometer in von Hamos geometry for 7-10 keV x-rays”. In: *Review of Scientific Instruments* 88.4 (2017), p. 043110. eprint: https://doi.org/10.1063/1.4981793. URL: https://doi.org/10.1063/1.4981793.

[150] P. M. Nilson et al. "A high-resolving-power x-ray spectrometer for the OMEGA EP Laser (invited)". In: *Review of Scientific Instruments* 87.11 (2016), p. 11D504. URL: https://aip.scitation.org/doi/abs/10.1063/1.4961076.

[151] K. U. Akli et al. "Temperature sensitivity of Cu K_α imaging efficiency using a spherical Bragg reflecting crystal". In: *Physics of Plasmas* 14.2 (2007), p. 023102. eprint: https://doi.org/10.1063/1.2431632. URL: https://doi.org/10.1063/1.2431632.

[152] P. Palmeri, G. Boutoux, D. Batani, and P. Quinet. "Effects of target heating on experiments using Kα and Kβ diagnostics". In: *Phys. Rev. E* 92 (3 2015), p. 033108. URL: https://link.aps.org/doi/10.1103/PhysRevE.92.033108.

[153] W. Seka et al. "Convective stimulated Raman scattering instability in UV laser plasmas". In: *The Physics of Fluids* 27.8 (1984), pp. 2181–2186. eprint: https://aip.scitation.org/doi/pdf/10.1063/1.864844. URL: https://aip.scitation.org/doi/abs/10.1063/1.864844.

[154] Paul Neumayer et al. "A pulsed-laser calibration system for the laser backscatter diagnostics at the Omega laser". In: *Review of Scientific Instruments* 79.10 (2008), 10F548. eprint: https://doi.org/10.1063/1.2953413. URL: https://doi.org/10.1063/1.2953413.

[155] J. D. Moody et al. "Backscatter measurements for NIF ignition targets (invited)". In: *Review of Scientific Instruments* 81.10 (2010), p. 10D921. eprint: https://doi.org/10.1063/1.3491035. URL: https://doi.org/10.1063/1.3491035.

[156] Edward Moses and Craig Wuest. "The National Ignition Facility: Status and Plans for Laser Fusion and High-Energy-Density Experimental Studies". In: *Fusion Science and Technology* 43 (2003), pp. 420–427.

[157] Craig R. Wuest George H. Miller Edward I. Moses. "The National Ignition Facility". In: *Optical Engineering* 43 (2004), p. 12.

[158] L.J. Waxer et al. "High-Energy Petawatt Capability for the Omega Laser". In: *Opt. Photon. News* 16.7 (2005), pp. 30–36. URL: http://www.osa-opn.org/abstract.cfm?URI=opn-16-7-30.

[159] M. Nicolaizeau and P. Vivini. "LMJ status: Second bundle commissioning and assessment of first years of service". In: *Proceedings of SPIE - The International Society for Optical Engineering* 10084 (2017). URL: https://www.scopus.com/inward/record.uri?eid=2-s2.0-85021963110&doi=10.1117%2f12.2250216&partnerID=40&md5=096991ce764768eed98b59b51b6098cc.

[160] N. Blanchot et al. "1.15 PW–850 J compressed beam demonstration using the PETAL facility". In: *Opt. Express* 25.15 (2017), pp. 16957–16970. URL: http://www.opticsexpress.org/abstract.cfm?URI=oe-25-15-16957.

[161] Dimitri Batani et al. "The HiPER project for inertial confinement fusion and some experimental results on advanced ignition schemes". In: *Plasma Physics and Controlled Fusion* (2011).

[162] Petra Koester et al. "Recent results from experimental studies on laserplasma coupling in a shock ignition relevant regime". In: *Plasma Physics and Controlled Fusion* 55 (2013), p. 124045.

[163] O Renner, M Šmíd, D Batani, and L Antonelli. "Suprathermal electron production in laser-irradiated Cu targets characterized by combined methods of x-ray imaging and spectroscopy". In: *Plasma Physics and Controlled Fusion* 58.7 (2016), p. 075007. URL: https://doi.org/10.1088/0741-3335/58/7/075007.

[164] Cristoforetti, G. et al. "Experimental observation of parametric instabilities at laser intensities relevant for shock ignition". In: *EPL* 117.3 (2017), p. 35001. URL: https://doi.org/10.1209/0295-5075/117/35001.

[165] Dimitri Batani et al. "Progress in understanding the role of hot electrons for the shock ignition approach to inertial confinement fusion". In: *Nuclear Fusion* 59 (2018).

[166] L. Antonelli et al. "Laser-driven strong shocks with infrared lasers at intensity of 1016 W/cm2". In: *Physics of Plasmas* 26.11 (2019), p. 112708. eprint: https://doi.org/10.1063/1.5119697. URL: https://doi.org/10.1063/1.5119697.

[167] P. M. Celliers et al. "Line-imaging velocimeter for shock diagnostics at the OMEGA laser facility". In: *Review of Scientific Instruments* 75.11 (2004), pp. 4916–4929. eprint: https://doi.org/10.1063/1.1807008. URL: https://doi.org/10.1063/1.1807008.

[168] Koki Kawasaki et al. "The role of hot electrons on ultrahigh pressure generation relevant to shock ignition conditions". In: *High Energy Density Physics* 37 (2020), p. 100892.

[169] Ph. Nicola et al. "Effect of nonthermal electrons on the shock formation in a laser driven plasma". In: *Physics of Plasmas* 22.4 (2015), p. 042705. eprint: https://doi.org/10.1063/1.4917472. URL: https://doi.org/10.1063/1.4917472.

[170] B. Yaakobi et al. "Measurement of preheat due to fast electrons in laser implosions". In: *Physics of Plasmas* 7.9 (2000), pp. 3714–3720. eprint: https://doi.org/10.1063/1.1287217. URL: https://doi.org/10.1063/1.1287217.

[171] B. Yaakobi et al. "Fast-electron generation in long-scale-length plasmas". In: *Physics of Plasmas* 19.1 (2012), p. 012704. eprint: https://doi.org/10.1063/1.3676153. URL: https://doi.org/10.1063/1.3676153.

[172] D. H. Froula et al. "Saturation of the Two-Plasmon Decay Instability in Long-Scale-Length Plasmas Relevant to Direct-Drive Inertial Confinement Fusion". In: *Phys. Rev. Lett.* 108 (16 2012), p. 165003. URL: https://link.aps.org/doi/10.1103/PhysRevLett.108.165003.

[173] D. T. Michel et al. "Experimental Validation of the Two-Plasmon-Decay Common-Wave Process". In: *Phys. Rev. Lett.* 109 (15 2012), p. 155007. URL: https://link.aps.org/doi/10.1103/PhysRevLett.109.155007.

[174] M. Hohenberger et al. "Shock-ignition relevant experiments with planar targets on OMEGA". In: *Physics of Plasmas* 21.2 (2014), p. 022702. eprint: https://doi.org/10.1063/1.4865373. URL: https://doi.org/10.1063/1.4865373.

[175] A. A. Solodov et al. "Measurements of hot-electron temperature in laser-irradiated plasmas". In: *Physics of Plasmas* 23.10 (2016), p. 102707. eprint: https://doi.org/10.1063/1.4965905. URL: https://doi.org/10.1063/1.4965905.

[176] S. Zhang et al. "Experimental study of hot electron generation in shock ignition relevant high-intensity regime with large scale hot plasmas". In: *Physics of Plasmas* 27.2 (2020), p. 023111. eprint: https://doi.org/10.1063/1.5119250. URL: https://doi.org/10.1063/1.5119250.

[177] W. Theobald et al. "Enhanced hot-electron production and strong-shock generation in hydrogen-rich ablators for shock ignition". In: *Physics of Plasmas* 24.12 (2017), p. 120702. eprint: https://doi.org/10.1063/1.4986797. URL: https://doi.org/10.1063/1.4986797.

[178] Theobald W. et al. "Spherical shock-ignition experiments with the 40 + 20-beam configuration on OMEGA". In: *Physics of Plasmas* 19.10 (2012), p. 102706. eprint: https://doi.org/10.1063/1.4763556. URL: https://doi.org/10.1063/1.4763556.

[179] W. Theobald et al. "Spherical strong-shock generation for shock-ignition inertial fusion". In: *Physics of Plasmas* 22.5 (2015), p. 056310. eprint: https://aip.scitation.org/doi/pdf/10.1063/1.4920956. URL: https://aip.scitation.org/doi/abs/10.1063/1.4920956.

[180] E. Llor Aisa et al. "The role of hot electrons in the dynamics of a laser-driven strong converging shock". In: *Physics of Plasmas* 24.11 (2017), p. 112711. eprint: https://doi.org/10.1063/1.5003814. URL: https://doi.org/10.1063/1.5003814.

[181] R. Nora et al. "Gigabar Spherical Shock Generation on the OMEGA Laser". In: *Phys. Rev. Lett.* 114 (4 2015), p. 045001. URL: https://link.aps.org/doi/10.1103/PhysRevLett.114.045001.

[182] S. Skupsky et al. "Improved laser beam uniformity using the angular dispersion of frequency modulated light". In: *Journal of Applied Physics* 66.8 (1989), pp. 3456–3462. eprint: https://doi.org/10.1063/1.344101. URL: https://doi.org/10.1063/1.344101.

[183] D. Batani et al. "Physics issues for shock ignition". In: *Nuclear Fusion* 54.5 (2014), p. 054009. URL: https://doi.org/10.1088/0029-5515/54/5/054009.

[184] H A Baldis et al. "Parametric instabilities in large nonuniform laser plasmas". In: *Plasma Physics and Controlled Fusion* 34.13 (1992), pp. 2077–2081. URL: https://doi.org/10.1088/0741-3335/34/13/043.

[185] M. Lafon et al. "Direct-driveignition designs with mid-Z ablators". In: *Physics of Plasmas* 22.3 (2015), p. 032703. eprint: https://doi.org/10.1063/1.4914835. URL: https://doi.org/10.1063/1.4914835.

[186] V. A. Smalyuk et al. "Implosion Experiments using Glass Ablators for Direct-Drive Inertial Confinement Fusion". In: *Phys. Rev. Lett.* 104 (16 2010), p. 165002. URL: https://link.aps.org/doi/10.1103/PhysRevLett.104.165002.

[187] B. Yaakobi et al. "Measurements of the divergence of fast electrons in laser-irradiated spherical targets". In: *Physics of Plasmas* 20.9 (2013), p. 092706. eprint: https://doi.org/10.1063/1.4824008. URL: https://doi.org/10.1063/1.4824008.

[188] M. J. Rosenberg et al. "Origins and Scaling of Hot-Electron Preheat in Ignition-Scale Direct-Drive Inertial Confinement Fusion Experiments". In: *Phys. Rev. Lett.* 120 (5 2018), p. 055001. URL: https://link.aps.org/doi/10.1103/PhysRevLett.120.055001.

[189] A. A. Solodov et al. "Hot-electron generation at direct-drive ignition-relevant plasma conditions at the National Ignition Facility". In: *Physics of Plasmas* 27.5 (2020), p. 052706. eprint: https://doi.org/10.1063/1.5134044. URL: https://doi.org/10.1063/1.5134044.

[190] A. Tentori et al. "Experimental characterization of hot-electron emission and shock dynamics in the context of the shock ignition approach to inertial confinement fusion". In: *Physics of Plasmas* 28.10 (2021), p. 103302. eprint: https://doi.org/10.1063/5.0059651. URL: https://doi.org/10.1063/5.0059651.

[191] D. K. Bradley et al. "High speed gated x ray imaging for ICF target experiments (invited)". In: *Review of Scientific Instruments* 63.10 (1992), pp. 4813–4817. eprint: https://doi.org/10.1063/1.1143571. URL: https://doi.org/10.1063/1.1143571.

[192] O. V. Gotchev et al. "KB PJX A streaked imager based on a versatile x-ray microscope coupled to a high-current streak tube (invited)". In: *Review of Scientific Instruments* 75.10 (2004), pp. 4063–4068. eprint: https://doi.org/10.1063/1.1786649. URL: https://doi.org/10.1063/1.1786649.

[193] S. Agostinelli et al. "Geant4 a simulation toolkit". In: *Nuclear Instruments and Methods in Physics Research Section A: Accelerators, Spectrometers, Detectors and Associated Equipment* 506.3 (2003), pp. 250–303. ISSN: 0168-9002. URL: https://www.sciencedirect.com/science/article/pii/S0168900203013688.

[194] Salvat. *PENELOPE: A code system for Monte Carlo simulation of electron and photon transport*. Nuclear Energy Agency, 2019.

[195] S. T. Perkins et al. *Tables and graphs of atomic subshell and relaxation data derived from the LLNL Evaluated Atomic Data Library (EADL), Z = 1–100*. Tech. rep. 'LLNL', 1991. URL: https://www.osti.gov/biblio/10121422.

[196] Xavier Llovet, Cedric Powell, Francesc Salvat, and Aleksander Jablonski. "Cross Sections for Inner-Shell Ionization by Electron Impact". In: *Journal of Physical and Chemical Reference Data* 43 (2014).

[197] Jason F. Myatt et al. "LPSE: A 3-D wave-based model of cross-beam energy transfer in laser-irradiated plasmas". In: *Journal of Computational Physics* 399 (2019), p. 108916. ISSN: 0021-9991. URL: http://www.sciencedirect.com/science/article/pii/S0021999119306217.

[198] Jocelain Trela. "Effect of hot-electrons on the hydrodynamic of shocks and implosions for shock ignition". PhD thesis. SPI Université de Bordeaux, 2019. URL: http://www.theses.fr/s204285.

[199] J. J. MacFarlane et al. "SPECT3D - A multi-dimensional collisional-radiative code for generating diagnostic signatures based on hydrodynamics and PIC simulation output". In: *High Energy Density Physics* 3.1-2 (2007), pp. 181–190.

[200] A. Colaitis et al. "Coupled hydrodynamic model for laser-plasma interaction and hot electron generation". In: *Phys. Rev. E* 92 (4 2015), p. 041101. URL: https://link.aps.org/doi/10.1103/PhysRevE.92.041101.

[201] Geant4 Collaboration. *Physics Reference Manual*. 2017.

[202] S.D. Baton et al. "Preliminary results from the LMJ-PETAL experiment on hot electrons characterization in the context of shock ignition". In: *High Energy Density Physics* 36 (2020), p. 100796. ISSN: 1574-1818. URL: https://www.sciencedirect.com/science/article/pii/S1574181820300550.

[203] C. Rousseaux et al. "Laser parametric instability experiments of a 3ω, 15kJ, 6-ns laser pulse in gas-filled hohlraums at the Ligne d'Intgration Laser facility". In: *Physics of Plasmas* 22.2 (2015), p. 022706. eprint: https://doi.org/10.1063/1.4907779. URL: https://doi.org/10.1063/1.4907779.

[204] C. Reverdin et al. "SPECTIX, a PETAL-PLUS X-ray spectrometer: design, calibration and preliminary tests". In: *Journal of Instrumentation* 13.01 (2018), pp. C01005–C01005. URL: https://doi.org/10.1088/1748-0221/13/01/c01005.

[205] R. Rosch et al. "First set of gated x-ray imaging diagnostics for the Laser Megajoule facility". In: *Review of Scientific Instruments* 87.3 (2016), p. 033706. eprint: https://aip.scitation.org/doi/pdf/10.1063/1.4942930. URL: https://aip.scitation.org/doi/abs/10.1063/1.4942930.

[206] Roberto Piazza. *" I capricci del caso : introduzione alla statistica, al calcolo della probabilit e alla teoria degli errori"*. Springer, 2009.

[207] John R. Taylor. *An Introduction to Error Analysis: The Study of Uncertainties in Physical Measurements*. 2 Sub. University Science Books, 1996. ISBN: 093570275X. URL: http://www.amazon.com/Introduction-Error-Analysis-Uncertainties-Measurements/dp/093570275X%3FSubscriptionId%3D13CT5CVB80YFWJEPWS02%26tag%3Dws%26linkCode%3Dxm2%26camp%3D2025%26creative%3D165953%26creativeASIN%3D093570275X.

[208] R. M. More, K. Warren, D. Young, and G. Zimmeraman. "Atomic Physics In Inertial Confiement Fusion". In: *Applied Atomic Collision Physics Volume II*. Lawrence Livermore National Laboratory, Livermore CA 94550, 1981.

[209] Richard M. More. "Processes in non ideal Plasmas". In: *29th Scottish Universities Summer School in Physics*. Lawrence Livermore National Laboratory, Livermore CA 94550, 1986, pp. 135–215.

[210] S Atzeni, A Schiavi, and J R Davies. "Stopping and scattering of relativistic electron beams in dense plasmas and requirements for fast ignition". In: *Plasma Physics and Controlled Fusion* 51.1 (2008), p. 015016. URL: https://doi.org/10.1088/0741-3335/51/1/015016.

[211] Martin J. Berger. "Monte Carlo Calculation of the Penetration and Diffusion of Fast Charged Particles". In: *Methods in computational physics, Volume 1*. Academic Press New York and London, 1963, pp. 135–215.

[212] J.M. Fernandez Varea, R. Mayol, J. Baro, and F. Salvat. "On the theory and simulation of multiple elastic scattering of electrons". In: *Nuclear Instruments and Methods in Physics Research Section B: Beam Interactions with Materials and Atoms* 73.4 (1993), pp. 447–473. ISSN: 0168-583X. URL: https://www.sciencedirect.com/science/article/pii/0168583X9395827R.

[213] Pedro Andreo and Anders Brahme. "Restricted Energy-Loss Straggling and Multiple Scattering of Electrons in Mixed Monte Carlo Procedures". In: *Radiation Research* 100.1 (1984), pp. 16–29. ISSN: 00337587, 19385404. URL: http://www.jstor.org/stable/3576517.

[214] L. Reimer, E. R. Krefting, Kurt Heinrich, and Dale Newbury Harvey Yakowitz. "The Effect of Scattering Models on the Results of Monte Carlo Calculations". In: *Use of Monte Carlo Calculations in Electron Probe Microanalysis and Scanning Electron Microscopy*. NATIONAL BUREAU OF STANDARDS, 1976, pp. 45–60.

[215] J. Baro, J. Sempau, J. M. Fernandez-Varea, and F. Salvat. "PENELOPE: An algorithm for Monte Carlo simulation of the penetration and energy loss of electrons and positrons in matter". In: *Nuclear Instruments and Methods in Physics Research B* 100.1 (1995), pp. 31–46.

[216] J Bar, J Sempau, J.M Fernndez-Varea, and F Salvat. "Simplified Monte Carlo simulation of elastic electron scattering in limited media". In: *Nuclear Instruments and Methods in Physics Research Section B: Beam Interactions with Materials and Atoms* 84.4 (1994), pp. 465–483. ISSN: 0168-583X. URL: https://www.sciencedirect.com/science/article/pii/0168583X94953414.

[217] C. Negreanu, X. Llovet, R. Chawla, and F. Salvat. "Calculation of multiple-scattering angular distributions of electrons and positrons". In: *Radiation Physics and Chemistry* 74.5 (2005), pp. 264–281. ISSN: 0969-806X. URL: https://www.sciencedirect.com/science/article/pii/S0969806X05002239.

[218] S.G. Brush, H.L. Sahlin, and E. Teller. "Monte Carlo Study of a One-Component Plasma. I". In: *jcp* 45.6 (1966), pp. 2102–2118.

[219] Y. T. Lee and R. M. More. "An electron conductivity model for dense plasmas". In: *The Physics of Fluids* 27.5 (1984), pp. 1273–1286. eprint: https://aip.scitation.org/doi/pdf/10.1063/1.864744. URL: https://aip.scitation.org/doi/abs/10.1063/1.864744.

[220] Douglass E. Post Charles J. Joachain. *"Atomic and Molecular Physics of Controlled Thermonuclear Fusion"*. Plenum Press New York and London, 1983, pp. 399–440.

[221] A. Ortner, A. Frank, Blazevic, and M. Roth. "Role of charge transfer in heavy-ion-beam plasma interactions at intermediate energies". In: *Phys. Rev. E* 91 (2 2015), p. 023104. URL: https://link.aps.org/doi/10.1103/PhysRevE.91.023104.

[222] A. Pineau, B. Chimier, S. X. Hu, and G. Duchateau. "Improved modeling of the solid-to-plasma transition of polystyrene ablator for laser direct-drive inertial confinement fusion hydrocodes". In: *Phys. Rev. E* 104 (1 2021), p. 015210. URL: https://link.aps.org/doi/10.1103/PhysRevE.104.015210.

[223] S. X. Hu et al. "First-principles investigations on ionization and thermal conductivity of polystyrene for inertial confinement fusion applications". In: *Physics of Plasmas* 23.4 (2016), p. 042704. eprint: https://doi.org/10.1063/1.4945753. URL: https://doi.org/10.1063/1.4945753.

[224] Francesc Salvat and JosM. Fernndez-Varea. "Semiempirical cross sections for the simulation of the energy loss of electrons and positrons in matter". In: *Nuclear Instruments and Methods in Physics Research Section B: Beam Interactions with Materials and Atoms* 63.3 (1992), pp. 255–269. ISSN: 0168-583X. URL: https://www.sciencedirect.com/science/article/pii/0168583X92951084.

[225] Francesc Salvat and Ricardo Mayol. "Elastic scattering of electrons and positrons by atoms. Schrdinger and Dirac partial wave analysis". In: *Computer Physics Communications* 74.3 (1993), pp. 358–374. ISSN: 0010-4655. URL: https://www.sciencedirect.com/science/article/pii/0010465593900199.

[226] David C. Joy. *"Monte Carlo Modeling for Electron microscopy and Microanalysis"*. Oxford Universit y Press, 1995.

[227] Chr. Moller. "Zur Theorie des Durchgangs schneller Elektronen durch Materie". In: *Annalen der Physik* 406.5 (1932), pp. 531–585. eprint: https://onlinelibrary.wiley.com/doi/pdf/10.1002/andp.19324060506. URL: https://onlinelibrary.wiley.com/doi/abs/10.1002/andp.19324060506.

[228] L. D. Landau, V. B. Berestetskii, E. M. Lifshitz, and L. P. Pitaevskii. *"Relativistic Quantum Theory. Vol. 4"*. Pergamon Press, 1971.

[229] E. M. Lifshitz L. D. Landau. *"Quantum Mechanics: Non-Relativistic Theory. Vol. 3"*. Pergamon Press, 1958.

[230] F. Rohrlich and B. C. Carlson. "Positron-Electron Differences in Energy Loss and Multiple Scattering". In: *Phys. Rev.* 93 (1 1954), pp. 38–44. URL: https://link.aps.org/doi/10.1103/PhysRev.93.38.

[231] J. M. Jauch and F. Rohrlich. *The theory of photons and electrons. The relativistic quantum field theory of charged particles with spin one-half.* 2nd ed. Texts and Monographs in Physics. Berlin: Springer, 1976. ISBN: 978-3-642-80953-8, 978-3-642-80951-4.

[232] E. M. Lifshitz L. D. Landau. *"The Classical Theory of Fields. Vol. 2"*. Pergamon Press, 1959.

[233] Sir Harrie Stewart Wilson Massey Nevill F. Mott. *"Theory of Atomic Collisions"*. Oxford University Press; 3 edizione, 1965.

[234] A. S. Davydov. *"Quantum Mechanics"*. Pergamon Press, 1965.

[235] John C. Stewart and Manuel Rotenberg. "Wave Functions and Transition Probabilities in Scaled Thomas-Fermi Ion Potentials". In: *Phys. Rev.* 140 (5A 1965), A1508–A1519. URL: https://link.aps.org/doi/10.1103/PhysRev.140.A1508.

[236] E. Nardi and Z. Zinamon. "Energy deposition by relativistic electrons in high-temperature targets". In: *Phys. Rev. A* 18 (3 1978), pp. 1246–1249. URL: https://link.aps.org/doi/10.1103/PhysRevA.18.1246.

[237] Vauzour Benjamin. "tude exprimentale du transport d'lectrons rapides dans le cadre de l'allumage rapide pour la fusion inertielle". Thse de doctorat dirige par Tikhonchuk, Vladimir et Santos, Joao Jorge Astrophysique, Plasmas, Corpuscules Bordeaux 1 2012. PhD thesis. University of Bordeaux, 2012. URL: http://www.theses.fr/2012BOR14496.

[238] Arnaud Debayle. "Theoretical study of Ultra High Intensity laser-produced high-current relativistic electron beam transport through solid targets". Thse de doctorat dirige par Tikhonchuk, Vladimir Sciences physiques et de l'ingnieur. Astrophysique, plasmas et corpuscules Bordeaux 1 2008. PhD thesis. SPI Universite de Bordeaux, 2008. URL: http://www.theses.fr/2008BOR13708.

[239] Laurent Yvan Andr Gremillet. "Etude thorique et exprimentale du transport des lectrons rapides dans l'interaction laser-solide trs haut flux". Thse de doctorat dirige par Amiranoff, Franois Physique des plasmas Palaiseau, cole polytechnique 2001. PhD thesis. Ecole Politechnique, 2001, 1 vol. (406 p.) URL: http://www.theses.fr/2001EPXX0022.

[240] Roberto Piazza. *"Note di fisica statistica (con qualche accordo)"*. Springer, 2011.

[241] Roberto Piazza. *"Statistical Physics, A Prelude and Fugue for Engineers"*. Springer, 2016.

[242] J. D. Jackson. *Classical Electrodynamics*. Second Edition. New York: Jhon Wiley and Sons, New York, 1975.

[243] G. Wentzel. "Zwei Bemerkungen ber die Zerstreuung korpuskularer Strahlen als Beugungserscheinung". In: *Zeitschrift fr Physik volume* 40 (1926), pp. 590–593.

[244] Richard Henry Dalitz and Rudolf Ernst Peierls. "On higher Born approximations in potential scattering". In: *Proceedings of the Royal Society of London. Series A. Mathematical and Physical Sciences* 206.1087 (1951), pp. 509–520. eprint: https://royalsocietypublishing.org/doi/pdf/10.1098/rspa.1951.0085. URL: https://royalsocietypublishing.org/doi/abs/10.1098/rspa.1951.0085.

[245] B. P. Nigam, M. K. Sundaresan, and Ta-You Wu. "Theory of Multiple Scattering: Second Born Approximation and Corrections to Molière's Work". In: *Phys. Rev.* 115 (3 1959), pp. 491–502. URL: https://link.aps.org/doi/10.1103/PhysRev.115.491.

[246] J. W. MOTZ, HAAKON OLSEN, and H. W. KOCH. "Electron Scattering without Atomic or Nuclear Excitation". In: *Rev. Mod. Phys.* 36 (4 1964), pp. 881–928. URL: https://link.aps.org/doi/10.1103/RevModPhys.36.881.

[247] S. Goudsmit and J. L. Saunderson. "The Multiple Scattering of Charged Particles". In: *Phys. Rev.* 56 (1 1939), pp. 122–123. URL: https://link.aps.org/doi/10.1103/PhysRev.56.122.2.

[248] S. Goudsmit and J. L. Saunderson. "Multiple Scattering of Electrons". In: *Phys. Rev.* 57 (1 1940), pp. 24–29. URL: https://link.aps.org/doi/10.1103/PhysRev.57.24.

[249] S. Goudsmit and J. L. Saunderson. "Multiple Scattering of Electrons. II". In: *Phys. Rev.* 58 (1 1940), pp. 36–42. URL: https://link.aps.org/doi/10.1103/PhysRev.58.36.

[250] H. W. Lewis. "Multiple Scattering in an Infinite Medium". In: *Phys. Rev.* 78 (5 1950), pp. 526–529. URL: https://link.aps.org/doi/10.1103/PhysRev.78.526.

[251] Gert Moliere. "Theorie der Streuung schneller geladener Teilchen I. Einzelstreuung am abgeschirmten Coulomb-Feld". In: *Zeitschrift fr Naturforschung A* 2.3 (1947), pp. 133–145. URL: https://doi.org/10.1515/zna-1947-0302.

[252] Siegfried Flugge. *Practical Quantum Mechanics*. Springer, 1994.

[253] M. Stegun Irene A. Abramowitz. *Handbook of Mathematical Functions*. Dover books on Advanced Mathematics, 1972.

[254] H. Bethe. "Zur Theorie des Durchgangs schneller Korpuskularstrahlen durch Materie". In: *Annalen der Physik* 397.3 (1930), pp. 325–400. eprint: https://onlinelibrary.wiley.com/doi/pdf/10.1002/andp.19303970303. URL: https://onlinelibrary.wiley.com/doi/abs/10.1002/andp.19303970303.

[255] H. Bethe. "Bremsformel fur Elektronen relativistischer Geschwindigkeit". In: *Zeitschrift fur Physik* 76.5-6 (1932), pp. 293–299.

[256] Niels Bohr. "XXII. The Penetration of Atomic Particles Through Matter". In: *The Penetration of Charged Particles through Matter (19121954)*. Ed. by Jens Thorsen. Vol. 8. Niels Bohr Collected Works. Elsevier, 1987, pp. 423–568. URL: https://www.sciencedirect.com/science/article/pii/S1876050308701725.

[257] U Fano. "Penetration of Protons, Alpha Particles, and Mesons". In: *Annual Review of Nuclear Science* 13.1 (1963), pp. 1–66. eprint: https://doi.org/10.1146/annurev.ns.13.120163.000245. URL: https://doi.org/10.1146/annurev.ns.13.120163.000245.

[258] Emilio Segre. *"Nuclei and Particles: An Introduction to Nucler and Subnuclear Physics"*. "Advanced Book Program", 1964.

[259] Enrico Fermi. "The Ionization Loss of Energy in Gases and in Condensed Materials". In: *Phys. Rev.* 57 (6 1940), pp. 485–493. URL: https://link.aps.org/doi/10.1103/PhysRev.57.485.

[260] David Bohm and David Pines. "A Collective Description of Electron Interactions: III. Coulomb Interactions in a Degenerate Electron Gas". In: *Phys. Rev.* 92 (3 1953), pp. 609–625. URL: https://link.aps.org/doi/10.1103/PhysRev.92.609.

[261] R.M. Sternheimer, M.J. Berger, and S.M. Seltzer. "Density effect for the ionization loss of charged particles in various substances". In: *Atomic Data and Nuclear Data Tables* 30.2 (1984), pp. 261–271. ISSN: 0092-640X. URL: https://www.sciencedirect.com/science/article/pii/0092640X84900020.

[262] Stephen M. Seltzer and Martin J. Berger. "Bremsstrahlung spectra from electron interactions with screened atomic nuclei and orbital electrons". In: *Nuclear Instruments and Methods in Physics Research B* 12.1 (1985), pp. 95–134.

[263] M. J. Berger and S. M. Seltzer. "Tables of Energy Losses and Ranges of Electrons and Positrons". In: *Studies in Penetration of Charged Particles in Matter*. 1964, p. 205.

[264] M. J. Berger et al. "Report 37". In: *Journal of the International Commission on Radiation Units and Measurements* os19.2 (2016), NP–NP. ISSN: 1473-6691. eprint: https://academic.oup.com/jicru/article-pdf/os19/2/NP/9586864/jicruos19-NP.pdf. URL: https://doi.org/10.1093/jicru/os19.2.Report37.

[265] National Institute of Standards and Technology. *ESTAR Database*. https://physics.nist.gov/PhysRefData/Star/Text/method.html.

[266] Yalovets A.P. Valchuk Volkov N.B. "Energy losses of fast electrons in a beam plasma". In: *Fizika Plazmy* 21 (2 1995), pp. 167–172.

[267] C. Deutsch et al. "Interaction Physics of the Fast Ignitor Concept". In: *Phys. Rev.* 77 (12 1996).

[268] Deutsch C. et al. "Erratum: Interaction Physics of the Fast Ignitor Concept [Phys. Rev. Lett. 77, 2483 (1996)]". In: *Phys. Rev. Lett.* 85 (5 2000), pp. 1140–1140. URL: https://link.aps.org/doi/10.1103/PhysRevLett.85.1140.

[269] A. Okabayashi et al. "Stopping and transport of fast electrons in superdense matter". In: *Physics of Plasmas* 20.8 (2013), p. 083301. eprint: https://doi.org/10.1063/1.4816812. URL: https://doi.org/10.1063/1.4816812.

[270] R. M. Sternheimer. "The Density Effect for the Ionization Loss in Various Materials". In: *Phys. Rev.* 88 (4 1952), pp. 851–859. URL: https://link.aps.org/doi/10.1103/PhysRev.88.851.

[271] A.P.L. Robinson et al. "Theory of fast electron transport for fast ignition". In: *Nuclear Fusion* 54.5 (2014), p. 054003. URL: https://doi.org/10.1088/0029-5515/54/5/054003.

[272] E. J. McGuire. "Born-approximation electron ionization cross sections for $Al^{n+}(0 \leq n \leq 11)$ and some ions of the Na isoelectronic sequence". In: *Phys. Rev. A* 26 (1 1982), pp. 125–131. URL: https://link.aps.org/doi/10.1103/PhysRevA.26.125.

[273] J. A. Harte and Y. T. Lee. "Suprathermal Electron Energy Loss in Partially Ionized Matter". In: *Lawrence Livermore National Laboratory 1982 Laser Program Annual Report*. Lawrence Livermore National Laboratory, Livermore CA 94550, 1983, pp. 175–177.

[274] M. Stanley Livingston and H. A. Bethe. "Nuclear Physics C. Nuclear Dynamics, Experimental". In: *Rev. Mod. Phys.* 9 (3 1937), pp. 245–390. URL: https://link.aps.org/doi/10.1103/RevModPhys.9.245.

[275] David Pines and David Bohm. "A Collective Description of Electron Interactions: II. Collective vs Individual Particle Aspects of the Interactions". In: *Phys. Rev.* 85 (2 1952), pp. 338–353. URL: https://link.aps.org/doi/10.1103/PhysRev.85.338.

[276] Glenn F. Knoll. *Radiation detection and measurement / Glenn F. Knoll*. English. 2nd ed. Wiley New York, 1989, xix, 754 p. : ISBN: 0471815047.

[277] A. Colatis et al. "Real and complex valued geometrical optics inverse ray-tracing for inline field calculations". In: *Physics of Plasmas* 26.3 (2019), p. 032301. eprint: https://doi.org/10.1063/1.5082951. URL: https://doi.org/10.1063/1.5082951.

[278] J.J Honrubia and J Meyer ter Vehn. "Three-dimensional fast electron transport for ignition-scale inertial fusion capsules". In: *Nuclear Fusion* 46.11 (2006), pp. L25–L28. URL: https://doi.org/10.1088/0029-5515/46/11/l02.

[279] J J Honrubia and J Meyer ter Vehn. "Ignition of pre-compressed fusion targets by fast electrons". In: *Journal of Physics: Conference Series* 112.2 (2008), p. 022055. URL: https://doi.org/10.1088/1742-6596/112/2/022055.

[280] Oleg N. Vassiliev. *"Monte Carlo Methods for Radiation Transport"*. Springer, 2017.

[281] Francesc Salvat, Aleksander Jablonski, and Cedric J. Powell. "elsepaDirac partial-wave calculation of elastic scattering of electrons and positrons by atoms, positive ions and molecules (New Version Announcement)". In: *Computer Physics Communications* 261 (2021), p. 107704. ISSN: 0010-4655. URL: https://www.sciencedirect.com/science/article/pii/S0010465520303465.

[282] Kuhl Tonya L. Laub Charlie. *How Bad is Good? A Critical Look at the Fitting of Reflectivity Models using the Reduced Chi-Square Statistic*. University Lecture. 2016.

[283] Rene Andrae, Tim Schulze-Hartung, and Peter Melchior. *Dos and don'ts of reduced chi-squared*. 2010. arXiv: 1012.3754 [astro-ph.IM].

[284] M. E. Rose A. Bethe and L. P. Smith. "The Multiple Scattering of Electrons". In: *Proceedings of the American Philosophical Society* 78.4 (1938), pp. 573–585. ISSN: 0003049X. URL: http://www.jstor.org/stable/984803.

[285] H. A. Bethe. "Molière's Theory of Multiple Scattering". In: *Phys. Rev.* 89 (6 1953), pp. 1256–1266. URL: https://link.aps.org/doi/10.1103/PhysRev.89.1256.

[286] M Touati et al. "A reduced model for relativistic electron beam transport in solids and dense plasmas". In: *New Journal of Physics* 16.7 (2014), p. 073014. URL: https://doi.org/10.1088/1367-2630/16/7/073014.